Transport de charge dans le photovoltaïque par imagerie multidimensionnelle de luminescence

Adrien Bercegol

▶ **To cite this version:**

HAL Id: tel-02879907
https://pastel.hal.science/tel-02879907

Submitted on 24 Jun 2020

THÈSE DE DOCTORAT

DE L'UNIVERSITÉ PSL

Préparée à l'École Nationale Supérieure de Chimie de Paris

Transport de charge dans le photovoltaïque par imagerie multidimensionnelle de luminescence

Charge transport in photovoltaics via multidimensional luminescence imaging

Soutenue par
Adrien BERCEGOL
Le 17.12.2019

Ecole doctorale n° 397
Physico-Chimie des matériaux

Spécialité
Physico-chimie

Composition du jury :

Emmanuelle, DELEPORTE Professeur, ENS Paris Saclay	*Rapporteur*
Xavier, MARIE Professeur, INSA Toulouse	*Rapporteur*
Zhuoying, CHEN Chargée de recherche, ESPCI	*Présidente du jury*
Sam D. STRANKS Lecturer, Cambridge University	*Examinateur*
Bernard, GEFFROY Ingénieur-chercheur, CEA	*Examinateur*
Daniel, ORY Ingénieur-chercheur, EDF R&D	*Examinateur*
Laurent, LOMBEZ Chargé de recherche, IPVF	*Directeur de thèse*

ACKNOWLEDGEMENTS

TABLE OF CONTENTS

FIGURE LIST

TABLE LIST

Index of symbols

Mathematical notation	Unit	Signification
$a(E)$	[ ]	Absorptivity
A_{cell} ; A_{field}	cm²	Area of the cell, the field
A_{21}	cm³/s	Einstein spontaneous emission coefficient
A_k	[ ]	Coefficient for each contribution U_k (section 3.3.4)
α	/cm	Absorption coefficient
α_{1sun}	/cm	Equivalent absorption coefficient at 1 sun
α_λ	/cm	Absorption coefficient at wavelength lambda
α_{PL}	/cm	Mean absorption coefficient on PL spectrum
$\alpha_0 d$	[ ]	Generic absorption parameter in sub-bandgap absorption model
$(b_i)_{i \in [1,m]}$	counts	Measurement on the photodetector (m measurement)
B_{12}	cm⁶/s	Einstein absorption coefficient
B_{21}	cm⁶/s	Einstein stimulated emission coefficient
β_k	/cm	Spatial pulsation of each contribution U_k (section 3.3.4)
c_0	m/s	Light speed (celerity)
D_{eff}	cm²/s	Effective diffusion coefficient
D_n ; D_p	cm²/s	Diffusion coefficient for electron / hole
$\Delta\mu$	eV	Quasi-Fermi level splitting (also QFLS)
Δn ; Δp	/cm³	Photogenerated electron/hole
$\delta\lambda$	nm	Grating bandwidth of the VBG
$\vec{\epsilon}$	V/cm	Electric field
E_i	eV	Intrinsic energy level
E_{peak}	eV	I_{PL} peak energy
E_{ph}	eV	Photon energy
$E_{f,n}$; $E_{f,p}$	eV	Fermi level for electron, hole
$\underline{E_g}$	eV	Bandgap
ε_0	F/m	Vacuum permittivity
EQE_{PV} (EQE_{LED})	[ ]	External quantum efficiency of a PV (or LED) device
η	%	PCE
E_u	eV	Characteristic energy for sub-bandgap absorption
f_{model}	[ ]	Generic model function for fitting purpose
f_{system}	[ ]	Spectral sensitivity of an optical system
f_{las}	Hz	Laser frequency
f_{vb} ; f_{cb}	[ ]	Saturation factor for V_b (C_b)

f_{wr}	[ ]	Wrinkle correction factor for I_{PL} profile
$FWHM$	cm	FWHM of the gaussian distribution
G_{1sun}	/cm²/s	Generation at 1 sun (AM1.5G)
g_{corr}	[ ]	PR correction factor (section 5.3.4)
G_{em}	[ ]	Electron multiplying gain on the em-ICCD
G_I	[ ]	Intensifier gain on the em-ICCD
G_n ; G_p	/cm³/s	Generation rate (electron/hole)
g_{rec} ; $\widetilde{g_{rec}}$	/cm³/s	Recycling term (w/ monochromatic PL assumption)
H_k	[ ]	Hadamard matrix
$\overline{h}$	eV s	Reduced Planck constant
I_{CCD}	counts	Rectified images on the HI CCD
$I_{CCD}*$	counts	Raw images on the HI CCD
$I_{CCD,d}$ (*)	counts	Dark rectified (raw) images on the HI CCD
I_I^x	[ ]	Neutral iodide in perovskite crystal
I_i^x	[ ]	Interstitial iodide in perovskite crystal
I_{las} ; $I_{las,d}$	counts	(dark) Rectified images from the laser
I_{ref}	counts	Reference spectrum for HI calibration
I_{trans}	counts	Transmitted spectrum on the HI set*up
$J_{n,diff}$; $J_{p,diff}$	C/cm²/s	Diffusion current (electron/hole)
$J_{n,drift}$; $J_{p,drift}$	C/cm²/s	Drift current (electron/hole)
J_n ; J_p	C/cm²/s	Total current
$\dot{j_\gamma}$	ph/s/eV	Photon flux at energy E (emitted by dS_{em} in solid angle $d\Omega_{em}$)
k_B	m² kg s⁻² K⁻¹	Boltzmann constant
K_p	ph.eV/cm3/s	Simplification parameter introduced in eq.(1-7)
K_{A1} ; K_{A2}	cm⁶/s	Auger recombination coefficients
L_{1sun}	cm	Equivalent diffusion length at 1 sun
L_{eff}	cm	Effective diffusion length
L_n ; L_p	cm	(Electron/hole) diffusion length
L_{PR}	cm	Photon recycling length
λ_{las}	nm	Wavelength (of the laser)
μ_n ; μ_p	cm²/V/s	Mobility (electron/hole)
n	/cm³	Electron concentration
n_0 ; p_0	/cm³	Intrinsic electron / hole concentration
n_{1sun}	/cm³	Charge carrier concentration at 1 sun (AM1.5G)
N_{acc}	[ ]	Number of accumulations on the CCD
n_{cts}/n_{ph}	[ ]	Absolute calibration factor for HI set-up
n_T	/cm³	Trapped electron concentration
N_T	/cm³	Trap site concentrations
$n_\gamma(E)$; dn_γ	ph/cm³	(contribution to) density of photon gas at energy E
n_{opt}	[ ]	Optical index
Ω	sr	Solid angle
Ω_{eff}	sr	Collection solid angle

Ω_{em} ; $d\Omega_{\mathrm{em}}$	sr	(Elementary) Emission solid angle
p	/cm^3	Hole concentration
p_{escape}	[ ]	Escape probability for photon
p_{rm}	[ ]	Generic parameter vector for fitting purpose
Φ_0	ph/cm^2/s	Fluence
Φ_{BB}	ph/s/eV/cm^3	Black-body radiation
φ_{c}	rad	Critical (total reflexion) angle
Φ_{prop}	ph/cm^3/s/eV	Propagated flux
$(\Pi_{\mathrm{i,k}})$ $i\in[1,m];k\in[1,\mathrm{n}]$	[ ]	Pattern matrix (m patterns of n pixel)
Ψ	rad	Angle between normal to dS_{em} and $d\Omega_{\mathrm{em}}$
q	eV	Electron charge
R_{aug}	/cm^3/s	Auger recombination rate
R_{em}	/s	Emission rate of a defect
R_{∞}	[ ]	Residual from convergence of spatial profile
R_{int}	/cm^2/s	Interface recombination rate
r_{max}	cm	Maximum radius considered on the fitting window
R_{n} ; R_{p}	/cm^3/s	Recombination rate (electron/hole)
R_{nrad}	/cm^2/s	Non-radiative recombination rate
R_{pop}	cm^3/s	Capture rate of a defect
R_{rad}	/cm^3/s	Radiative recombination rate
R_{t}	[ ]	Local spectral ratio on HI set-up
$R_{\mathrm{X}}(E)$	[ ]	Reflection coefficient at energy E
$R_{1\rightarrow2}$	/s	Transition rate from state 1 to 2
$R_{2\rightarrow1}$	/s	Transition rate from state 2 to 1
R_{eh}	cm^3/s	Internal radiative recombination coefficient
$R_{\mathrm{eh}}*$	cm^3/s	External radiative coefficient (corrected from reabsorption)
R_{sp}	ph/cm^3/s/eV	Spontaneous emission rate
S_{c}	cm/s	Contact recombination velocity
S_{front} ; S_{back}	cm/s	(front / back) Surface recombination velocity
S_{pix}	cm^2	Surface imaged by a pixel
S_{em} ; dS_{em}	cm^2	(Elementary) Emission surface
σ_{cv}	cm	Kernel of convolution
σ_{n} ; σ_{p}	cm^2	Capture cross-section of a defect
T	K	Temperature
$\underline{t}_{\mathrm{del}}$	ns	Gating delay on the em-ICCD
t_{exp}	s	Exposure time
t_{∞}	ns	Convergence time of spatial profile
t_{las}	ns	Detection time of the laser
t_{width}	ns	Gating width on the em-ICCD
τ_{1sun}	ns	Equivalent lifetime at 1 sun
τ_{n} ; τ_{p}	ns	(Electron/hole) lifetime
Θ	[ ]	Coefficient for sub-bandgap absorption model
U_k	[ ]	Sinusoidal contribution in chapter 3

V	V	Voltage (chapter 6)
V ; dV	cm^3	(Elementary) Volume
V_{bi}	V	Built-in voltage
V_{I}^{+}	[ ]	Iodide vacancy in perovskite crystal
$<\vec{v_{\text{n}}}>$; $<\vec{v_{\text{p}}}>$	cm/s	Average velocity of electron/hole
V_{oc}	V	Open circuit voltage
$V_{\text{oc}}^{\text{rad}}$	V	Open-circuit voltage at the radiative limit
V_{abs}	cm^3	Absorber volume
w_{SCR}	cm	Width of the SCR
X	[ ]	Generic signal (space-, time- and/or spectrally-resolved)
X^*	[ ]	Reconstructed sisgnal
(X_{k}) $k \in [1,n]$	[ ]	Spatially resolved signal (n pixel)
z_0	cm	Absorber thickness

Index of abbreviations

Abbreviation	Meaning
ABX_3	Perovskite crystalline structure
AM1.5G	Reference solar spectrum
C_b	Conduction band
CCD	Charge coupled device
CIGS	Cu(In,Ga)Se : Copper, Indium, Gallium diselenide
CMOS	Complementary Metal Oxide Semiconductor
DFT	Density functional theory
DMD	Digital Mirror Device
DSSC	Dye-sensitized solar cell
EDS	Electron dispersive spectroscopy
em-ICCD	Electron-multiplied intensified CCD
EQE	External quantum efficiency
ETL	Electron transport layer
FA	Formamidinium (CH_3NH_2)
FTO	Fluoride-doped tin oxide
HI	Hyperspectral imager
HTL	Hole transport layer
I_{EL}	Electroluminescence intensity
I_L	Luminescence intensity
I_{PL}	Photoluminescence intensity
III-V	Semi-conductor with atom from group 3 & 5
IPVF	Institut du photovoltaïque d'Ile-de-France
ITO	Indium tin oxide
I-V	Intensity-voltage characteristics
KPFM	Kelvin probe force microscopy
LED	Light-emitting device
MA	Methylammonium (CH_3NH_3)
MAPI	Methylammonium lead iodide ($CH_3NH_3PbI_3$)
MBE	Molecular beam epitaxy
MCP	Multi-channel plate
MEMS	Micro-electromechanical system
MOCVD	Metalorganic chemical vapor deposition
NA	Numerical aperture
PCE	Power conversion efficiency
PR	Photon recycling
PSC	Perovskite solar cells
PV	Photovoltaic
QFL	Quasi-Fermi level
QFLS	Quasi-Fermi level splitting (also $\Delta\mu$)
SCR	Space charge region

SEM	Scanning electron microscope
SLM	Spatial light modulator
SPI	Single pixel imaging
SRH	Shockley-Read-Hall
TCO	Transparent conductive oxide
THz	TeraHertz
TR-FLIM	Time-resolved fluorescence imaging
TRMC	Time-resolved microwave conductivity
TRPL	Time-resolved PL
UV	Ultraviolet
V_b	Valence band
V_{oc}	Open-circuit voltage
VBG	Volume Bragg grating
WF	Wide-field
Z_1, Z_2	Zones for TRPL analysis

Introduction

Photovoltaic (PV) devices offer a direct conversion of light source into electricity, providing a much-needed solution to meet climate targets and move towards a low-carbon economy. Indeed, the electricity consumption of mankind in 2018 could be matched by the production of 100 000 km^2 of photovoltaic panels (0.07% of Earth surface)[1]. The international energy agency (IEA) forecasts that PV energy will overcome wind energy in 2025, as well as hydro in 2030 and coal in 2040 (in terms of installed capacity)[1]. This is not only due to its ever-decreasing cost of production but also to its continuous increase of power conversion efficiency (PCE) over the last decades. The influence of both factors is explicit in Figure 0(a), which displays the average module price (in USD/Watt peak) as a function of cumulative module shipments. In order to approach the theoretical limit for power conversion efficiency, which is about 31% in classical devices and about 47% in tandem devices combining two absorber materials[2,3], it is crucial to work on both the electronic and optical performances, both affecting the output power.

In this thesis, we focus on PV materials and devices produced at IPVF (Institut du Photovoltaïque d'Ile-de-France). This research institute notably aims at developing tandem solar cells. They consist in the superposition of an already industrially mature Silicon solar cell, which efficiently collects the near-infrared photons (NIR) and of another solar cell with an absorber having a wider bandgap. Several materials and device architectures are currently investigated, but they should convert more efficiently the energetic photons (blue, UV) and transmits the red/NIR photons to the bottom cell (Si). This is sketched in Figure 0(b), in which the power spectrum for each cell is represented, along with the power spectrum available in the solar radiation incident on Earth surface.
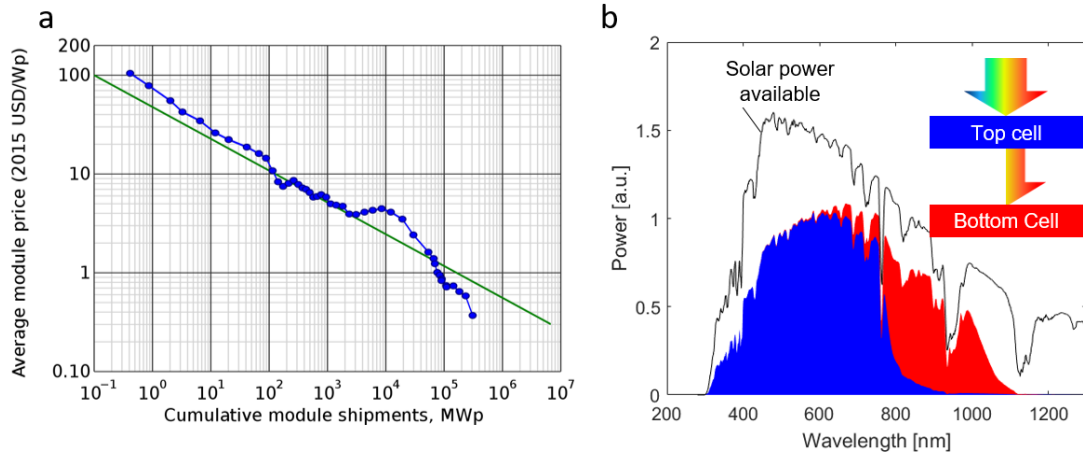
Figure 0 (a) The green line, which shows that module price decays by 20% for each doubling of the cumulative shipment (also Swanson's law[4]) is a fit to the blue experimental line. (b) Power conversion sketched for a tandem solar cell under solar spectrum. The top cell absorbs the more energetic photons and transmits the remaining to the bottom cell. Thermalization and transmission losses are accounted.

In optoelectronics, and in the field of photovoltaics in particular, photoluminescence (I_{PL}) analysis methods are used to optimize devices. Being contactless and non-destructive, they can be used at different steps of the life cycle of a solar cell, from the growth (in-situ) to the use (in-operando). For instance, their use for in-line quality checks during production, or for fault detection on photovoltaic fields is already reported[5,6]. I_{PL} analysis methods are based on the fact that the luminescence intensity is directly related to the product of charge carrier concentrations (electron / hole). They therefore constitute a powerful tool for characterizing charge transport mechanisms (see chapter 1). In this thesis, we focus on describing methods based on multidimensional luminescence imaging. This technique includes spatial, spectral and temporal analysis of the light flux emitted by photovoltaic materials under excitation. Its implementation requires the development of optical assemblies as well as digital methods of data processing.

Two set-ups have been mostly used throughout this doctoral work: (i) the hyperspectral imager (HI, section 2.1), which provides access to spectrally-resolved images (one image per wavelength) and (ii) the time-resolved fluorescence imager (TR-FLIM, section 2.2) which outputs time-resolved images (one image per unit of time). While the HI was already fully assembled when this work began, the TR-FLIM set-up was barely assembled and its development was finished during the thesis. Its two main components are a pulsed laser and a fast camera. Its operating principles will be thoroughly described, and its proof of concept on a reference photovoltaic material (GaAs) will also be presented (chapter 3). It demonstrates that TR-FLIM allows the assessment of transport and recombination properties with a single experiment. We will show how the use of wide-field (WF) illumination and collection allows to get rid of artefacts linked to classical optical microscopy (e.g. confocal microscopy), induced by charge transport away from the illumination zone. Furthermore, this WF illumination constitutes a realistic excitation scenario for PV materials and devices, due to its large area and relatively low power. To go deeper than these already refined study of charge transport in halide perovskites, a new set-up dedicated to 4D I_{PL} imaging was designed and is under development (section 2.3). It allows to acquired 4D I_{PL} data sets (2D spatial + spectral + temporal) by combining the concept of single pixel imaging to a streak camera. In this manuscript, we will describe its operating principles, which are protected by a filed patent, as well as its initial development realized with the help of a master student. A first proof of concept obtained on a perovskite layer will be presented.

These advanced characterization techniques notably enable the study of charge transport in an emerging class of materials with very promising photovoltaic properties: halide perovskites. Solar cells with perovskite absorbers have indeed exhibited a tremendous increase in terms of PCE over the last decade[7,8], while being crafted with abundant and cheap raw materials and using a low thermal budget. Nonetheless, the limiting factors preventing their commercialization are the up-scalability of fabrication techniques, and their long-term stability[9]. Indeed, the fundamental physics and different transport properties of halide perovskites have still not been fully understood and described[10] (section 1.3). Throughout this manuscript, charge carrier diffusion in mixed

cation halide perovskites will be brought to light thanks to several transport experiments. It will also be distinguished from photon recycling, which constitutes a complementary transport mechanism whereby a luminescence photon is reabsorbed and regenerates a charge. The first experiment is based on a surface excitation, after which the charge carriers diffuse in-depth into the perovskite thin film (chapter 4). The second experiment is based on a point excitation, following which the charge transport is essentially radial (chapter 5). In both cases, the diffusion and recombination of charge carriers will be imaged with a high temporal and spectral resolution. This should allow to quantify their impact by means of optimization algorithms that fit the experimental results to physical models (continuity equation).

Imaging methods are also adapted to the investigation of the impact of chemical and morphological inhomogeneities on local optoelectronic properties. This will be illustrated by the study of the influence of wrinkles appearing at the surface of Cs-rich perovskite (section 5.5).

Eventually, we will make use of multidimensional imaging techniques to probe lateral structures featuring a 20μm wide perovskite channel in-between two electrodes (chapter 6). By applying a fast electric bias across the channel ($<$1μs), we isolate the drift of charge carriers from that of the ions composing perovskite. Experiments at larger time scale (electric field applied 10 minutes) will also allow us to image the movement of halide ions. This multi-dimensional experiment should bring us as close as ever to the operating principles of a PV device, which operate with light and bias.

1. Theoretical background

1.1.   LUMINESCENCE ANALYSIS

1.1.1. DETAILED BALANCE

Photovoltaic (PV) devices directly convert energy from light into electricity. In this thesis, we focus mainly on the absorbing material inside PV device. One of its main physical propertie is the bandgap E_g, which is defined as the energy difference between the conduction band (C_b) and the valence band (V_b). It can be seen as an optical absorption threshold as the incident photons with energy $E_{ph} > E_g$ are converted into excited charge carriers: electrons and holes. Each of these two populations can be described by an (electro)chemical potential where their energy difference leads to the appearance of an internal voltage; it is the photovoltaic effect[11].

Absorption and emission compensate each other at thermal equilibrium due to detailed balance considerations, as was first discovered by Kirchoff[12] in 1860. This can be expressed using Einstein coefficients from the quantum theory of radiation inside a two-state system[13] (B_{12} for absorption, B_{21} for stimulated emission and A_{21} for spontaneous emission). Please note that we derive here an internal equilibrium between photon gas and matter, which does not include external illumination such as sunlight. In this formalism, the transitions rates $R_{1\rightarrow2}$ & $R_{2\rightarrow1}$ at thermal equilibrium write:

$$R_{1\rightarrow2} = R_{2\rightarrow1} \Leftrightarrow n_1 B_{12} n_\gamma(E) = n_2 A_{21} + n_2 B_{21} n_\gamma(E) \qquad (1\text{-}1)$$

In eq. (1-1), n_1 & n_2 are the carrier population in state 1 & 2, which would correspond to the ground (e.g. V_b) and excited (e.g. C_b) state in a PV absorber. n_γ corresponds to the density of the photon gas inside the material. The $n_2 A_{21}$ term represents the spontaneous emission rate R_{sp} of a semi-conductor, which was derived in 1954 by van Roosbroeck & Schockley[14]. This rate can be written at a given energy E inside a semi-conductor of optical index n_{opt}:

$$R_{sp}(E) = \frac{n_{opt}^3}{\pi^2 \bar{h}^3 c_0^3} \frac{a(E) E^2}{\exp\left(\frac{E}{k_B T}\right) - 1} \qquad (1\text{-}2)$$

In eq.(1-2), the absorptivity $a(E)$ of the semi-conductor appears (first predicted by Kennard[15]). While it would be 1 in a blackbody, its value varies with E in semi-conductors from ≈ 1 above E_g to ≈ 0 below E_g. Semi-conductors are thus called 'gray-bodies'. As an example, the absorptivity of a perovskite layer ($E_g=1.55$eV) is shown in Figure 1-1, along with the spontaneous emission of this semi-conductor as described in eq. (1-2). It notably differs from the black-body radiation (thermal radiation at 300K). The luminescence I_L is defined as the portion from this photon gas they emit as radiation. For a semi-conductor with E_g around 1 eV at 300K, it is essentially formed by infrared photons.
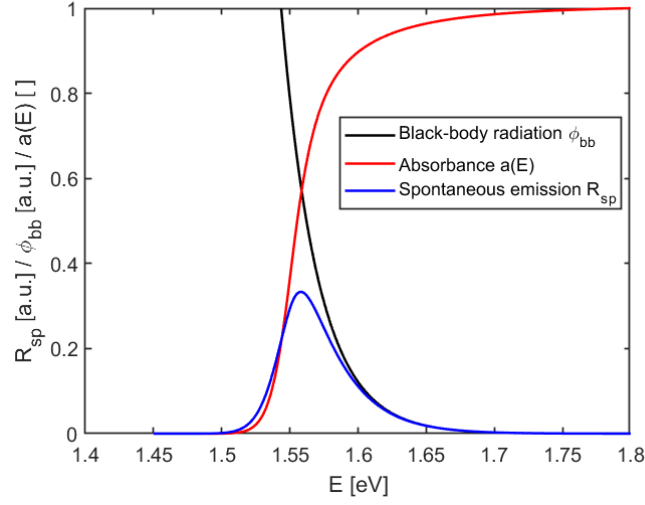
Figure 1-1 Gray-body radiation decomposedas the product of absorptivity a(E) and black-body radiation. Calculation is done for E_g= 1.55eV, E_u=15meV, Θ=1.5, $\alpha_0 d$=10 (see section 1.1.4 for more details on spectrum)

Now, if an external source (light, chemical reaction, electricity) provides energy to the material, the luminescence signal is enhanced by orders of magnitude (10^{20} more intense for a typical perovskite layer under AM1.5G solar spectrum). In the case of light excitation, the radiation is called photoluminescence (I_{PL}), while it is called electroluminescence (I_{EL}) in the case of electric stimulation. Provided that each population (electron, hole) can still be described by a Fermi-Dirac distribution, quasi-Fermi level for electrons ($E_{F,n}$) and holes ($E_{F,o}$) can be defined and used in Lasher-Stern equation[16] (eq. (1-3)). It notably contains the quasi-Fermi level splitting (QFLS, or $\Delta\mu$=$E_{F,n}$-$E_{F,p}$) which quantifies the (electro)chemical potential of charge carriers inside the PV absorber (i.e. the aforementioned internal voltage)[17].

$$R_{sp}(E) = \frac{n_{opt}^3}{\pi^2 \bar{h}^3 c_0^3} \frac{a(E)E^2}{\exp\left(\frac{E\text{-}\Delta\mu}{k_B T}\right)\text{-}1} \tag{1-3}$$

1.1.2. RADIOMETRIC CONCERNS

Knowing the internal spontaneous emission rate is a first step towards characterization by luminescence imaging, but the formula giving the radiated flux is still missing. We now consider a volume V with homogeneous concentration of excited charge carriers n & p. We express in (1-4) its spontaneous emission as a photon density per energy per solid angle, where the isotropicity of R_{sp} explains the $1/4\pi$ factor:

$$R_{sp}(E,\Omega) = \frac{n_{opt}^3}{4\pi\bar{h}^3 \pi^2 c^3} \frac{a(E)E^2}{\exp\left(\frac{E\text{-}\Delta\mu}{k_B T}\right)\text{-}1} \tag{1-4}$$

The flux j_γ going out of V by a small surface dS_{em} (drawn on V), in a direction defined by the solid angle $d\Omega_{em}$ making an angle Ψ with the normal to dS_{em} would then be expressed as:

$$j_\gamma = R_{\text{sp}}(E,\Omega)\, d\Omega_{em} \cos(\Psi)\, dS_{\text{em}} \frac{c_0}{n_{\text{opt}}} \qquad (1\text{-}5)$$
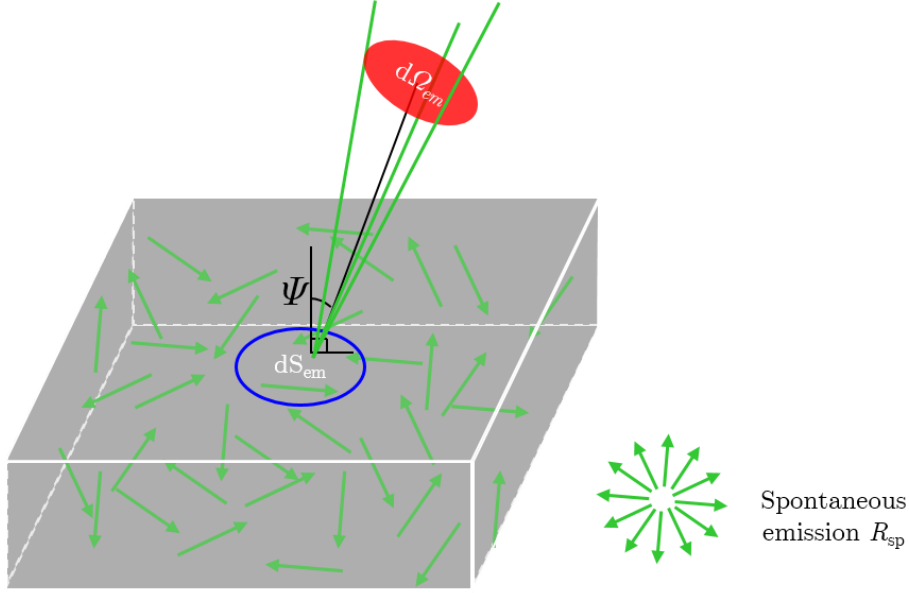
Figure 1-2 Volume of semi-conductor material and photons in equilibrium, in which the spontaneous emission R_{sp} and from which a photon flux j_γ is emitted through dS_{em} in the direction $d\Omega_{em}$.

This equation notably tells us that the intensity incident on a surface at distance r from the emission point decays quadratically as r increases (i.e. as $1/r^2$). Based on the $\cos(\Psi)$ factor appearing in eq. (1-5), the angular repartition of j_γ follows Lambert's cosine law[18]. In the case when V is the absorber in homogeneous excitation conditions, j_γ gives a physical definition of the monitored photoluminescence signal I_{PL}. In this scenario, dS_{em} would correspond to the region of interest at the sample surface, while $d\Omega_{\text{em}}$ would correspond to the collection solid angle from the imaging set-up (see section 2.1.3). But eq. (1-5) also applies for small volumes dV smaller than the absorber itself ($dV < V_{\text{abs}}$). Photon recycling, which consists in charge transport mediated by photons, will be studied in the presented formalism (see section 5.3.4).

A more convenient expression of R_{sp} can be obtained when $E\text{-}\Delta\mu >> k_B T$, which is typically the case for any I_{PL} spectrum considered in this thesis. We approximate the Fermi-Dirac statistics by an exponential term (Boltzmann distribution) $\exp(\text{-}E/k_{\text{B}}T)$ and convert[19] the $\exp(\text{-}\Delta\mu/k_{\text{B}}T)$ term into $np/n_0 p_0$. Also, we abbreviate all the physical constants into a single parameter K_{p}, which reduces eq. (1-4) to:

$$R_{\text{sp}}(E,\Omega) \approx \frac{K_p np}{n_0 p_0}\, a(E) E^2 \exp\left(\frac{\text{-}E}{k_B T}\right) \qquad (1\text{-}6)$$

An interesting application consists in integrating the previous formula at thermal equilibrium, when only intrinsic charge carriers are present. In this case ($np = n_0 p_0$), the radiative recombination writes $R_{\text{eh}} n_0 p_0$ and can be determined with eq. (1-7)[20]. This will be used to determined $n_0 p_0$ from R_{eh} values in section 5.4.3.

$$4\pi \int_E K_p a(E) E^2 \exp\left(\frac{\text{-}E}{k_B T}\right) dE = R_{\text{eh}} n_0 p_0 \qquad (1\text{-}7)$$

1.1.3. MODELING ABSORPTION PROPERTIES

Having a proper expression for the absorptivity $a(E)$ of the considered volume is now required to extract optoelectronic properties from I_{PL} measurements. In this section, we rely on Katahara et al.[21] who allowed a treatment of I_{PL} spectra taking into account sub-bandgap absorption. We first express $a(E)$ as a function of the absorption coefficient $\alpha(E)$ and the thickness of the slab z_0 in eq.(1-8). In a general case, this absorptivity depends on the occupation probabilities of C_{b} and V_{b} (f_{vb} - f_{cb}), which strongly depend on $\Delta\mu$. Yet, we place ourselves in the non-degenerate case where E_{g}-$\Delta\mu > 6k_{\mathrm{B}}\mathrm{T}$, in which C_{b} & V_{b} are not saturated (i.e. f_{vb}-f_{cb}=1). $a(E)$ consequently remains independent from $\Delta\mu$.

$$a(\mathrm{E}) = 1 - \exp\big(\text{-}\,\alpha(\mathrm{E})\,[f_{\mathrm{vb}} \text{-} f_{\mathrm{cb}}]\,z_0\big) \tag{1-8}$$

A slightly enhanced version of this expression includes the multiple reflection in the semi-conductor slab, with reflexion coefficient $R_X(E)$ identical at both front and rear interfaces:

$$a_{\mathrm{RX}}(\mathrm{E}) = \frac{\big(1 \text{-} R_{\mathrm{X}}(E)\big)\big(1 \text{-} \exp\big(\text{-}\,\alpha(E)\,[f_{\mathrm{vb}} \text{-} f_{\mathrm{cb}}]\,z_0\big)\big)}{1 \text{-} R_{\mathrm{X}}(E)\,\exp\big(\alpha(E)\,[f_{\mathrm{vb}} \text{-} f_{\mathrm{cb}}]\,z_0\big)} \tag{1-9}$$

The previous equations are valid for a spatially homogeneous semi-conductor layer with homogeneous $\Delta\mu$ (in particular in-depth), as it cannot be treated as a unique volume with photon gas at equilibrium otherwise. To deal with inhomogeneities, one should divide the slab into infinitesimal volumes coupled to each other via photonic and electronic fluxes[22–24]. In any case, the absorption coefficient remains to be calculated. It is here described by an ideal band-band term convoluted with a sub-bandgap absorption, in which the tail states decay at a pseudo-exponential rate inside the bandgap (coefficient $0.5 < \Theta < 2$ and characteristic energy E_{u}).

$$\alpha(E) = \frac{\alpha_0}{2E_{\mathrm{u}}\Gamma\left(1 + \dfrac{1}{\Theta}\right)} \int_{\text{-}\infty}^{\infty} \exp\left(\text{-}\left|\frac{u}{E_{\mathrm{u}}}\right|^{\Theta}\right)\sqrt{E\text{-}E_{\mathrm{g}}\text{-}u}\; du \tag{1-10}$$

1.1.4. SIX PARAMETERS FOR ONE PHOTOLUMINESCENCE SPECTRUM

Previous considerations leave us with 6 free parameters to describe an I_{PL} spectrum and we will next give a brief overview of their influence. For this purpose, we calculate I_{PL} spectrum emitted by a semi-conductor layer using eqs. (1-5), (1-8) and (1-10). More precisely, we conducted a parameter variation around the expected values for perovskite which is the most studied material in this thesis. Even if these parameters can sometimes be correlated, we vary one parameter at a time for the sake of simplicity.

At first, the temperature of the charge carriers T is investigated in Figure 1-3(a-b). It solely impacts the high-energy section of I_{PL}, in which $a(E>>E_g)\approx1$. Indeed, T does not impact the absorptivity in our non-degenerate model (E_{g}-$\Delta\mu < 6k_{\mathrm{B}}\mathrm{T}$ and so f_{vb}-f_{cb}=1), as displayed in eq. (1-10). Then, the QFLS influence is seen in Figure 1-3(c-d) and it mainly dictates the total intensity of the signal without changing its shape. This observation is relevant for any spectrally-integrated technique for which I_{PL} intensities are compared. For example, if we use a time-resolved sensor with spectral sensitivity

$f_{\text{system}}(E)$, one detects $\int_E f_{\text{system}}(E) I_{\text{PL}}(E,t) dE$. Now, as I_{PL} spectrum is not changed over the decay (constant E_g, T, $\alpha_0 z_0$, Θ, E_u), the temporal signal is proportional to the evolution of $\exp(\Delta\mu(t)/k_B T)$ and hence to the product of charge carrier concentration (np).

The four last parameters all appear in the sub-bandgap absorption derivation. Their influence will be notably seen in the low-energy part of I_{PL} spectrum, in which $a(E)$ decays faster than $E^2 \exp(-E/k_B T)$ increases. We start with the bandgap E_g in Figure 1-3(e-f), which has a direct influence on the energetic position of the absorption on-set, as well as of the I_{PL} peak. The enhanced intensity at lower bandgap lacks physical meaning, it could find its origin in the absorption parameter α_0 in the next parameter $\alpha_0 z_0$. (z_0 being the thickness of the layer). The latter tends to soften the absorption on-set without shifting its energetic position. It remains hardly measured and will generally be fixed to 10 in this thesis, as it is strongly correlated to E_g. The last parameters are dedicated to the tail states in the bandgap. As explicated in the last section, they describe a stretched exponential decay with rate Θ and characteristic energy E_u. As an example, we would have $\Theta=1$ for a mono-exponential decay and E_u would correspond the Urbach energy[25]. The simulations presented in Figure 1-3(i-l) give more insight into their influence on I_{PL} spectra and absorptivity. At fixed Θ value, a smaller E_u describes a "cleaner" bandgap with less tail states. It notably goes with a sharper slope on the I_{PL} spectrum for the lowest E_u. The influence of Θ is less evident and cannot be captured easily with a single parameter variation. It remains noteworthy that Figure 1-3(k) underlines the lack of direct relation between E_g and I_{PL} peak position. Indeed, when sub-bandgap absorption is high ('dirty' bandgap), I_{PL} spectrum has a peak shifted inside the bandgap. The reader is referred to Katahara *et al.* for further insight into sub-bandgap absorption, which is a complex function of Θ & E_u.

A numerical model to extract material properties from I_{PL} measurements was designed[26]. It minimizes the distance between experimental I_{PL} and theoretical ones, by variating the fitting parameters (bandgap, QFLS, sub-bandgap absorption). An optimization approach is conducted.
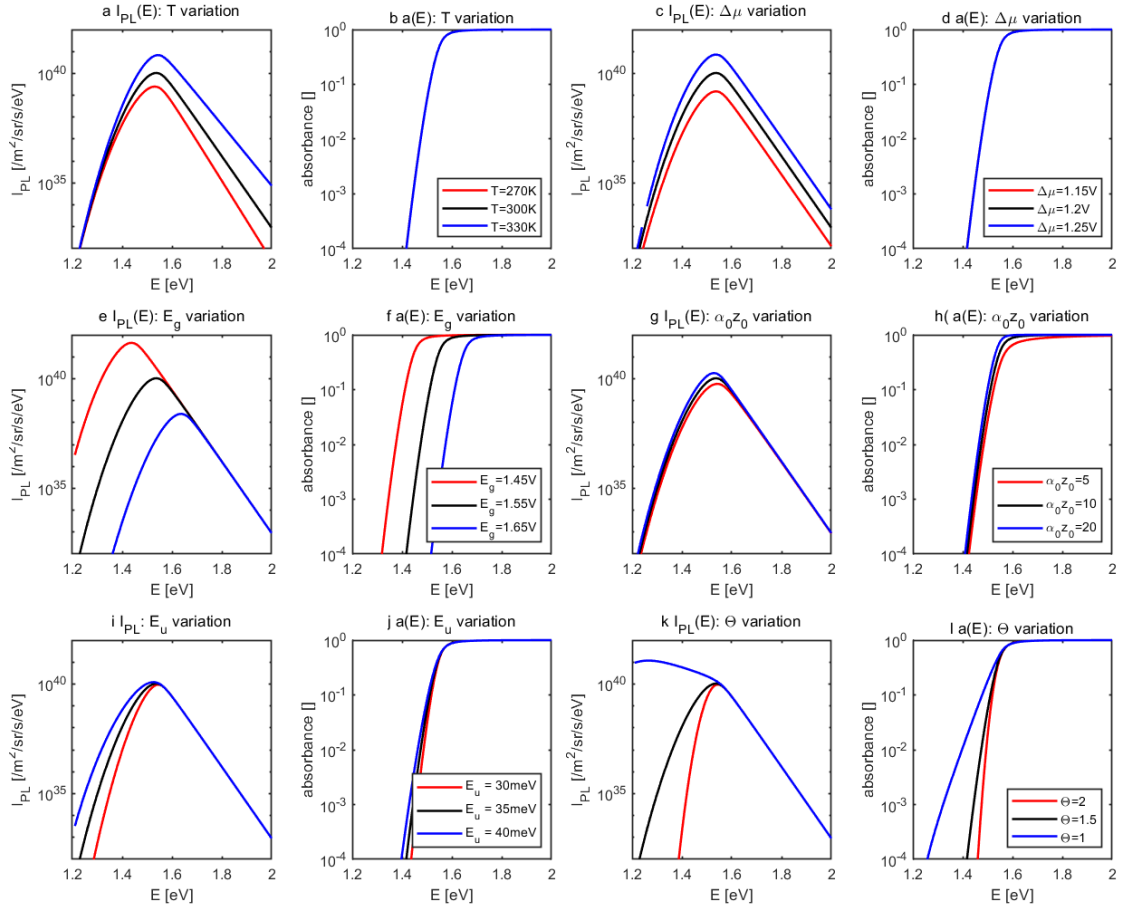
Figure 1-3 Photoluminescence emission and absorptivity calculated from the generalized Planck lawin eq. (1-5). (a) (b) represents T variation, (c) (d) Δμ variation, (e) (f) E_u variation, (g) (h) Θ variation, (i) (j) E_g variation, (k) (l) $\alpha_0 z_0$ variation, while other factors are left constant at values from (T=300K, Δμ=1.2V; E_u=35meV; Θ=1.5; E_g=1.55eV; $\alpha_0 d$=10)

1.2. TRANSPORT IN A SOLAR CELL

In this section we study charge carrier transport (diffusion & recombination) in PV materials. The model applies for steady-state but also for time-resolved measurements having a time step above 40ps (streak camera time resolution). This time scale is significantly longer than carrier-carrier interaction in the considered materials[27,28], which allows us to define each carrier population (n & p) with eq. (1-11) even if the system is out of thermal equilibrium. In the following, intrinsic Fermi level E_i, intrinsic concentrations n_0 & p_0 and photo-generated concentrations Δn & Δp are used:

$$n = n_0 + \Delta n = n_0 \exp\left(\frac{E_{F,n} - E_i}{k_B T}\right)$$
$$p = p_0 + \Delta p = p_0 \exp\left(-\frac{E_{F,p} - E_i}{k_B T}\right)$$

(1-11)

1.2.1. Electron & hole current

Charge carrier in a non-degenerate and non-relativistic gas have a thermal energy of $k_B T/2$ per particle per degree of freedom. Their individual motion has random direction and is frequently interrupted by scattering. In the presence of electric field $\vec{\mathcal{E}}$, an average velocity $<\vec{v_n}>$ ($<\vec{v_p}>$) describes a net motion of the electron population along $\vec{\mathcal{E}}$ direction (Drude model[29]). After solving Newton's law on this population, a steady-state velocity is derived as a function of electron mobility μ_n (μ_p):

$$\begin{aligned} <\vec{v_n}> &= -\mu_n \vec{\mathcal{E}} \\ <\vec{v_p}> &= \mu_p \vec{\mathcal{E}} \end{aligned}$$ (1-12)

This allows us to provide the following expression for drift currents $\overrightarrow{J_{n,drift}}$ ($\overrightarrow{J_{p,drift}}$):

$$\begin{aligned} \overrightarrow{J_{n,drift}} &= -q\,n <\vec{v_n}> = q\,n\,\mu_n \vec{\mathcal{E}} \\ \overrightarrow{J_{p,drift}} &= q\,p <\vec{v_p}> = q\,p\,\mu_p \vec{\mathcal{E}} \end{aligned}$$ (1-13)

The previously introduced mobility depends on the carrier effective mass, which accounts for its interaction with impurity (i.e. dopants[30] or defects) as well as with the lattice (phonons). These interactions lead to scattering, which eventually slow down the field-accelerated particles. We have thus eq. (1-12) which remains for drift velocities below saturation velocities, which is not reached for the moderate electric fields at stake in a solar cell ($\mathcal{E} \approx 10^4$ V/cm & $\mu \approx 1$ cm^2/V/s). In addition to $\overrightarrow{J_{drift}}$, another current must be defined when the charge carrier distribution is inhomogeneous. It is induced by the random thermal motion and cancels itself when carrier distribution homogenize. It includes the diffusion coefficient D_n (D_p), which is directly linked to μ_n (μ_p) by Einstein relations[31] ($D = \mu k_B T/q$):

$$\begin{aligned} \overrightarrow{J_{n,diff}} &= q\,D_n\,\nabla n \\ \overrightarrow{J_{p,diff}} &= -q\,D_p\,\nabla p \end{aligned}$$ (1-14)

The total electron/hole current is $\vec{J} = \overrightarrow{J_{drift}} + \overrightarrow{J_{diff}}$ and can sometimes be zero with two non-zeros drift and diffusion currents. We here give its expression as a function of the quasi-Fermi level for electrons and holes (deriving n expression from (1-11)):

$$\begin{aligned} \overrightarrow{J_n} &= q\,n\,\mu_n \vec{\mathcal{E}} + n\,\mu_n \left(\nabla E_{F,n} - \nabla E_i\right) \\ \overrightarrow{J_p} &= q\,p\,\mu_p \vec{\mathcal{E}} + p\,\mu_p \left(\nabla E_{F,p} - \nabla E_i\right) \end{aligned}$$ (1-15)

Knowing that the electric field directly relates to the gradient of intrinsic level via $q\vec{\mathcal{E}} = \nabla E_i$, we eventually reach a meaningful expression of $\vec{J}$ as a function of the gradient of QFL only:

$$\overrightarrow{J_n} = n\,\mu_n \nabla E_{F,n} \; ; \; \overrightarrow{J_p} = p\,\mu_p \nabla E_{F,p}$$ (1-16)

1.2.2. CONTINUITY EQUATION
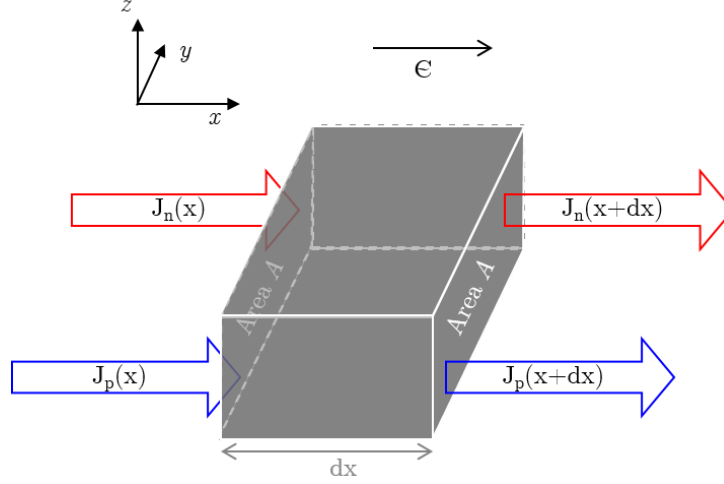
Figure 1-4 Sketch of semi-conductor volume dV=Adx in an electric field E

We consider here a small volume $dV=A dx$ inside a semi-conductor, which contains electron & hole concentration n & p. The derivation presented here applies for strongly symmetric configurations (y-axis and z-axis translation symmetry). During a small time dt, we write n & p variation as a function of the local generation G_n (G_p) and recombination R_n (R_p), also accounting for the incoming electron & hole current J_n (J_p):

$$\partial n(x)\ dV = dt\left[G_n(x)\text{-}R_n(x)\right] dV + A\ dt\left[J_n(x)\text{-}J_n(x+dx)\right] / q$$
$$\Leftrightarrow \frac{\partial n}{\partial t}(x) = G_n(x) \text{-} R_n(x) + \frac{1}{q}\frac{\partial J_n}{\partial x}(x) \tag{1-17}$$

We used a Taylor expansion of $J_n(x)$ in (1-17), which equally applies for holes:

$$\frac{\partial p}{\partial t}(x) = G_p(x) \text{-} R_p(x) \text{-} \frac{1}{q}\frac{\partial J_p}{\partial x}(x) \tag{1-18}$$

Now, we replace J expression with the one derived in the previous section and finally get the generic form for the continuity equation inside PV materials:

$$\frac{\partial n}{\partial t}(x) = G_n(x) \text{-} R_n(x) + D_n \frac{\partial^2 n}{\partial x^2} + \mu_n \frac{\partial(n\,\mathcal{E})}{\partial x}$$
$$\frac{\partial p}{\partial t}(x) = G_p(x) \text{-} R_p(x) + D_p \frac{\partial^2 p}{\partial x^2} \text{-} \mu_p \frac{\partial(p\,\mathcal{E})}{\partial x} \tag{1-19}$$

Several declinations of this differential system prevail to adapt it to the physical observations. In a time-resolved regime following a pulsed excitation, G=0 at all times and the generation depends on the absorption profile of the laser, which gives the initial condition. In a steady-state regime, writing $\partial n/\partial t$=0 removes the need for an initial condition. The intensity of the photogeneration, also called injection level or fluence, is accounted in photons /cm^2/pulse (pulsed regime) or photons/cm^2/s (steady-state regime). In both cases, the spatial boundary conditions will play a crucial role (surface recombination velocity, central symmetry point). While the diffusion current will play a role as soon as $n(x)$ ($p(x)$) is inhomogeneously distributed, the drift current is observed for non-zero $\vec{\mathcal{E}}$. The latter can be externally applied, or internal when electrons and holes

have different distributions ($n{\neq}p$), which leads to ambipolar diffusion[32]. For what concerns R_n (R_p), their various expressions are treated in the next section.

1.2.3. GENERATION AND RECOMBINATION

We here start with radiative recombinations, as they were already described in section 1.1. At thermal equilibrium, they are compensated with radiative generations. For an excited semi-conductor, their rate R_rad is amplified by orders of magnitude in comparison to thermal recombination & generation. They are described by a volumic rate R_eh (defined in (1-7)) and their net contribution to R_n or R_p is:

$$R_\text{rad} = R_\text{eh}\left(np - n_0^2\right) \tag{1-20}$$

In addition to radiative recombinations, Auger recombinations, interface recombination and trap-assisted recombinations contribute to the global decay of charge carrier population. While interface recombinations have a spatial dependence in the semi-conductor and will be treated separately, the other types can be represented on a sole energetic scale, as in Figure 1-5.
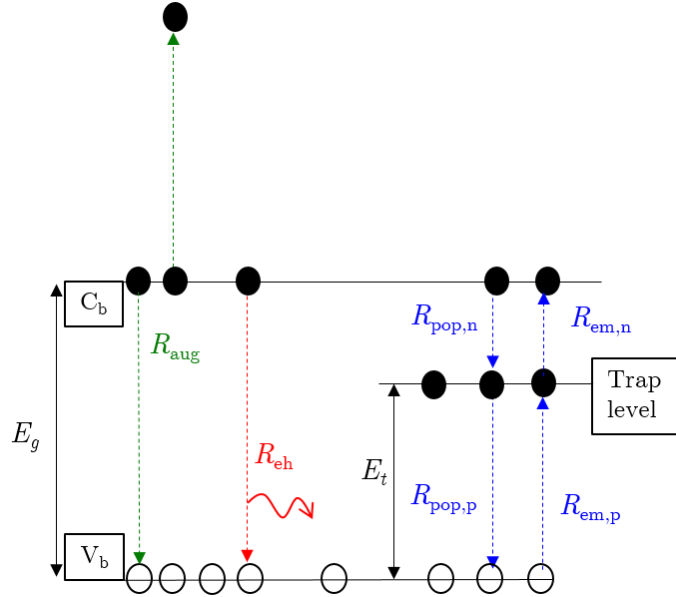
Figure 1-5 Band diagram and recombination type (Auger : green, radiative : red & trap-assisted blue). The various recombination rates are defined in the equations of this section.

The first one relies on the Auger effect[33,34]: as an example, an electron falls back from a certain energetic level (here C_b) to a vacancy in a lower one (here V_b), thereby exciting another charge carrier to an even higher level (here above C_b) This three-particle process has a volumic rate depending strongly on the charge carrier concentration:

$$R_\text{aug} = K_\text{A1}\, n\left(np - n_\text{i}^2\right) + K_\text{A2}\, p\left(np - n_\text{i}^2\right) \tag{1-21}$$

Now remain the trap-assisted non-radiative recombinations. They do not only depend on the pure material band structure (as R_eh, K_A1 or K_A2), but also on the presence of impurities and crystallographic defects, which generate trap for carriers. In the Shockley-Read-Hall (SRH) formalism[35,36], each trap has an energetic level E_t and a capture cross-

section for each carrier type σ_n (σ_p). In a toy model including a single kind of trap, it yields a capture (R_{pop})/emission (R_{em}) rate for each carrier type:

$$\text{Electron}: R_{pop,n} = \sigma_n\, v_{th}\; ; \; R_{em,n} = \sigma_n\, v_{th}\, N_C \exp(-\,(E_c\text{-}E_t)\,/\,k_B T)$$
$$\text{Hole}: R_{pop,p} = \sigma_p\, v_{th}\; ; \; R_{em,p} = \sigma_p\, v_{th}\, N_V \exp(-\,(E_t\text{-}E_v)\,/\,k_B T)$$
(1-22)

At this point, it is very noteworthy that emission rates are thermally activated, whereas capture rates are constant. On the one hand, these traps might appear in the bulk semi-conductor and lead to the differential system presented in (1-23). It is made of rate equations rule the populations in the trap level depending on the trap center concentrations N_T and on the filled trap concentrations n_T:

$$\frac{\partial n}{\partial t} = R_{aug} - R_{rad} - R_{pop,n}\, n\,(N_T - n_T) + R_{em,n}\, n_T$$
$$\frac{\partial n_T}{\partial t} = R_{pop,n}\, n\,(N_T - n_T) - R_{em,n}\, n_T - R_{pop,p}\, n_T\, p + R_{em,p}\,(N_T - n_T)$$
(1-23)
$$\frac{\partial p}{\partial t} = R_{aug} - R_{rad} - R_{pop,p}\, n_T\, p + R_{em,p}\,(N_T\text{-}n_T)$$

Despite not accounting for drift/diffusion currents, this system does not have an analytical solution, and describes processes happening at various time scales. For a shallow trap (i.e. activation energy around $k_B T$), emission rates for electron and hole diverge by orders of magnitude, which makes the numerical solving complex. There are fortunately multiple possibilities to simplify Eq. (1-23), as for example one can neglect the slowest capture/emission rates[37], or forget about Auger recombinations when the *injection* is low ($n<10^{18}$ /cm^3 in perovskite[38]). We will not enumerate them here but the relevant assumptions will be declined in the model section of each experimental chapter (sections 3.3, 4.3, 5.4.1, 6.2.3).

On the other hand, traps might appear at any interface in the system and especially at the boundaries of the absorber. For a 1D model with boundaries at $x=0$ & $x=x_0$, we would model interface recombination of electrons with a surface recombination velocity S:

$$D_n\, \frac{\partial n}{\partial x}(x=x_0) = S_{right}\, n(x=x_0)$$
$$D_n\, \frac{\partial n}{\partial x}(x=0) = S_{left}\, n(x=0)$$
(1-24)

As a partial conclusion, we briefly described and expressed the various recombination currents in a PV material. They are all included in the recombination term R in eq. (1-19), except for the interface recombination which will appear in the boundary conditions of the differential system.

1.2.4. INFLUENCE ON PHOTOVOLTAIC PERFORMANCE

We will now focus on the effective consequences of transport properties on photovoltaic operation, during which a current transports the charge carriers from their generation point inside the absorber to the transport layers/contacts. The extraction is efficient if and only if they do not recombine through Auger or trap assisted phenomenon before reaching the external circuit. For thin film solar cells (CIGS, perovskite)[39], as well

as for modern architectures of Silicon solar cells with passivated contacts[40], this transport is essentially diffusive. The diffusion properties have two complementary aspects: the sensitivity to a carrier concentration gradient (diffusion coefficient D), and the average time available for the diffusion process (lifetime τ). Optimizing the solar cell efficiency thus requires to maximize the average diffusion length ($L_n = \sqrt{D_n \tau_n}$), such as it is at least superior to the cell thickness. However, this might not be a sufficient as illustrated by Rau's reciprocity relations[41], which we detail here under.

The first reciprocity relation between photovoltaic quantum efficiency EQE_{PV} (electrons out / photons in) and electroluminescent emission I_{EL} at the applied potential V writes:

$$I_{\text{EL}}(E) = \text{EQE}_{\text{PV}}(E)\, \phi_{\text{BB}}(E) \left[\exp\left(\frac{qV}{k_{\text{B}}T}\right) - 1 \right] \qquad (1\text{-}25)$$

The second one relates the light emission quantum efficiency of a light-emitting device (LED) EQE_{LED} (photons out / electrons in) to the V_{oc} deficit of the solar cell. This deficit is deduced from the radiative open-circuit voltage $V_{\text{oc}}^{\text{rad}}$ that would be obtained in a device without non-radiative recombination, neither in the bulk nor at the interfaces:

$$\Delta V_{\text{oc}} = V_{\text{oc}}^{\text{rad}} - V_{\text{oc}} = - \frac{k_{\text{B}}T}{q} \ln(\text{EQE}_{\text{LED}}) \qquad (1\text{-}26)$$

They are valid for any device where the main recombination channel is linear to charge carrier concentration[41,42], and were recently extended to p-i-n solar cell structure[43]. They translate analytically the common saying: "a good solar cell is also a good LED". For a variety of solar cell devices, they show that the combination of I_{PL} and I_{EL} measurements allows for a detailed loss analysis[44]. They allow us to easily illustrate the relevance of mobility and lifetime together by considering two extreme cases. One the one hand, a low-mobility cell at the radiative limit (no non-radiative recombination) would have an excellent V_{oc} as $\text{EQE}_{\text{LED}}=1$ (eq. (1-26)). It would however have a low EQE_{PV} as carriers would not be collected and hence a low J_{sc}. It would notably emit photoluminescence both at open-circuit and short-circuit conditions. On the other hand, a high-mobility cell with a short lifetime would have an excellent EQE_{PV} (perfect carrier collection), but a non-optimal EQE_{LED} due to the partial non-radiative recombination of the injected carriers, leading to a V_{oc} deficit (eq. (1-26)). This deficit scales logarithmically and can remain acceptable for relatively high loss in EQE_{LED}, making this type of high-mobility cell preferred for PV applications.

We comment now shortly on perovskite absorbers, which will be the main focus on this dissertation. As we will see, they are limited by trap-assisted and bimolecular recombination (next section and Chapter 4), which constitute a non-linear charge recombination pathway. This hinders the application of reciprocity relations, even in their generalized derivation in a *p-i-n* configuration[43], which would also require doping. Still, these relations allowed to illustrate how crucial is the distinction between mobility and lifetime.

1.3.PEROVSKITE, AN EMERGING CLASS OF MATERIAL

1.3.1. CHEMISTRY & TUNABLE BANDGAP
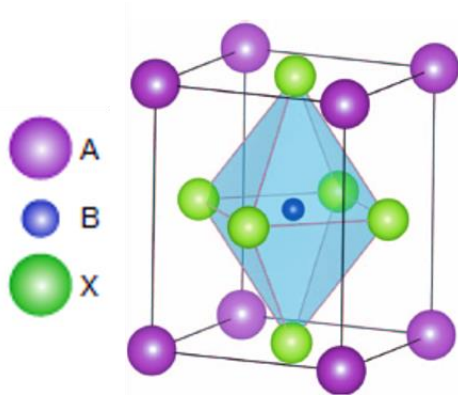
Figure 1-6 Generic perovskite crystal structure (ABX₃).

Perovskite crystal structure ABX_3 was initially discovered in 1839 by mining in the Ural Mountains. This structure has been used to fabricate materials since. Interesting semi-conducting properties in halide perovskites had been spotted in the 90s[45,46], and their most famous representative has been $CH_3NH_3PbI_3$ (MAPI) for 10 years. It was first used[47] as a sensitizer in a dye-sensitized solar cell (DSSC). A wide research field has then developed and several atoms/molecules have been included in the ABX_3 structure to reach higher power conversion efficiency (PCE) and stability. Starting with the B site, it is mostly occupied by Pb for PV applications despite intense research to replace it with the less toxic Sn[48,49]. As displayed in Figure 1-6, the central metallic cation forms an octahedron with halide X^- anions[50–52], which can be either iodide I^-, bromide Br^- or chloride Cl^-. Eventually, various organic & inorganic cations (MA, CH_3NH_2 or FA[50,53,54], Cs[55], Rb[56,57]) can be employed on the A-site. Their screening is done so as to match the remaining size between each lead halide octahedron, according to Goldschmidt tolerance factor[58] and octahedral factor[59]. If a too large cation is used, the 3D-structure collapses and lower-dimensional structures (quasi-2D or 2D[60,61], or even quantum dots[62–64]) are formed. If a too small cation like K is used, it segregates at the grain boundaries/interfaces of the material[65,66]. Cubic phase of the perovskite structure is most studied for PV applications, but halide perovskites transition to tetragonal phase at low temperature (around 150K), as will be discussed in the next section. The polarity of MA / FA molecules leads to ferroelectric peculiarities, which play yet a negligible role in the photovoltaic devices built with halide perovskite[67].

Metal halide perovskite are semi-conductors. Their bandgap is strongly impacted by the chemical composition and especially by the halide. For example, the original MAPI perovskite has its bandgap around 1.55eV, whereas the pure bromide ($MAPbBr_3$) one is 2.3eV and the pure chloride ($MAPbCl_3$) one is above 3eV. On the contrary, changing the A-site cation leads to less significant change, as $FAPbI_3$ ($CsPbI_3$) perovskite has a 1.48eV (1.72eV) bandgap[54]. As the previously listed compounds share a similar crystal structure, their mixing is possible and a full-range covering of the visible spectrum can be realized with this material family. The (in)direct character of the bandgap has been heavily debated recently. The presence of a Rashba splitting, creating an indirect bandgap below the direct one[68–70] was investigated. The rapid radiative recombination observed by ultrafast luminescence analysis allowed to discard this assumption, and the community now agrees on the direct character of the bandgap[71,72]. Charge carrier recombination

phenomena in halide perovskite are discussed further in the next sub-section. Mixed cation, iodide-rich or pure iodide compound are considered throughout this manuscript. Most represented are $(MA_{0.16}FA_{0.84})$ Pb $(I_{0.83}Br_{0.17})_3$ and $Cs_{0.05}(MA_{0.16}FA_{0.84})_{0.95}$ Pb $(I_{0.83}Br_{0.17})_3$. They have been chosen for their high potential as top-cell of Si-based tandem[73,74], as well as for their relative stability.

Lead halide perovskite know several fabrication techniques (sequential deposition[75], solvent engineering[76], spin-coating[77], vapor-assisted solution process[78] or iodide management[79]). Samples considered in this manuscript were produced via spin-coating[77], which consists in depositing drops of a solution containing the species in the desired stoichiometry on a substrate that is then rotated at high speed (several krpm). During this rotation, an anti-solvent is dropped to rinse the perovskite layer. The final annealing step happens at T<150°C. This process, as well as many others considered for perovskite production[75,76,79–81], requires low thermal budget and rather abundant materials. This constitutes one of the reasons for their great potential for producing low-cost electricity. The film composition given in this manuscript corresponds to the composition of the solution deposited, but could differ from the dry composition. Precise quantitative techniques exist to get the dry stoichiometry exist[82] but were not easily accessed at IPVF.

This material family is highly sensitive to environmental stresses such as humidity, oxygen, light[83,84]. The most visual degradation pathway leads to the irreversible breakdown of perovskite crystal structure into the PbI_2 salt (yellowish compound at room temperature), while others lead for example to oxide formation at the exposed interface[85]. We mention here the so-called Hoke effect as an example. It describes the reversible phase segregation of mixed halide perovskite under illumination. It sets an upper limit to bromide integration at approx. 20% on the X-site for (MA,FA)-based perovskite[86,87] (resp. 40% on the X-site for (FA,Cs)-based perovskite[88]). This condition is respected for the samples considered here after. Stability issues are out of the scope of this manuscript, and were mitigated by storing samples in dark vacuum box, and realizing experiments at most after 1 hour of air exposure at room temperature, 50% humidity.

As seen previously, several ions constitute the perovskite crystal structure, which constitutes a soft lattice in which ions move rather easily[89–91]. Diffusion coefficients for halide ions are in the order of magnitude expected for an ionic semi-conductor[91,92]. Any vacancy in this structure (missing atom) creates a defect able to capture a charge carrier. As an example, a positively charged iodide vacancy V_I^+ constitutes a potential electron trap, whereas a neutral iodide (I_I^x) could trap a hole and create a vacancy V_I^+ and an interstitial iodide I_i^x [93]. $(I_I^x+h^+ = I_i^x+V_I^+)$. Furthermore, electron, hole and ion contribute to the definition of the internal electric field, and ion accumulation at interfaces can endanger charge collection. Continuity equation applies to electron/hole, but also to ion. This will be studied in details in Chapter 6.

1.3.2. TRANSPORT PROPERTIES

Studying transport in perovskite materials consist in determining the generation, recombination and diffusion characteristics, so that the continuity equation (eq. (1-19)) can be solved in any excitation & geometrical configuration. For what concerns generation, photon absorption with Beer-Lambert law applies for external illumination (sun, laser) as well as for radiative recycling. Absorption coefficients used in this law have been studied thoroughly in perovskite absorbers. They are displayed for a MAPI crystal in Figure 1-7, in which the phase transition around T=180 K is visible thanks to an abrupt change of bandgap. These absorption spectra also present excitonic features enhancing the absorption at $E=E_g$ at low temperature[94], which vanish at room temperature due to the weak exciton binding energy[95–97].
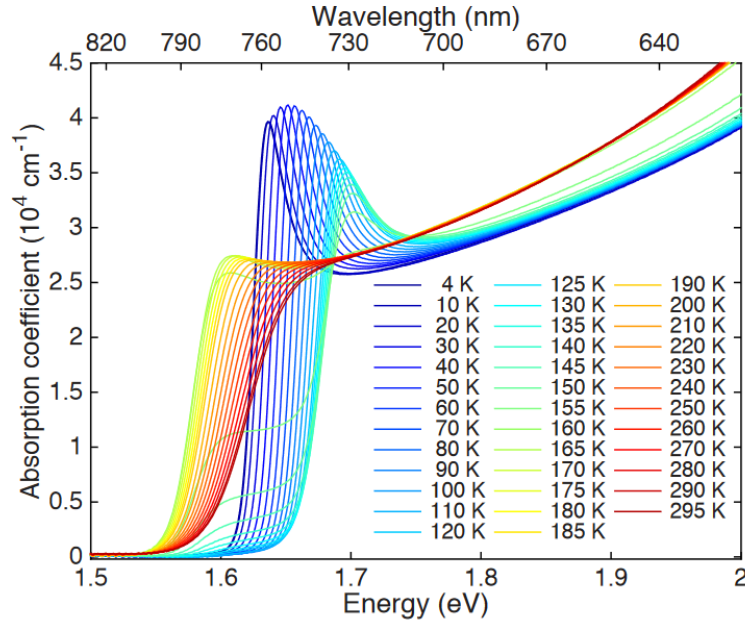
Figure 1-7 Absorption spectra of CH₃NH₃PbI₃ for the full temperature range from 4 K to 295 K as a function of energy (eV) on the bottom axis and wavelength (nm) on the top axis. Reproduced from Davies et al.[94] under Creative Commons

Exciton dissociation generates free charges. Before describing their recombination, it is very noteworthy to point out the intrinsic character of halide perovskite, in which extrinsic doping has never been achieved. Now, electron/hole recombination described by the differential system (1-23) can be reduced under certain assumptions to simpler rate equations that can be solved analytically. A simplistic recombination term was first used by Xing et al. in 2013, who first measured an I_{PL} lifetime τ_n around 10 ns on a MAPI layer[98]. The model quality was soon enhanced with the inclusion of trap levels as in (1-23), in order to reproduce the increasing I_{PL} decay rate at increasing excitation level[37,99–101]. Quantifications for the trap concentrations were derived thanks to several transient measurement techniques (transient absorption[99,102,103], transient THz conductivity[104,105], TRPL[37,106,107], time-resolved microwave conductivity TRMC[101]). Temperature-dependent studies were even realized in order to locate more precisely the

trap energetic level within the bandgap[108]. Despite a strong discrepancy regarding this level inside the bandgap[10,109], a strong consensus still exists on the relatively small concentration in non-radiative recombination centers. Physical reasons for this very long lifetime of charge carriers (sometimes up to several μs[85]) are still an open question[110]. One of the explanation relies in the high energy formation of deep traps, in comparison to shallow levels. Indeed, density functional theory (DFT) calculations predicted the favored formation of benign point defects[111], especially when MAPI (or FAPI) is deposited in I-rich conditions[112]. Another explanation presents the low phonon energy as responsible of the long lifetime, as several phonons would have to be emitted so that the energetic gap between C_b and trap (or trap & V_b) is crossed[113].

Last but not least, the diffusion properties of halide perovskite remain to be discussed in this section. The knowledge of D (or equally of μ) allows to derive $\overrightarrow{J_{diff}}$ & $\overrightarrow{J_{drift}}$ in any situation. A wide range of mobility values has been reported in the literature, going from 0.05 to 100 cm^2/Vs [54,103,114–116]. These huge variations in term of transport properties can be ascribed to the quality of perovskites absorbers, to their chemical composition and to the grade of crystallinity of the thin films[117]. Yet, the great variety of measurement techniques applied to determine diffusion properties could also explain this discrepancy. Electric ones based on the principle of time-of-flight have been used[99,118] but are probably biased by ion migration (see section 6.2.4). The initial conductivity of the sample in a TRMC experiment also yields an approximate quantification of the mobility[62,85,101]. Optical techniques are also widely used: one can here cite reports from transient absorption imaging[119–121], THz probe[122], I_{PL} spectroscopy[24,123] or imaging[124,125]. The results associated to these techniques are further discussed in section 4.5 & 5.4.3, with particular interest given to the photon recycling phenomenon[23] that also influences the charge transport.

1.3.3. INTEGRATION INTO PHOTOVOLTAIC DEVICE

Perovskite layers owe their ever-increasing popularity in the energy materials community to their use as absorber layer in PV devices. Indeed, perovskite solar cells (PSC) have shown an unprecedented rapid increase of the conversion efficiency[126,127]. If the first perovskite solar cell had a DSSC architecture[47] with a perovskite thickness inferior to 100 nm, other structures with thicker layers were employed then. In 2012, perovskite layers were still deposited on top of a meso-porous TiO_2 bead, which yielded higher efficiency solar cell[128]. This TiO_2 interface acted as electron transport layer (ETL), while a Spiro-OMeTAD layer at the other interface acted as hole transport layer (HTL). The structure was completed by a transparent conductive oxides (TCO) as FTO at the front contact, and by an Au metal electrode at the back contact. The full stack represents the devices used throughout this manuscript, and is seen on a cross-sectional view under a scanning electron microscope (SEM) in Figure 1-8. Even if a general overview of the PSC structure is outside the scope of this literature review, we recall here some concurrent PSC architectures with the planar one (without the meso-porous interface) deposited on textured Silicon[126], or the back-contact one[129].
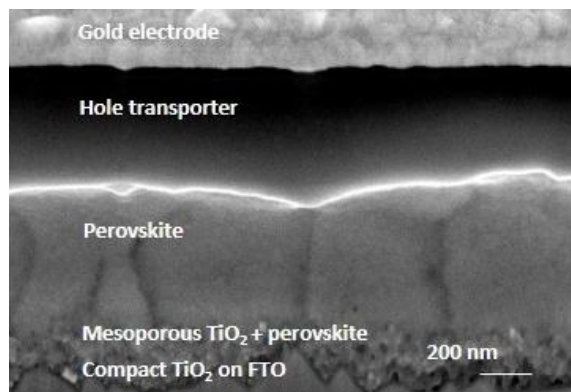
Figure 1-8 Cross-sectional view of a perovskite solar cell Hole transporter refers to the HTL which is Spiro-OMeTAD[74].

Several other layers can be employed as transport layers inside perovskite solar cells. Replacing the TiO_2 has early been a concern due to its prone degradation when exposed to UV light[130,131]. Inorganic SnO_2 and ZnO are developed to do so[132]. For what concerns Spiro-OMeTAD, its cost and sensitivity explain the extensive research for alternative HTL (like polymers P3HT & PTAA[133] or inorganic Cu-SCN[115] for example). The non-radiative recombination happening at the perovskite/ETL (-/HTL) interfaces generally constitute the main recombination pathway[134,135], which also drives the research towards their optimization and/or replacement. For this purpose, alternative improvements rely on interface passivation using mixed 2D/3D perovskite[60] or ultra-thin PMMA barrier[136,137]. The considered PSC (similar as represented in Figure 1-8) operate as pin solar cell[39,138]. Under illumination, an intrinsic zone without electric field is present in the absorber. Henceforth, charge collection works out of diffusion and it is most relevant to characterize L_n & L_p.

PSC are instable. Not only because perovskite and TL layers are sensitive[83], but also because the perovskite/TL interface are complex chemical environments where degradation pathways are nested[139]. Irreversible changes are detrimental to the sustainability of an eventual commercial product, but even reversible transformations matter as they hinder characterization approaches. A very frequent instability consists in the hysteretic behavior in the I-V curves under illumination. This generates uncertainty concerning the effective maximum power point of the solar cell. Probable causes for this hysteresis are interface trapping[140,141] or ion migration[142]. In addition to this hysteresis between forward and reverse scan, several kinds of light-soaking effects[143–145] have been observed.

2. Experimental methods

In this section, we give the operating principles of the luminescence imaging set-ups used in this dissertation. The hyperspectral imager (HI) yields spectrally-resolved I_{PL} images in absolute units and will be described first (section 2.1). Then will come the time-resolved fluorescence imaging (TR-FLIM) set-up, which gives time-resolved I_{PL} images (section 2.2). Eventually, a new set-up adapted to get 4D I_{PL} images (2D spatial, spectral, temporal) will be presented (section 2.3).

2.1.   HYPERSPECTRAL IMAGER

In this section, we describe the operating principles of the HI. The acquisition of raw I_{CCD}* images, their rectification[a], and calibration is described. We explain how the signal is corrected for each pixel of the sensor from the read noise, the dark current noise of the camera as well as from the spectral transmissions along all the optical path, and the spatial inhomogeneity of the optical system (flat-field). After calibration of the rectified images, a datacube $I_{PL}(x,y,\lambda)$ is obtained. It can be equally seen as a collection of spectral images (one image per λ) or as a collection of I_{PL} spectra (one for each pixel). These spectra are expressed in absolute units (photons/eV/s/m^2/sr) of luminance, and can thus be fitted with the generalized Planck law (see section 1.1.3). The spatial resolution is 1µm for the highest magnification objective and for visible/NIR wavelength range. The spectral resolution is 2nm.

2.1.1. ACQUIRING AND RECTIFYING IMAGES

The HI, sketched in Figure 2-1, is based on classical optical microscope. The studied sample is illuminated by a light source (i.e. WF illumination), which consists for example in spread laser beam. This illumination light is reflected by a beam splitter and shined on the sample through a microscope objective. The sample absorbs the excitation light and emits a photoluminescence signal, which is collected by the same microscope objective. This PL beam is then transmitted by the beam splitter, which sorts out any laser light reflection on the sample surface.

---

[a] As it will be explained soon, the raw data are not usable as such and must be "rectified". This pre-treatment is called "rectification".
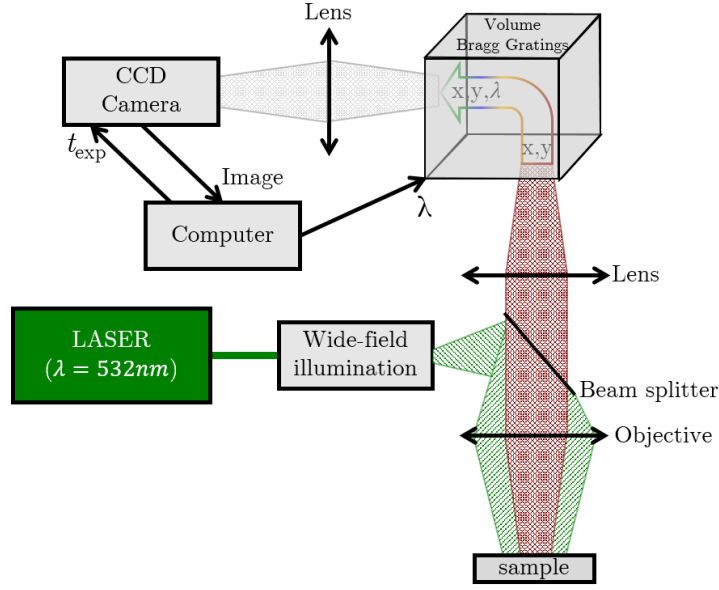
Figure 2-1 Sketch of the hyperspectral imager (also HI) in a configuration with wide-field illumination of a sample emitting red luminescence. The computer collects the images from the CCD, and controls the central wavelength of the HI as well as the exposure time of the CCD.

At this point, luminescence images could be formed by the first lens but they would be panchromatic (spectrally integrated). In order to collect spectrally-resolved images, we use a 2D spectral filter developed by Photon Etc based on volume Bragg gratings (VBG). This crucial optical component analyzes an image (input beam at the bottom of the cube in Figure 2-1) and outputs a shifted image that contains a combination of spectral and spatial information. To be more specific, the spatial y-axis on I_{CCD}^{*} images is not impacted, while the x-axis contains mixed spatial and spectral information centered at a precise wavelength λ. Focusing this output beam on the CCD sensor for an exposure time t_{exp} results in I_{CCD}^{*} image. As the central wavelength can be tuned, it is possible to acquire a set of n distorted images I_{CCD}^{*} at increasing $\lambda_{1...}$ λ_{n}, which corresponds to the raw cube of data. As an example, a set of I_{CCD}^{*} images acquired on a perovskite sample is shown in Figure 2-2(a). The I_{CCD}^{*} signal is more intense to the right of the image at λ_{1}, and to the left of the image at λ_{6}. This is a signature of the spatial/spectral shift in the output beam of the VBG. It can be corrected by a linear operation (so-called rectification) applied on them. As displayed in Figure 2-2(b), it yields a set of n spectral $I_{CCD}(x,y,\lambda)$ images, also called rectified cube. The I_{CCD} signal is correctly localized on the image, i.e. every pixel contains solely information on its conjugated point in the sample plane. The rectified cube indicates that the most intense emission wavelength is λ_{3} or λ_{4} for all pixel, which was not easily inferred by the raw images.

a- Raw I_{PL} images at $\lambda_1 \ldots \lambda_6$

b- Rectified I_{PL} images at $\lambda_1 \ldots \lambda_6$
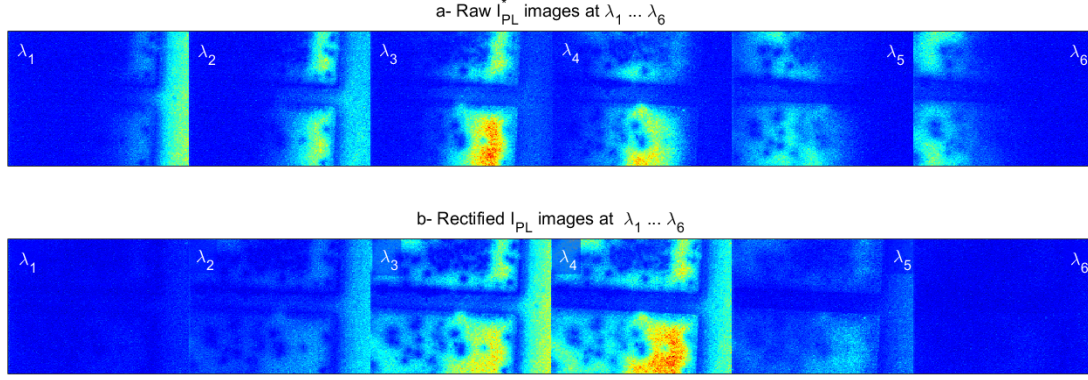
Figure 2-2 Raw acquisitions at 6 increasing wavelengths on the CCD sensor of the HI. It is imaging the output beam from the volume Braggs gratings. After rectification, the spatial component is correct on each of the 6 spectral images.

2.1.2. CALIBRATING THE TRANSMISSION OF THE SYSTEM

The spectral images from the rectified cube remain to be calibrated to get quantitative information regarding the emitted photon flux. This procedure is thoroughly described in A. Delamarre thesis[146]. The first step consists in acquiring a "dark" image $I_{CCD,d}$ without illuminating the sample, at the same exposure time t_{exp}. It allows to correct the read noise and dark current noise of the camera. We here also normalize with the exposure time to get to the detected intensity per unit of time $(I_{CCD} - I_{CCD,d})/t_{exp}$.
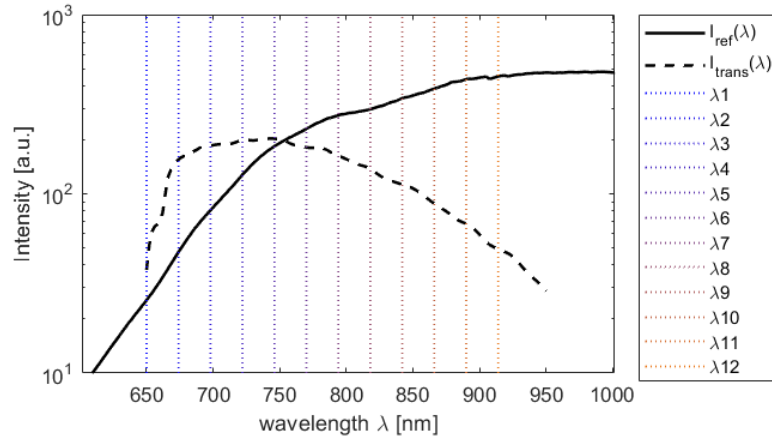
Figure 2-3 Reference spectrum of the calibration lamp, and measured spectrum I_{trans} (spatially averaged). 12 characteristic wavelengths used also used in Figure 2-4 are indicated by straight colored lines.

Then, the transmission along the optical path is calibrated by imaging an homogeneous light source with a known spectrum $I_{ref}(\lambda)$, which is represented in Figure 2-3. In practical, we shine a calibrated lamp (Spectral Products) into an integrating sphere located at the sample position. A small aperture in this sphere allows the light with I_{ref} spectrum to go out with a spatially homogenous output, which angular repartition follows the Lambert's cosine law. This leads us to a proper calibration of the transmission of the optical system for each spatial location, each wavelength and each angular emission. In order to illustrate the relevance of this calibration step, we first consider the spatially integrated $I_{trans}(\lambda)$ spectrum. It differs greatly from $I_{ref}(\lambda)$, which is

explained by the weak response of the Silicon CCD sensor in the infrared and by spectral filters on the optical path. Now, the factors affecting the transmission are spatially heterogeneous. This is evident by looking at rectified images $I_{trans}(x,y,\lambda)$ displayed in Figure 2-4. We use these images to correct the spatial inhomogeneity of the optical system (flat-field), by using a local spectral ratio $R_t(x,y,\lambda)$:

$$R_t(x,y,\lambda) = \frac{I_{ref}(\lambda)}{\left[I_{trans}(x,y,\lambda) - I_{trans,d}(x,y,\lambda)\right]/\delta t} \qquad (2\text{-}1)$$
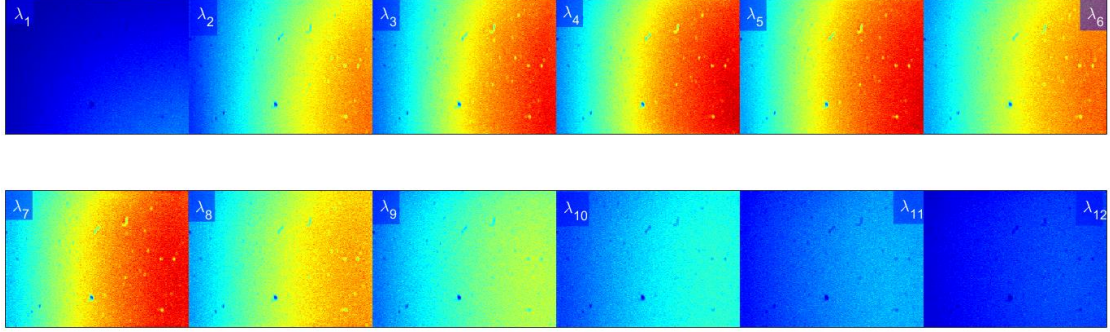
Figure 2-4 Rectified images from a lambertian source with known spectrum. The spatial inhomogeneity is due to optical aberrations associated to the wide-field collection. The dark dots in the image are dead pixel of the CCD sensor.

2.1.3. GETTING TO ABSOLUTE UNITS

After the previous step, one obtains the spatially and spectrally-resolved calibrated intensity in counts. Here we will explain how to convert counts into physical units (luminance).

Counts to number of photons: At this step, we image the output of a fiber in which a laser is coupled in. The output of power is known and converted to a photon number per unit of time n_{ph}. A perfect collection of all photons out of the fiber is ensured by the use of a fiber having a smaller numerical aperture (NA) than the one of the collection microscope objective. As previously explained, the images of the laser formed on the CCD (I_{las}) are corrected from the background noise using a "dark" acquisition $I_{las,d}$. Next, I_{las} are converted into count numbers n_{cts} in eq. (2-2) by using the correcting factor R_t derived in eq. (2-1).

$$n_{cts} = \iint_{x,y} \int_{\lambda} \frac{\left(I_{las}(x,y,\lambda) - I_{las,d}(x,y,\lambda)\right)}{\delta t_{las}} R_t(x,y,\lambda)\, dx\, dy\, d\lambda \qquad (2\text{-}2)$$

In order to get from counts on the CCD to number of photons, the correction factor n_{cts}/n_{ph} can be used. The derived factor is not wavelength-dependent, as the spectral sensitivity is already accounted for by R_t.

Grating bandwidth normalization: This is analogous to the normalization with the exposure time. Indeed, set to λ, the VBG lets through light of wavelength in the range from $\lambda - \delta\lambda/2$ to $\lambda + \delta\lambda/2$. Hence, the registered intensity is integrated over a wavelength

bandwidth of $\delta\lambda$. To normalize to physical units, one has to divide the intensity obtained previously by $\delta\lambda$.

Spatial normalization: The intensity is detected pixel-by-pixel, each pixel representing a surface S_{pix} of the sample, which is determined by imaging a target with known dimensions. To get the number of photons by unit sample surface, one has to divide the previous result by S_{pix}.

Solid angle normalization: The imaging system collects light in a solid angle which is defined by the microscope objective. With an objective of numerical aperture NA, this angle is calculated to be $\Omega_{\text{eff}}=\pi(NA)^2$. To get photon flux per unit solid angle, one has to divide the previous result by this effective collection angle. Here, a lambertian emission from the sample is assumed.

Eventually, we have the following formulas allowing to convert the rectified datacube $I_{\text{CCD}}(x,y,\lambda)$ into a calibrated datacube $I_{\text{PL}}(x,y,\lambda)$ representing the photoluminescence emission in physical units. For $(S_{\text{pix}},\delta\lambda,\Omega_{\text{eff}},t_{\text{exp}})$ inputs in SI units, I_{PL} is expressed in photons /sr /s /m^2 /m in eq. (2-3) or in photons /sr /s /m^2 /eV in eq. (2-4).

$$I_{\text{PL}}(x,y,\lambda)=\frac{I_{\text{CCD}}(x,y,\lambda)\text{-}I_{\text{CCD,d}}(x,y,\lambda)}{t_{\text{exp}}}R_{\text{t}}(x,y,\lambda)\frac{n_{\text{ph}}}{n_{\text{cts}}}\frac{1}{\delta\lambda}\frac{1}{S_{\text{pix}}}\frac{1}{\Omega_{\text{eff}}} \qquad (2\text{-}3)$$

$$I_{\text{PL}}(x,y,E)=\frac{I_{\text{CCD}}(x,y,\lambda)\text{-}I_{\text{CCD,d}}(x,y,\lambda)}{t_{\text{exp}}}R_{\text{t}}(x,y,\lambda)\frac{n_{\text{ph}}}{n_{\text{cts}}}\frac{1}{\delta\lambda}\frac{1}{S_{\text{pix}}}\frac{1}{\Omega_{\text{eff}}}\frac{hc}{q\lambda^2} \qquad (2\text{-}4)$$

2.1.4. DEGREES OF FREEDOM

Despite a quite tedious calibration procedure, the HI constitutes a powerful tool for characterizing photovoltaic materials and devices. It allows to characterize the QFLS of any material with 0.01 eV uncertainty provided that whole spectrum is fitted[147,148]. Its high flexibility shall also be underlined. At first, various illumination sources can replace the standard wide-spread green laser. A local illumination can be obtained by removing the wide-field illumination set-up (chapter 5). Also, LED can be used to have illumination with broader spectrum, or better homogeneity. Electroluminescence signals are monitored without any external illumination, and the HI is perfectly suited to study their spatial dependency[149]. On the collection side, several optical systems with magnification going from x1/10 to x100 can be used to access information from the macro-scale to the micro-scale.

2.2. TIME-RESOLVED FLUORESCENCE IMAGING

We will focus more on this set-up that has been developed during my PhD, even if some preliminary results had already been acquired. As explained in section 1.1.4, a time-resolved sensor with spectral sensitivity f_{system} measures a signal proportional to exp(-$\Delta\mu/k_{\text{B}}T$) when the signal spectral shape is unchanged. This assumption is verified for the sample measured with the TR-FLIM throughout the manuscript. Henceforth, I_{PL} will

here be used for the spectrally-integrated intensity of PL flux without consideration of its absolute calibration, as it still remains proportional to np product.

2.2.1. TIME-RESOLVED EM-ICCD CAMERA

The main component of the TR-FLIM set-up is the intensified, time-gated, electron-multiplied CCD (em-ICCD) camera (PIMAX4, Princeton instruments). Photons incoming on the em-ICCD camera are first hitting a light intensifier, which consists in 3 components: a photocathode, a multi-channel plate (MCP), and a phosphor screen. They are sketched in Figure 2-5, which displays the conversion of incoming photons into electrons by the photocathode. When the em-ICCD is gated ON (Figure 2-5(a)), these electrons are accelerated towards the MCP which multiplies them with a certain intensifying gain G_I. The collimation of the system is preserved by the high voltage applied, which ensures that electrons propagate straight. They drift further to the phosphor screen that converts them back to photons. Eventually, the electron-multiplied CCD sensor images the phosphor screen with a supplementary gain G_{em}.
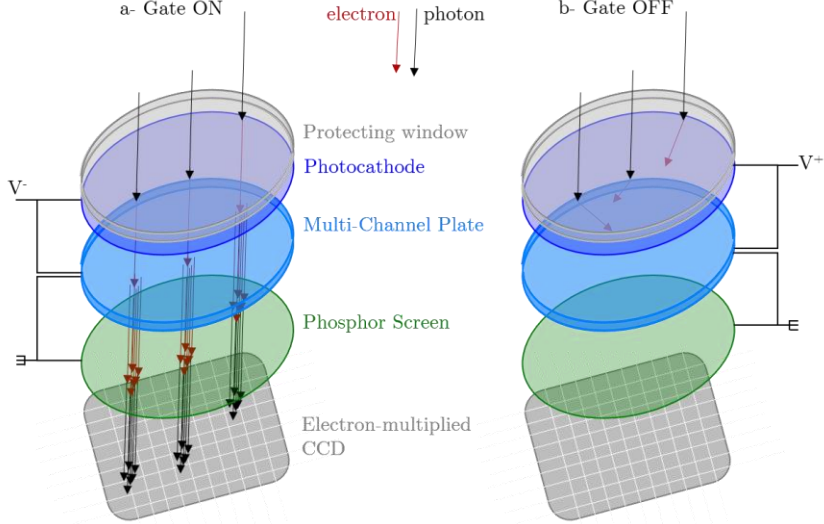
Figure 2-5 Sketch of the em-ICCD camera under operation (a) and when the intensifier is disabled by switching its polarity (b)

Now, when the em-ICCD is gated off, the electrons generated by the photocathode remain confined to its vicinity (Figure 2-5(b)). The gating of the light intensifier can be controlled with ps-resolution and is crucial to the time resolution of our camera. It is equivalent to the mechanical shutter of classical camera. For what concerns our PIMAX4 camera, the gating width t_{width} (time span during which the gate is ON) can be continuously tuned above 2ns, while some discrete ps-gating modes can lower the time resolution down to 750ps. It is triggered by an electronic input signal (from the laser), to which an adjustable delay t_{del} is added. CCD readout happens after N_{acc} accumulations on the sensor, whereby an accumulation correspond to a gate opening.

In practical cases, two acquisition modes are used. The repetitive one consists in acquiring several images at the same t_{del} & t_{width}. The sequential one consists in progressively delaying t_{del} while keeping t_{width} constant and taking an image for each t_{del}

value. This is typically realized with t_{del} values going from the beginning (t_{las}) until the end of the luminescence decay. The precise values used are recalled in "Imaging Specifics" section of each chapter (3.1.2, 4.1.3, 5.1.2 & 6.1.2).

2.2.2. COMPLETE TIME-RESOLVED IMAGING SET-UP

In addition to the aforementioned em-ICCD camera, we mainly use a pulsed laser (TALISKER, Coherent) as illumination source. It delivers 15 ps-wide light pulses (λ=532 nm) at a tunable repetition rate (from 200 kHz to 1 MHz), as well as a synchronized electric output that is used as a trigger for the camera. This is sketched in Figure 2-6, which displays the electric and optical connections between each component of the TR-FLIM set-up. For what concerns the optical part, the laser is focused in a speckle removal filter based on a 50 µm pinhole, and goes through a wide-field illumination optical system. The TR-FLIM set-up has the same microscope architecture as the previously introduced HI. Hence, a microscope objective and beam splitter are again used to illuminate the sample and to collect the PL flux emitted, which is transmitted to the em-ICCD camera. On the electronic part, the computer controls the laser frequency f_{las} and fluence ϕ_0, as well as the different gating (t_{del}, t_{width}) and gain (N_{acc}, G_I, G_{em}) parameters of the camera.
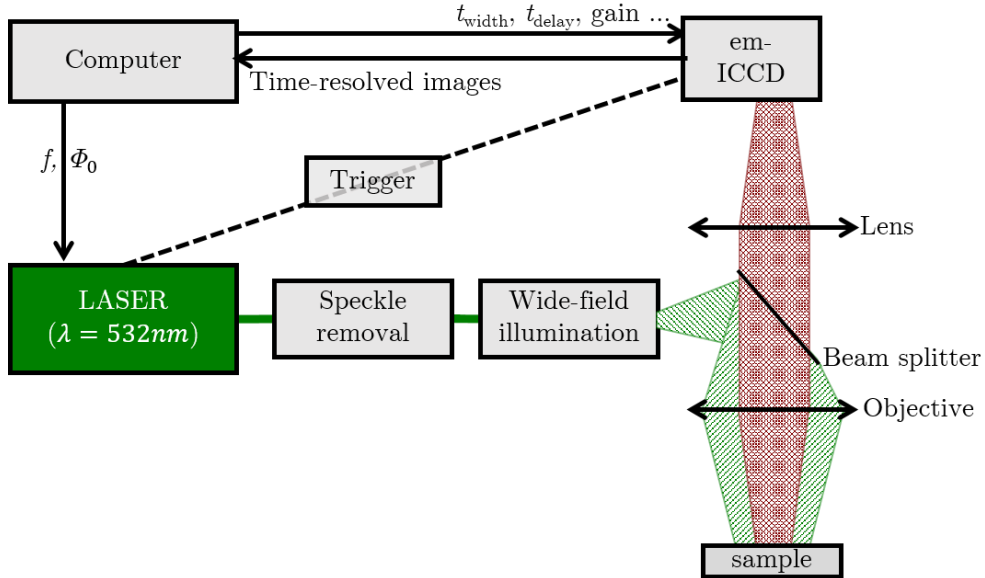
Figure 2-6 Sketch of the time-resolved fluorescence imaging (TR-FLIM) set-up.

Here, it is very noteworthy that supplementary synchronizations to the system are available. In chapter 6, we use a modified version of the TR-FLIM set-up, in which the em-ICCD camera is still triggered by the laser and operated as a time-gated camera with gating delay t_{del} & width t_{width}, but also sends another trigger signal with another delay t_{del2} to a function generator (AFG 3000 Tektronix). The latter will then generate a pulsed electric bias synchronous to the optical excitation, so that the photoluminescence signal of the sample/device can be observed as a function of a pulsed electric field.

2.2.3. ACQUIRING TIME-RESOLVED IMAGES

Each experiment requires a careful setting of the gating and gain values. At first, it is required to measure the delay value at which the laser is hitting the sample. This is a critical step that should be realized with caution as the laser might damage the intensifier. Hence, it is recommended to realize it at rather high gain and low laser power. Practically, one should gradually increase laser power thanks to a tunable neutral density filter, until the signal is higher than the background.

The relative intensity of the signal is measured by using a t_{width} value larger than the laser period $1/f_{\text{las}}$, so that at least one laser pulse is incoming on the sample whatever t_{del} value. At this point, the intensity of the laser can be tuned cautiously as explained at the beginning of the sub-section. Then, a dichotomy approach based on a progressive reduction of t_{width} to $1/2f_{\text{las}}$ $1/4f_{\text{las}}$... is followed. The delay time t_{del} is changed until the temporal position of the laser pulse is known for the targeted width t_{width}. Here, it shall be noted that the measured value for t_{las} slightly evolves with t_{width} (around 2ns difference when switching from $t_{\text{width}}<1\text{ns}$ to $t_{\text{width}}>5\text{ns}$). This may be due to electronic bugs but can be compensated by measuring t_{las} for each t_{width} used in the measurement campaign.

The gain parameters (the number of accumulations on the CCD N_{acc}, the intensifier gain G_{I} and the electronic gain G_{em}) are optimized for each experiment. They are kept constant during a sequential acquisition of time-resolved I_{PL} images. Henceforth, they should be determined so as to avoid any saturation when the signal is maximal (i.e. at $t_{\text{del}}=t_{\text{las}}$). An example of sequential acquisition with variable t_{del} and fixed t_{width} & gain parameters is given in Table 2-1. For a power study such as presented in chapter 3, 4 & 5, the gain parameters should be adjusted for each fluence so that the signal to noise ratio remains high. To compare relative I_{PL} intensity from sample to sample at a given laser power, these gain parameters should be kept constant as their impact has not been calibrated.

Gate delay t_{del} (past t_{las})	Gate width t_{width} (ns)	On-CCD accumulat° N_{acc}	Gain G_{I} [a.u.]	Gain G_{em} [a.u.]
0, 2, 4 ...98, 100	2	1000	10	20

Table 2-1 Example of sequential acquisition on the TR-FLIM, during which the gain parameters are fixed while t_{del} changes.

In chapter 6, we do not use sequential acquisition to reconstruct $I_{\text{PL}}(x,y,t)$ but snapshot acquisition. This consists in taking several repetitive acquisitions at incremental time delays while adjusting gate width and gain parameters for each delay value. The example of snapshot given in Table 2-2 shows that gain parameters can be increased at long times, when I_{PL} is naturally weaker. This enhances image quality but hampers any comparison between I_{PL} intensity at different t_{del} values.

Gate delay t_{del} (past t_{las})	Gate width t_{width} (ns)	On-CCD accumulat° N_{acc}	Gain G_{I} [a.u.]	Gain G_{em} [a.u.]

0	2	1000	10	20
10	5	10000	10	20
100	50	10000	100	100

Table 2-2 Example of snapshot acquisition on the TR-FLIM, during which the gain parameters can be varied at each delay.

2.2.4. DEGREES OF FREEDOM

In the previous subsections, we already introduced the degrees of freedom linked to the acquisition modes of the camera, as well as those offered for the synchronization of external devices (e.g. electric pulse synchronized to the laser pulse). Here, we could also add the relative variety regarding the illumination sources and collection. As an example, we make use of another laser than the TALISKER for the experiments presented in chapter 5. We used a tunable laser (Fianium) mainly because of unavailability of the TALIKSER, but it could also allow to vary the excitation wavelength. In addition to the pulsed excitation necessary to a time-resolved acquisition, a continuous wave source could added to the illumination path, so that samples are observed while being light soaked. As for the hyperspectral imager, collection objectives can be varied from *1/10 to *100 magnification, allowing to get I_{PL} intensities from the macro-scale to the micro-scale.

2.3.4-D PHOTOLUMINESCENCE IMAGING

This set-up has been designed by the PhD candidate and developed by a master student under his supervision. A patent protecting its operating principles has been filed (Deposit number 19315037.2). It relies on principles related to single pixel imaging (SPI) which are recalled first, before the set-up is described in details. A proof of concept is realized in two steps. The first step consists in acquiring a "single-pixel image" of a monochromatic pattern with a photodetector (subsection 2.3.2). The second step showcases the first 4D I_{PL} acquisition, which was here realized on a perovskite layer and demonstrates the feasibility of simultaneous spatial, spectral and temporal resolution (subsection 2.3.3). For more details concerning the optical design, the electronic control and the synchronization of the set-up, the reader is referred to Marie Legrand's master thesis[150].

2.3.1. SINGLE PIXEL IMAGING (SPI)

Figure 2-7 Digital Mirror Device and its use in Single pixel imaging (a) visual of the DMD projecting a pattern (b) sketch of the SPI experiment
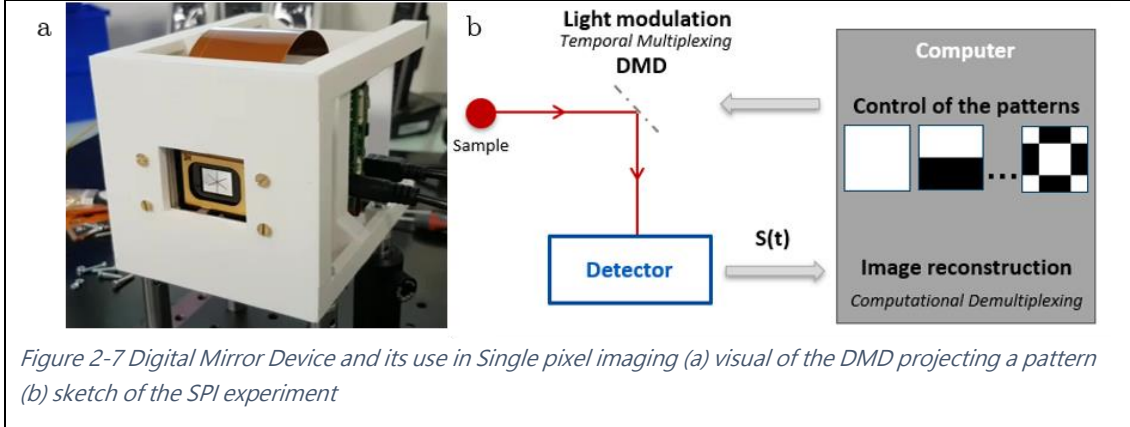
The developed system is based on the principles of Single Pixel Imaging (SPI)[151,152], which allows us to realize 2D spatial imaging with a single element photodetector, whereas classical imaging systems (CCD, CMOS) use 2D sensors to capture 2D images. The key component of this technology is a spatial light modulator (SLM) reflecting light to the photodetector following a geometrical pattern Π (displayed in Figure 2-7(a)). Analysing the output signal (total intensity detected) and demodulating it with the projected patterns allow the image reconstruction. This micro-electro mechanical system (MEMS) is made of 1024x728 micro-mirrors having 13µm pitch that can be controlled independently. It allows to perform acquisitions of selected parts of the sample and combine them to reconstruct the whole picture. This operating principle is sketched in Figure 2-7(b). By using this SLM, we are restricted to binary patterns Π as each mirror reflects 100% or 0%, on the contrary to liquid crystal devices allowing gray-scale modulation[153]. The output signal from the detector can be computed an intensity measurement for each pattern $b(\Pi)$. Image reconstruction algorithms are then applied to associate each location of the sample with an I_{PL} intensity. In the next sub-section, we will present a rather basic SPI set-up that will be used in order to validate the operating principles of SPI. It will also allow us to validate our spatial reconstruction algorithm. Thereafter, we will present the 4D I_{PL} imaging set-up employing a streak camera as detector.

2.3.2. 2D IMAGING SET-UP BASED ON SPI

Before describing the optical set-up, we focus on the mathematical background. Let us consider a sample emitting a spatially-resolved signal $(X_k)_{k \in [1,n]}$, where the whole spatial variation is modeled by a single parameter (1D). Let us also consider a SLM displaying a series of binary patterns $(\Pi_i)_{i \in [1,m]}$. For each acquisition b_i of the photodetector, light from x_k is reflected to the photodetector if and only if $\Pi_{i,k}=1$. Henceforth, the photodetector collects an information $(b_i)_{i \in [1,m]}$, which is described by:

$$b_i = \sum_{k=1}^{n} \Pi_{i,k} \, X_k \qquad (2\text{-}1)$$

Following this approach, the problem of interest can be described mathematically by finding the target image X from the pattern matrix Π and the measurement vector b:

$$\Pi X = b \qquad\qquad (2\text{-}2)$$

In the case where Π is a square matrix (e.g. $m=n$ with as many measurements per pixel), the previous linear system has an exact solution if and only if the patterns form a spatial basis. That's why we will next make use of a specific class of binary matrix forming an orthogonal basis[154]: Hadamard matrix H_k. The case where $m<n$ is called "compressive sensing" as it makes use of less measurements than the targeted spatial resolution. It is frequently encountered in SPI applications as it allows to significantly reduce the acquisition time[151]. Yet, compressive sensing requires assumptions on the image sparsity or on their gradient, and greatly increases the post-treatment time of the images, in particular for the targeted application of 4D I_{PL} imaging. Therefore, we decided to stick to the Hadamard basis (with $m=n$) for our first developments. More details about image reconstruction are available in Marie Legrand's master thesis[150].

The experimental set-up for our proof of concept of SPI includes an illuminated sun-shaped object (displayed in Figure 2-8(b)- its shape represents a "sun"), which image is formed on the DMD. The latter displays patterns from Hadamard basis with 24x32 spatial resolution ($m=768$), and reflects light into a powermeter (Thorlabs S130C), which output power $b(t)$ is displayed for the first 70 patterns in Figure 2-8(a). Patterns are changed with a 5Hz frequency, whereas the power intensity is read with a much higher frequency (around 300Hz) in order to increase the signal to noise ratio. We then sampled $b(t)$ to obtain a unique b_i value for each pattern Π_i, represented with green crosses in Figure 2-8(a). As the pattern matrix is easily inverted, we used eq.(2-2) to obtain a reconstructed image $X^*=\Pi^{-1}b$, which is displayed in Figure 2-8(c). The shape of the "sun" and its surrounding rays appear clearly on X^*. The intensity is higher at the center of the image, which could be explained by optical losses far from the optical axis (non-gaussian conditions). Still, the black round frame of the object is also imaged by our SPI set-up, as we could check by plotting X^* in logarithmical scale in Figure 2-8(d).
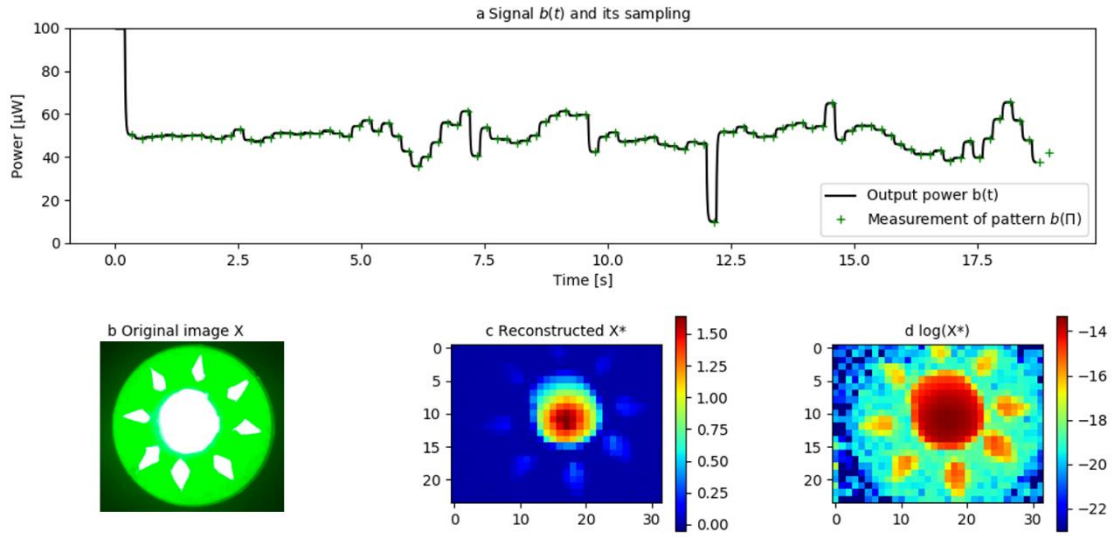
Figure 2-8 Proof of concept of image reconstruction from SPI (a) Output signal from photodetector on the first 70 patterns, sampled with one measurement per pattern (green cross) (b) Original image pictured with a phone camera (c) reconstructed image X* as determined by solving $X' = \Pi^{-1}b$. d) logarithm of X*

2.3.3. 4D IMAGING SET-UP BASED ON SPI

In the 4D I_{PL} imaging set-up, the single element photodetector is more complex than a photodiode. Indeed it will return the spectral and temporal information contained in the beam spatially hashed by the DMD. This photodetector is composed of a spectrometer (Figure 2-9(a)) and a streak camera (Figure 2-9(b)). The first one splits the input beam according to the photon wavelength and outputs a dispersed line signal. The horizontal line determines a spectral axis (displayed in Figure 2-9(b)). It enters into the streak camera and gets converted to "photo-electrons" by the photocathode (AB in Figure 2-9(b)). As in the light intensifier presented in section 2.2.1, they propagate straight due to a reverse bias applied on the spectral axis. Now, a second orthogonal bias is swept (C in Figure 2-9(b)). It is synchronized with the laser frequency and deflects the photo-electrons as a function of time. The first incoming electrons go to the top of the phosphor screen (D in Figure 2-9(b)), whereas the last ones are deflected to the bottom of this compound. A CCD sensor images the phosphor screen and transmits the acquired spectral-temporal characteristic to the computer.

The complete 4D PL imaging set-up is sketched in Figure 2-10. Same illumination path as for the TR-FLIM is used. Yet, I_{PL} signal emitted by the sample is imaged on the DMD and not on the em-ICCD camera. The DMD displays consecutively the patterns $(\Pi_i)_{i \in [1,m]}$ that spatially hashes the I_{PL} image, as in the experiment presented in sub-section 2.3.2. This hashed flux is then focused on the entrance of the spectrometer. For each pattern, a temporal spectral output $b_i(\lambda, t)$ is obtained by the spectro/streak camera, with λ varying between λ_i & λ_f and t varying between t_i & t_f. The reference time ($t=0$) is triggered by the laser, as for TR-FLIM set-up. Details regarding the DMD control, its synchronization with the streak camera are available in Marie Legrand's report[150].
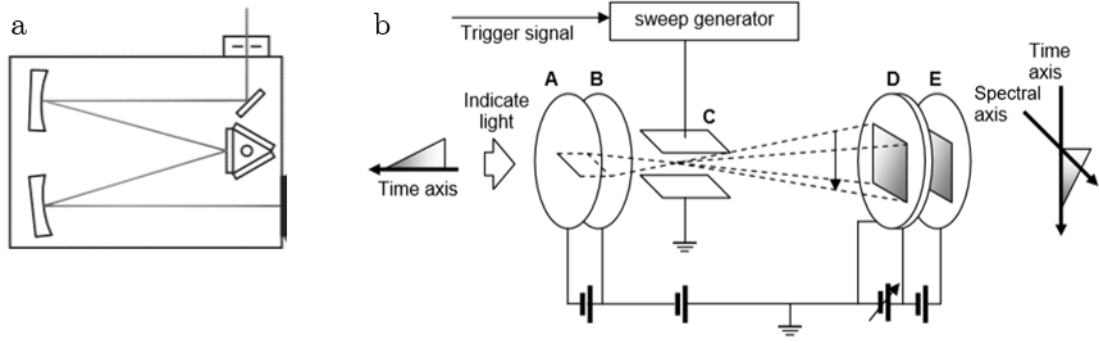
Figure 2-9 Spectrometer and streak camera (a) The spectrometer is represented with light input on top of the image and output on the right. Light is dispersed by a grating on the triangular compound [155]. (b) Streak camera with light path from the left to the right. (A: window; B: photocathode; C: deflecting electring field; D: phosphor screen; E: CCD sensor) [156]

The reconstruction phase is operated by the computer, using again the inverse pattern matrix. For each wavelength and time, the linear operation described in eq. (2-3) applies and an I_{PL} signal resolved in time, spectrum and space is eventually obtained.

$$\forall(\lambda,t)\ I_{PL}(\text{pixel } k,\lambda,t) = \sum_{i=1}^{m} \left(\Pi^{-1}\right)_{i,k}\ b_i(\lambda,t) \tag{2-3}$$
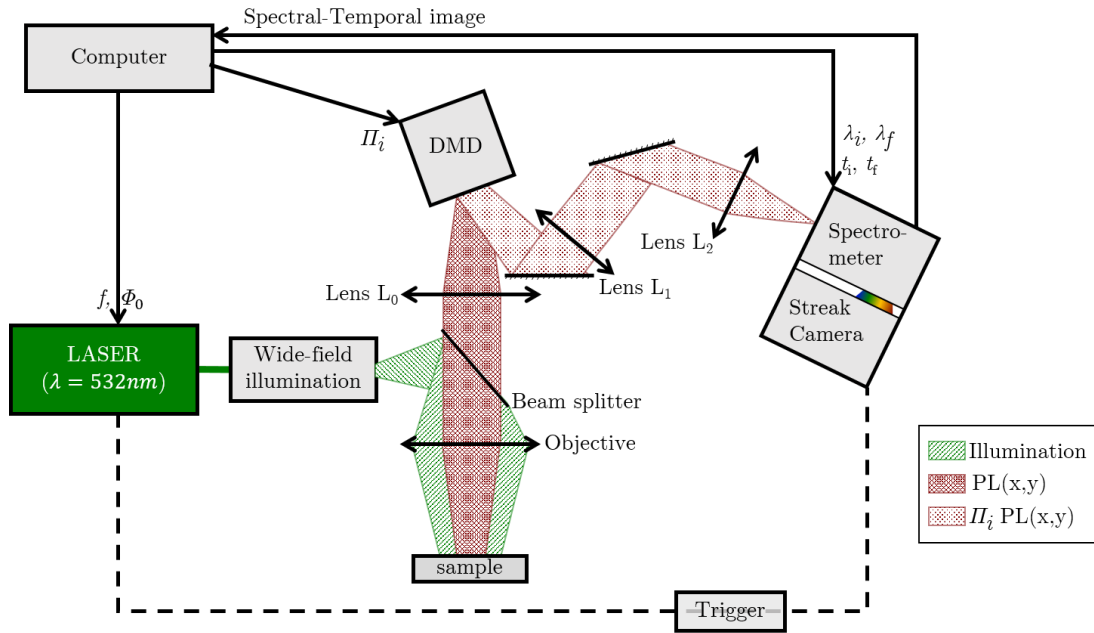
Figure 2-10 4D PL imaging set-up as developed for the proof of concept. The sample under illumination (WF spread laser) emits photoluminescence. It is imaged on the DMD, which displays a pattern Π_i that spatially hashes the PL image. This hashed flux is then focused on the entrance of the spectrometer.

An experimental proof of concept has been performed on a perovskite sample under local illumination, which is obtained by removing the wide-field illumination set-up. A similar experiment is studied with TR-FLIM and HI in chapter 5. A Nikon objective with numerical aperture 0.6 and magnification 50 was used The region of interest on the sample is restricted to some µm around the point illumination. Henceforth, the Hadamard set of pattern was displayed on a limited area of the DMD, around the conjugate point

of the illumination center. This was located using a dichotomy approach on the set of active mirrors, until the mirror reflecting the most light was found. Then we defined a set of Hadamard patterns distributed around this mirror with 6x8 resolution (m=48) and converted the acquired $b_l(\lambda,t)$ images into an hypercube I_{PL}(x,y,λ,t). Spectral-temporal images on a 3x3 group around the illumination center are represented in Figure 2-11. This group of 3x3 pixels is a spatial extract of the full 6x8 resolution, which representation on a single figure is not feasible. The significant variations in signal intensity between the central pixel and surrounding ones are evident. The wealth of the acquired data is further represented in Figure 2-12, which displays I_{PL} spectra at short times (t<1ns) and long times (4ns<t<10ns) for each pixel. When the signal to noise ratio is high enough, an I_{PL} peak value λ_{max} is calculated and indicated in the subplot. It is determined at 762 nm for the central point and increases up to 780 nm for the surrounding pixel, which is in accordance with the photon propagation phenomenon observed in chapter 5. More visibly maybe, the high-energy tail of the spectrum is cut in the surrounding pixels, which shape resemble ϕ_{prop} derived in section 5.3.2. This experiment deals as proof of concept for the 4D I_{PL} imaging set-up.
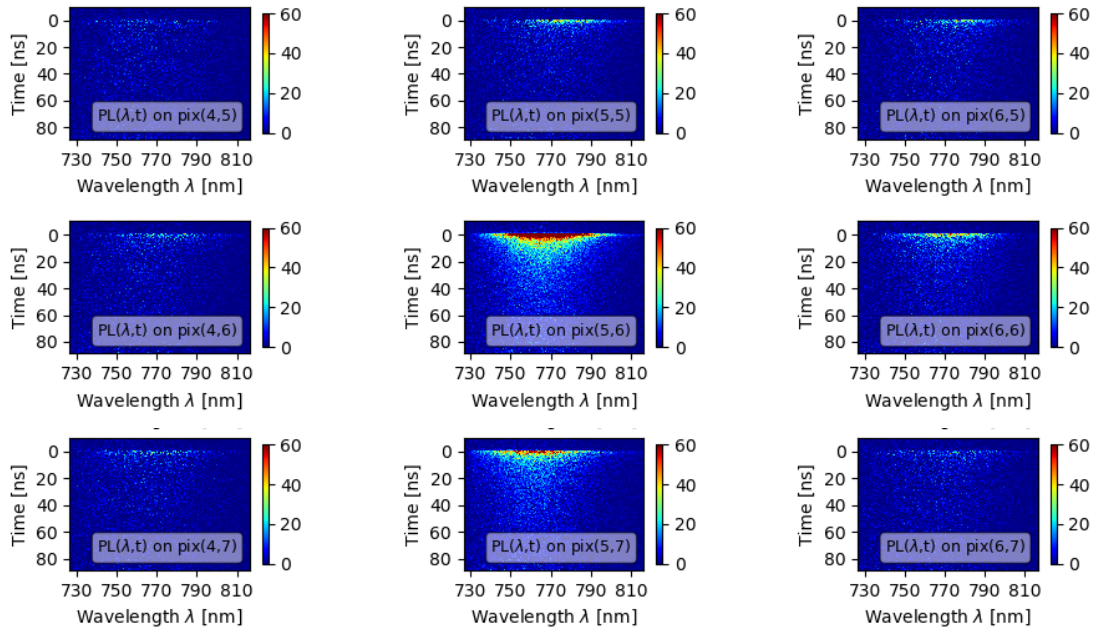
Figure 2-11 Output from the 4D I_{PL} imaging set-up after reconstruction conducted by solving eq. (2-3), and represented on 3x3 pixel around the one conjugated to the illumination center.
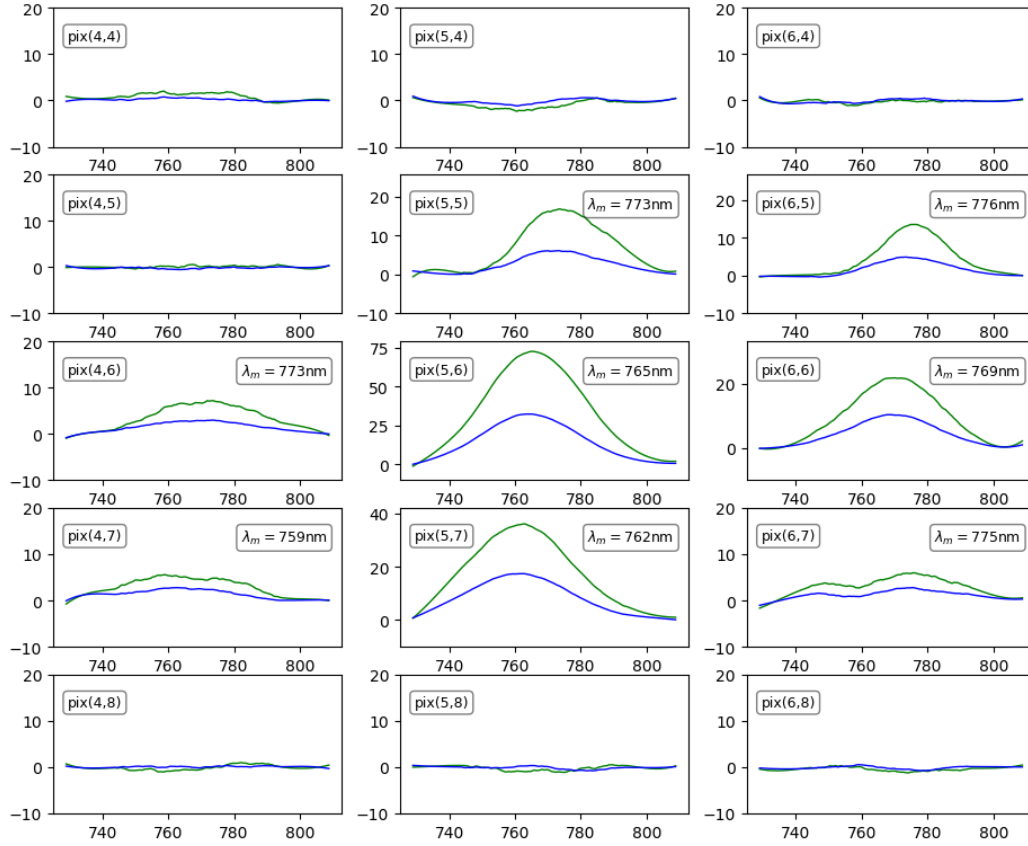
Figure 2-12 Space- & time-resolved I_{PL} spectra (green : $I_{PL}(\lambda, t<1ns)$; blue ; $I_{PL}(\lambda, t>4ns)$) extracted on 5x3 pixel around the one conjugated to the illumination center. When the signal to noise ratio is high enough, a PL peak value λ_{max} is calculated and indicated in each subplot

2.4. FITTING METHODS

Following concerns globally apply for the multi-dimensional data-sets (also called data cubes) acquired with the previously introduced imaging techniques. Their post-processing shares a similar architecture throughout the manuscript. This section is not dedicated to the construction of physical models, but to the mathematical background necessary to check their validity, correspondence to the measurement.

2.4.1. BINNING, CLUSTERING, SMOOTHING

The spatial dimension of these data cubes is the main reason for the gigantic memory size they occupy. For example, a TR-FLIM acquisition with t_{width} varying between 0 and 1 µs with 1ns step occupies up to 1 Go, as the CCD sensor has 1024x1024 pixels. A first step to reduce the size of the acquisition consists in binning the CCD sensor, whereby groups of $n_B \times n_B$ pixel are constituted and read together by the CCD sensor (generally n_B=2 or 4). The knowledge of the spatial resolution of the system allows to select the appropriate binning factor n_B, which is generally chosen to avoid over-resolution. A second step to reduce the size of the data cubes consists in clustering. It is often realized according to prior knowledge of the sample geometry. A symmetry of the device (axial

47

in chapter 3 & 6, radial in chapter 5) allows to consider mean I_{PL} intensities along one spatial dimension. Also, different behaviors observed during the acquisition (Z_1 & Z_2 in chapter 4, or wrinkles in section 5.5) can lead to the definition of region of interests with more complex geometries, on which I_{PL} is as well averaged. This whole clustering process results in time- (or spectrally-) resolved data set which will be easier to fit to physical models.

Smoothing experimental results is realized with Savitzky-Golay filter or moving averages for the time-resolved acquisitions, which signal to noise ratios decreases sharply for long times past the laser pulse. For what concerned the hyperspectral maps, advanced convolution techniques have been developed together with signal post-processing experts from EDF R&D[26,157]. They rely on a spectral and spatial deconvolution, in which the kernels are fixed by the resolutions of the system. This deconvolution is combined to Anscombe transformation, which acts on the Poisson noise by giving it a Gaussian distribution.

2.4.2. MODELING & FITTING

Let us now consider a model f_{model} taking a parameter vector p_{rm} as input and $X^*=f_{model}(p_{rm})$. An example of such model is the function that outputs the I_{PL} decay for a theoretical perovskite at known fluence Φ_0 (constant parameter) with transport (D_n) & recombination (R_{eh}, τ_n, S) parameters as input (fitting parameters). In this case, f_{model} first derives the solution of a partial derivative equation (continuity equation) using *pdepe* function from Matlab[158], and then calculates the resulting I_{PL} by integrating the *np* product in-depth.

Fitting the acquired datacube X to the model f_{model} consists in determining the optimal p_{rm} vector minimizing the reconstruction error:

$$\min_{p_{rm}} |X^* - X|_{norm} \tag{2-4}$$

Several norms (or distances) can be used but we often rely on $|\ |_{log1}$ which calculates the difference between $\log(X)$ and $\log(X^*)$. This allows to better reproduce the signal on its whole decay (or spectrum), including when it becomes lower at long times after the laser ($t >> t_{las}$), or at energies lower or higher than the bandgap. If one would apply $|\ |_1$ or $|\ |_2$ while fitting a time-resolved I_{PL} decay, the beginning of the decay would be over-fitted and the decay tail would be poorly reproduced.

The optimization problem summarized in eq. (2-4) is solved using Matlab, using either the Curve Fitting package (*fit* function), or the Optimization package (*fminsearch* function). In any case, the multi-parameter model f_{model} is defined with parameter values normalized around their expected value, so that convergence issues due to low or high numeric values are avoided. In our example, one would replaces R_{eh}, which value is expected to be between 10^{-12} and 10^{-8}, by $R_{eh}/10^{-10}$ and indicate the normalizing factor as constant parameter.

The 'trust-region' algorithm was mostly used to solve optimization problems[159]. It was launched several times with random values for the initial parameter vector. Out of all the local minima determined, the best parameter vector (lowest minimum for $|X^*\text{-}X|$) was kept and used to determine the fitted values. The reliability of the fitting method is first verified qualitatively by comparing the reconstructed $X^*=f_{\text{model}}(p_{\text{rm}})$ to the original measurement X, and verifying that the "physical" features of the decay (spectrum) are preserved. A second (quantitative) step consists in calculating the variation of the reconstruction error ($|X^*\text{-}X|$) for small variation of p_{rm} around the optimal values. Example of such verification are displayed in Figure 4-7(c), or Figure 6-5.

3. Lateral transport & recombination in a photovoltaic cell

In this first experimental chapter, we introduce time-resolved fluorescence imaging as an optical characterization method for optoelectronic devices. Under wide-field illumination, we will probe the lateral diffusion and recombination of minority charge carriers inside a Gallium Arsenide (GaAs)-based solar cell. This cell acts as a proof of concept device. By conducting the analysis of its I_{PL} signal, we intend to demonstrate the relevance of optoelectronic characterization by TR-FLIM. In a first time, we introduce the reader to the experimental details specific to this chapter (section 3.1). Then, we conduct a thorough exploration of the acquisitions by plotting the data along its spatial and temporal dimensions (section 3.2). Thanks to this data analytics, we are able to design a model matched to the physical phenomena at stake, i.e. transport, bulk and contact recombination (section 3.3). The model is derived from the continuity equation, and subsequently solved analytically. A fitting procedure adapted to the TR-FLIM output is developed and applied to reconstruct the experimental I_{PL} transients (section 3.4). Key optoelectronic properties for the considered device will then be extracted from these fits. Finally, we will comment on the particular advantage of using wide-field illumination (section 3.5).

3.1. EXPERIMENTAL DETAILS

3.1.1. SAMPLE STRUCTURE
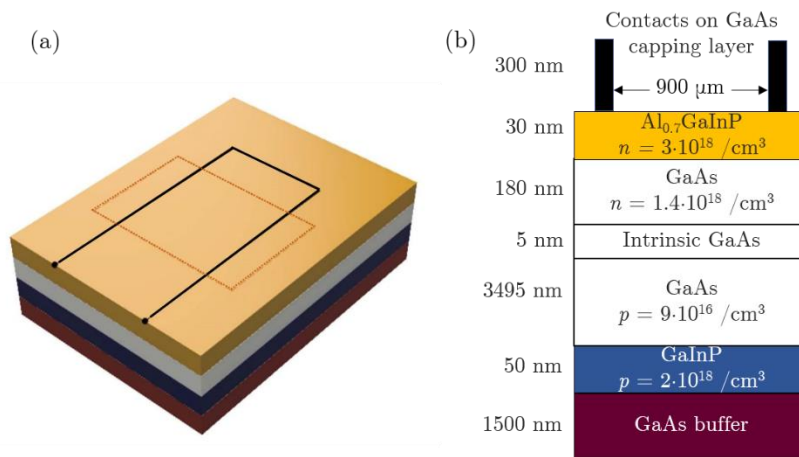
Figure 3-1 Structure of the investigated III-V solar cell(a) 3D sketch (not to scale) of the illuminated solar cell, where the fork-shaped contact (black lines) and the light collection zone (dotted orange square) are represented (b) (a). Layer structure of the illuminated solar cell

The investigated sample consists in a standard GaAs (gallium-arsenide) solar cell. Its layer structure is displayed in Figure 3-1(b). Figure 3-1(a) displays its 3D structure and notably shows the contact geometry, as well as the light collection area ($A_\text{f} = 1\text{mm}^2$). The cell power conversion efficiency is 18.8%, and its V_OC is 0.983 V. The investigated photoluminescence signal peaks at 1.44 eV, which designates the GaAs absorber layer as the emitting layer[149]. As the considered sample shows a lateral symmetry (parallel to the contact direction in the collection zone), we will often focus on the intensity integrated along the y-axis (contact axis). Note that the simple cell geometry was here chosen for the sake of clarity and that the presented experiment would also apply for more complex device configurations.

3.1.2. IMAGING SPECIFICS

The experimental set-up for TR-FLIM was presented in section 2.2. For our study, sequential acquisitions were realized. The gating time was varied stepwise between $t=t_\text{las}$ (taken as reference) and $t=300$ ns, whereas the gate width remained constant at 1 ns. A wide-field illumination was obtained with a home-built opto-mechanical set-up, which was not yet including a rotating diffuser (hence the speckle appearing in Figure 3-4(a)). With the considered configuration, the geometrical resolution is 1 μm. The illuminated area A_0 is larger than the active area of the solar cell ($A_\text{cell} = 5.2\text{mm}^2$). The photon flux incident on the sample was varied between $\Phi_0=3\text{x}10^{11}/\text{pulse}/\text{cm}^2$ and $8\Phi_0$.

3.2. PROJECTIONS OF THE DATA SET

3.2.1. TEMPORAL ASPECT

Any TR-FLIM experiment is followed by an exploratory phase, during which the acquired $I_\text{PL}(x,y,t)$ cube gets plotted along its temporal and spatial dimensions. We will here show the complementarity of these two exploration directions. At first, Figure 3-2 displays an I_PL image taken 10 ns after the laser pulse. The two blue stripes (lowest I_PL) on the image represent the metallic contacts (also on Figure 3-(c)), which are separated by a 900μm distance. Different cross-sections (b to e) parallel to the contacts are distributed equally between left and right contact. We calculated the mean time-resolved I_PL decays on these lines, and show them in Figure 3-3(b)-(f) for increasing incident powers.

At short times after the pulse, I_PL decays faster close to the contact than in the center of the cell. Despite being in open-circuit condition, the contacts seem to induce a locally higher recombination rate, which results in a I_PL intensity drop. On the contrary, a mono-exponential decay (straight line in semi-log scale) is apparent at the center of the cell, which hints that a unique recombination process dominate the charge carrier dynamics there.

51
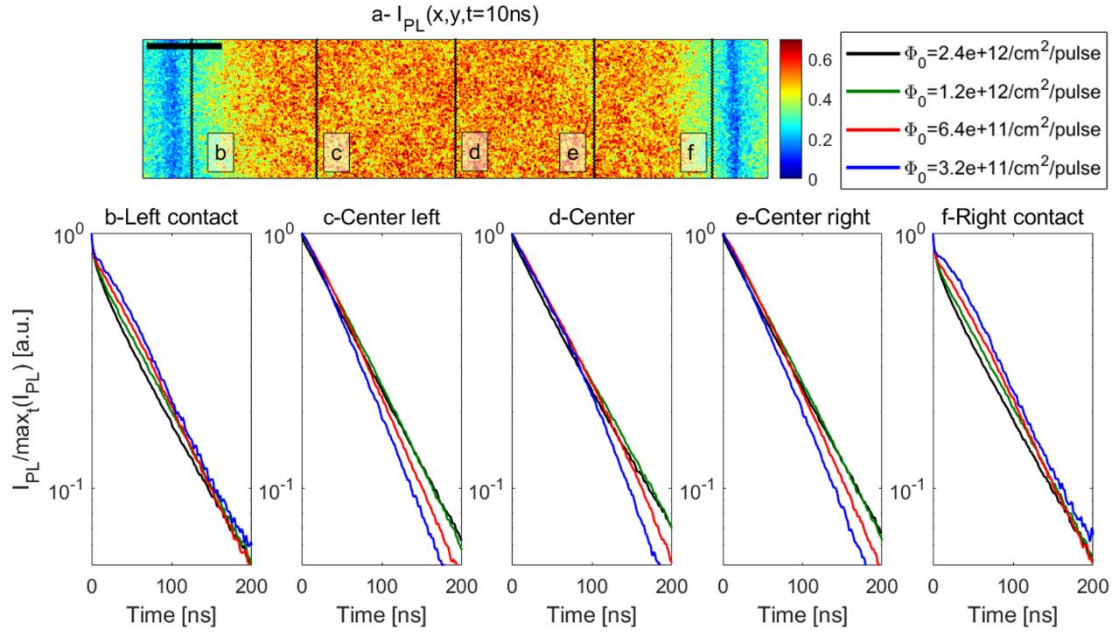
Figure 3-2 Photoluminescence image of a GaAs solar cell at open-circuit conditions (a). It is taken at t=10ns after the laser pulse. The scaling bar is 100 μm. Each black line corresponds to an extraction zone for the normalized TRPL decays shown in b-e. Several decays are represented with a color for each power Φ_0 (see caption on the top right corner)

At long times after the pulse, the decay speed seems homogeneous for each zone, even if it still depends on the injection level Φ_0. Similar observations are done at for left & right contact (Figure 3-3(b)&(f)), as well as for center left & center right (Figure 3-3(c)&(e)), pointing out the influence of the cell geometry on the probed I_{PL} signal.

3.2.2. SPATIAL ASPECT

After having considered temporal extractions of the dataset, we look at spatial extractions in Figure 3-3. For increasing time after the laser pulse, I_{PL} profiles orthogonal to contact direction are displayed. The contact zone appear as deeps at $x=\pm450\mu m$ and the profiles are normalized to their maximum for each time and injection level. Their shape change from a flat and almost uniform profile after the pulse to a steeper profile after a hundred of nanoseconds. One can note that the lower injection level is more rapidly quenched next to the contact, whereas the higher injection level remains rather flat at $t=50ns$. This constitutes another justification for the power study. Here again, the I_{PL} decay seems to be dominated by the recombination at the contacts, as I_{PL} is progressively quenched from this zone to the cell center. This calls for the development of a model for minority carriers including contact recombination and diffusion.
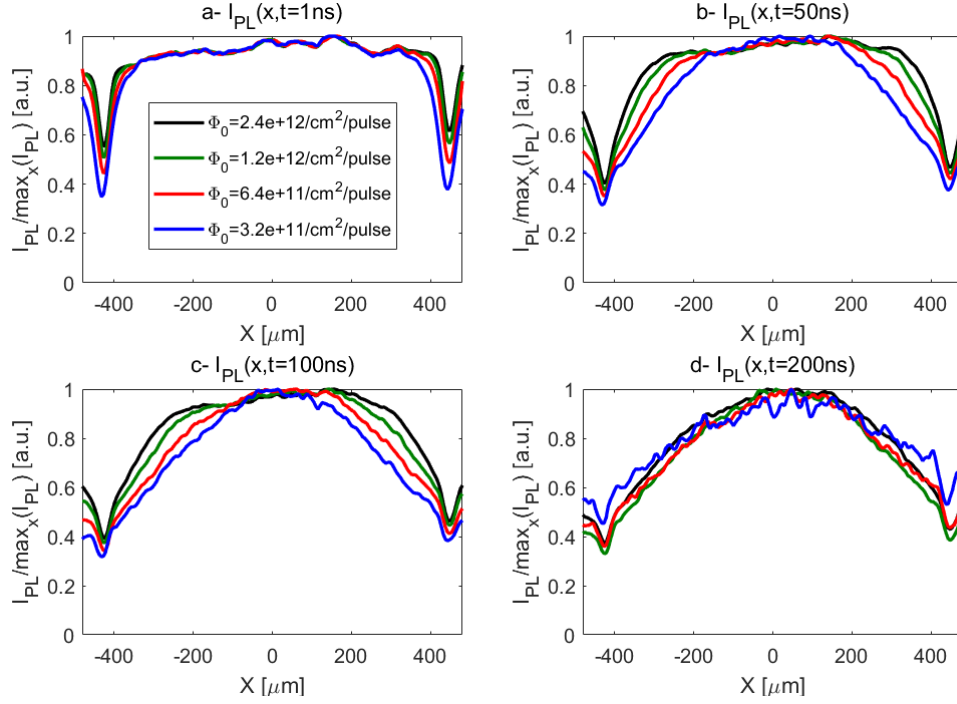
Figure 3-3 Experimental I_{PL} profile at t = 1, 50, 100, 200 ns after the laser pulse, for the same power study as in Figure 3-2.

3.2.3. SUMMARY

Now that we explored the spatial and temporal dimensions of the data cube, we can propose a graph summarizing the rich information it contains. Indeed, Figure 3-4(a)-(c) consists in a series of time frames revealing the time-resolved I_{PL} images at t=0, 10 and 100ns, while the global decay and deformation of I_{PL} profiles appear in Figure 3-4(d)-(f). Yet, visually taking into consideration the whole power study requires the previously introduced spatial and temporal extractions.

Thanks to the previous remarks, we can assess the phenomena most likely to influence the evolution of I_{PL} in such a solar cell. In addition to the obvious SRH recombination happening homogeneously in the bulk, non-radiative recombination at the contact seem to play a predominant role, as well as diffusion of charge carriers from the center of the cell to the recombining contact. Therefore, the next section is dedicated to the development of a physical model able to reproduce the whole I_{PL} evolution.
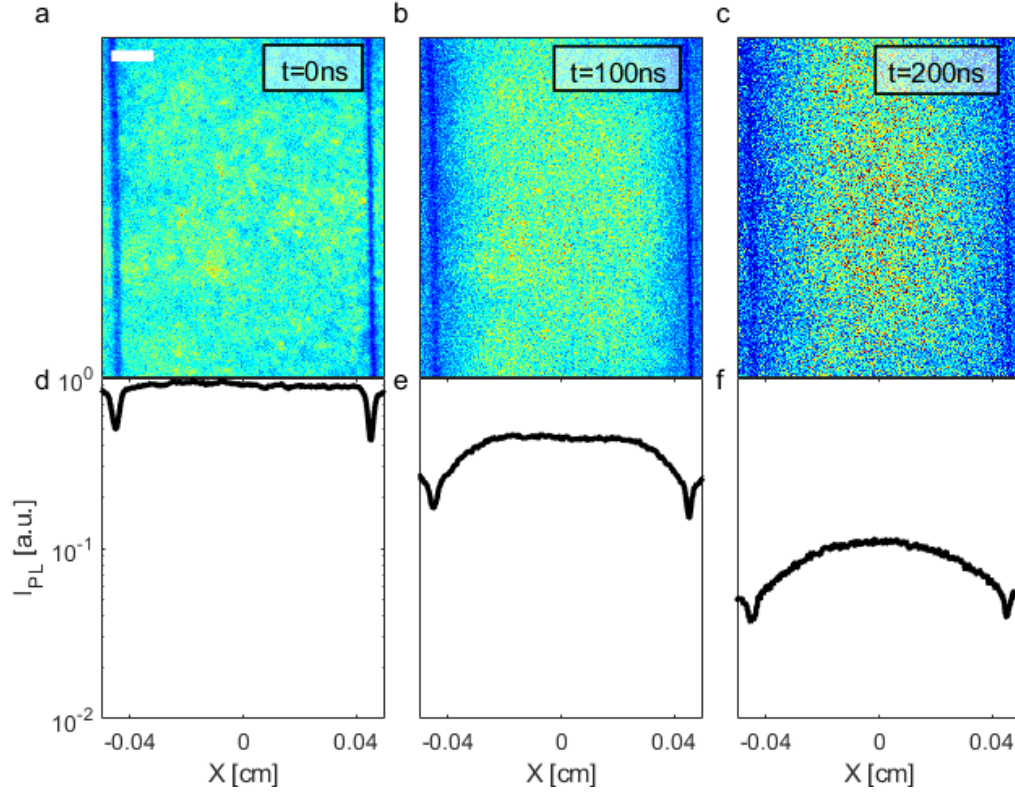
Figure 3-4 Photoluminescence images (a-c) and spatially integrated intensity profiles (d-f) for a complete GaAs solar cell in open-circuit condition, at incremental time steps following the laser pulse. (d-f) share the same vertical scale. Scaling bar is 100 μm long.

3.3. MODELING TRANSPORT

3.3.1. ABOUT NEGLECTING IN-DEPTH DIFFUSION

To develop the following model, a homogeneous charge carrier concentration throughout the thickness of the absorber layer is assumed. Even if absorbing the laser pulse generates an exponentially decaying concentration profile (as of Beer-Lambert absorption), it is totally homogenized in less than 1ns. This is due to the high mobility of charge carriers in a III-V material such as GaAs[160]; this condition might not be satisfied in all PV absorbers. We provide further justification by solving the continuity equation (introduced in section 1.2.2) and displaying the vertical concentration profiles for photo-generated carriers $\Delta n(z)$.
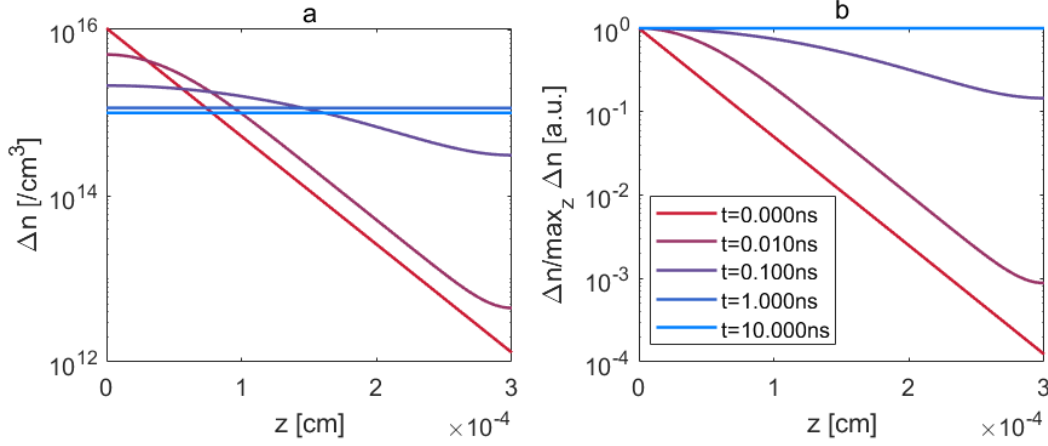
Figure 3-5 Vertical concentration profile for photo-generated electrons, at various time after the laser pulse (a), which are also shown normalized to their maximum (b). Simulation realized assuming standard diffusion properties for the GaAs layer : $D_n = 75cm^2/s$, $S_f = 10^2 cm/s$, $\tau_n = 75ns$[160]

Therefore, in-depth diffusion of minority carriers does not play a significant role in the present which focuses on a longer time scale (ns scale mostly). Once again if we consider other materials with lower mobility, this consideration needs to be revisited or we need to look at longer time scale as we will demonstrate in section 4.3.2.

Furthermore, we optically determined that the quasi-Fermi level splitting equals the open-circuit voltage in a similar device, which validates the assumption that there is no in-plane potential gradient inside our sample (i.e. homogeneous concentration of carrier in the sample depth).[149]

3.3.2. ABOUT NEGLECTING THE ELECTRIC FIELD

The electric field inside the solar cell, as well as the drift current it induces, will be neglected throughout this study. Our justification mainly relies on the negligible width of the depletion region w_{SCR} as compared to the absorber thickness. Indeed, if we consider a classic homojunction architecture, the electric field will be confined in the depletion region, where free charge carriers are absent and all dopants are ionized. This depletion region is located around the p-n junction and its width is defined by[161] :

$$w_{SCR} = \sqrt{2 \times \frac{\epsilon_0}{q} \times V_{bi} \times \left(\frac{1}{n_{0,GaAs}} + \frac{1}{p_{0,GaAs}} \right)} = 48 \text{ nm} \tag{3-1}$$

where the doping levels ($n_{0,GaAs}$ and $p_{0,GaAs}$) of the n- and the p-type parts of the absorber layer can be read in Figure 3-4(c), and V_{bi} is the built-in voltage defined by :

$$V_{bi} = \frac{kT}{q} \ln \left(\frac{n_{0,GaAs} p_{0,GaAs}}{n_i^2} \right) = 1.3 \text{ V} \tag{3-2}$$

Now, we made the point that w_{SCR} is 2 orders of magnitude lower than the cell thickness. Henceforth, taking the drift zone into account would slightly modify our assumption of a vertically uniform concentration profile. Still, it corresponds to a second-order correction to our model. One could also show interest for the transitory drift regime. Following Maiberg's calculations, the depletion region appears on the ps time scale, like

the homogenization of the vertical concentration profile[162], which further confirms the negligible aspect of the drift in our study.

3.3.3. CONTINUITY EQUATION

In section 3.2, we introduced the 3 main phenomena governing the charge transport in the considered device: bulk recombination, contact recombination and diffusion. In section 3.3.1 & 3.3.2, justifications were presented for taking only them into account and for excluding in-depth diffusion and the drift current. A final assumption relies in the fact that no trap centers are active in our high quality GaAs, which finally results in the electro-neutrality rule $\Delta p(x,t) = \Delta n(x,t)$, where Δn and Δp are the concentration of photo-generated electrons and holes.

Now, the incoming photon flux Φ_0 being low, Δn remains lower than the doping level p_0 and hence we can assume a monomolecular recombination regime[19]. Indeed, in p-doped semi-conductor such as GaAs, the radiative recombination rate R_{rad} yields (3-3), where R_{eh} is the radiative constant.

$$R_{rad} = R_{eh}\Delta n\left(\Delta p + p_0\right) = R_{eh}\Delta n p_0 \propto \Delta n \tag{3-3}$$

Here, we also used the weak injection regime assumption (i.e. $\Delta n << p_0$) to describe the radiative recombination rate as solely depending on the minority carrier population[19]. Observing I_{PL} in our TR-FLIM set-up is equivalent to having access to the in-depth integration of Δn. As we assume a homogeneous in-depth charge carrier concentration, we can write:

$$I_{PL}(x,t) \propto \Delta n(x,t) \tag{3-4}$$

This assumption allows us to explain the temporal and spatial variations of I_{PL} with the transport of minority charge carriers[19], which is ruled by equation (3-5) in the bulk and by equation (3-6) at the contacts (localized at $x=\pm450\mu m$):

$$D_{eff}\frac{\partial^2\Delta n}{\partial x^2} - \frac{\partial\Delta n}{\partial t} + \frac{\Delta n}{\tau_n} = 0 \tag{3-5}$$

$$S_c n = D_{eff}\frac{\partial\Delta n}{\partial x} \tag{3-6}$$

In this model, τ_n is the minority carrier lifetime, D_{eff} is the minority carrier effective diffusion coefficient in the solar cell, and S_c is the recombination velocity at the contact. An effective diffusion length can be defined by $L_{eff}S_c = D_{eff}$ [163]. The wide-field uniform illumination Φ_0 and the thickness of the absorber z_0 dictate the initial condition:

$$\Delta n(t=0,x) = \frac{\Phi_0}{z_0} \tag{3-7}$$

3.3.4. SOLVING THE CONTINUITY EQUATION

An analytical solution to this model can be determined[164], and can be written as a sum of sinusoidal contributions $U_k(x)$, with spatial pulsation β_k:

$$\Delta n(x,t) = \left(\sum_k A_k\, U_k(x) \exp\left(-D_{eff}\beta_k^2 t\right)\right)\exp\left(-\frac{t}{\tau_n}\right) \tag{3-8}$$

$$U_k(x) = \cos(\beta_k x) + \frac{S_c}{D_{\text{eff}}\beta_k}\sin(\beta_k x) \tag{3-9}$$

$$A_k \in \mathbb{R} \; ; \; \tan(\beta_k x_0) = \frac{2D_{\text{eff}}\beta_k/S_c}{D_{\text{eff}}^2\beta_k^2/S_c^2 - 1} \tag{3-10}$$

A_k coefficients are determined by projecting the spatial initial condition on the basis formed by $U_k(x)$ contributions. On the temporal scale, the TRPL decay is locally multi-exponential, and τ_n has a global influence. On the spatial scale, the I_{PL} profile is equivalent to $A_1 U_1(x)$ after a certain time t_∞. This can be evidenced by dividing the general solution in eq. (3-8) by $A_1 U_1(x)\exp(-t/\tau_n)$, to which it will be equivalent at long times:

$$\frac{\Delta n(x,t)}{A_1 U_1(x) e^{\frac{t}{\tau_n}}} = 1 + \left(\sum_{k>1}\frac{A_k}{A_1}\frac{U_k(x)}{U_1(x)}\exp\left(-D_{\text{eff}}(\beta_k^2-\beta_1^2)t\right)\right) = 1 + R_\infty(x,t) \tag{3-11}$$

Now, it is obvious that the second term of this sum $R_\infty(x,t)$ tends to 0 at exponential speed at long times. What's more, it is dominated by its first term:

$$R_\infty(x,t) \sim \frac{A_2}{A_1}\frac{U_2(x)}{U_1(x)}\exp\left(-D_{\text{eff}}(\beta_k^2-\beta_1^2)t\right) \tag{3-12}$$

Thanks to eq. (3-12), one can estimate the time t_∞ after which the I_{PL} spatial profile is equivalent to $A_1 U_1(x)$, which would be:

$$R_\infty(x,t) < e^{-3} \Leftrightarrow t > t_\infty = \frac{3}{D_{\text{eff}}(\beta_2^2-\beta_1^2)} \tag{3-13}$$

Here, one can note that a greater value for D_{eff} induces a smaller value of t_∞ which is consistent with the physical intuition. Indeed, a faster diffusion will accelerate the convergence to stable I_{PL} profile.

3.3.5. FITTING PROCEDURE

This mathematical analysis finds an application with the following fitting method. At first, τ_n is determined by fitting a single TRPL decay far from the contact. Indeed, one can consider the differential equation (3-5) at short times, in which the homogeneous illumination is zero (homogeneous generation). Then the decay rate appears as the derivative of $\log(\Delta n)$:

$$\frac{\partial \log \Delta n}{\partial t}(x,t=0) = -\frac{1}{\tau_n} \tag{3-14}$$

Our fitting procedure will then determine optimal values for (S_c, D_{eff}), by fitting the experimental decays I_{PL} to the theoretical profiles from eq. (3-8). It is equivalent to solving the optimization problem presented in eq. (3-15), where the analytical solution is compared point by point to the spatially normalized intensity profiles $I_{\text{PL}} / \max_x (I_{\text{PL}})$. On the contrary to τ_n, the precise determination of D_{eff} and S_c requires the combination of temporal and spatial data, which underlines the utility of the TR-FLIM set-up.

$$\min_{D_{\text{eff}}, S_n} \sum \left(\frac{I_{\text{PL}}(x,t)}{\max\limits_{x}\left(I_{\text{PL}}(x,t)\right)} - \frac{n(x,t)}{\max\limits_{x} n(x,t)} \right)^2 \qquad (3\text{-}15)$$

3.4. DETERMINATION OF TRANSPORT PROPERTIES

3.4.1. SENSITIVITY TO FITTING PARAMETER

Figure 3-6(a) confirms that τ_n has a global influence throughout the cell. On the same figure, (d) & (f) allow to underline the great influence of L_{eff} & S_c at the contact, while (c) & (e) demonstrate their negligible impact at the center. The quick reading procedure at the center of the cell is recommended. On the spatial scale, L_{eff} has a great influence on the final (long-time) PL profile (see (g)) while S_c has an non-existent impact (h). This sensitivity analysis justifies the choice of (L_{eff} , S_c, τ_n) as fitting parameters, by attributing each of them a specific area of the dataset where their influence will be probed solely.
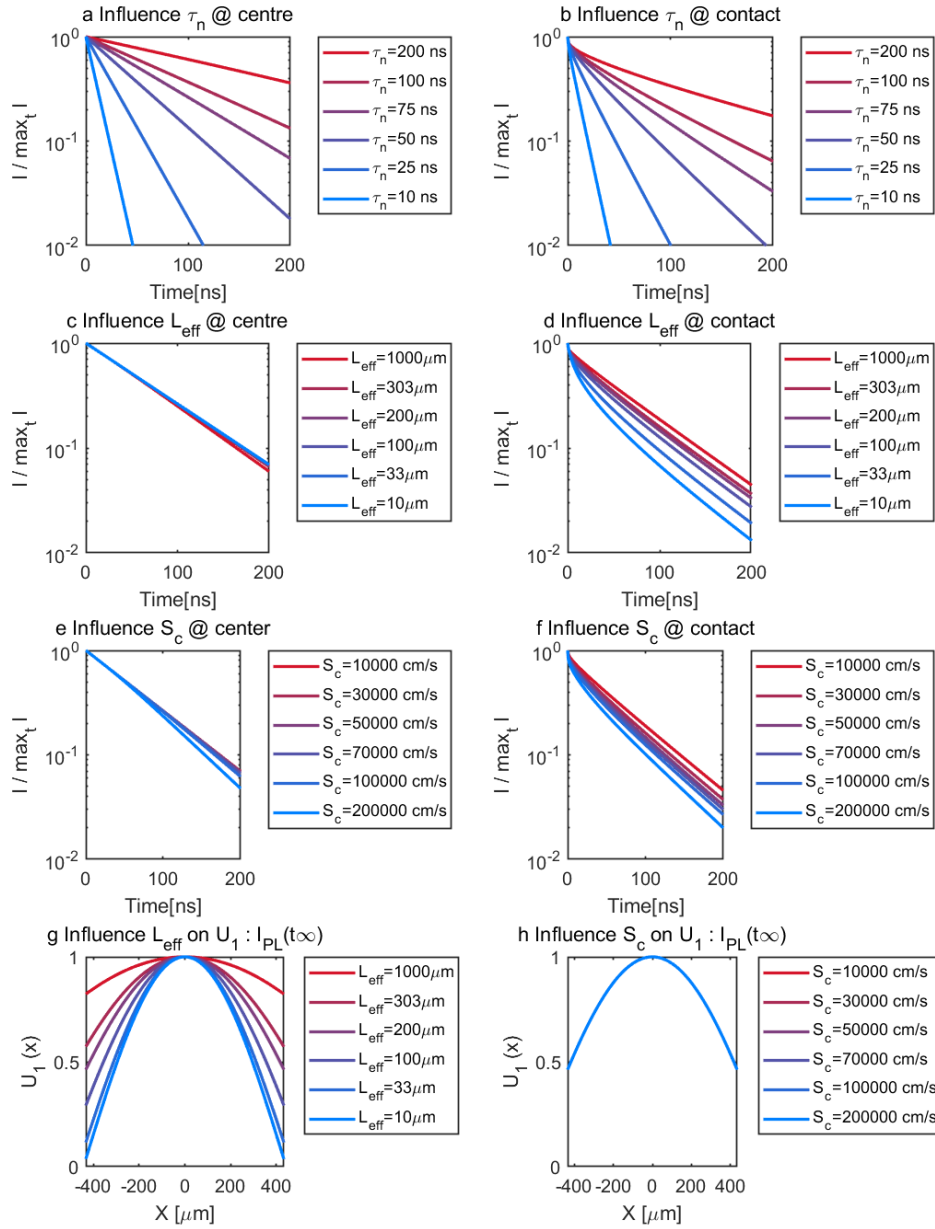
Figure 3-6 Simulations of I_{PL} transients/profiles according to eq. (3-8)at the center of the cell (a,c,e) and at the contact (b,d,f). τ_n is varied in (a,b). L_{eff} is varied in (c,d), and S_c is varied in (e,f). Simulations of PL profile at long times according to eq. (3-9) for L_{eff} and S_c variation. When one parameter is varied, others stay at the following values :L_{eff}=200μm, S_c=5 10^4cm/s, τ_n=75ns.

3.4.2. ABOUT OUR III-V SOLAR CELL
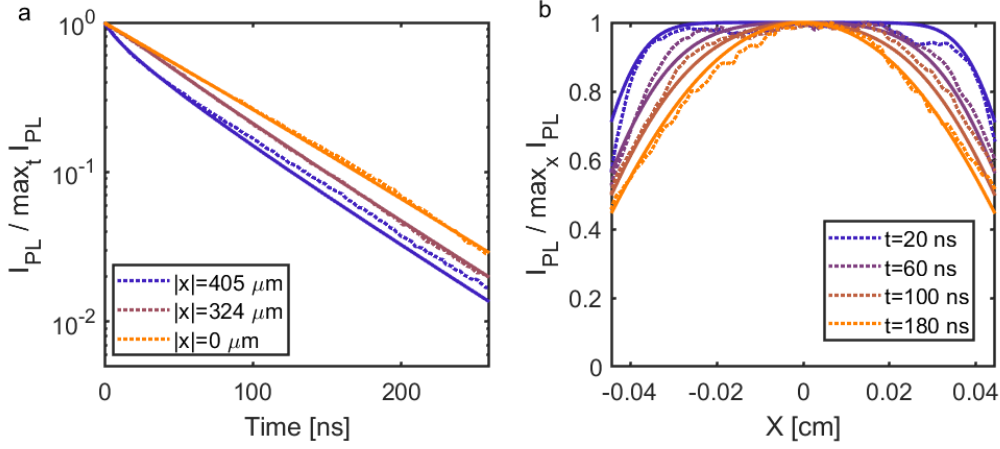
Figure 3-7 Fitting results vs experimental I_{PL} transients/profiles(a) PL experimental (dotted lines) and fitted (plain lines) decay at |x|=0, 324, 405 µm. (b) PL experimental (dotted lines) and fitted (plain lines) profile at t = 20; 60; 100; 140; 180 ns. Fluence level for both figure is Φ_0=1.2 x 10^{12} /cm² /pulse.

In Figure 3-7, dotted lines show I_{PL} decays and profiles acquired on a GaAs solar cell at a moderate fluence level Φ_0=1.2x10^{12} /pulse/cm². Similarly to Figure 3-2, normalized temporal intensity profiles at various locations in the solar cell (from contact to center) are displayed in Figure 3-7 (a). Normalized spatial intensity profiles at various time delays after the pulse are displayed in Figure 3-7 (b). As explained in eq. (3-14), we first determine the bulk lifetime τ_n by fitting the I_{PL} decay far from the contact (x=0µm) as a mono-exponential decay. It yields τ_n = 75 ns.

In the same figure, plain lines show the numerical solution for the fitted parameters τ_n=75 ns, D_{eff}=2160 cm²/V/s, and S_c=1.2x10^5 cm/s. With this small amount of parameters, both spatial and temporal evolution of the I_{PL} intensity are reproduced with a good accuracy, except in the vicinity of the contact. Furthermore, the observed convergence of the PL profile after 100ns is consistent with the proposed calculation of t_∞ in eq. (3-13) as well as with the value of L_{eff}=190 µm.

In order to validate this fitting approach, we studied the evolution of the reconstruction error induced by little changes in the fitting parameters. This error is displayed by the contour lines in Figure 3-8 and its steep rise demonstrates the robustness of our method. Its isotropic rise (concentric circles) indicate the weak correlation between fitting parameters. The physical constants determined for various fluence levels are displayed in Table 3-1. D_{eff} confidence intervals are calculated according with error propagation. The effective diffusion length remains constant, whereas the drop in contact recombination velocity indicates a saturation. It also induces a drop of D_{eff}, as the loss at the contacts is reduced while L_{eff} remains constant. Eventually, the very slow reduction of τ_n validates again the assumed monomolecular recombination regime[162].

Φ_0 [/pulse/cm^2]	$\dfrac{\Delta n_{t=0}}{p_0}$	τ_n [ns]	L_{eff} [μm]	S_n [x 10^5 cm/s]	D_{eff} [cm^2/s]
3 x 10^{11}	1%	75 ± 1	180 ± 20	3.2 ± 0.4	5760 ± 900
6 x 10^{11}	2%	75 ± 1	190 ± 20	2.0 ± 0.2	3800 ± 550
1.2 x 10^{12}	4%	75 ± 1	180 ± 20	1.2 ± 0.1	2160 ± 390
2.4 x 10^{12}	8%	72 ± 1	180 ± 20	0.7 ± 0.1	1440 ± 260

Table 3-1 Fitted physical parameters for each injection level. p_0 is the doping concentration of the absorber. For the whole range of fitting parameters indicated, the reconstruction error rises by less than 10%.
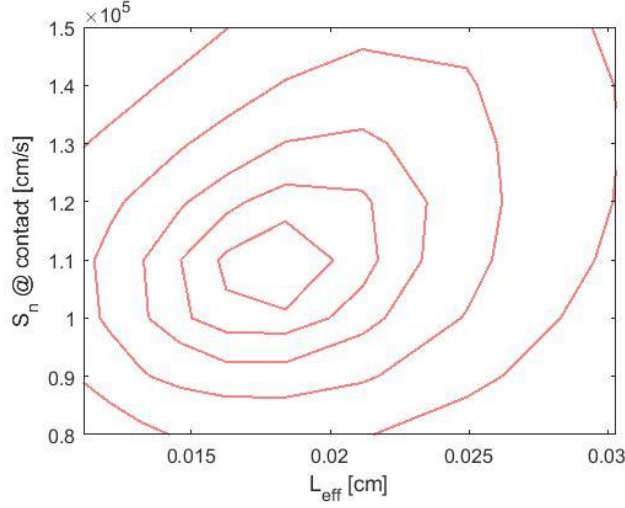
Figure 3-8 Reconstruction error between the experimental transient and the theoretical modelcalculated with the least square method. This corresponds to n_0=1.2x10^{12}/cm^2/pulse and τ_n=75ns. Contour lines limit an area where the reconstruction error does not rise by more than 10 %, 25 %; 50 % ; 100 % ; 200 %

3.5. DISCUSSION

In the previous sections, we demonstrated that a single contactless experiment was enough to characterize the lateral transport of minority carriers in a fully assembled solar cell. By measuring and modeling the temporal and spatial evolution of the PL intensity, we could determine τ_n, L_{eff} and S_c, unlike many other characterization methods which necessitate a supplementary input parameter[32,165–167].

The model we propose to reconstruct the data cube is simple yet trustable. It was already used in a vertical direction (from the front contact to the back contact) to fit results from TRPL or Time of flight experiments in bulk GaAs[164,165], or more recently to model the lateral transport in the same material[32,168]. Nonetheless, we implement it in a novel approach, i.e. for the lateral transport inside a solar cell. Again, its robustness is proved by the simultaneous reconstruction of both temporal and spatial evolution of the PL intensity. Note that a symmetrical situation ($S_{c,\text{left}}$=$S_{c,\text{right}}$) was considered here for the sake of clarity, but that this model is extensible to more complex geometrical configurations.

In particular, this model highlights an effective diffusion length L_{eff}, which assesses the geometrical extent of the contact. Such an effective diffusion length was already observed for an in-depth application of the model, with a front and a back surface recombination velocity[153,169]. In our case, it characterizes the mean path length laterally travelled by charge carriers in the fully assembled solar cell. Considering its value significantly larger than commonly measured diffusion length inside low-doped GaAs[32,167], it seems clear that the lateral transport to the contact happens (at least partially) in another layer, which could be the AlGaInP top layer. It so happens in other optoelectronic devices, such as the AlGaInP LEDS containing a current spreading layer[170]. In any case, L_{eff} reflects the charge extraction efficiency under realistic excitation conditions and could be used to optimize the design of the contact and front sheet, as done with the measurements of $R_{\square}$ by electroluminescence[171,172].

Also, our fitting procedure gives access to the lifetime associated to the main recombination channel, i.e. the bulk lifetime τ_n of the absorber. Its value being independent of the injection level, it corresponds to the monomolecular rate. It is comparable to that found by Nelson and Sobers for a similar p-doping level[173]. On the contrary, the last fitting parameter, S_c, shows a strong injection dependence. The saturation of the surface states inducing the high recombination rate could explain the S_c drop. This is suggested by Cadiz et al. who assessed the injection dependence in the surface recombination model, by studying a bare GaAs/GaInP interface. They stated that S_c^{-1} depends logarithmically on n_0[174], which is reproduced by our power study with a good agreement. A higher Φ_0 could induce a lower S_c at the contact, and a variable $S_c(\Delta n)$ could be introduced in the model. This would correspond to a good quality second-order correction. However, it implies to develop a more complex numeric model, as no exact solution to the differential system can then be determined.
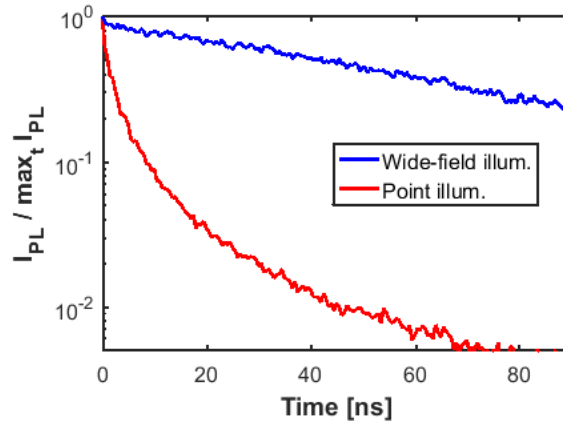
Figure 3-9 I_{PL} transient for a wide-field illumination and a local excitation taken in between fingers,, integrated on a 10 µm×10 µm square (Φ_0=3x10^{12}/pulse/cm^2 in WF & Φ_0=2x10^{14} /pulse/cm^2 in point illumination).

The advantage taken from using wide-field illumination is eventually discussed here. Our TR-FLIM technique could be compared to micro-photoluminescence mapping as it has been used to measure carrier transport with a contactless method. It probes the lateral diffusion by changing the collection area (i.e by changing the pinhole size in

confocal system). Nevertheless, it usually works at relatively high fluence and requires a tabulated information as input such as the radiative coefficient.[175]

Furthermore, we can compare our wide field excitation to a punctual one and observe the effect on the carrier dynamics. Resulting I_{PL} transients are shown in Figure 3-9. With the local illumination, the dark surrounding acts as a low biased diode attracting the minority carrier. Due to this lateral diffusion of photoelectrons far from the excitation region, a quick drop in the local PL intensity is observed. On the contrary, the PL decays at a constant rate corresponding to the bulk lifetime for a wide-field illumination. This notably illustrates the importance of properly scaling the excitation and photon collection conditions to the raw absorber diffusion length and to the effective diffusion length in the finished optoelectronic device[21,176,177]. Yet, it remains possible to probe transport properties by using a point illumination on the TR-FLIM set-up, as we will prove in Chapter 5.

3.6.   CONCLUSION

In this chapter[178], we introduced an optical contactless characterization method: TR-FLIM, which consists in acquiring time-resolved PL images of an optoelectronic device in order to determine transport properties. A first successful application on a GaAs-based solar cell leads to the simultaneous determination of τ_n, L_{eff} and S_c, without any prior knowledge about its physical properties. This chapter opens the gate to further studies of other optoelectronic devices with TR-FLIM, especially in Si solar cells where the development of passivating contacts call for precise measurement of S_c[179].

4. In-depth transport in a perovskite thin film

In this chapter, we focus on diffusion properties in perovskite materials, as they play a crucial role in solar cell operation, during which charge carriers diffuse to the transport layers[39]. These diffusion properties have two complementary aspects: the sensitivity to a carrier concentration gradient (diffusion coefficient D), and the average time available for the diffusion process (lifetime τ). A wide range of D values have been reported in the literature[54,103,114,115]. Here we propose to evaluate D and τ by measuring TRPL decays in perovskite layers.

Time resolved optoelectronic characterization techniques have thoroughly been used to investigate the transport properties inside perovskite solar cells. At the picosecond scale[109], transient optical transmission spectroscopy allowed determining the best electron/hole transport layers (E/HTL), by studying the charge carrier extraction speed at interfaces[80,180]. At the ns scale, bulk transport and recombination become dominant[109]. TRPL decays are well adapted to this time scale, and their analysis paved the way towards a deeper understanding of charge carrier transport inside perovskite absorbers[181,182]. At first, the low binding energy of the exciton[95,123] explained their negligible concentration under realistic excitation conditions (1 sun illumination, room temperature). This initiated the switch from an organic point of view (exciton quenched at the contact) to an inorganic one (free charges diffusing to the contacts)[109,115]. In a second phase, this technique also allowed to underline the predominant role of trap states in recombination kinetics, for various chemical compositions of perovskite[37,101,104,183]. Considering the multiple time-dependent phenomena in bulk perovskite, a unique PL lifetime is not sufficient to assess its quality[10], on the contrary to physical parameters extracted thanks to more detailed models.

In this chapter, we describe briefly the sample matrix considered, which includes several chemical compositions and interface conditions (section 4.1.1) and leads to various PV performance (section 4.1.2). After presenting an overlook of the dataset (spatial and temporal aspects) in section 4.1, we develop a charge carrier transport model able to reconstruct I_{PL} transients in section 4.3. Fitting the model to the acquired I_{PL} transients allows us to fully characterize in-depth transport and recombination. We do so in various perovskite absorbers and compare them to emerge common properties (section 4.4). Finally, we discuss the validity of different models and the physical signification of the fitting parameters in section 4.5.

4.1.   EXPERIMENTAL DETAILS

4.1.1. SAMPLE STRUCTURE

While the general formula for hybrid organic-inorganic halide perovskites is fixed by the crystalline structure they share (ABX_3), numerous possibilities in the chemical composition arise for the choice of the cation A^+ (methylammonium cation MA^+, formamidinium cation FA^+, Cs^+, Rb^+)[54–56,184], the halide X^- (I^-; Br^-; Cl) [54,80,185], and the central metal cation B^{2+} (Pb^{2+} or Sn^{2+})[186]. For our study, we selected various absorber layers for their bandgap adapted to PV applications, and for their relative stability to phase segregation[87,125]. The number of monovalent cations A^+ varies from one to three. The simplest hybrid perovskite compound is $MAPbI_3$ (noted P_1), to which FA^+ or {FA^+ and Cs^+} or {FA^+ and Rb^+} are added, giving the following different compositions $MA_{0.17}FA_{0.83}Pb(I_{0.83}Br_{0.17})_3$ (noted P_2), $(MA_{0.17}FA_{0.83})_{0.95}Cs_{0.05}Pb(I_{0.83}Br_{0.17})_3$ (noted P_3) and $(MA_{0.17}FA_{0.83})_{0.95}Rb_{0.05}(I_{0.83}Br_{0.17})_3$ (noted P_4).

For TRPL characterization, samples were prepared with an architecture both perovskite/fluorine-doped tin oxide (FTO) and perovskite/ mesoporous(mp)-TiO_2/ blocking(bl)-TiO_2/ FTO. The latter is represented in cross-sectional view in Figure 4-1(c). FTO was commercially available while bl-TiO2 was synthetized by spray pyrolysis and mp-TiO2 was spun coated and subsequently sintered. Perovskite absorbers were prepared with minor modifications regarding previously reported procedures (Ahn et al.[77] for P_1, and Saliba et al. [55,56] for P_2, P_3, and P_4). The thickness of perovskite layer z_0 is around 500 nm, as seen in the cross section image in Figure 4-1(c). Concerning the devices used for PV characterization, the Spiro-OMeTAD later was deposited by spin coating, and the Au layer was deposited by thermal evaporation over TiO_2 containing devices to complete the solar cell. More details concerning the sample preparation is available in the Supplementary Information of the article, online[187].

4.1.2. PV CHARACTERIZATION
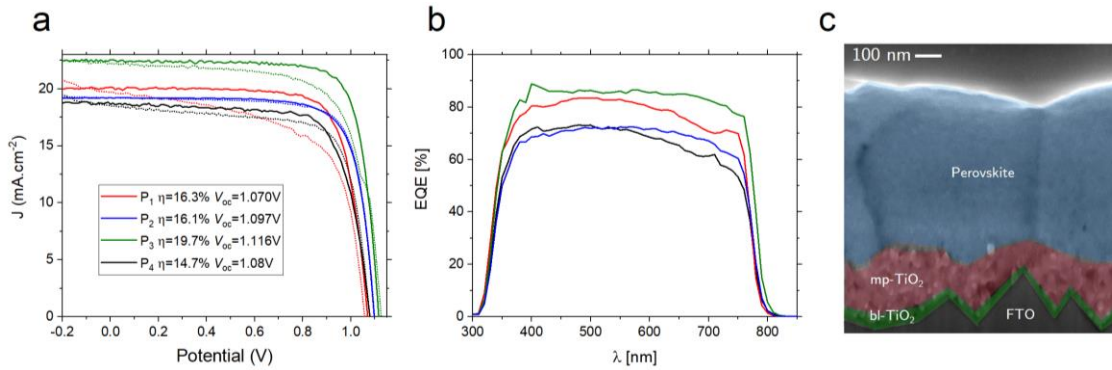
Figure 4-1 J-V; EQE and cross section SEM image of the investigated sample: (a) J-V characteristics recorded in reverse conditions (80mV/s, full line) and forward conditions (80 mV/s, dotted line) of the devices based on perovskite absorber with various chemical composition. Extracted electrical parameters are indicated in the caption. (b) External Quantum Efficiency measurements on the same devices. (c) Focused Ion Beam (FIB) image, highlighting the layer structure of the sample probed by TRPL, when mp/bl-TiO₂ is the back interface.

The cell performances are strongly linked to the absorber composition as shown in Figure 4-1(a), where the electrical parameters from our different record cells fabricated in our lab are summarized. The PCE of the mono-cation perovskite P_1 reaches a maximum value of $\eta = 16.3$ %. However, the voltage scan direction has a drastic influence on the PCE, as the forward scan (increasing potential) leads to an absolute 3 % loss in PCE ($\eta = 13.1$ %). This hysteresis, also discussed in section 1.3.3, hampers the analysis of I-V curves.

This hysteresis is largely mitigated by the partial substitution of MA through an additionial organic cation (FA) in the perovskite structure. If the maximum PCE values remain stable ($\eta = 16.1$ % for P_2), the sensitivity of the electrical parameters to the measurement conditions is reduced. The PCE in forward conditions is 16.2 % and the currents of the EQE and the J-V closely match. Interestingly, the cell performance is further enhanced with the incorporation of Cs cation (P_3), as its PCE reaches 19.7 % ($\eta = 17.6$ % for a forward scan). On the contrary, the use of the Rb as third cation in P_4 leads to a lower cell performance with a maximum PCE of 14.7 %.

4.1.3. Imaging specifics

For our study, we use the TR-FLIM set-up introduced in section 2.2. The gating time was varied with a 2ns-step between $t=t_{las}$ (taken as reference) and $t=1$ μs, whereas the gate width remained constant at 2 ns. The wide-field illumination is obtained thanks to a home-built opto-mechanical set-up that also filters laser speckles. The intensity of the photon flux incident on the sample was varied, over three order of magnitude ($\Phi_{0,1}=2.5\text{x}10^{10}$; $\Phi_{0,2}=2.25\text{x}10^{11}$; $\Phi_{0,3}=1.6\text{x}10^{12}$/pulse/cm^2/pulse). The illuminated area ($\approx$1 mm^2) is larger than both light collection areas Z_1 & Z_2 ($A_{Z1}=A_{Z2} \approx$0.1 mm^2), themselves significantly larger than the diffusion area inside the samples ($\approx$1-10 μm^2). Hence, lateral diffusion of charge carriers does not lead to any artefacts[21] and we can focus on their in-depth diffusion and recombination.

4.2.   PROJECTIONS OF THE DATASET

4.2.1. Spectral aspect

For all sample considered, the probed PL signal originates from the perovskite layer. This is evidenced in Figure 4-2, where the PL spectrum emitted by each sample is shown, without any hint towards a secondary phase emitting. The absolute PL spectra of P_1 (MAPI) is one order of magnitude less intense than P_2-P_3-P_4. This already indicates its lower quality, which will be further commented in the results section 4.4. These spectra will also be used later in this chapter for photon reabsorption consideration (see section 4.3.4).
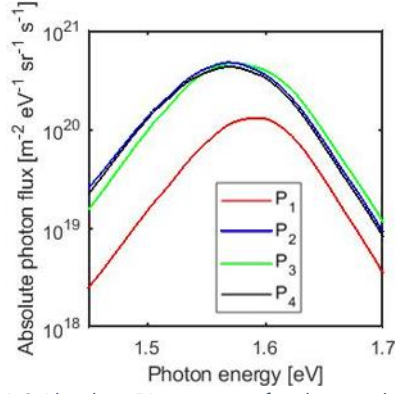
Figure 4-2 Absolute PL spectrum for the considered perovskite samples, optically excited at λ = 532 nm at $\Phi_0 = 5.5 \times 10^3$ W·m^{-2}.

4.2.2. SPATIAL ASPECT

For each of the perovskite composition, time-resolved I_{PL} movies have been acquired. While $I_{PL}(x,y,t=0ns)$ images (not shown here) are as homogeneous as the wide-field illumination, relevant information for recombination can be extracted from I_{PL} images taken 10 ns after the laser pulse. They are shown in Figure 4-3(a-d). The geometry of the cell corresponds to perovskite/FTO (Z_1) on the left and perovskite/mp-TiO$_2$/bl-TiO$_2$/FTO on the right, as sketched in Figure 4-3(e). On each figure (a-d), whitish rectangles indicate the future zone of interests, on which I_{PL} decays are averaged. Already on this data extraction, we can see that the TiO$_2$ back interface quenches I_{PL} at long times after the laser pulse, which generally points out a higher recombination rate. Also a relative spatial homogeneity of I_{PL} is observed, which further justifies the spatial mean we consider here. Solely on Cs-containing P$_3$ composition, wrinkles appear in this batch. The reader is referred to section 5.5 for more information on these wrinkles. Notably, the spatial aspect bears a restrained message in this chapter in which we use a wide-field illumination on rather homogeneous samples.
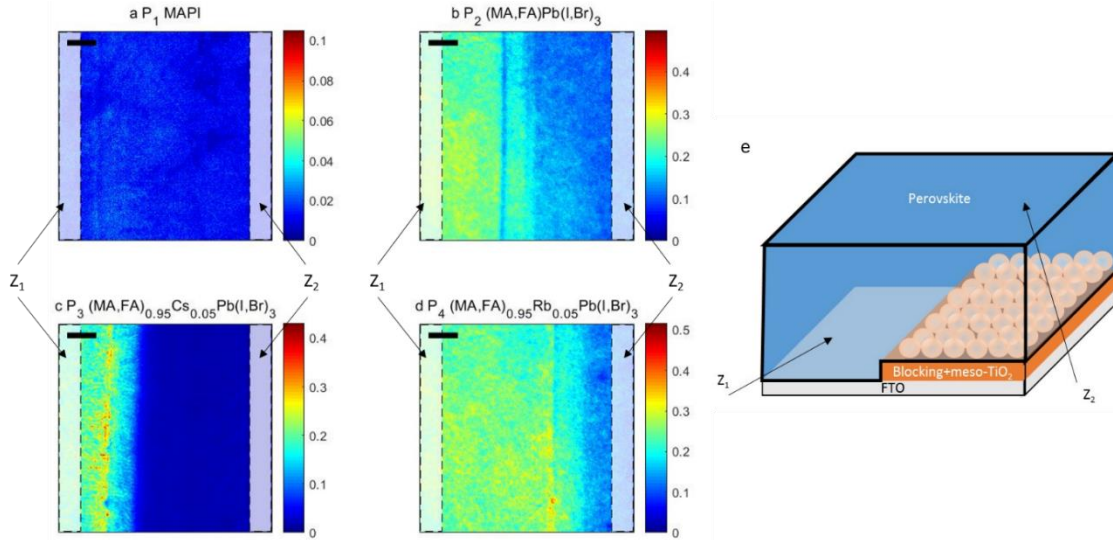
Figure 4-3 Photoluminescence images taken 10 ns after the laser pulse$I_{PL}(x,y,t=10ns)$) in arbitrary units for different compositions considered throughout this study (P$_1$ to P$_4$ from a to d). On the left of each image, Z_1 appears with a whitish framed area, while, Z_2 appears on the right. (e) summarizes the sample structure investigated. Scaling bar is 100μm long

4.2.3. Temporal aspect

The temporal extraction on a zone corresponds to the frequently used TRPL decay. For the zone Z_1, I_{PL} decays appear in Figure 4-4(a-c). While P_2 to P_4 feature similar behaviors with a fast I_{PL} drop at short times and a slower decay up to the end of the acquisition (t=1.5µs), the P_1 composition decays drastically faster. When deposited on bilayer-TiO$_2$ interface (zone Z_2), this fast decay for P_1 is also observed (see Figure 4-4(d-f)). The Cs-rich composition (P_3) also displays a faster decay.
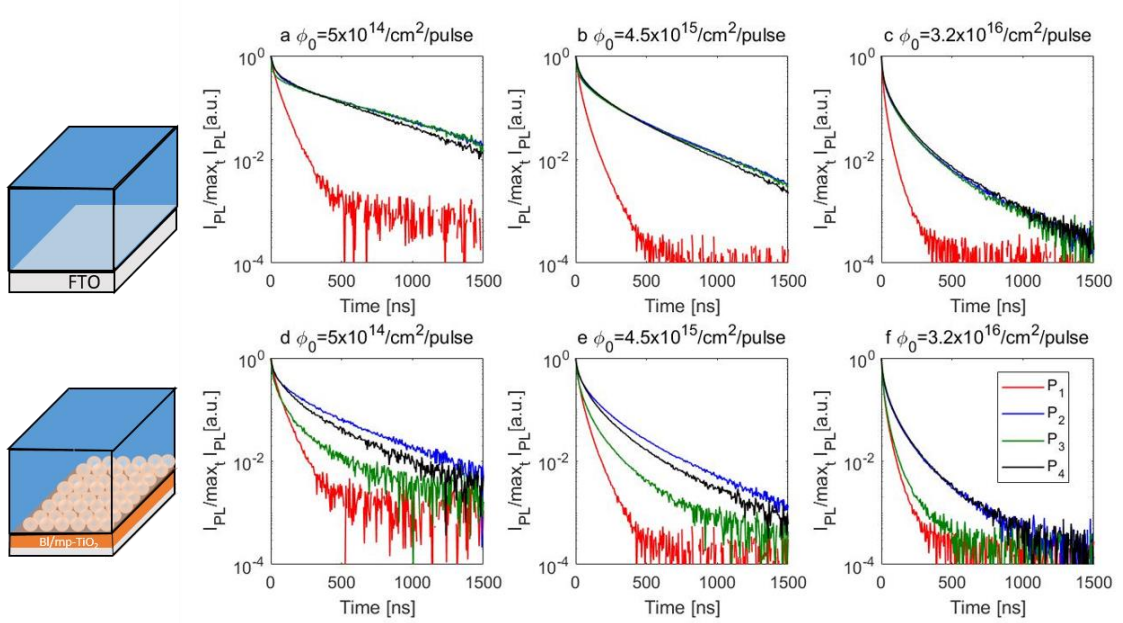
Figure 4-4 Photoluminescence decays for perovskite deposited at increasing injection levels, on FTO (a-c), and on bilayer-TiO$_2$ (d-f)

The phenomenological analysis of this group of I_{PL} decays will here remain limited. Recently, empirical models have been developed to explain non-exponential decays in perovskite thin films, like the stretched exponential model[186,188] or the bi-exponential model[50,131]. However, they fail to reproduce transients from a power study, and can only yield relative quantification of recombination and transport processes. As an illustration, the bi-exponential model would yield injection-dependent "lifetimes", which would be hard to convert into a clear diagnostic. In the next section, we will develop a physical model that is consistent at any injection level.

4.3. MODELING TIME-RESOLVED PHOTO-LUMINESCENCE

In this section, we start from a well-established model including traps[37,85] (section 4.3.1), which we complete by considering the in-depth diffusion of charge carriers (section 4.3.2) and by deriving I_{PL} from charge carrier concentration (4.3.4). Another model summarizing the trap-induced recombination by a non-radiative lifetime will also be introduced (section).

4.3.1. MODELING TRAPS

We model the perovskite layer as a semi-conductor with low intrinsic concentrations ($n_0 \approx 10^7/\text{cm}^3$, see section 5.4.3) and no doping (see section 1.3.2), in which we will write $\Delta n = n$ and $\Delta p = p$. In addition to electron and hole population, we consider a third population called "trapped electrons" n_T, which concentration has to remain lower than the total traps concentration N_T. These 3 populations are represented on an energetic diagram in Figure 4-5(a), where arrows indicate the recombination pathways along with their associated rates R_{pop} (electron capture, similar to $R_{\text{pop,n}}$ in section 1.2.3), R_{dep} (hole capture, similar to $R_{\text{pop,p}}$ in section 1.2.3) and R_{eh}* (net band-to-band recombination, including generation due to photon recycling). The following rate equations (4-1), (4-2) & (4-3) allow to follow their concentration in time. They include the assumption that $R_{\text{em,n}} = R_{\text{em,p}} = 0$, which is equivalent to say that the trap level is rather deep in the gap, so that any emission is forbidden.

$$\frac{\partial n}{\partial t} = -R_{\text{eh}} \, n \, p - R_{\text{pop}} \, n \, (N_T - n_T) \tag{4-1}$$

$$\frac{\partial n_T}{\partial t} = R_{\text{pop}} \, n \, (N_T - n_T) - R_{\text{dep}} \, n_T \, p \tag{4-2}$$

$$\frac{\partial p}{\partial t} = -R_{\text{eh}} \, n \, p - R_{\text{dep}} \, n_T \, p \tag{4-3}$$

One can then focus on the evolution of the trapped population n_T in a pulsed excitation regime. Its time average value stabilizes at $n_{T,0}$[189], as the relaxation lifetime have typical values within the µs to ms range[37,125]. Henceforth, it can be assumed constant during a TRPL decay, which lasts at most few µs. As the typical evolution time for the trapped population is slower than the TRPL decay, it can be interesting to express the mean trapped electron concentration between two pulses:

$$\overline{n_T} = f_0 \int_{t=0}^{t=1/f_0} n_T(t) \, dt \tag{4-4}$$

Considering that the traps are empty when the laser is turned on, $\overline{n_T}$ is growing after each pulse and always lower than N_T. Hence, it converges to a value we call $n_{T,0}$. Here, it should be noted that we model the trapped electron population as homogeneous in the depth of the absorber. This corresponds to a fair assumption, as the inhomogeneous regime lasts approx. 100ns, whereas the laser pulses hit the sample every 25 µs. In a practical way, we numerically determine $n_{T,0}$ by running (4-1), (4-2) & (4-3) for each set of fitting parameters, before solving the differential system including one carrier population only and in-depth diffusion which we will define in the next sections.

4.3.2. MODELING IN-DEPTH TRANSPORT

In addition to the charge carrier recombination kinetics, one should also consider the in-depth transport thanks to a diffusion term in the continuity equation. In fact, the absorption length of the perovskite layer ($1/\alpha_{532} = 100$ nm)[98] is significantly lower than its thickness ($z_0 = 500$ nm), and its value at the excitation wavelength is not significantly affected by chemical compositional tailoring[57,190–192]. As a consequence, the photo-

generated carriers are concentrated close to the front interface at short times after the laser pulse, as illustrated by the sketch in Figure 4-5(b) and by numerical simulations displayed in Figure 4-6. In-depth concentration of the electrons (and holes) inside a perovskite layer evolve to a flat distribution after 100ns. The time required for the in-depth homogenization mainly depends on the diffusion coefficient D. In fast diffusion materials such as III-V semi-conductors, this effect has no influence on TRPL decay as the carriers homogenization in-depth occurs in a few ps[193] (see sub-section 3.3.1). It becomes visible in some photovoltaic absorbers such as CIGS[162] and as we will see, it has a significant effect on I_{PL} decays in perovskite materials.
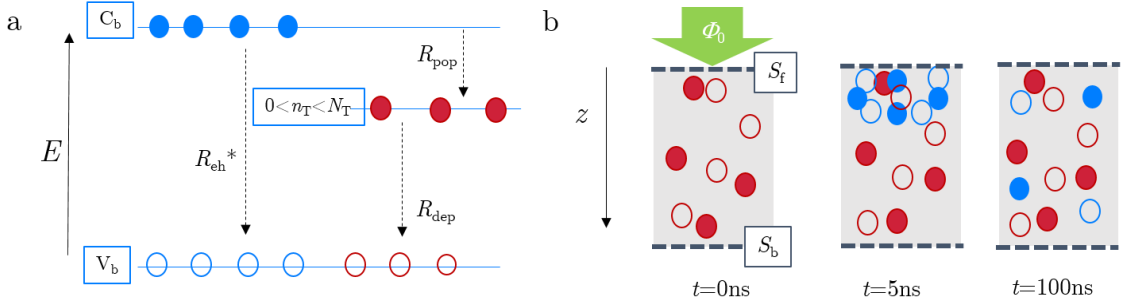
Figure 4-5 Sketch showing the allowed energetic transitions in perovskite(a). C_b and V_b stand for conduction and valence band. R_{eh*} is the net band-to-band recombination rate, R_{pop} is the trap capture rate, R_{dep} is the trap-assisted recombination rate. n_T is the trapped electron concentration, which has to remain lower than the total trap concentration N_T. (b)- Sketch showing the slow in-depth diffusion of charge carriers, following an incoming photon flux Φ_0 at t=0ns. Full (empty) circles stand for electrons (holes). Blue symbols stand for photo-generated charge carriers, while red ones stand for trapped electrons and photo-doped holes.
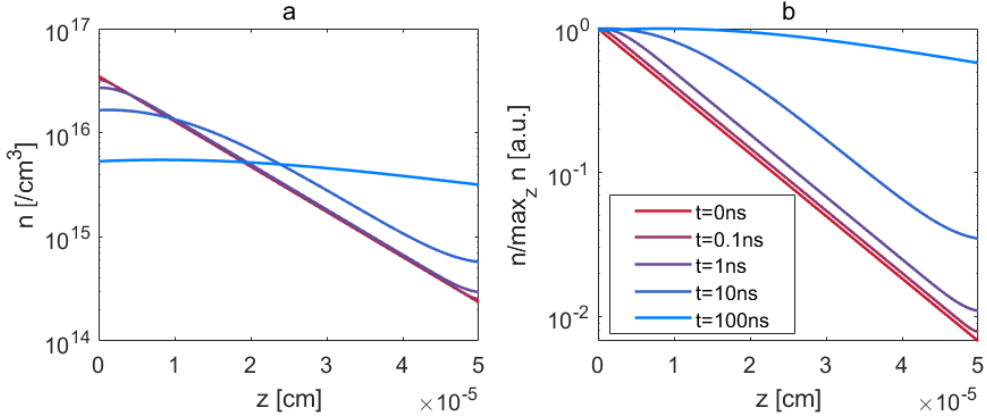
Figure 4-6 In-depth concentration profile for electrons (or holes) inside a perovskite layer, following an optical pulsed excitation at λ = 532 nm. This calculation is realized by solving the continuity equation with D_n=5x10^{-3}cm^2/s; R_{eh}=1.3x10^{-10}cm^3/s; τ_n=1370ns, S_f=40cm/s, as determined in section 4.4

4.3.3. TRAP-DIFFUSION MODEL

Now, we assume that the two physical phenomena sketched in Figure 4-5(b), in-depth diffusion and trap-assisted recombination, dominate the charge carriers kinetics in a pulsed excitation regime. We also assume a local electro-neutrality:

$$p(z,t){=}n_{T,0}{+}n(z,t) \tag{4-5}$$

This implicitly induces that the diffusion coefficients for electrons and holes are similar, which is consistent with previous observations in intrinsic perovskite material[39] and will be confirmed by experiments presented in section 6.2.3. This also allows us to reproduce the whole transport of charge carriers by writing a simple rate equation for a single population (4-6), with spatial Von Neumann boundary conditions (4-7) and (4-8):

$$\frac{\partial n}{\partial t}{=}{-}R_{eh}^{*}n\big(n_{T,0}{+}n\big){-}R_{pop}n\big(N_T{-}n_{T,0}\big){+}D_n\frac{\partial^2 n}{\partial z^2} \tag{4-6}$$

$$\forall t, z{=}0 \rightarrow D_n\frac{\partial n}{\partial z}{=}S_f n \tag{4-7}$$

$$\forall t, z{=}z_0 \rightarrow D_n\frac{\partial n}{\partial z}{=}{-}S_b n \tag{4-8}$$

The temporal initial condition is determined by the absorption properties of the sample, before any in-depth diffusion or front surface recombination can happen:

$$t{=}0 \rightarrow n{=}\Phi_0\alpha_{532}\exp{(-\alpha_{532}z)} \tag{4-9}$$

4.3.4. CALCULATING I_{PL}

Once this differential system solved, the PL intensity I_{PL} remains to be calculated. For the considered intrinsic semi-conductor, it can be expressed as:

$$I_{PL} \propto \int_0^{z_0} R_{eh}^{*}n\big(n_{T,0}{+}n\big)\exp{(-\alpha_{PL}z)}dz \tag{4-10}$$

In this formula, partial reabsorption of the PL signal is considered as radiative recombination happening close to the front interface contribute more to I_{PL} than others. Indeed, the reabsorption probability of these photons is lower. We model it thanks to the coefficient α_{PL}, which corresponds to the average absorption coefficient for the photoluminescence signal. It can be determined from the $\alpha(E)$ extracted from external quantum efficiency measurement displayed in Figure 4-1(b). For this purpose, we assume first that the normalized EQE reflects the internal quantum efficiency (IQE) of the device and then that IQE(E) can be approximated by the internal absorbance of the device A(E) (i.e. perfect collection of photo-carriers). As A(E) = (1-exp(-α(E)*z_0), it follows that the absorption coefficient is : α(E)~-1/z_0*ln(1-IQE(E)). This estimation is limited around the bandgap of the absorber. Then, α(E) can be convolved with the PL spectrum I_{PL}(E) displayed in Figure 4-2, with the following formula:

$$\alpha_{PL}{=}\frac{\int_{E=0}^{E=\infty}\alpha(E)\,I_{PL}(E)\,dE}{\int_{E=0}^{E=\infty}I_{PL}(E)\,dE} \tag{4-11}$$

Calculations lead to 2.5±1 x 10^3 /cm for P_1 P_2 and P_4 and to 5±1 x 10^3 /cm for P_3. The PL reabsorption described in eq. (4-10) notably induces a photon recycling phenomenon inside the absorber, which we take into account with a relative correction of the fitted external radiative coefficient R_{eh}*, in order to determine the internal radiative coefficient $R_{eh}{=}R_{eh}$*/(p_{escape}), with $p_{escape}{=}12.5\%$ [85,94,135,194]. Even if taking a

constant p_{escape} for different back interfaces is a gross assumption, we keep the advanced photon propagation & recycling concerns for the next chapter (see section 5.3).

4.3.5. TRAPFREE-DIFFUSION MODEL

The amount of free parameters in the aforementioned trap model is high (R_{eh}, R_{pop}, R_{dep}, D_n, N_T, S_{air}, S_{TiO2}). This would call for a high number of experiments to control them. In the published version of this chapter[187], we could not fit R_{pop} and R_{dep} values and thus extracted them from the literature. They were assumed constant for all compositions. It would be possible to study their value by using a temperature-dependent study[195], but we did not have the facility to do so during this doctoral work. However, we suggest here a model[94,122] that is not impacted by this uncertainty. It is based on the same assumption of electro-neutrality (4-5), and make use of the same boundary conditions (4-7)(4-8), initial condition (4-9) and I_{PL} integration using (4-10). It simply replaces (4-6) with (4-12), where a mono-molecular lifetime τ_n appears.

$$\frac{\partial n}{\partial t} = -R_{eh}^* n^2 - \frac{n}{\tau_n} + D_n \frac{\partial^2 n}{\partial z^2} \tag{4-12}$$

In section 4.4.3, we will show that both approaches tend to similar conclusions.

4.4.   RESULTS

In this section, we fit I_{PL} transients to the aforementioned trap-diffusion model. This process allows us to quantify bulk non-radiative & radiative, as well as interface recombination pathways, along with diffusion properties (section 4.4.1), which ultimately allows to calculate equivalent L_n and τ_n at 1 sun excitation (section 4.4.2). The concurrent trapfree-diffusion model introduced in section 4.3.5 is also investigated in section 4.4.3.

4.4.1. FITTING TO TRAP-DIFFUSION

Our trap-diffusion model was first tested on mixed cation perovskite layers directly deposited on FTO. An optimization algorithm is employed to minimize the logarithmical difference from experimental to numerical transients. Experimental I_{PL} transients obtained at increasing fluence levels are displayed in Figure 4-7(a), along with the optimized numerical ones. In the fitting process, the trap-related recombination rates were fixed to literature values (R_{pop} = 2x10^{-10} cm^{-3}s^{-1}, R_{dep} = 8x10^{-12} cm^{-3}s^{-1})[37], while the main optoelectronic parameters related to the perovskite layer were fitted, yielding an external radiative recombination coefficient R_{eh}^* = 1.3x10^{-10} cm^{-3}s^{-1}, a trap concentration N_T = 6.5x10^{14} cm^{-3}, a diffusion coefficient D_n = 4.7x10^{-3} cm^{2}s^{-1}, and a front interface recombination velocity S_{air}, with values ranging between 140 cm/s at high fluence and 100 cm/s at low fluence. A complementary experiment was then realized for the same perovskite deposited on mesoporous TiO$_2$. Resulting I_{PL} transients are shown in Figure 4-7(b). Even though the decays do not look like those acquired on FTO, they can still be numerically reproduced by our model. More specifically, they are fitted thanks to a single parameter variation: the back surface recombination velocity S_b. Indeed, this parameter was taken as a reference on Z_1 (S_{FTO}), while it is fitted to S_{TiO2} = 40 cm/s on Z_2.

Now, several parameters were fitted and their eventual correlation is therefore investigated. We calculate the set of parameter values for which the reconstruction error rises by less than 10% and represent it on a 3D view in Figure 4-7(c). Their concentric aspect translates the non-correlation of parameters. We deduced from these volumes the confidence intervals for each parameter, and included them in Table 4-1. They witness for the precision of the fit.

c: P_2 R_{eh}=1.3x10^{-10}/cm^3/s ; N_T=6.5x10^{14}/cm^3 D_n=4.75x10^{-3}cm^2/s
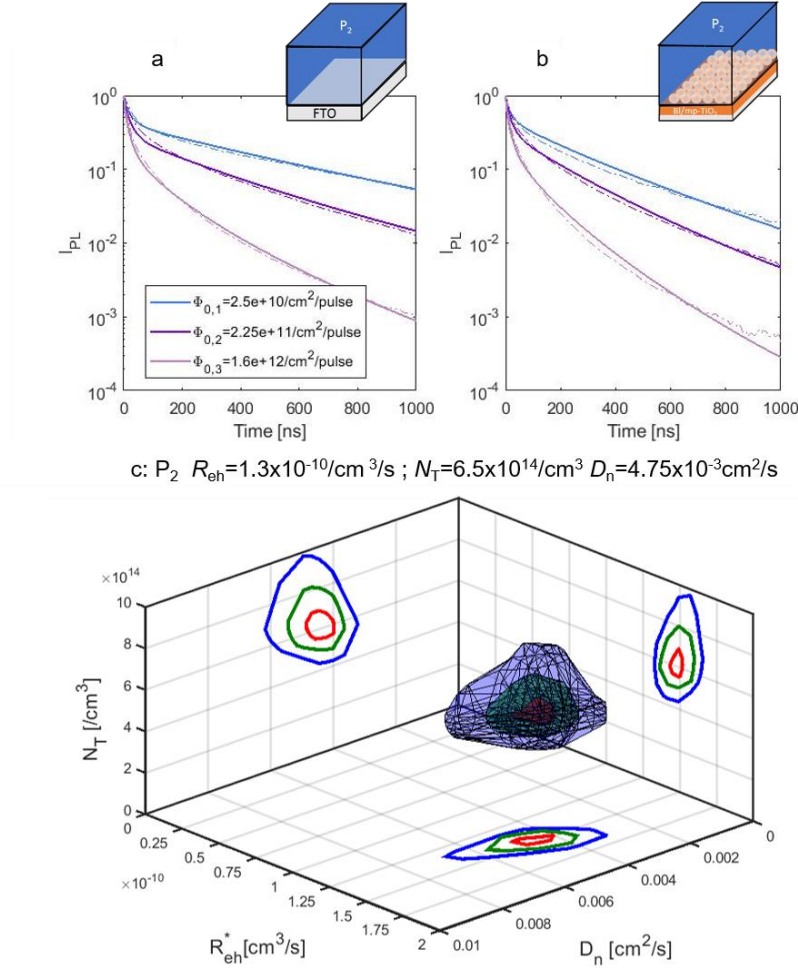
Figure 4-7 (a)-Experimental (dotted lines) and numerically fitted (plain lines) I_{PL} decays for a mixed cation perovskite $MA_{0.17}FA_{0.83}Pb$ ($I_{0.83}Br_{0.17}$)$_3$ (also P_2) layer deposited on FTO (A) or on mesoporous-TiO$_2$ (b).Various orders of magnitude of the fluence level Φ_0 have been tested.(c) Iso-surfaces showing a set of parameters (R_{eh}* D_n N_T) leading to a reconstruction error not higher than 10 % (red), 20% (green), 50% (blue) of the optimal reconstruction error. The green one is used for confidence intervals indicated in Table 4-.

We repeated this same experiment for samples P_1, P_3 and P_4, having a similar architecture but different absorbers. Experimental and numerical transients are available in the published version of this chapter[187]. Again, our model allows a fair reproduction of TRPL transients in the FTO/P_n architecture for all samples considered, and allows to extract key optoelectronic properties for bulk and perovskite/air interface. Once again, the confidence intervals indicated in Table 4-1 are narrow, except for the diffusion coefficient/length in MAPbI$_3$ (which could be attributed to the quick degradation of this

single cation perovskite). Concerning the second architecture on mesoporous TiO$_2$, the previously explained introduction of S_{TiO2} leads to a successful fitting for sample P$_1$ and P$_4$, but is not sufficient to explain the physical phenomena involved at the TiO$_2$ interface in Cs-containing sample (P$_3$).

	Sample P$_1$ MAPbI$_3$	Sample P$_2$ MA$_{0.17}$FA$_{0.83}$... Pb(I$_{0.83}$Br$_{0.17}$)$_3$	Sample P$_3$ (MA$_{0.17}$FA$_{0.83}$)$_{0.95}$ ...Cs$_{0.05}$... Pb(I$_{0.83}$Br$_{0.17}$)$_3$	Sample P$_4$ (MA$_{0.17}$FA$_{0.83}$)$_{0.95}$ ...Rb$_{0.05}$... Pb(I$_{0.83}$Br$_{0.17}$)$_3$
$R_{eh*}=R_{eh}/p_{escape}$ [x10^{-10} cm^{-3}·s^{-1}]	4.0 [3.0 ; 5.0]	1.3 [1.2 ; 1.4]	1.2 [1.1 ; 1.3]	1.1 [0.95 ; 1.2]
D_n [x10^{-3}cm^{2}s^{-1}]	0.8 [0.1 ; 100]	4.7 [3.5 ; 6.5]	6 [4.8 ; 8.0]	3.1 [2.1 ; 4.8]
N_T [x10^{14} cm^{-3}]	560 [500 ; 600]	6.5 [5.5 ; 9]	4.2 [3.5 ; 5.5]	80 [75 ; 85]
S_{air} [cm·s^{-1}] $\Phi_{0,1}/\Phi_{0,2}/\Phi_{0,3}$	120/180/180	100/100/140	60/80/140	60/75/100
S_{TiO2} [cm·s^{-1}] $\Phi_{0,1}/\Phi_{0,2}/\Phi_{0,3}$	80/80/80	60/40/40	Unconverged	100/100/60

Table 4-1 Physical parameters for each sample probed. R_{eh}, D_n N_T and S_{air} (perovskite/air interface) are determined by fitting TRPL transients on FTO, while S_{TiO2} is determined on TiO$_2$ and corresponds to the perovskite/mp-TiO$_2$ interface. For the whole range of fitting parameters inside the confidence intervals, the reconstruction error rises by less than 20%.

4.4.2. EXTRACTING 1-SUN PROPERTIES FROM PULSED EXPERIMENTS

Classical optoelectronic properties such as the lifetime τ_n and the diffusion length L_n can be derived from this transport model thanks to the following procedure. If one starts from the simple formula $L_n=\sqrt{(D_n\tau_n)}$, a difficulty quickly arises as τ_n is strongly injection-dependent for an intrinsic semi-conductor with a bimolecular recombination regime. Here, we determine the charge carrier concentration by solving the differential system under a steady state illumination ($G_{1sun}=2\times10^{17}$/cm^2/s) absorbed with a mean absorption coefficient $\alpha_{1sun}=5\times10^4$ /cm. This corresponds to the differential system presented in section 4.3, where eq. (4-6) becomes eq. (4-13), in which the $\partial n/\partial t$ term is equal to 0 (permanent regime). To obtain the optoelectronic parameters matched to each composition, we make use of the fitted values S_{air}, S_{TiO2}, $R_{eh}*$ and N_T while solving the differential system. It converges to a unique stable solution representing the steady state electron concentration n_{1sun}. Thereafter, τ_{1sun} and L_{1sun} can be calculated thanks to eq. (4-14) & (4-15).

$$0 = G_{1sun} - R_{eh}^* \, n_{1sun} \, (n_{T1sun}+n_{1sun})- R_{pop} \, n_{1sun} \, (N_T-n_{T1sun})+ D_n \frac{\partial^2 n_{1sun}}{\partial z^2} \qquad (4\text{-}13)$$

$$\tau_{1sun}=\frac{\int n_{1sun} \, dz}{G_{1sun}} \qquad (4\text{-}14)$$

$$L_{1sun}=\sqrt{D_n\tau_{1sun}} \qquad (4\text{-}15)$$

As an illustration, we display values derived for L_{1sun} as a function of τ_{1sun} in Figure 4-8(a). Fits realized on Z$_1$ (circles) are done with $S_f=S_{air}$ and $S_b=0$, while those on Z$_2$ (squares) are realized with $S_f=S_{air}$ and $S_b=S_{TiO2}$. The confidence intervals for each fitting

parameter, as displayed in Table 4-, are taken into consideration as several points are drawn on the scatter plot for each zone.
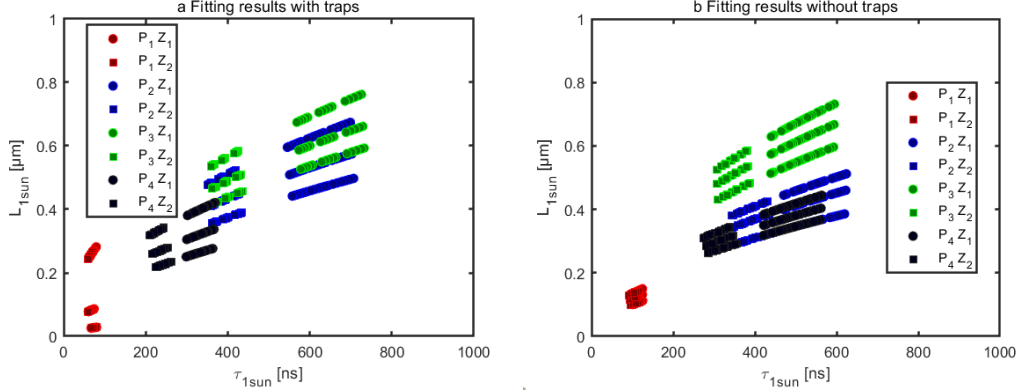
Figure 4-8 (a) Scatter plot of values determines for τ_{1sun} & L_{1sun} from eq. (4-14) & (4-15), accounting for the confidence intervals of each fitting parameter (N_T, S_{air}, R_{eh}, D_n) with $S_b=0$ for Z_1 and $S_b=S_{TiO2}$ for Z_2. (b) Same for the trap-free model with (τ_n, S_{air}, R_{eh}, D_n) with $S_b=0$ for Z_1 and $S_b=S_{TiO2}$ for Z_2.

4.4.3. FITTING TO TRAPFREE-DIFFUSION

Less parameters in a model can yield a lower fitting quality, but it also participates in its self-consistency and reliability. In this sub-section, we present another round of fit realized on the same experimental data with the trapfree-diffusion model. While the values for D_n and R_{eh}^* are similar to the previous section 4.4.1, τ_n is a new parameter that would be fitted to a higher value for a sample with less traps. It represents a straightforward indicator of non-radiative recombination in the bulk: the SRH lifetime. For what concerns interface S values, they are similar for S_{TiO2} and tend to be lower for S_{air}. Noteworthy, the fitting procedure is still yielding good reproduction of the dataset at any fluence Φ_0. Moreover, the same conversion from pulsed illumination into continuous 1 sun illumination applies, and one can derive values for τ_{1sun} and L_{1sun} by solving the differential system in permanent regime. This is shown in Figure 4-8(b), in which we can see that the kinetic/diffusion model and traps/diffusion model lead to similar values for those parameters – around 500 ns for τ_{1sun} and around 500 nm for L_{1sun}. As our primary objective is to assess the relevance of these materials for PV operation, both model seem to be both as valid.

	Sample P_1 MAPbI$_3$	Sample P_2 MA$_{0.17}$FA$_{0.83}$... Pb(I$_{0.83}$Br$_{0.17}$)$_3$	Sample P_3 (MA$_{0.17}$FA$_{0.83}$)$_{0.95}$ ...Cs$_{0.05}$... Pb(I$_{0.83}$Br$_{0.17}$)$_3$	Sample P_4 (MA$_{0.17}$FA$_{0.83}$)$_{0.95}$ ...Rb$_{0.05}$... Pb(I$_{0.83}$Br$_{0.17}$)$_3$
$R_{eh*}=R_{eh}/p_{escape}$ [x10^{-10} cm^{-3}·s^{-1}]	3.3 [2.5 ; 4]	1.3 [1.2 ; 1.4]	1.3 [1.2 ; 1.4]	1.05 [0.95 ; 1.15]
D_n [x10^{-3}cm^{2}s^{-1}]	1.4 [1 ; 1.8]	3.4 [2.8 ; 4]	7.5 [6.5 ; 9]	2.9 [2.4 ; 3.5]
τ_n [ns]	190 [160 ; 210]	1370 [1200 ; 1500]	1154 [1000 ; 1300]	1000 [900 ; 1100]

S_{air} [cm·s^{-1}] $\Phi_{0,1}/\Phi_{0,2}/\Phi_{0,3}$	150/200/60	40/40/10	40/30/0	40/20/0
S_{TiO2} [cm·s^{-1}] $\Phi_{0,1}/\Phi_{0,2}/\Phi_{0,3}$	80/80/80	60/40/40	Unconverged	100/100/60

Table 4-2 Physical parameters for each sample probed. τ_n, D_n, N_T and S_{air}(perovskite/air interface) are determined by fitting TRPL transients on FTO, while S_{TiO2} is determined on TiO$_2$ and corresponds to the perovskite/mp-TiO$_2$ interface. Diffusion length L_{1sun}, lifetime τ_{1sun} and associated tolerance intervals are calculated using eq. (4-14)&(4-15)

4.4.4. INDIVIDUAL ACCESS TO BACK & FRONT SURFACE RECOMBINATION VELOCITIES

Here, we will introduce an experiment realized to decorrelate front and back surface recombination velocities, for which a device with transparent interfaces is required. It is thus applied on a full device adapted to tandem integration, in which the perovskite (composition P_3) is sandwiched into transparent layers. We acquired I_{PL} decays with 3 increasing flux and 2 illumination directions. This allowed us to study the interfaces it forms with the transport layers, as sketched in Figure 4-9. We fitted the 6 transients together with the trap-diffusion model. The diffusion coefficient was evaluated at D_n=8.8x10^{-3}cm^2/s, the bimolecular recombination R_{eh}^*=1.3x10^{-10}cm^3/s and the trap concentration N_T=1.1x10^{16}/cm^3. Both surface recombination velocities S_{Spiro} & S_{TiO2} were determined as highly injection-dependent. Results are summarized in Table 4-3 below.
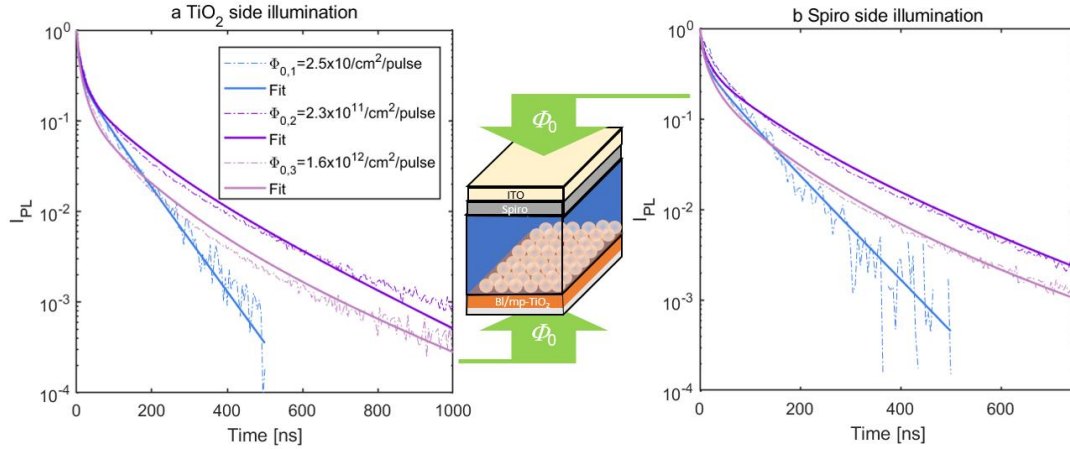
Figure 4-9 Fitted I_{PL} transients acquired at increasing photon flux $\Phi_{0,1},\Phi_{0,2}$&$\Phi_{0,3}$,illuminating on TiO$_2$ side (a) as well as on Spiro Side (b) on a semi-transparent device. In-between (a) & (b) is represented a sketch showing the double side illumination on the semi-transparent device.

This fit with double illumination was used for a quick ageing study of a semi-transparent device adapted to tandem integration[74]. The comparison of fitted values for fresh and aged (1 month in dark) revealed similar values for N_T & R_{eh}. On the contrary, D_n was smaller after ageing (down to 2.8x10^{-3} cm^2/s), slowing down charge transport and contributing to a more difficult extraction, as the equivalent diffusion length L_{1sun} was lowered from 550 nm to 290 nm.

For what concerns the interfaces, S values notably take higher values at low injection ($\Phi_{0,1}$), which is consistent with the quicker decay observed at this fluence. In this case,

it could correspond to a carrier extraction at the front interface (in reference to laser), as we work in a full device where internal electric field might help the collection. More work on this injection dependence of S could bring precious hints on the interfacial charge carrier processes[139]. In any case, S_{TiO2} was measured at higher values after ageing, which points out the degradation of the TiO_2 interface, generally attributed to the UV effect[131].

	Device (fresh)	Device (aged, 20 days dark)
$R_{eh*}=R_{eh}/p_{escape}$ $[\times 10^{-10} \text{ cm}^{-3}\cdot\text{s}^{-1}]$	1.3 [1.1 ; 1.5]	1.6 [1.4 ; 1.8]
D_n $[\times 10^{-3}\text{cm}^2\text{s}^{-1}]$	8.8 [7.4 ; 9.7]	2.8 [2.5 ; 3.1]
N_T $[/\text{cm}^3]$	110 [100 ; 130]	100 [80 ; 115]
S_{Spiro} $[\text{cm}\cdot\text{s}^{-1}]$ $\Phi_{0,1}/\Phi_{0,2}/\Phi_{0,3}$	660/40/1	370/32/1
S_{TiO2} $[\text{cm}\cdot\text{s}^{-1}]$ $\Phi_{0,1}/\Phi_{0,2}/\Phi_{0,3}$	1300/210/180	1000/300/225

Table 4-3 Physical parameters for the semi-transparent device probed with double side illumination

4.5. DISCUSSION

Thanks to a complete model for TRPL decays, we could highlight the main phenomena governing the charge carriers transport and recombination in perovskite, leading to a versatile description of their kinetics for a wide range of fluence level. In this section, we first show the relative weight of each of the considered recombination pathway in I_{PL} decays (4.5.1), before focusing on the main ones successively: at the interface (4.5.2), slow carrier diffusion in-depth (4.5.3), non-radiative carrier recombination (4.5.4).

4.5.1. MAIN RECOMBINATION PATHWAY

The main recombination channel for charge carriers dictates their global decay rate. It changes during the TRPL decay, and also as the excitation fluence is varied. We here present a method able to analyze the influence of radiative recombination R_{rad}, non-radiative recombination R_{nrad} and interface recombination R_{int}. It requires to integrate each recombination current over the depth with the following formulas:

$$R_{rad}(t) = \int_0^{z_0} R_{eh}^* \, n(t,z) \, [n_{T0} + n(t,z)] \, dz \tag{4-16}$$

$$R_{nrad}(t) = \int_0^{z_0} R_{pop} \, n(t,z) \, [N_T - n_{T0}] \, dz \tag{4-17}$$

$$R_{int}(t) = S_f \, n(t,z=0) \tag{4-18}$$

As a result, it is possible to attribute early and later time PL kinetics to different terms in the rate equation by analyzing the decays of each recombination current R_s. In Figure 4-10, the main recombination pathway appears as the highest recombination

current at each time and each fluence. The result of this analysis for each composition is displayed in Table 4-4, where we can see that trap-assisted (also non-radiative) recombination globally dominate the second part of the decay, while other two phenomena must be considered to explain the faster PL decay at short times. On the one hand, charge carriers are concentrated in a smaller volume at short times, which favors the radiative recombination process, as electrons and hole "meet" more often[162]. On the other hand, they diffuse away from the defects located at the front interface, which eventually slows down the early decay. Both are especially relevant in low-mobility perovskite absorbers.
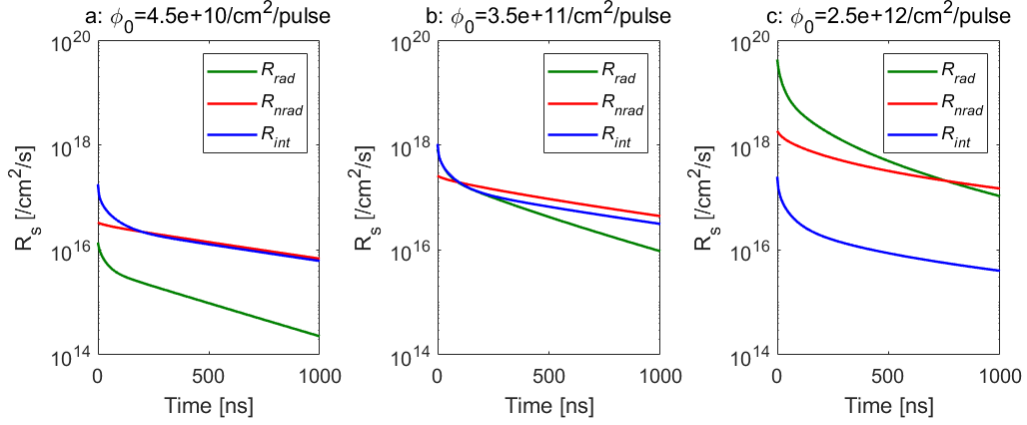
Figure 4-10 Temporal evolution of recombination terms simulated for perovskite P_2, at the same excitations powers employed during TRPL decay (a: $\Phi_{0,1}$ b: $\Phi_{0,2}$ c: $\Phi_{0,3}$) These terms are defined in eq. (4-16), (4-17) & (4-18)

	MAPbI$_3$ (P$_1$)		Perovskite P$_2$		Perovskite P$_3$		Perovskite P$_4$	
	Short times	Long times	Short times	Long times	Short times	Long times	Short times	Long times
$\Phi_{0,1}$	Interface	Trap/ Non-rad.	Interface	Trap/ Non-rad.	Interface	Trap/ Non-rad.	Interface	Trap/ Non-rad.
$\Phi_{0,2}$	Interface	Trap/ Non-rad.	Interface	Trap/ Non-rad.	Interface	Trap/ Non-rad.	Interface	Trap/ Non-rad.
$\Phi_{0,3}$	Radiative	Trap/ Non-rad.	Radiative	Radiative	Radiative	Radiative	Radiative	Trap/ Non-rad.

Table 4-4 Major recombination pathways at short times (t = 0.. 20 ns) and long times (t>100 ns), calculated for each perovskite composition studied here.

4.5.2. ABOUT INTERFACE RECOMBINATION

Moreover, our model allows us to quantify the recombination rate attributed to the interfaces, generally guilty of the most radiative losses in solar cells[134,196,197]. While S_{air} refers to the perovskite/air interface, S_{TiO2} refers to the one located at mp-TiO$_2$/perovskite. All samples considered in this study were half-cells and hence these velocities correspond to recombination at interfacial defects rather than electrical injection, which is often observed in full devices at short-circuit[54]. In section 4.4.1, the interface formed at FTO/perovskite was taken as reference for S_b, as our experiment

cannot effectively distinguish between bulk and back surface recombination[162], and we only illuminated from the air/perovskite side. In section 4.4.4, we presented further developments around this model. Indeed, we realized an experiment where we acquired two set of TRPL decays by illuminating one side after another, which is a more appropriate method distinguish the influence of both interfaces[74].

Still, the successful fitting of the data of the zone Z_2 of the samples allows us to assess that the mp-TiO$_2$/perovskite induces a higher recombination current than the FTO/perovskite one. This can be explained by the larger contact surface at such a meso-structured interface. Now, S_{TiO2} remains lower than S_{air}, showing a preserved interface crystalline quality, in comparison to the one obtained after exposure to the ambient atmosphere. Eventually, it can be noted that both S_{air} and S_{TiO2} demonstrate a slight injection-dependence. Even if a fine modeling of interface recombination was out of the scope of the study realized on perovskite half-cells, it can be noted that these recombination velocities quantify the interface recombination current. They are not a fixed material property as they depend on the interfacial trap density – where the traps might saturate as the fluence increases – and on the Fermi level position at the interface[174,198].

4.5.3. ABOUT SLOW DIFFUSION

Concerning the diffusion coefficient, we found low values of D_n being in the same order of magnitude for every sample. It implies a relative long time to obtain a homogeneous in-depth carrier distribution. A direct application of the Einstein law ($D_n = \mu_n kT/q$) leads to μ_n values comprised between 0.1 and 0.3 cm^2/(V.s), which locates our batch in the lower values for polycrystalline solution processed perovskites[103,114,115]. This might seem contradictory with the value of PCE as high as 19% obtained with such an absorber. However, these low D_n values are compensated with the very long lifetime τ_{1sun} of charge carriers, which we display in Figure 4-8. Their high values ensure that the diffusion length L_{1sun} remains larger than z_0, thus preserving an efficient charge carrier collection.

This experimental insight into slow diffusion could bring crucial information regarding the recent discovery of a Rashba splitting in MAPbI$_3$ [69,70,199], as well as in CsPbI$_3$ [200]. This effect linked to spin-orbit coupling leads to the coexistence of a direct and an indirect bandgap, the first one being beneficial to absorption, and the latter drastically enhancing the lifetime of the carriers. The main recombination pathway for photo-generated carriers relies on a phonon coupling, or on the overcoming of an activation barrier[68,201]. Regarding a recent study from Kirchartz et al., a slow diffusion together with high PCE is possible thanks to this particular band structure[202]. However, it should be noted that the significance of this spin-orbit coupling is still under debate in the perovskite community[94].

4.5.4. ABOUT TRAP RELEVANCE

On the contrary to the previously discussed topics (interface recombination & slow diffusion), non-radiative recombination are modeled differently in trap-diffusion and trapfree model. We start by commenting the values obtained with the trap-diffusion

model, in which the fitted trap concentration is highly dependent on the chemical composition of the considered sample, with values varying between 4.2 $\times 10^{14}$ cm^{-3} for sample P_3 and 5×10^{16} cm^{-3} for sample P_1. The latter is consistent with N_T values previously reported in MAPbI$_3$ absorbers, for various energetic positions[37,188,203]. The influence of traps on the charge carrier kinetics in a pulsed excitation regime mainly happens through the photo-doped charges they fix in the valence band by trapping electrons on the long term[37,85,101]. This is mainly described by their concentration N_T, which lower value in P_2 and P_3 confirm the effective trap passivation through cation substitution previously observed[52,204]. What's more, the good correlation between the effect of chemical composition on N_T and V_{oc} values underlines the significant role of these traps in solar cell operation. The trapfree-diffusion model gives higher lifetime values when N_T is lower, and hence the link between non-radiative recombination and V_{oc} loss is maintained. To the best of our knowledge, physical models including diffusion and recombination had not been applied to I_{PL} decays before. Furthermore, previous physical models for perovskites predicted mono-exponential decays at low fluence[37,135], which were not observed in any half-cells. This confirms the relevance of models presented here above. Eventually, we stress here some recent reports (posterior to this study) using diffusion/recombination models on I_{PL} transients[205–207].

4.6.   CONCLUSION

In this chapter, we developed charge carrier transport models incorporating for the first time a combination of the recombination dynamics and the slow in-depth diffusion after a pulsed excitation. We applied them to the simultaneous fitting of I_{PL} decays at various fluence levels, for different PV-compatible perovskite compositions. For each of them, we quantified non-radiative & radiative recombination, as well as diffusion properties. We showed the path to translate this thorough representation of charge carrier transport into 1 sun equivalent lifetime and diffusion length. In addition, our models have a vertical component, which opens the way for independent characterization of ETL/- and HTL/perovskite interfaces.

The variation in chemical composition of perovskite absorbers mainly impacts the trap concentration (or bulk non-radiative recombination), while the slow diffusion remains characteristic for any batch. The best PCE (19.7%) obtained after Cs incorporation could be explained by a reduction in trap state density ($N_T = 4.2 \times 10^{14}$/cm^3 or $\tau_n = 1370$ ns). It is notably high despite the underlined slow diffusion, as it gets compensated by a high τ_{1sun}. Henceforth, L_{1sun} remains above the absorber thickness and charge collection is ensured.

5. Lateral transport in a perovskite thin film

The development of high efficiency solar cells relies on the management of electronic and optical properties that need to be accurately measured. As the conversion efficiencies increase, there is a concomitant electronic and photonic contribution that affect the overall performances of the photovoltaic devices. Here we show an optical method based on the use of complementary multi-dimensional imaging techniques. It allows us to collect and analyze the luminescence signal with high spatial, spectral and temporal resolution. We apply it to probe several transport properties of semiconducting materials, thereby decoupling and quantifying the electronic and photonic contributions. Example of application is shown on halide perovskite thin film for which a large range of transport properties is given in the literature, depending on the film fabrication route but also on the measurement technique (see section 1.3).

We focus here more precisely on previous uses of local illumination on perovskite. Looking at steady-state I_{PL} images allows to assess the lateral diffusion length of charge carriers[32,168,188] and underline the transport anisotropy in unpassivated polycrystalline $CH_3NH_3PbI_3$ (MAPI) films[208]. Time-resolved diffusion profiles have also been observed[120,209–212] and the widening of the I_{PL} profiles give insight into the carrier mobility. Nonetheless, multi-dimensional approaches were still missing. Regarding the PR, several studies have underlined this optical process in perovskite absorber, either by focusing on the slow radiative recombination process[122,213,214], or by highlighting the long-range charge carrier regeneration[24,194,215]. However, a model able to decorrelate electronic and photonic contributions to transport is still missing.

In this chapter, we make use of the developed I_{PL} imaging platform on perovskite thin films, which first leads to a quantitative optical experiment based on point pulsed illumination. Experimental details specific to this chapter are presented in section 5.1, before section 5.2 gives a quick overlook on the data set. By its analysis, we evidence the contribution of optical effects such as the photon recycling as a well as the photon propagation where emitted light is laterally transported without being reabsorbed (section 5.3). This latter effect has to be considered to avoid overestimated transport properties. In section 5.4, we quantify these transport properties by rigorously solving the complete time dependent continuity equation, yielding a method valid for several semiconductor materials. Further application of multi-dimensional imaging platform on a sample presenting heterogeneities is presented in section 5.5.

81

5.1. EXPERIMENTAL DETAILS

5.1.1. SAMPLE DESCRIPTION

In this chapter we investigate from section 5.1 to 5.4 a triple cation mixed halide perovskite thin film $((MA_{0.14},FA_{0.86})_{0.95}Cs_{0.05}Pb(I_{0.84},Br_{0.16})_3)$ [P$_3$] spin coated on glass. The absorption coefficient of perovskite was determined using a combination of transmission/reflexion measurements at photon energies above the bandgap and Fourier transform photocurrent spectroscopy at all energies, which are absolutely calibrated thank to the first ones. The resulting absorption coefficient measurement is displayed in the published version of this chapter[216], and accompanied by further details on the material fabrication process. The local illumination is applied on homogeneous regions, whereas inhomogeneities are the focus of section 5.5. In this section, we use samples having the same chemical composition [P$_3$] but a slightly different production process leading to wrinkle formation, but also a slightly modified one without Cs [P$_2$] having no wrinkle.
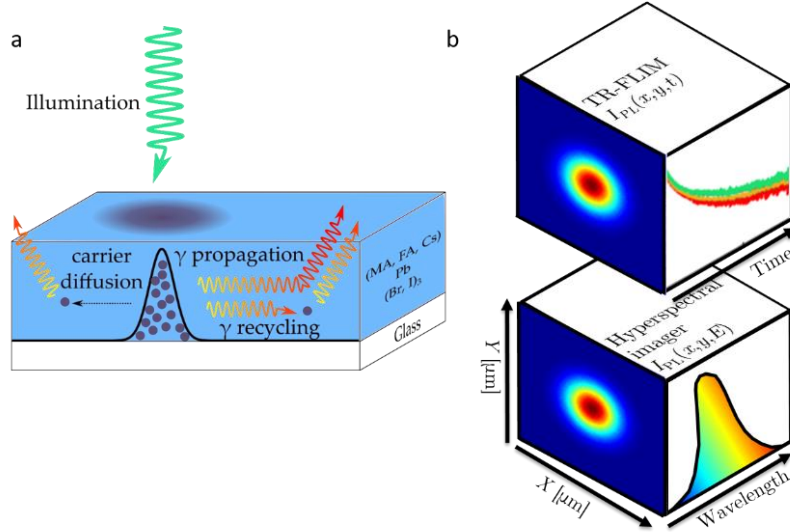
Figure 5-1 Sketch of the experimental observations and of the physical mechanisms taking place(a) Sample structure and sketch showing the triple mechanism (carrier diffusion, photon propagation and photon recycling) studied here (b) sketch showing the acquisition in 3 dimensions with time-resolved fluorescence imaging (TR-FLIM) or hyperspectral imaging (HI), for a point illumination sketched in the left face.

5.1.2. IMAGING SPECIFICS

Multi-dimensional luminescence analysis requires the use of the hyperspectral imager and of the TR-FLIM set-ups. This experimental approach is summarized in Figure 5-1. In both cases, the sample is illuminated through an infinity-corrected X100 Nikon objective with numerical aperture 0.95 and the luminescence is collected through the same objective. For both setup, the optical excitation is made with a supercontinuum Fianium Laser set at 550nm with pulse width 6ps, and repetition rate of 1MHz. The diffraction limit in these conditions is 350nm. We have evaluated by measurement of the

optical transfert function that the spot has a diameter of 950+/-50 nm. The minimum gate width of the camera is 480 ps which allows a temporal resolution of the system about 750 ps. It is used in the point illumination experiment, for the high flux (Φ_0=5x10^6 /pulse), while a longer gate width (5ns) is used for the low flux (Φ_0=10^5/pulse).

5.2.   PROJECTIONS OF THE DATASET

5.2.1. SPATIAL ASPECT

As the diffusion is theoretically isotropic from the local excitation spot, we mostly averaged the recorded luminescence signal I_{PL} in radial coordinates r in order to significantly enhance our sensitivity with a higher signal to noise ratio. The spatial analysis of the signal is hence a radial mean. It corresponds to a fair analysis if one looks at the symmetry in spectral or time images.

5.2.2. TEMPORAL ASPECT
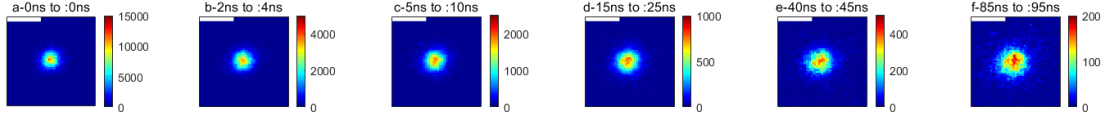
Figure 5-2 I_{PL} maps of a perovskite sample after point pulsed illumination(a) at t=0ns and then integrated between larger time steps, which are indicated in the title of each sub-figure (b) to (f). Scaling bar is 5μm long
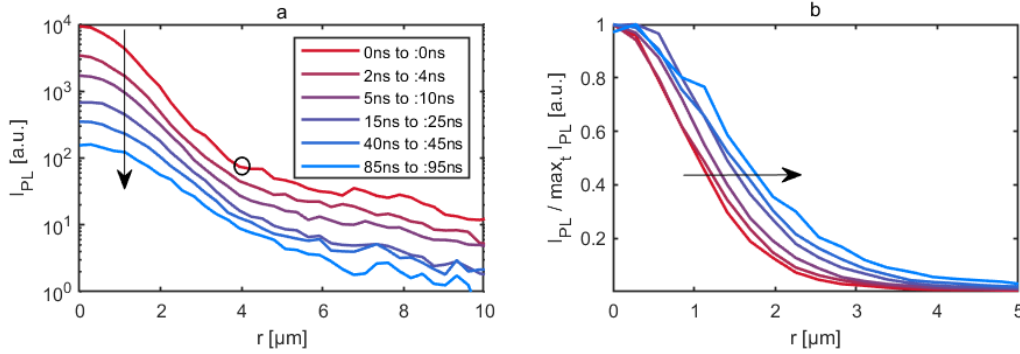
Figure 5-3 I_{PL} profiles of a perovskite sample after point pulsed illumination(a) their progressive decay is shown in the same scale for each profile, with the same time steps as in Figure 5-2, (b) same I_{PL} profiles normalized to their maximum (at r=0μm), where the lateral broadening is underlined

The time-resolved images give a first hint towards diffusion away from the excitation spot. In Figure 5-2, I_{PL} images acquired after the pulsed point illumination are shown. Each colorbar being scaled to the maximum, the radial broadening of I_{PL} flare is evident. The global decay of the maximum value of the radially averaged profiles is illustrated in Figure 5-3(a). An inflexion point (circled in black on the graph) is unexpected in the t=0ns profile, as the excitation beam is Gaussian and should appear as straight line in logarithmical scale. It will be explained in section 5.3. In Figure 5-3(b), a normalized view allows us to underline the broadening of the radial I_{PL} profiles, which full-width at half maximum (*FWHM*) is enhanced two-fold in 100ns. Quantitative analysis of these transients is presented in section 5.4.

One could also extract time-resolved I_{PL} decays at each radius r (commonly called TRPL decays). This is realized in Figure 5-4, on which the global decay of I_{PL} in time and space is again seen. The farther from the excitation spot, the slower the I_{PL} decay, as can be seen in normalized I_{PL} decays in Figure 5-4(b). However, this extraction from the dataset is hardly exploitable, and we will favor I_{PL} profiles in the next steps.
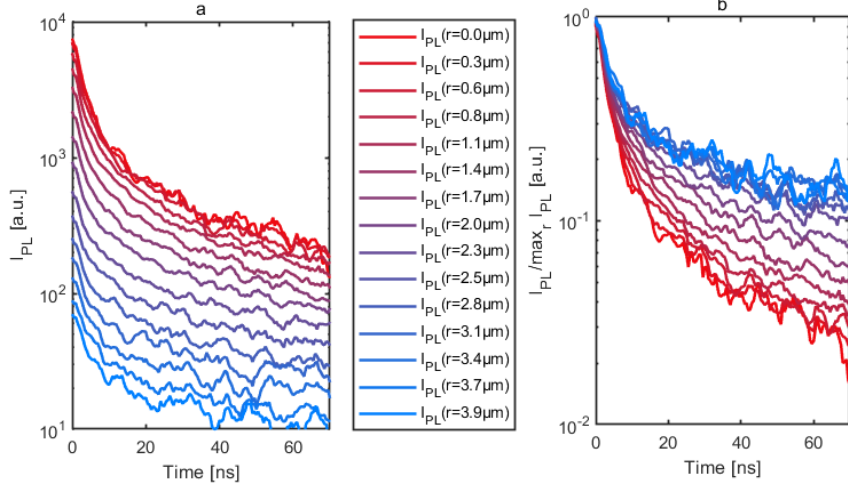
Figure 5-4 I_{PL} decays of a perovskite sample after point pulsed illumination at incremental distances from the illumination point(a), also normalized to their maximum at t=0ns in (b)

5.2.3. SPECTRAL ASPECT
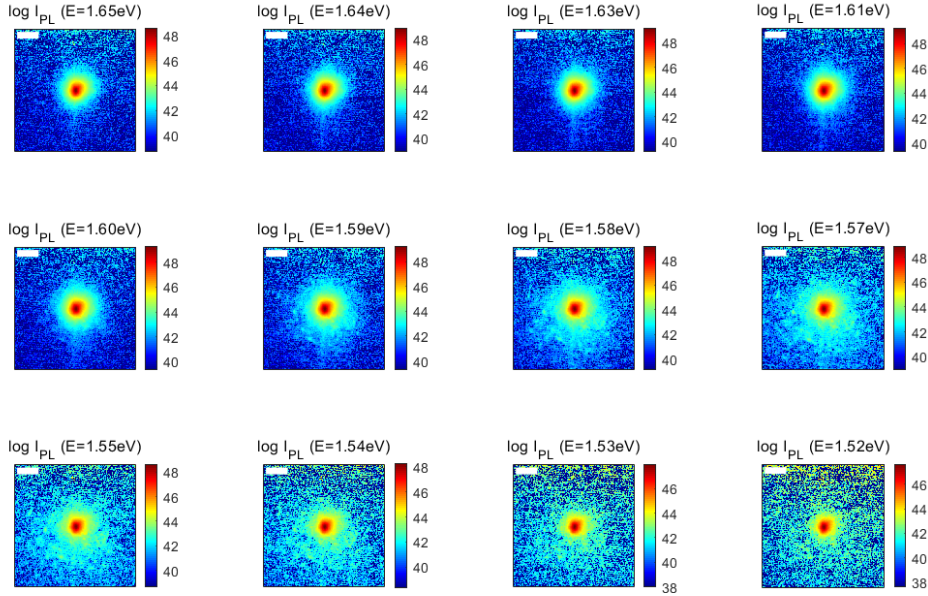
Figure 5-5 PL spectral images at distinct photon energies. The color scale is logarithmical and scaled to the maximum of each image. Scaling bar is 5 µm long.

Spectrally-resolved images appear identical in linear color scale, and are thus shown in logarithmical color scale in Figure 5-5. These images can also be summarized in two graphs shown in Figure 5-6. On the one hand, the I_{PL} spectra are shown at increasing distances from the excitation point. On the other hand, each spectral image (from Figure

5-5) can be represented by a radially averaged profile, as done in Figure 5-6(b). One can notice than starting from $E < E_{\text{peak}} = 1.6\text{eV}$ on the spectral images, the central I_{PL} flare is progressively enlarged. As E decreases, the signal to noise ratio becomes progressively too low for a clear image, whereas the I_{PL} profile at $E = 1.52\text{eV}$ remains easily read. Further analysis will unveil the predominant role of photonic propagation and photon recycling in the next section.
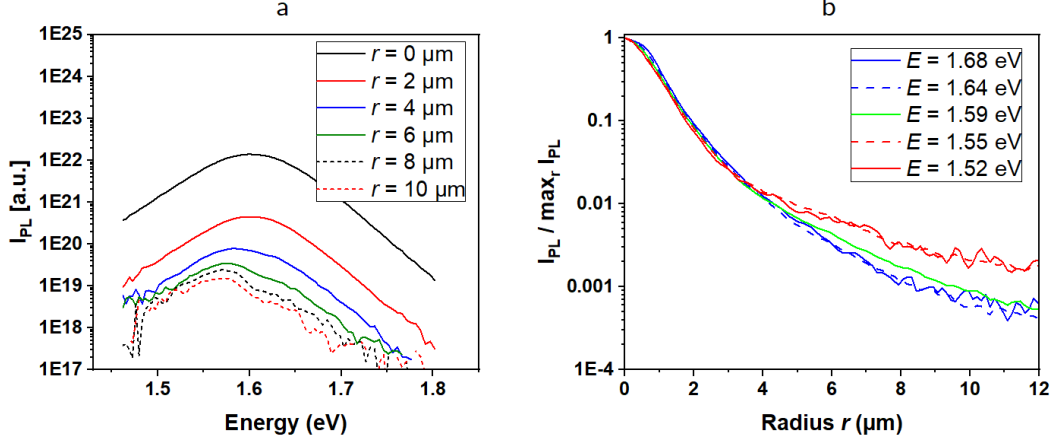
Figure 5-6 I_{PL} spectra at increasing distances from the laser spot(a) PL profiles for each emitted photon energy from 1.52 eV to 1.68 eV. (b)

5.3.MODELING PHOTONIC

5.3.1. EVIDENCING THE PHOTONIC REGIME

The I_{PL} profiles at fixed E values (Figure 5-6(b)) reveal the presence of two different regimes. At a shorter distance, the PL spectra is independent from the photon energies E_{ph}. At a longer distance, it appears that I_{PL} for the less energetic photons $E_{\text{ph}} < E_{\text{peak}}$ is maintained over a longer distance as compared to $E_{\text{ph}} > E_{\text{peak}}$; E_{peak} being the emission energy at which the maximum PL intensity is reached. Indeed, the ratio between $I_{\text{PL}}(1.52\text{eV})$ and $I_{\text{PL}}(1.65\text{eV})$ increases (i.e. the red wavelengths of the PL signal propagate farther).

These long-range photons end up either by getting partially reabsorbed to excite charge carrier, which ultimately recombine (PR), or by being coupled out of the thin film. If all of them were reabsorbed, we would observe a local I_{PL} emission and expect no I_{PL} spectra variation. However, the I_{PL} spectra at different distance from the excitation spot are presented in Figure 5-6(a) and a spectral change for r > 3 µm is apparent. It indicates a strong contribution of a simple photon propagation at longer distance without contribution to the PR. The following expression of I_{PL} summarizes the previous considerations and splits the monitored signal I_{PL} between a propagated flux Φ_{prop} which progressively red-shifts as r increases, and a local I_{PL} emission with a constant spectrum:

$$I_{\text{PL}} = \Phi_{\text{prop}} + R_{\text{eh}}^* \, n^2 \tag{5-1}$$

This interpretation was first introduced by Pazos-Outon et al.[194], and we confirm it by analytical calculations accounting for total internal reflexions of the isotropically emitted PL photons. The contribution of propagated PL photons is described analytically by Φ_{prop} derived the next sub-section.

5.3.2. LONG-RANGE PHOTONIC PROPAGATION
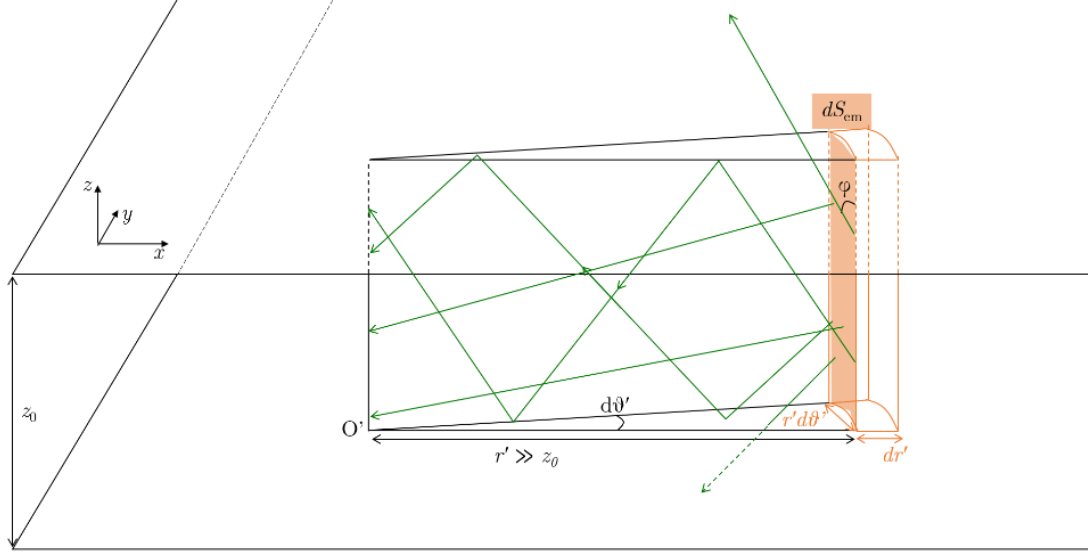
Figure 5-7 Geometrical sketch of the elementary volume dV in the long-range scenario, showing the photons (green rays) emitted in dV (orange), towards the origin of a secondary frame, where the recycling term g_{rec} is calculated. Various solid angles of emission ultimately propagate towards the origin thanks to total internal reflection at front and back interfaces for $\varphi_c < \varphi < \pi - \varphi_c$.

To analyse the propagation of photons, we start from the radiometric formalism described in section 1.1.2. We adapt it to derive the photonic density $n_{\gamma 2}$ propagated towards the origin of a secondary frame (r',ϑ',z). This origin might be distinct from the center of charge carrier distribution. We consider the flux $j_{\gamma 2}$ emitted from dV depicted in orange in Figure 5-7 towards an elementary surface dS_{O} placed at O (r'=0). It depends on the photon density in dV, and on the emission surface dS_{em} and solid angle $d\Omega_{\mathrm{em}}$, which values are given in Table 5-1.

Total internal reflexions of the PL have to be considered and several photon trajectories link two points, as indicated with green rays in Figure 5-7. We consider them by varying the angle φ between the PL ray and (Oz). The critical angle can be defined using Snell-Descartes law : φ_{c}=asin($1/n_{\mathrm{opt}}$). For $\varphi < \varphi_{\mathrm{c}}$ and for $\varphi < \pi$ - φ_{c}, photons are emitted out of the thin film. For π - $\varphi_{\mathrm{c}} > \varphi > \varphi_{\mathrm{c}}$, they eventually reach the origin. To account for the Lambertian emission through the elementary surface dS_{em}, a solid angle of emission $d\Omega_{\mathrm{em}}(\varphi)$ has to be defined. It reads:

$$d\Omega_{\mathrm{em}}(\varphi) = \frac{dS_{\mathrm{O}}}{\frac{r'^2}{\sin^2\varphi}} = \frac{dS_{\mathrm{O}}\sin^2\varphi}{r'^2} \qquad (5\text{-}2)$$

Parameter	Description	Value [long-distance]
dV	Emission volume	$dr'\ r'\ d\vartheta'\ z_0$
$a(E)$	Absorptivity of dV	$\alpha(E)\ dr$
dS_{em}	Emission surface	$r'\ d\vartheta'\ z_0$
$d\Omega_{em}$	Emission solid angle	$\dfrac{dS_O\ \sin^2\varphi}{r'^2}$

Table 5-1 Summary of values used for photon propagation calculation in the long-range scenario

The flux $j_{\gamma 2}$ propagates from (r',ϑ',z) towards O and gets attenuated, which we account of by adding a Beer-Lambert term $\exp(-\alpha(E)\sin(\varphi)/r)$. Henceforth, the contribution of dV to $n_{\gamma 2}$ writes:

$$dS_O\,dn_{\gamma 2}(E)=n_\gamma(X,E,\Omega)\int d\Omega_{em}\,\sin(\varphi)\,dS_{em}\exp\left(-\frac{\alpha(E)\sin(\varphi)}{r'}\right)d\varphi \tag{5-3}$$

Next, we develop eq. (5-3) by expressing $n_\gamma(X,E,\Omega)$ using van-Roosbroeck-Schockley formalism (also eq. (1-2)), and reach another expression for $dn_{\gamma,2}$:

$$dS_O\,dn_{\gamma,2}(E)=\frac{K_p n^2\left(r',\vartheta'\right)}{n_0 p_0}E^2\alpha(E)\exp\left(-\frac{E}{k_B T}\right)dr'...$$
$$...\int_{\varphi_c}^{\pi-\varphi_c}dS_{em}\sin\varphi\,d\Omega_{em}(\varphi)\exp\left(-\frac{\alpha(E)r}{\sin(\varphi)}\right)d\varphi \tag{5-4}$$

Then, one can integrate $dn_{\gamma,2}$ over the semi-conductor slab, making use of the known expressions of $d\Omega_{em}$, dS_{em} from Table 5-1. We obtain the long-range propagated photon density per energy:

$$dS_O\,n_{\gamma,2}(E)=\frac{K_p}{n_0 p_0}E^2\alpha(E)\exp\left(-\frac{E}{k_B T}\right)...$$
$$...\int_{r'=0}^{\infty}\int_{\vartheta'=0}^{2\pi}\int_{\varphi_c}^{\pi-\varphi_c}\frac{n^2(r',\vartheta')dS_O\,z_0\,\sin^3\varphi}{r'}\exp\left(-\frac{\alpha(E)r'}{\sin(\varphi)}\right)dr'd\vartheta'd\varphi \tag{5-5}$$

Where the surface on which we integrate the propagating flux (dS_O) can now be simplified:

$$n_{\gamma,2}(E)=\frac{K_p}{n_0 p_0}E^2\alpha(E)\exp\left(-\frac{E}{k_B T}\right)...$$
$$...\int_{r'=0}^{\infty}\int_{\vartheta'=0}^{2\pi}\int_{\varphi_c}^{\pi-\varphi_c}\frac{n^2(r',\vartheta')z_0\,\sin^3\varphi}{r'}\exp\left(-\frac{\alpha(E)r'}{\sin(\varphi)}\right)dr'd\vartheta'd\varphi \tag{5-6}$$

To determine the propagated flux at a certain distance r from the symmetry center of the charge carrier concentration, one needs to define a secondary frame with polar coordinates centered at the point $(r,0)$, and then it is possible to calculate $\Phi_{prop}(r,E)$ within this secondary frame by rewriting (5-6): (N.B. $\Phi_{prop}(r,E)=n_{\gamma,2}(E)$)

$$\Phi_{\text{prop}}(r,E) = \frac{K_p E^2 \alpha(E) \exp\left(-\dfrac{E}{k_B T}\right)}{n_0 p_0} \ldots$$

$$\ldots \iint_{(r',\vartheta')\text{ frame centered in }(r,0)} dr' d\vartheta' \, z_0 \frac{n^2(r',\vartheta')}{r'} \int_{\varphi_c}^{\pi-\varphi_c} d\varphi \, \sin^3 \varphi \, \exp\left(-\frac{\alpha(E)r'}{\sin \varphi}\right) \tag{5-7}$$

We changed r (from the primary frame) from 3 to 20 µm and simulated the evolution of the spectrum and the intensity of the propagated PL, thereby generating a family of propagated spectra $\Phi_{\text{prop}}(r)$. This model was verified by fitting the PL spectra extracted from hyperspectral maps acquired around a point pulsed illumination. They were reproduced as the linear combination of the calculated propagated flux to a direct PL emission, taken as proportional to $I_{\text{PL}}(r{=}0)$, described by:

$$\frac{I_{\text{PL}}(r)}{\max_E\left(I_{\text{PL}}(r)\right)} = \beta \frac{\Phi_{\text{prop}}(r)}{\max_E \Phi_{prop}(r)} + (1-\beta) \frac{I_{\text{PL}}(r{=}0)}{\max_E I_{\text{PL}}(r{=}0)} \tag{5-8}$$

Normalizations are employed so that the sum of coefficients for both contributions is 1. Results are displayed in Figure 5-8, and showcase an excellent reproduction quality. The relative weight of direct and waveguided contribution is indicated in the legend of each subplot. The weight of direct emission is 100% at 3 µm and decreases to 40% at r=9 µm. The weight of propagated spectrum follows an opposite trend.
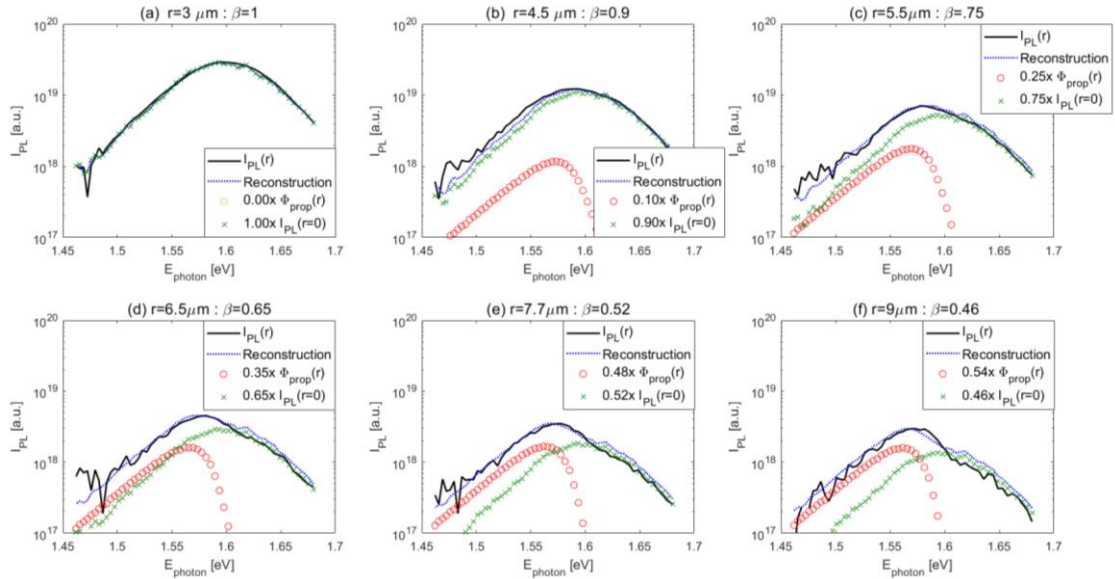
Figure 5-8 Optimal reconstruction of I_{PL} for increasing distances to the excitation point. Fit is based on a linear combination of direct contribution (green crosses) and propagated one (red circles), as explicated in eq. (5-8).

This assesses the photon propagation regime and confirms the trapping of photoluminescence signal inside the thin film leading to photonic propagation and recycling over longer distance than what could be inferred from experiments realized on single crystals[215,217]. At long range, the photon recycling phenomenon is not quantified here, but it will be studied at short range, where it plays a dominant role in transport.

5.3.3. SHORT-RANGE PHOTONIC PROPAGATION
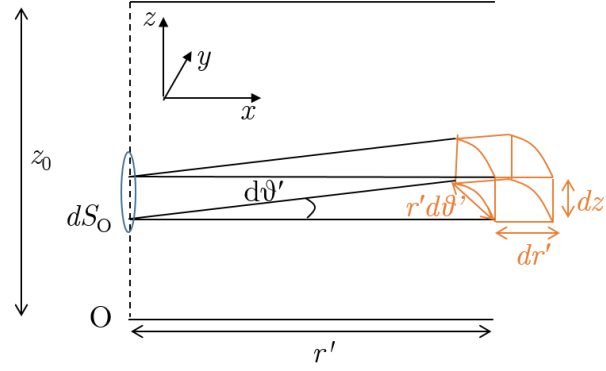
Figure 5-9 Sketch of the elementary volume dV in the short-range scenario(orange box here above) inside a semi-conductor slab with thickness z_0

Here again, we start back from eq. (1-2) that we adapt to derive the photon flux $j_{\gamma 1}$ emitted from dV towards the origin of a secondary frame. Figure 5-9 displays a 3D view of the elementary volume, along with geometrical parameters allowing us to write dS_{em} and $d\Omega_{em}$ in Table 5-2. The role of the angle φ in eq. (5-4) is taken over by an in-depth integration from 0 to z_0, as no guided modes are considered for this short-range calculation. We derive $dn_{\gamma 1}$ by integrating the incoming flux through an elementary surface dS_O placed at O ($r'=0$). An attenuation term is added and corresponds to Beer-Lambert theory. This yields:

$$dS_O\, dn_{\gamma 1}(E) = n_\gamma(X,E,\Omega)\, d\Omega_{em}\, dS_{em} \exp\left(-\frac{\alpha(E)}{r'}\right) \tag{5-9}$$

Parameter	Description	Value
dV	Emission volume	$dr'\ r'\ d\vartheta'\ dz$
$a(E)$	Absorptivity of dV	$\alpha(E)\ dr$
dS_{em}	Emission surface	$r'\ d\vartheta'\ dz$
$d\Omega_{em}$	Emission solid angle	$\dfrac{dS_O}{r'^2}$

Table 5-2 Summary of values used for photon propagation calculation in the short-range scenario

Eventually, the photon density at the origin propagated from dV towards O, can be written as in eq. (5-10):

$$dS_O\, dn_{\gamma,1}(E) = \frac{dS_O\, n_\gamma(r',\vartheta',E,\Omega)}{r'^2} \exp(-\alpha(E)r')\ r'\ d\vartheta'\ dz \tag{5-10}$$

In the next step, we replace $n_\gamma(r',\vartheta',E,\Omega)$, knowing that the absorptivity (and hence emissivity) of dV is $\alpha(E)dr'$.

$$dn_{\gamma,1}(E) = \frac{K_p \cdot n^2(r',\vartheta')}{n_0 p_0}\, \alpha(E)E^2\ \exp\left(-\frac{E}{k_B T}\right)\ \frac{\exp(-\alpha(E)r')}{r'}\ dr'\ d\vartheta'\ dz \tag{5-11}$$

The integration over the whole volume remains. It yields the formula of $n_{\gamma,1}$, which we also call $\Phi_{\text{prop}}(r,E)$ as in eq. (5-7) in the long-range scenario:

$$\Phi_{\text{prop}}(r,E) = \iiint_{(r',\vartheta',z') \text{ frame centered in } (r,0,0)} \frac{K_p n^2(r',\vartheta)}{n_0 p_0} \ldots$$
$$\ldots \alpha(E) E^2 \exp\left(-\frac{E}{k_B T}\right) \frac{\exp(-\alpha(E)r')}{r'} \, dr' d\vartheta' dz \tag{5-12}$$

This formula remains valid if the charge carrier concentration is near the origin. Hence, the whole volume refers to r' values comprised between 0 and some multiples of z_0 at most. Otherwise one should consider the other scenario from the previous section 5.3.2. Eq. (5-12) notably applies to derive the panchromatic reabsorbed density at $(r,0,0)$, which we call g_{rec}:

$$g_{\text{rec}}(r) = \iiint_{(r',\vartheta',z') \text{ frame centered in } (r,0,0)} \frac{K_p n^2(r',\vartheta')}{n_0 p_0} \ldots$$
$$\ldots \int \alpha^2(E) E^2 \exp\left(-\frac{E}{k_B T}\right) \frac{\exp(-\alpha(E)r')}{r'} \, dE dr' d\vartheta' dz \tag{5-13}$$

5.3.4. TAKING INTO ACCOUNT PHOTON RECYCLING

Under steady-state homogeneous illumination, the recycling is proportional to the PL emission and a single correction factor g_{corr} can be applied on the measured external radiative coefficient value $R_{\text{eh}}*$, to obtain the internal radiative coefficient R_{eh}[122,181,214]. It is defined as $g_{\text{corr}} = R_{\text{eh}}/R_{\text{eh}}*$ and was used in section 4.3.4. However, this assumption does not hold in a more general case[218], in particular for transient experiments or for inhomogeneous illumination conditions. For this reason, we investigated the behavior of g_{rec} depending on the charge carrier concentration profile.

We applied this calculation on Gaussian charge carrier distribution with *FWHM* comprised between 1 and 3 µm, representative of the temporal evolution of the charge carrier distribution between $t = 0$ ns and $t = 100$ ns. Notably, *FWHM* value is 1.5 µm at $t = 10$ns. The recycling term is represented in Figure 5-10(a) as a function of the radius r, along with the local PL emission intensity. Electronic transport happens at the nanosecond scale and immediate photon propagation is assumed, which allows to associate the same time coordinate to a PL emission profile and a PL recycling profile. At first sight, they behave similarly at short distances, but can strongly differ for large values of r.

Figure 5-10(b) shows the local correction factor g_{corr} introduced as $R_{\text{eh}}/R_{\text{eh}}*$ here above, which is written in different terms in the following equation:

$$g_{\text{corr}}(r) = 1 - \frac{g_{rec}(r)}{\iint n_\gamma(r,E,\Omega) \, dE d\Omega} = 1 - \frac{\text{recycling}}{\text{emission}} \tag{5-14}$$

For each value of *FWHM*, a threshold appears where the PL emission drops, whereas the PL recycling maintains its intensity, as the PL signal emitted at the center propagates and gets reabsorbed farther inside the material. For example, g_{rec} and $R_{\text{eh}}n^2$ trends split before $r = 3$µm *FWHM* = 1µm. As a consequence, the ratio $I_{\text{PL}}/g_{\text{rec}}$ drops drastically and

g_{corr} values become negative (the recycling contribution becoming higher than the emission contribution). Past this threshold, the recycling is not proportional to the local emission. Henceforth, thanks to the analytic expression of g_{rec} in eq. (5-13), we determine a constant value for g_{corr}=0.43±0.05 over the first microns of the distribution, on which the recycling is proportional to the local PL emission.
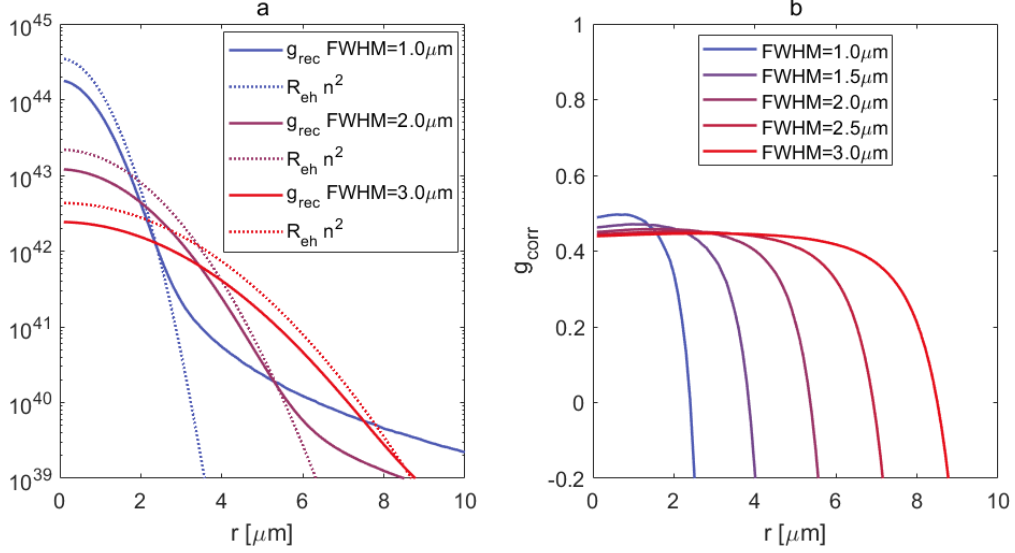
Figure 5-10 Contributions to rate equation (5-19) for a gaussian charge carrier distributionwith FWHM=1..3µm, and $\Phi_0 = 5 \times 10^6$ photons per pulse.(a) The PL emission ($R_{eh}n^2$) is displayed in dotted lines, while the recycling is in plain lines. Vertical scale is in arbitrary units. (b) The local R_{eh} correction factor, as defined in the equation above, is displayed for gaussian charge carrier distributions with FWHM=1..3µm.

5.3.5. MONO-CHROMATIC EQUIVALENT FLUX

The approximation of considering the PL as monochromatic with a single absorption coefficient α_{PR} can be useful to gain some physical intuition. It was notably used in section 4.3.4 to calculate I_{PL} while knowing the in-depth concentrations of n & p. We investigate here its validity for photon recycling calculation.

$$\alpha_{PR} = \frac{\int \alpha_{PR}(E) E^2 \exp\left(-\frac{E}{k_B T}\right) dE}{\int E^2 \exp\left(-\frac{E}{k_B T}\right) dE} \tag{5-15}$$

It allows to separate spatial and energetic integrals as in the equation below, and we will comment on its validity.

$$\widetilde{g_{rec}(r)} = \iiint_{(r',\vartheta',z') \text{ frame centered in } (r,0,0)} \frac{K_p n^2(r',\vartheta')}{n_0 p_0} \alpha_{PR} \frac{\exp(-\alpha_{PR} r')}{r'} dr' d\vartheta' dz' ...$$

$$... \int_E E^2 \exp\left(-\frac{E}{k_B T}\right) dE \tag{5-16}$$

This is equivalent to:

$$\widetilde{g_{rec}}(r) = \iiint_{(r',\vartheta',z') \text{ frame centered in } (r,0,0)} \frac{R_{eh}}{4\pi} n^2(r',\vartheta')\alpha_{PR} \frac{\exp(-\alpha_{PR}r')}{r'} dr'd\vartheta'dz' \quad (5\text{-}17)$$

In Figure 5-11, the individual contributions of each wavelength to the recycling term are displayed for a Gaussian distribution with FWHM = 1.5µm. The plain line and the squared line remain close at short distance, which shows that eq. (5-16) (average absorption coefficient) is valid at short distances. This approximation might underestimate the long-range photonic transport, as both trends diverge for r > 5µm, but this is outside of the scope of the short-range calculation derived in section 5.3.3.
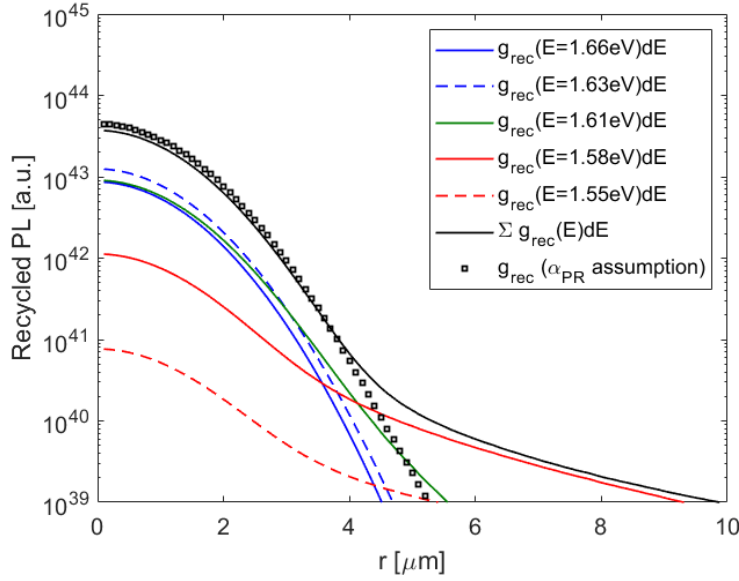
Figure 5-11 Contribution of each PL wavelength to the recycling. The black plain line giving the sum of all contributions was also displayed in Figure 5-10(a). The squared curve was derived under the assumption of a fixed absorption coefficient for the whole PL emission, also named α_{PR}.

5.3.6. ABOUT OUR MODEL FOR PHOTONIC TRANSPORT

This study addressed the measurement of optical properties related to photon propagation inside a thin film. Previous models based on ray optics[122,213] or detailed balance considerations[214,219] had allowed to quantify the recycling process at the device scale for a homogeneous illumination. They assumed either an angular randomization at each reflection, which leads to the famous "$4n^2$ limit" derived by Yablonovich[220], or a reflection as of Snell-Descartes law. We employed inhomogeneous illumination to monitor transport and hence we needed a more precise model. The developed one places itself in the black-body formalism and assumes an isotropic emission which directly depends on the local quasi-Fermi level splitting. Since the emissivity is linked to the absorptivity, it also allows us to derive the reabsorption of the emitted flux (PR), notably accounting for possible total internal reflexions. It reproduces very well the deformation of PL spectra at long range. However, a small amount of outcoupling of these guided modes is necessary for us to observe the photon propagation flux.

A similar model was employed to assess the trapping of PL photons inside CsPbBr$_3$ micro-wires[221]. We complete their analysis by separating the monitored I_{PL} signal into a propagated and a locally emitted component, which allows us to characterize short-range and long-range transport properties. Another technique to account for this photon flux consists in transforming the continuity equation for electrons and holes into a coupled differential system with various photon fluxes[194,218]. This was mainly used to predict long-range photon recycling but not to separate short-range electronic and photonic transport. In the present study, we do so by using a single differential equation summarizing the photon diffusion in a unique regeneration term, which results in a simple model adapted to fitting multiple parameters at once.

5.4. DETERMINATION OF TRANSPORT PROPERTIES

Table 4-3 summarized previous considerations for the interpretation of spectrally-resolved measurements. In a nutshell, we can relate the $I_{PL}(r<3\mu m)$ to the local charge carrier concentration, while further spectral analysis is required to investigate transport properties using $I_{PL}(r>3\mu m)$. This spectral analysis indicates that $I_{PL}(E>E_{peak})$ can be ascribed to locally induced PL emission, as $\Phi_{prop}(E>E_{peak}) \approx 0$ for large values of r. This long-range charge carrier concentration is assumed to represent photon recycling, which will be justified with the next derived electronic diffusion length (450nm). Hence, a characteristic length L_{PR} for the photon recycling can be extracted by fitting the decay of $I_{PL}(r)$ for $E > E_{peak}$ with an exponential attenuation length. It decays with characteristic length of 2.5µm. Knowing that the PL decreases quadratically with the carrier concentration n, L_{PR} is measured around 5µm. This length applies for photon recycling after a point pulsed illumination. This photonic transport is essentially lateral and probably affected by the film thickness.

r [µm]	Spectrally-resolved I_{PL} $I_{PL}(E<E_{peak})$	Spectrally-resolved I_{PL} $I_{PL}(E>E_{peak})$	Time-resolved I_{PL} $I_{PL}(t)$
$r>3\mu m$	$I_{PL}=R_{eh}{}^*n^2$	$I_{PL}=R_{eh}{}^*n^2$	$I_{PL}=R_{eh}{}^*n^2$
$r>3\mu m$	$I_{PL}=\Phi_{prop}+R_{eh}{}^*n^2$	$I_{PL}=R_{eh}{}^*n^2$	$I_{PL}=\Phi_{prop}+R_{eh}{}^*n^2$

Table 5-3 Summary of the main physical contributions in the luminescence spatial variation. Physical interpretation of the monitored signal I_{PL} (r) using HI (column 2 & 3) or TR-FLIM (column 4). Two distinct zones appear, limited by r = 3µm. The photon propagation regime corresponds to Φ_{prop} and local PL emission to $R_{eh}*n^2$. The 3 µm value is defined empirically from the change in the PL profile in Figure 2 and matches with the value of 1/α at E = 1.57 eV

5.4.1. MODEL ASSUMPTIONS

We model perovskite thin films as intrinsic semi-conductors, where we can write as in Table 4-3:

$$\forall \text{ (for all) } t, \ r<3 \text{ µm} : I_{PL}(r,t) \propto n^2(r,t) \tag{5-18}$$

Non-radiative recombinations are considered monomolecular, and are described thanks to a Shockley-Read-Hall lifetime τ_n, while radiative recombinations are modeled via the internal radiative coefficient R_{eh}[94]. Auger recombination are neglected as they take a

significant share in the recombination process only for $n > 10^{18}$cm^{-3} [218,222]. Ambipolar effects are not considered, as electron and hole have similar mobilities in metal halide perovskite[98,121], which we also investigate in chapter 6. The local excitation creates a charge carrier gradient, which homogenizes through charge carrier diffusion[19] (diffusion coefficient D_n) as well as through photon diffusion[218]. The local reabsorption of this photon flux leads to the emergence of an additional generation term g_{rec} in the continuity equation[122]. In the following, we will neglect the in-depth dimension to focus on the lateral transport. For this purpose, we will restrain our dataset to the long times, when in-depth diffusion has already happened (typically $t>10$ns for 600nm-thick perovskite layers[187], as established in Table 4-4). Finally, the diffusion equation writes in polar coordinates:

$$\frac{\partial n}{\partial t}(r,t) = D_n \nabla n(r,t) - \frac{n(r,t)}{\tau_n} - R_{eh}n^2(r,t) + g_{rec}(r,t)$$

$$\Leftrightarrow \frac{\partial n}{\partial t}(r,t) = D_n \nabla n(r,t) - \frac{n(r,t)}{\tau_n} - R_{eh}^* n^2(r,t)$$

(5-19)

The equivalence sign in (5-19) refers to the definition of an external radiative coefficient R_{eh}^* accounting for local PL emission corrected by photon recycling. We demonstrated in section 5.3.4 that is valid for $r < 4$µm provided that the charge carrier distribution verifies $FWHM > 1.5$µm. Henceforth, our fitting approach is valid for $t > 10$ns, when this charge carrier concentration is not too peaked.

5.4.2. PEROVSKITE THIN FILM
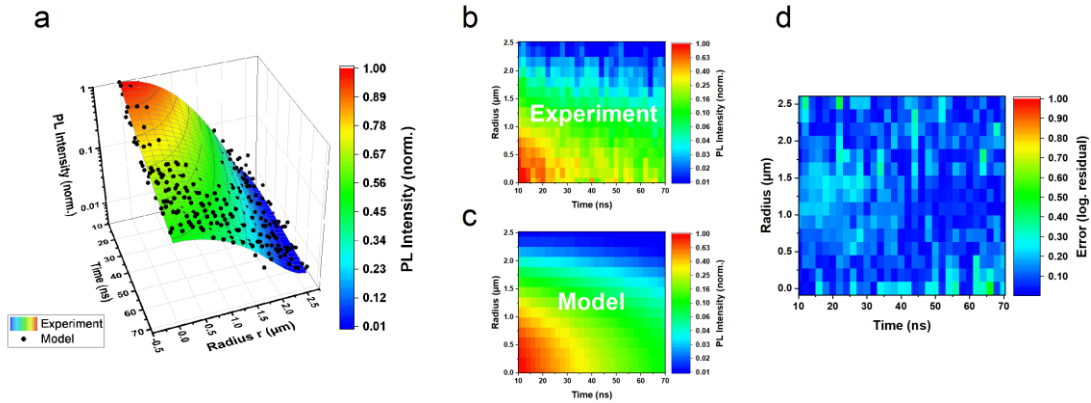
Figure 5-12 Determination of the pure electronic diffusion properties(a) Surface showing the best fit between $I_{PL}(r,t)$ calculated with the diffusion-recombination model in eq. (5-19) and experimental data (black circles) acquired on a mixed halide perovskite thin film ($\phi_0 = 5x10^6$ photons per pulse). Fake colors indicate the PL intensity (b) is a 2D map of the experimental data whereas (c) is a 2D map of the modeling results. (d) Logarithmic residuals map from the modeling.

In the published version of this chapter, time-resolved I_{PL} profiles from the power study are fitted separately, yielding concordant values for D_n, R_{eh}^*, and τ_n that are displayed in Table 5-4. The fit realized at high fluence is shown in details in 3D and plan views in Figure 5-12(a-c). The logarithmic difference between experimental and numerical values was miniminzed, and Figure 5-12(d) shows that it remains negligible at any fitting point. The fit realized at low fluence is not sensitive to R_{eh}^*, which is consistent with the

decreased weight of bimolecular recombination as n decays. Thanks to g_{corr}, we can also derive the internal radiative coefficient $R_{eh} = 1.0 \times 10^{-10} \pm .4 \times 10^{-10}$ cm^{3}s^{-1}. An equivalent electronic diffusion length can be determined around 450 nm. It is derived at $n = 10^{16}$/cm^3 – a relevant value for PV operation at 1 sun excitation[38,223] – and take into account SRH and radiative recombinations for the definition of the lifetime. At such a fluence, the radiative lifetime is 660ns, while the non-radiative one remains at 110ns.

Parameter	Fitting $\phi_0=5\times10^6$/pulse	Fitting $\phi_0=10^5$/pulse	Fitting both power together
D_n [cm^2/s]	0.027 ± 0.007	0.035 ± 0.02	$[0.012 - 0.045]$
τ_n [ns]	110 ± 30	94 ± 30	$[76 - 96]$
R_{eh}^* [x10^{-10} cm^3/s]	0.44 ± 0.2	?	$[0.2 - 0.3]$
$FWHM$ [µm]	1.15 ± 0.05	1.15 ± 0.05	$[0.97 - 1.17]$

Table 5-4 Transport and recombination parameters determined by fitting I_{PL} profiles.
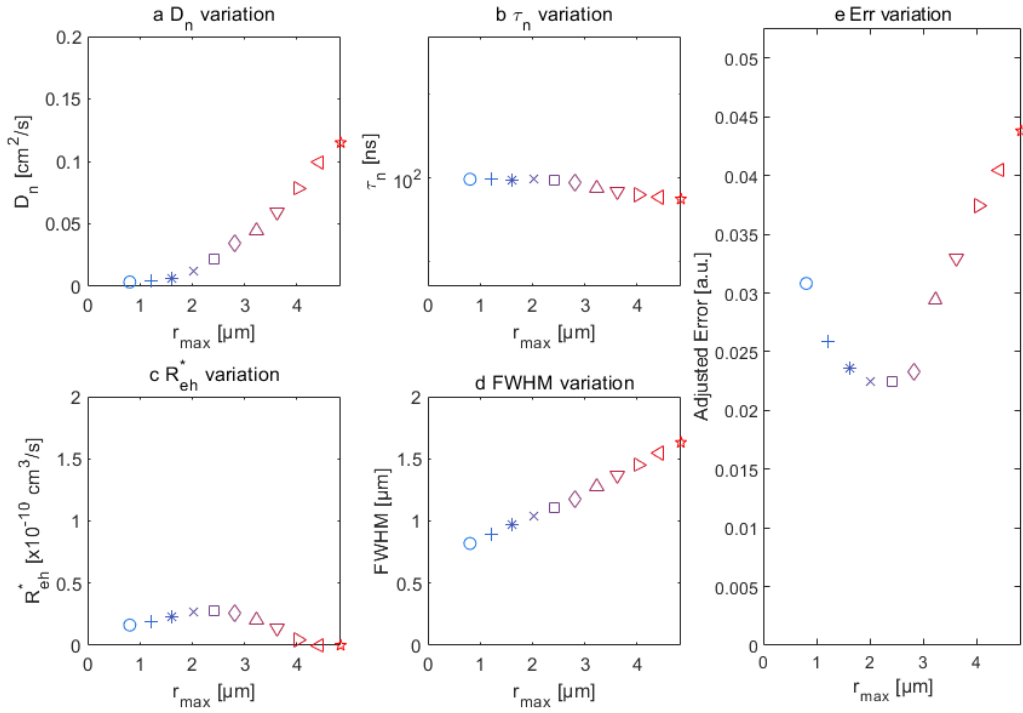
Figure 5-13 Sensitivity to space-domain restriction. Values for the parameters D_n (a) τ_n (b) R_{eh}^* (c) and FWHM (d), determined by our optimization algorithm fitting I_{PL} profiles for both power at the same time, while varying r_{max} in the space-domain restriction. The adjusted error indicating the reproduction quality is displayed in (e).

In the actual version of this chapter, we update the results by fitting $I_{PL}(0<r<r_{max},t>10\text{ns})$ profiles for both fluence at the same time. In order to fit several curves with a single set of parameters, an optimization approach is used with Matlab function "fminsearch", whereas the "Curve Fitting" toolbox was used up to now. This approach enhances the precision of the results and was preferred for further application of the model. We subsequently adjust the control experiments realized while varying the space-domain restriction. This consists in fitting $I_{PL}(0<r<r_{max},t>10\text{ns})$ profiles for various values of r_{max}. This investigation results in the variation of each fitting parameter

as a function of r_max, which is plotted in Figure 5-13. While τ_n & $R_\text{eh}{}^*$ are stable throughout the variation of r_max, FWHM and D_n show significant variation as r_max increases. In order to discriminate the various fitted values, we rely not only on the previous section about photonic propagation but also on to the reconstruction error in Figure 5-13(e). We thus exclude r_max values exceeding 3µm, for which D_n would be strongly overestimated as photonic transport would also be fitted with electronic diffusion (fitted D_n values get even above 0.1 cm^2/s for $r_\text{max}>$4µm). Too low values for r_max are also avoided, as the adjusted error in Figure 5-13(e) increases.
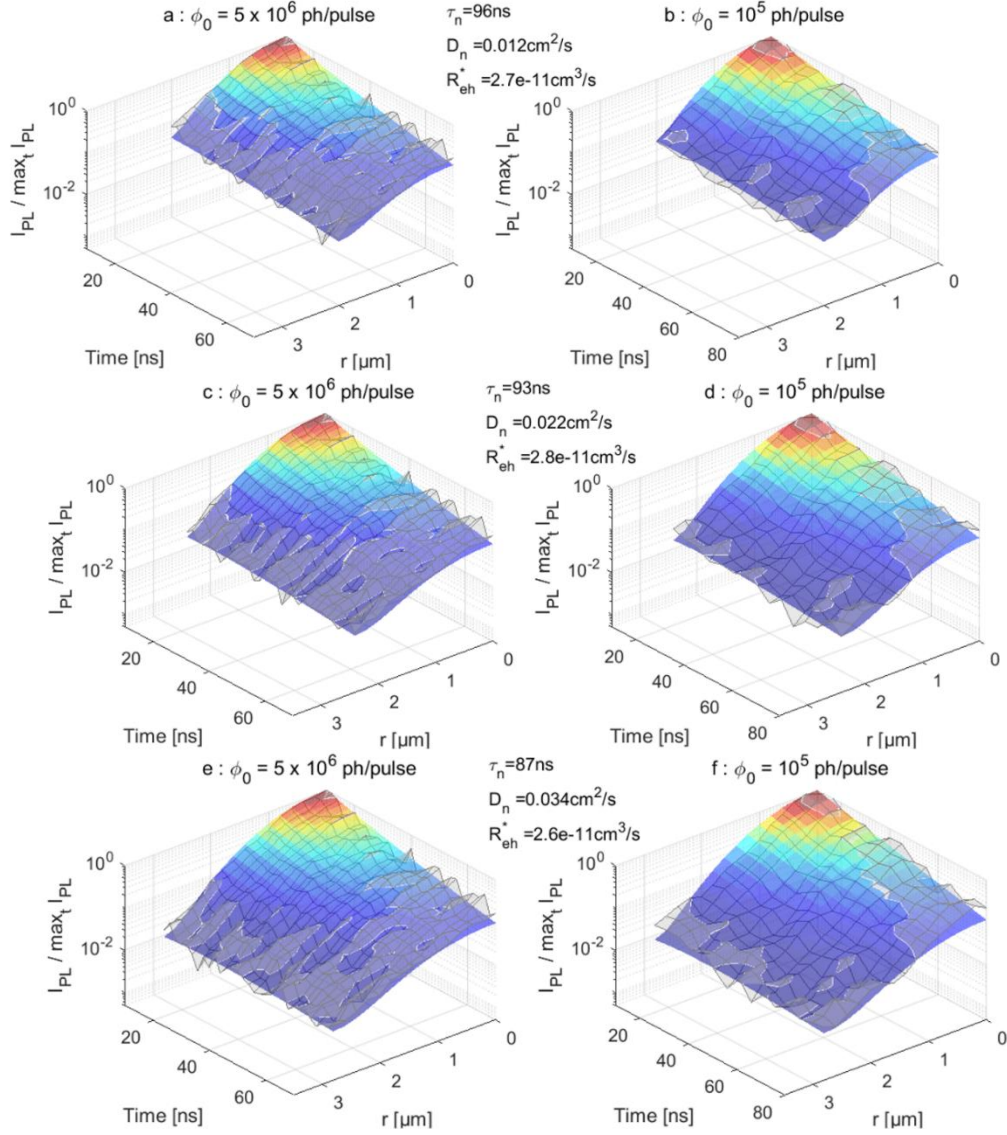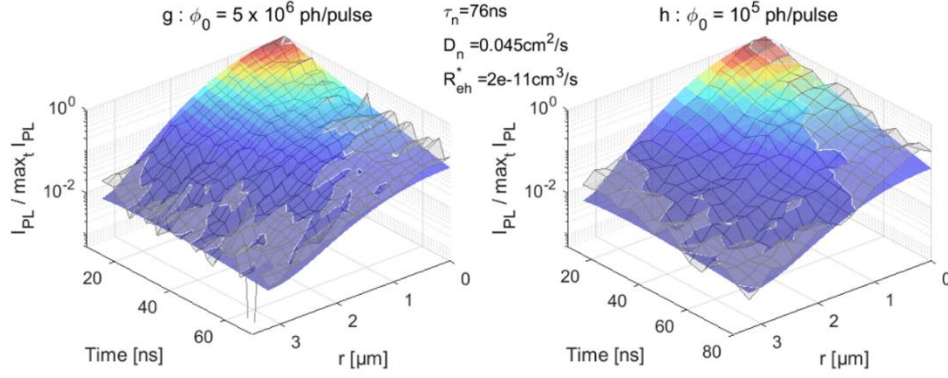
Figure 5-14 Fitting results for the optimization approach applied on I_{PL} profiles with varying space-domain restrictions. Best-fit appear in color surface and experimental in transparent surface. Displayed r_{max} values were selected as the optimal ones as from Figure 5-13. (rmax= 1.7µm (a)-(b) // r_{max} = 2.1 µm (c)-(d) // r_{max}= 2.5µm (e)-(f) // r_{max} = 2.9µm (g)-(h)). A textbox displays the fitted values for τ_n D_n & R_{eh} for each r_{max} value.*

The 4 remaining scenario with lowest reproduction error are displayed in Figure 5-14. For each of them, it provides a 3D view of low power and high power experimental profiles and optimal reconstruction. It leads to the confidence intervals for each parameter, which is given in the last column of Table 5-4. The apparent quality of the fit is equally good on both power for a single set of power-independent parameters.

5.4.3. DISCUSSING THEREOF

The obtained electronic and photonic parameters are in line with the values one can find separately in the literature. In our work, the monomolecular lifetime τ_n values are effective lifetimes and take into account the non-radiative recombination phenomena occurring at the bulk and at the interfaces. This could explain their low values, in comparison to studies where they refer only to the bulk[85,214]. Also, trapping and detrapping events from shallow traps are neglected in our first order approach. These might induce a quicker PL quenching far from the excitation spot, where empty traps could remain. This could as well explain the low value derived for τ_n, in comparison with previous studies accounting for traps[37,85,187]. Hopping mechanism from trap to trap might also contribute to the transport and explain the low values determined for D_n, which we discuss next.

For what concerns R_{eh}*, its value is not only dependent on the material quality, but also on the geometry of the excitation profile and of the thin film itself. Once corrected with g_{corr}=0.43, it leads to the internal radiative coefficient R_{eh}, which closely matches calculated ones[218], and measured ones[94,102]. Being an intrinsic material property, it also allows to determine the charge carrier intrinsic concentration n_0^2 (4.4x10^14 cm^-3 according to eq. (1-7)).

Finally, charge carrier extraction in photovoltaic devices based on perovskite layers works out of diffusion[39] and hence internal electric fields play a negligible role. We also recall that our measurement was applied on neat films, in which no built-in electric field due to heterointerfaces with transport layers is likely to happen. Our experiment is thus

97

well suited to probe the diffusion properties relevant for PV operation. As previously mentioned in the introduction a large range of transport parameters might be found for perovskite absorbers. Besides the different sample qualities and compositions, one origin might be found in the concomitant electronic and photonic contribution investigated in this chapter.

On the one hand, previous works have underlined the photon propagation as well as the PR and we here confirm these results[24,194,215,221]. However, so far no complete model was developed in order to determine the transport properties. On the other hand, several experiments based on luminescence analysis (especially time-dependent experiments) measure the carrier lifetime and transport properties. Nevertheless, they do not take into account the two photonic contributions[24,99,123,188,208,224]. This fact goes along with pump-probe experiments where the spatial contribution probes the solely carrier diffusion[119–121]. Although the photon propagation can be ignored in the latter experiment, the PR affects the carrier concentration and should be considered. Those experiments derived fairly high values for D_n[119,121], which are an order of magnitude higher than observed in this study. In a general way, luminescence experiments based on point pulsed illumination in perovskite might deliver lifetime values not so much impacted by PR[224], but the diffusion away from the excitation spot remains influenced by PR and it is not straightforward to characterize carrier transport with it. A recent study illustrates this artifact where the authors determined D_n by fitting the time-resolved PL signal away from the excitation and attributed the whole dynamics to the electronic diffusion, which could yield an over-estimated determination of $D_n > 1 \mathrm{cm}^2\mathrm{s}^{-1}$ [124]. Also, we want to highlight here a simple idea to monitor solely the direct emission and not the propagated one. This consists in adding a color filter at E_{peak} in the collection branch to get rid of long-range photons, which allows then to distinguish electronic and photonic diffusion.

We have shown that both charge carrier diffusion (led by mobility and lifetime) and photon diffusion (led by absorption properties) contribute to the transport. It is important to know the weight of PR in the transport as it has a beneficial effect on V_{oc}[225]. Nevertheless, it gets mitigated if light management happens, as it leads to a better light in- and out-coupling. Indeed, the escape probability of PL photons is directly included in the formula giving the V_{oc} boost induced by PR[226].

5.4.4. INGAP THIN FILM
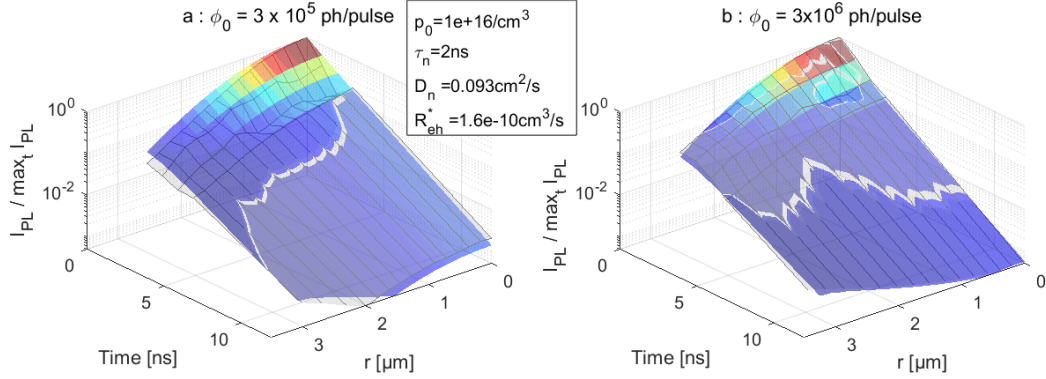
Figure 5-15 Fitting I_{PL} profiles acquired on InGaP sampleat low (a) and high injection (b). Best-fit appear in color surface and experimental data in transparent surface. A textbox indicates the optimal values for diffusion and recombination parameters.

We further applied the transport characterization method to III-V materials produced at IPVF. These semi-conductors are doped and present different mobility for minority and majority carriers. Henceforth, a model adapted to ambipolar diffusion, for which all necessary equations are available in section 1.2, is used. The application of the method developed in the previous sections requires that the effective minority carrier lifetime is superior to the time-resolution of the TR-FLIM, so that "long-time" images can be compared to the "short-time" images to assess lateral diffusion. This prevented us to apply it on AlGaAs materials[227], where the effective lifetime was assessed to be as low as 100ps with the streak camera. On the contrary, we could study samples made of InGaP also suited to tandem integration due to their high bandgap.

Parameter	MOCVD : $p_0=10^{16}/cm^3$	MOCVD : $p_0=5\times10^{16}/cm^3$	MBE : $p_0=10^{17}/cm^3$	MOCVD : $p_0=5\times10^{17}/cm^3$
D_p [cm^2/s]	830	166	83	16
D_n [cm^2/s]	0.15	0.33	0.15	0.05
τ_n [ns]	1.9	1.9	2.2	1.9
R_{eh}^*[x10^{-10} cm^3/s]	0.5	0.4	.9	2.5
$FWHM$ [µm]	1.30	1.15	1.2	1.15

Table 5-5 Transport and recombination parameters determined by fitting I_{PL} profiles on InGaP thin films produced by MetalOrganic Chemical Vapor Deposition (MOCVD) or Molecular Beam Epitaxy (MBE), with different doping concentrations.

Four compositions were investigated and the *p*-type doping of the material was varied, as well as the production method. We applied the fitting procedure optimizing the reconstruction of low *(Φ_0=3x10^5* photons per pulse) and high (*Φ_0=3x10^6* photons per pulse) injection with a single set of parameters, as in 5.4.2. Similar space domain restriction was used, but no time domain restriction as the diffusion as slow in III-V materials. The reconstruction quality is good for both injection levels, as displayed in Figure 5-15 for low doping concentration. The optimal values for fitting parameters is given in Table 5-5. The minority carrier lifetime is constant at 1.9ns for MOCVD samples, and elevates at 2.2ns for MBE samples. R_{eh}^* & D_n values evolve from sample to sample.

The diffusion of minority carriers is slower in heavily doped samples (D_n=0.05cm^2/s for p_0=5x10^{17}/cm^3), which is expected. The external radiative coefficient value is also increased when doping is stronger, but it remains close to the literature value of 5x10^{-11} cm^3/s [228]. Here, it shall be noted that only the temporal part of multi-dimensional imaging was applied on the samples. It is assumed that photon propagation and recycling are not too different when a 500nm thick perovskite sample deposited on glass is changed with a 200nm thick one of InGaP deposited on GaAs.

5.5. APPLYING MULTIDIMENSIONAL IMAGING TO HETEROGENEOUS MATERIALS

This section is extracted from "Spatial inhomogeneity analysis of Cesium-rich wrinkles in triple cation perovskite", except for the sub-section 5.5.4 which deals with photon propagation concerns applied to wrinkled samples, and brings a new proof for the separation of electronic and photonic diffusion.

5.5.1. WRINKLES IN TRIPLE CATION PEROVSKITE
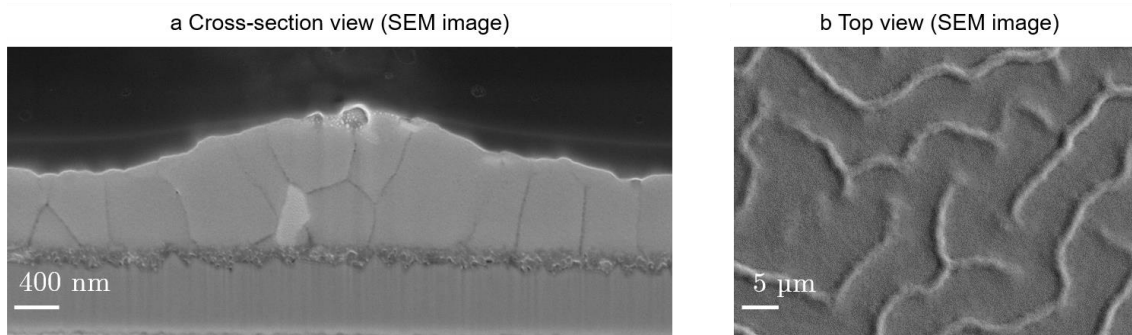
Figure 5-16 Morphological properties of a wrinkle-containing perovskite sample. Focused Ion Beam was used to observe a cross-section SEM of a perovskite PV device (B) SEM image (top-view) of a similar perovskite layer deposited on FTO/bl-TiO₂/mp-TiO₂

The addition of cesium in the perovskite film can lead to the formation of veins-shaped roughness, which are represented in Figure 5-16 and will here be called wrinkles. In a triple cation perovskite containing 5% Cs in the A-site (P$_3$), the inter-wrinkle distance is 12±1.5 µm, whereas their average width is around 3 µm. EDS mapping indicated a local cesium excess in the wrinkles, as well as depletion in nitrogen. This EDS analysis is presented in the published version of this section[229].

Wrinkling had already been observed during this phase for mixed organic cations (as P$_2$ composition)[230], and also P$_3$ composition[231]. As an example, Bush et al. modified the in-plane compressive stress during film formation and could then inhibit wrinkle formation[231]. More recently, Braunger et al. also studied their appearance in (FA,Cs)Pb(I,Br)$_3$ perovskite[232], pointing out a 12.8% to 15.3% rise in average power conversion efficiency. Here, we mainly study the optoelectronic inhomogeneities in wrinkled sample.

5.5.2. HYPERSPECTRAL IMAGING

Advanced photoluminescence (PL) imaging tools lead us to a deeper understanding of the impact of this morphological features on PV operation[134,233,234]. At first, we apply hyperspectral imaging to unravel the bandgap inhomogeneities induced by the Cs spatial distribution. Advanced I_{PL} imaging methods allow us to analysis the optoelectronic properties of the wrinkles. At first, we used the HI to record spectrally resolved I_{PL} images with a micrometric resolution. Figure 5-17(a) displays the I_{PL} peak position as well as the optical microscopy images for the P_2 and P_3 samples. For the latter, blue I_{PL} spectral shifts are observed at the very same location as the wrinkles (see Figure 5-17(b)). This spectral shift goes to ΔE=10±2 meV (from 1.57 eV to 1.58 eV). This could be explained by a smaller grain size in the wrinkle[51,235], which we did not observe in SEM analysis, and which is in contradiction with the bigger grain size on wrinkles observed by Braunger et al[232]. On the contrary, it is consistent[55] with the enhanced concentration in Cesium, previously observed by EDS.
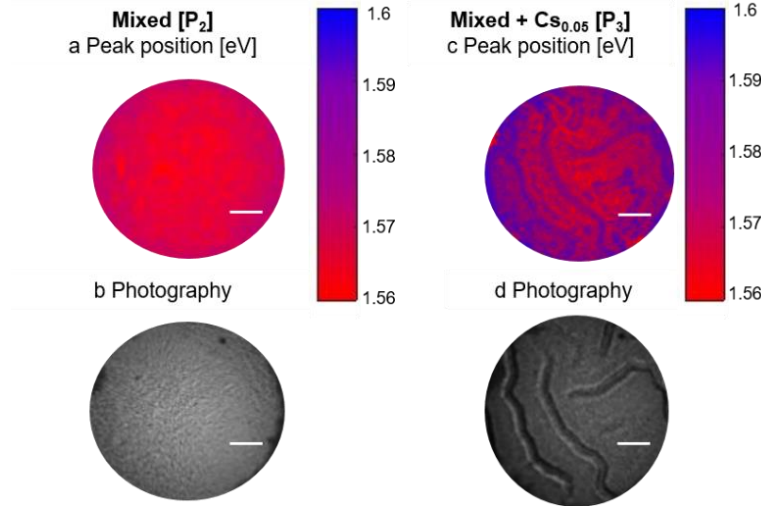
Figure 5-17 Spectral aspect of multi-dimensional I_{PL} imaging of a wrinkle-containing perovskite sample, showing the peak position of the local I_{PL} spectrum, measured on a P_2 perovskite (a-b) or on a P_3 perovskite (c-d). At the bottom, photographies are taken with uniform illumination, allowing to correlate blue shift of the PL peak to the wrinkles

5.5.3. TIME-RESOLVED IMAGING

We then look at time-resolved I_{PL} maps recorded a triple cation perovskite thin film. Figure 5-18 summarizes the recorded data where we display I_{PL} images integrated between 0ns and 100ns after the excitation (Figure 5-18(a)) but also later (Figure 5-18(b-c)). At short times, the I_{PL} maps show features uncorrelated to the wrinkles. At long times (typically $t > 100$ns), their geometrical aspect constitutes a pattern having similar dimensions than the wrinkles observed on the SEM pictures and HI data. As a qualitative summary, the temporal evolution of the I_{PL} profiles shows a global decay, as well as a convergence from a rather flat to a profile shaped by the wrinkles.
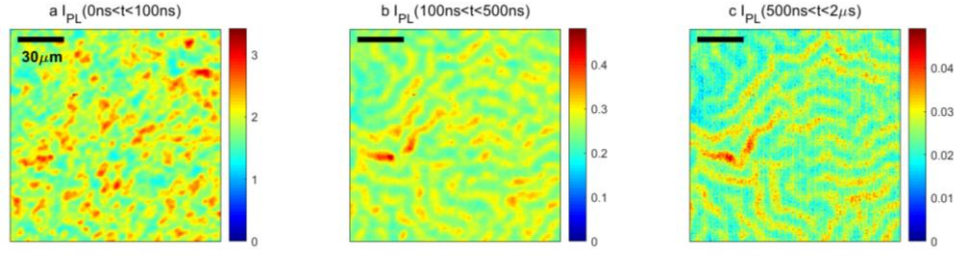
Figure 5-18 Temporal aspect of multi-dimensional PL imaging of a wrinkle-containing perovskite sample, showing the temporal evolution of PL signal after the laser pulse (at t=0ns).

As demonstrated in section 4.5.1, in-depth diffusion of photo-generated carriers and trapping[37,104] govern the global kinetics[187] at short times, whereas the variations at longer times (typically $t > 100$ns) are dominated by bimolecular radiative recombination[94]. At that time, n & p are homogeneous in-depth, which allows us to write I_{PL} as a function of the local thickness $z_0(x,y)$ in eq. (5-20), in which an average absorption coefficient for PL emission (α_{PL}) is used:

$$I_{PL}(x,y) \propto \int_0^{z_0(x,y)} R_{eh}^*(x,y)\,n(x,y)\,p(x,y)\exp(-\alpha_{PL}z)\,dz$$
$$\Rightarrow t > 100\text{ns} : I_{PL}(x,y) \propto [R_{eh}^* np](x,y) \times f_{wr}(z_0) \qquad (5\text{-}20)$$

This equation tells us that I_{PL} depends solely on the electron and hole concentrations (n and p) and on a correction factor f_{wr} directly linked to the thin film thickness, as a thicker perovskite layer (e.g. wrinkle) emits more luminescence. With this deeper knowledge, we investigate further the long-time profile by looking at $I_{PL}(t>500$ns$)$ image in Figure 5-19(a). Cross-sections profiles were taken orthogonally to the wrinkle directions and are represented separately in Figure 5-19(b-d). If wrinkles and inter-wrinkles zones had similar optoelectronic properties, n and p would be equal at any point (x,y) in eq. (5-20). Under this assumption, the PL profiles would exactly represent the morphological profile f_{wr}, which is not the case as the wrinkle lateral width is at most 2 µm, whereas the more emissive zones in the PL profile is 5 to 8 µm wide. Henceforth, we rule out the hypothesis that long-time PL maps are explained by the perovskite local thickness only, and suggest that τ_n inhomogeneities mainly explain them.

To demonstrate the previous suggestion, we designed a drift diffusion modeling with Silvaco Atlas, where a simple wrinkle morphology was investigated. Two scenarios are considered. The former includes similar trap density in and out the wrinkle, while the latter includes a lower trap density in the wrinkle. More details on these models are available in the published version of this section[229]. In the first case, the long-time I_{PL} profiles mimic the wrinkle shape, while in the second case, the lower local trap density in the wrinkle widens the long-time I_{PL} profile. This is explained through the lateral diffusion of carriers from the trap-limited zones to the inter-wrinkle zone. This global trend confirms that Cs content in the vein locally decreases the non-radiative recombination rate and induces this wide profile, which is consistent with previously observed Cs-induced trap passivation in triple cation perovskite[55,184,204].
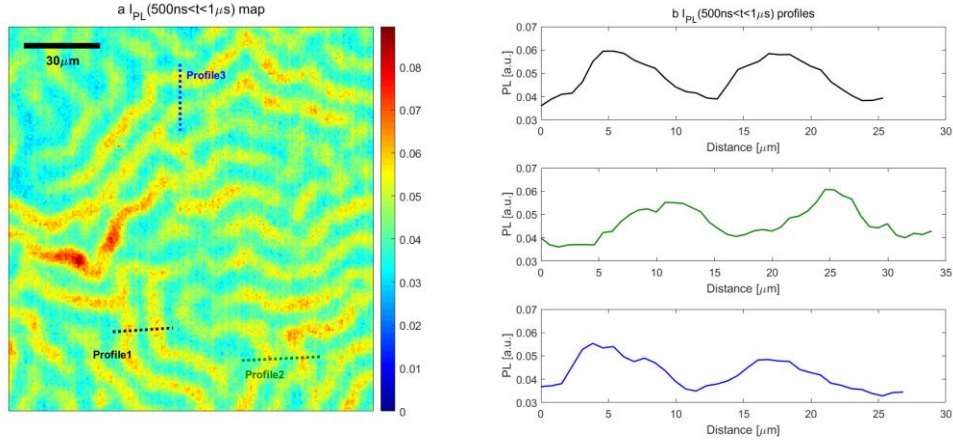
Figure 5-19 Cross-sections profiles drawn in $I_{PL}(500ns<t<1\mu s)$ map(a) displaying the wrinkle-shaped profile in arbitrary units (b-d)

5.5.4. Photon propagation in wrinkled samples
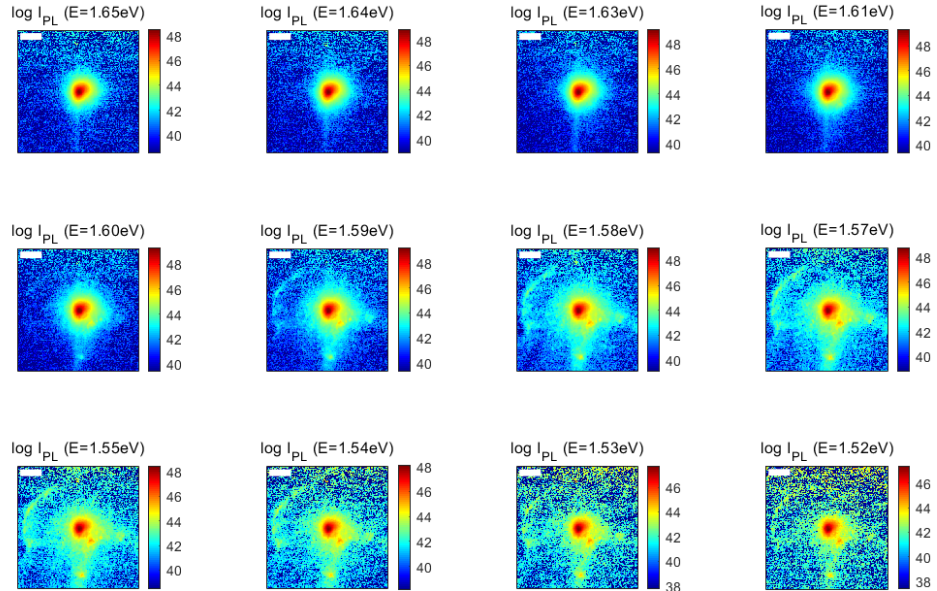
Figure 5-20 PL spectral images at distinct photon energies of a wrinkled sample. Similarly to Figure 5-5, the color scale is logarithmical and scaled to the maximum of each image. Scaling bar is 5 µm

We finally applied a local illumination on a wrinkled sample, in order to provide further proof for the photon propagation regime. As wrinkles constitutes local roughness, they are able to couple out a propagated flux by breaking the planarity of the waveguide. We observe this in Figure 5-20 on I_{PL} images at $E < E_{peak}$, for which the propagated contribution is seen at $r > 3$ µm (as demonstrated in section 5.3). In these images, the radial symmetry of I_{PL} (which was observed for a flat sample in Figure 5-5) is broken and two arch shapes appear. They remain visible for each $E < E_{peak}$ and correspond to two wrinkles able to couple out Φ_{prop}. In other words, the waveguided PL flux is expelled out of the thin film when it would encounter the wrinkle. It is very noteworthy that previous conclusions based on hyperspectral imaging (section 5.5.2) are not impacted by photon propagation. Indeed, the out-coupling of a propagated component tends to shift

the local I_{PL} to the 'red' (i.e. low E), whereas we observed a 'blue' shift on the wrinkle. Concerning section 5.5.3, photon propagation concerns could not be considered in the modeling (neither eq. (5-20) nor Silvaco modeling). Including them could allow the quantification of lifetime in inhomogeneous samples.

As a partial conclusion, multi-dimensional PL imaging was carried out on a sample containing wrinkles, in order to assess the impact of this chemical heterogeneity. The hyperspectral map indicates a blue shift in the PL spectrum on the wrinkles, which is consistent with the Cs enrichment[184]. Time-resolved I_{PL} images pointed out a slower I_{PL} decay on the wrinkle, possibly indicating a shallow trap passivation by the richer Cs. Multi-dimensional imaging also applies for the optoelectronic characterization of heterogeneous materials, as triple cation perovskite can sometimes be.

5.6.   CONCLUSION

In conclusion, transport in a semi-conductor thin film happens via 2 channels. The first one consists in electron and hole diffusion through scattering and it can be described by a diffusion coefficient, which takes low values in metal halide perovskite. Henceforth, this transport is essentially short-range. The photon recycling constitutes the second one and can be observed at any range. Indeed, it does not only induce long-range transport, but also significantly influences short-range transport. Thanks to time-resolved PL profiles acquired after a pulsed point illumination, we have been able to decorrelate both electronic and photonic regimes and to quantify their impact on charge carrier transport. Additionally, a photon propagation regime was observed, confirming the guided propagation of PL photons inside the thin film. In a nutshell, we determine precise values for bulk-related parameters, namely the charge carrier mobility and monomolecular lifetime, the external radiative coefficient, as well as for device-related light management parameters, namely the photon escape probability and the long-range photon recycling length. The introduced contactless experiment is based on multi-dimensional PL imaging and can find interest in any semi-conducting materials where both electronic and photonic contribution happen, especially on high quality materials.

6. Electron, hole and ion transport

Fundamental physics and different transport properties of halide perovskites have still not been fully understood and described[10] (see also section 1.3). In particular, a deep comprehension of the interplay between electronic and ionic transport phenomena is crucial for the optimization of the energy harvesting after light absorption. This is also a fundamental question[91,92,236] as ionic motion is usually associated with defect creation, difficulties in doping control and low carrier lifetimes, one does not expect a semi-ionic conductor to be also an excellent photovoltaic converter.

On the one hand, electronic charge transport in halide perovskites has been well investigated using advanced optical methods, which allowed to observe and disentangle the two main phenomena: charge diffusion and photon recycling[23,216] (also described in chapter 5). Due to the low exciton binding energy, electron and hole behave as free carriers at room temperature[95]. In most studies, an ambipolar charge transport is assumed as the doping concentration is known to be small[110]. Only a few pieces of evidence of a balanced electron/hole transport (i.e. electron mobility μ_n = hole mobility μ_p) have been provided so far[116,117,204].

On the other hand, ion migration has been studied early in halide perovskites. In 2014, Xiao et al. applied an electric field on a $CH_3NH_3PbI_3$ (MAPI) lateral structure reporting a switchable photovoltaic effect[237], later explained by ion migration[238,239]. Ion migration is also considered as the main culprit for the hysteretic behavior of PSC's [239–242]. Despite a great number of experimental observations, the physics behind such an ionic migration remains unclear[243]. Indeed, their activation energy is still debated, as well as the influence of grain boundaries and the impact of temperature and light[91,92,236]. The halide ions (I^-/Br^-) are mostly concerned, as organic MA^+ / FA^+ and inorganic Pb^{2+} are expected to drift on much longer time scales[91,92,243]

Overall, the complex interactions between ions, electrons and holes has been recently underlined, as excess charge-carrier have been shown to accelerate ion migration[244] and as iodide-induced defect creation has been theoretically derived[245]. Numerical drift-diffusion models taking into account both the motion of ionic species and electronic charge carriers have been proposed[246]. Recently, Snaith' research group showcased the incorporation of additive ionic salt $BMIBF_4$ as an efficient way to prevent ion migration, paving the way towards stable PSC[247].

In this chapter, we present a set of experiments under electric bias based on multi-dimensional luminescence imaging to probe the individual electronic transport as well the ionic one. Thanks to multi-dimensional imaging coupled with a proper sample design, we have been able to study lateral transport of charge carriers in hybrid mixed halide perovskites (chapters 4, 5). Besides, measuring the local variations of the luminescence signal under electric bias allows a direct access to charge carrier collection and transport properties for each kind of charge carrier. In a first set of experiments, we inhibit ion

105

migration by applying a pulsed electric bias and only observe the electronic transport (section 6.2). The ionic migration was activated in a second set of experiments where the bias was applied for a longer period of time (10 min). The use of a spectrally and spatially resolved systems allows us to acquire absolute I_{PL} images, and to image the quasi-Fermi level splitting $\Delta\mu$ as well as the bandgap E_g evolution during the bias exposure (section 6.3). We discuss the correlation between all these parameters and the link between non-radiative recombination pathways and ionic migration.

6.1. EXPERIMENTAL DETAILS

6.1.1. SAMPLE DESCRIPTION

The samples architecture is depicted in Figure 6-1(a-b). Firstly, a coplanar Au electric contacts was evaporated on a specific mask design made by UV lithography on a glass substrate, leaving a 20 µm channel between the gold electrodes. To prevent gold in-diffusion inside the perovskite layer[83], 50 nm of ITO were sputtered on top of the Au layer. Finally a double cation perovskite thin film ($FA_{0.83}MA_{0.17}$ Pb ($Br_{0.16}I_{0.84}$)$_3$) was deposited. Cross-section images displayed in Figure 6-1(c) confirm the conformal deposition on the lateral structure, and indicate a 800nm perovskite thickness.
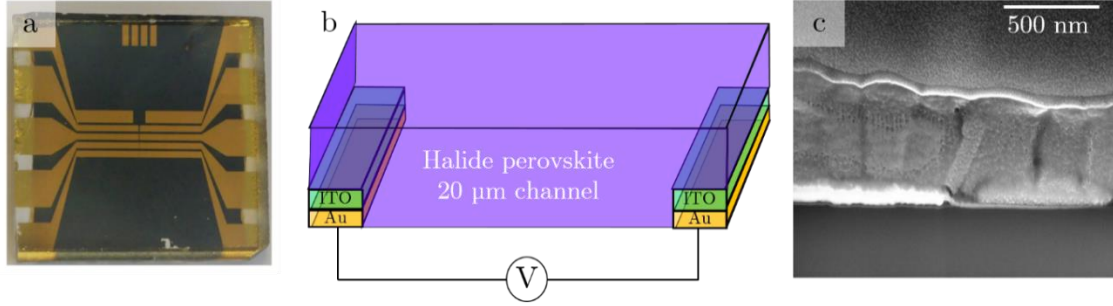
Figure 6-1 Structure of the perovskite channels (a) sample image through glass. Top channel width is 1 mm and serves as scale. (b) sketch of lateral structure inside the white circle in (a). (c) Cross-section image of the perovskite channel at the vicinity of the contact, where a double layer Au(shiny)/ITO is seen. The thickness of the perovskite layer is approx. 800nm, while the distance between electrical pads is 20µm. A double layer is deposited on top of perovskite for protection (Ti).

6.1.2. IMAGING SPECIFICS

For the time-resolved images, wide-field illumination was realized with pulsed laser Talisker with rather low frequency f_{las}=200kHz, and rather high fluence ϕ_0=5 10^{11} ph/cm^2/pulse. It is homogeneous on the surface imaged by the CCD sensor of the TR-FLIM. The photoluminescence is collected through a Nikon 100x objective. The PL is filtered through short-pass and long-pass filters (DMLP650R and FES750, Thorlabs). A pulsed electric field generated by a function generator AFG 3000 (Tektronix) is synchronized with laser illumination. The TR-FLIM is described in details in section 2.2. Snapshot acquisitions at t=0, 10 & 100 ns with different gain parameters at each time step, in order to get optimal image quality also at long times.

For the spectrally-resolved images, the sample is illuminated through an infinity-corrected X50 Nikon objective with numerical aperture of 0.8 (λ=532nm, $\Phi_0 \approx$ 1mW/cm^2) and the photoluminescence is collected through the same objective. The hyperspectral imager described in section 2.1 is used to obtain calibrated images of luminance. In the chosen experimental conditions, the acquisition of the data cube takes 40 s. Post-treatment of the data cubes includes a deconvolution and fit to the generalized Planck law, which are realized with a dedicated Matlab routine[26].

6.2. ELECTRON/HOLE TRANSPORT

6.2.1. FAST-BIAS TIME-RESOLVED IMAGING
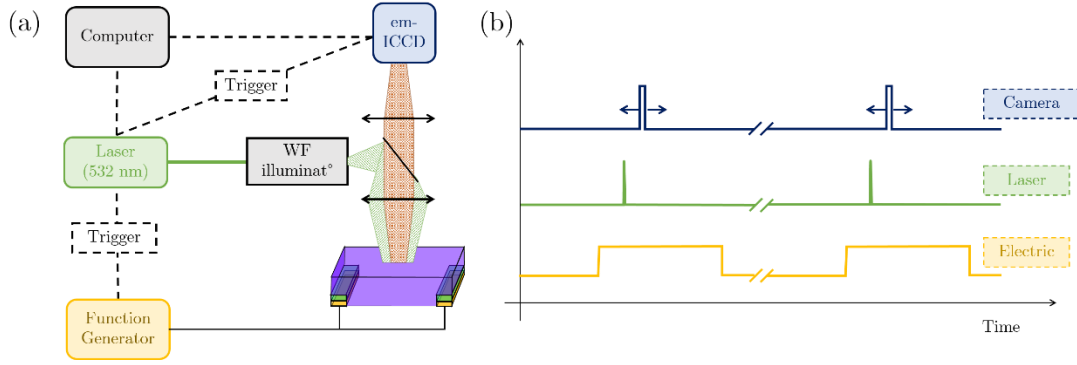
Figure 6-2 Sketch of the modified version of TR-FLIM (a) Sketch of the fast-bias time-resolved luminescence imaging set-up. (b) Sketch of the time sequence between laser pulse, electric pulse and camera gate openings.

In the following, we apply a wide-field pulsed illumination (λ=532nm) on the perovskite structure. The experimental set-up is displayed in Figure 6-2(a); it includes an intensified, time-gated, electron-multiplied CCD (em-ICCD) camera, a pulsed laser and a function generator. In order to spatially separate the electron and hole population after their homogeneous photo-generation, we applied a 5V potential resulting in a 2500 V/cm electric field across the channel, while recording time-resolved photoluminescence images $I_{\mathrm{PL}}(x,y,t)$. To avoid artefacts that might be caused by photon propagation - the sample could act as a waveguide as explained in section 5.3[23,216]- small energy photons are filtered out by an appropriate short pass filter. As ion migration would ultimately screen the electric field in a lateral structure, we have applied the electric potential for a short period of time (300 ns after each laser pulse). The sequence of the synchronization of the whole system is sketched in Figure 6-2(b) (i.e. the gate camera opening time, the laser pulse and the electrical pulse). Indeed, to allow the system to relax before the following excitation we switched off the bias for several micro-seconds (>5µs). Moreover, based on time-of-flight calculation realized with the highest mobility measured for $V_{\mathrm{I+}}$ vacancies (5x10^{-7} cm^2/V/s)[248], their mean displacement for a 300 ns-long bias would be around 3x10^{-6} µm, and it would take 1.6 s for them to cross the channel. It was also observed by time-resolved KPFM measurements that a few ms were necessary for the electric field to be screened in a 300nm-thick perovskite solar cell[249]. As a conclusion, the electric potential duration time is several orders of magnitude shorter than the typical ion migration time.

6.2.2. I_{PL} QUENCHING AT THE POSITIVE ELECTRODE
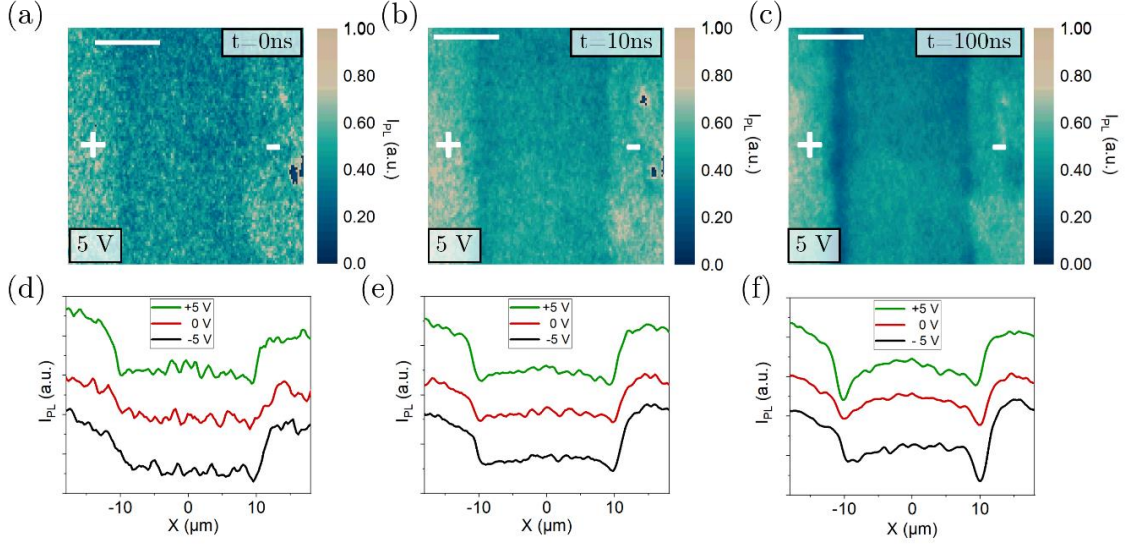
Figure 6-3 Summary of fast-bias experimental results (a)-(c) PL images at incremental time steps after the laser pulse (scaling bar 10μm). (d)-(f) Integration of the PL intensity along the y axis (parallel to the electrodes). Bias is applied on the left. A positive electric field is present for |x|<10μm for V=5V, and a negative electric field for V=-5V.

The luminescence signal is representative of the electronic carrier transport that we aim at investigating. We can interpret the intensity of the local PL signal $I_{\mathrm{PL}}(x,y,t)$ as the in-depth integrated local product of electron and hole concentrations[216] (similarly to section 4.3.4):

$$I_{\mathrm{PL}}(x,y,t) \propto \int_{z} n(x,y,z,t)\; p(x,y,z,t)\; \exp(-\alpha_{\mathrm{PL}}z)\; dz \tag{6-1}$$

In Figure 6-3(a)-(c) three time resolved PL image are shown, respectively at 0 ns, 10 ns and 100 ns after the laser excitation, while a 5V potential is applied on the left electrode. The PL signal appears globally more intense for the perovskite deposited on top of Au/ITO, probably due to the back-reflection of PL photons. The corresponding time-resolved profiles $I_{\mathrm{PL}}(x,t)$ are displayed in Figure 6-3(d)-(f) at 5V, -5V and 0V (integration over the y-axis). The 0 V profile, in which no electric field is applied across the channel, is used as reference. Noteworthy, also on 0 V profile, a PL drop at the edge of both contacts can be observed. We ascribe this behavior to a large trap density in this region composed by smaller grains, sometimes poorly interconnected. The PL profile inhomogeneities could be explained by a fast current extraction in this zone. We exclude this possibility by realizing a control experiment without connecting the contacts, similarly to an open-circuit condition. In both cases, 0 V and disconnected contacts, a similar drop at the edge was observed. A further proof is provided by the analysis of the I_{PL} over the whole sample, by comparing the I_{PL} on the zone of the stack Au/ITO/Pvk and on the zone of the bare perovksite thin film. We can notice that the signal appears more intense in the region Au/ITO/Pvk, in contrast with an efficient charge extraction which would lead to a dramatic quenching of the I_{PL}.

When a bias is applied, a progressive I_{PL} drop clearly appears, both at t=10ns and t=100ns, close to the positively biased edge of the channel (at x=-10 µm for V=5V). The reversibility of this effect was investigated by flipping the direction of the electric field: a symmetric trend is observed for the opposite bias (-5V). In addition, we have tested the system for an applied bias of ±2 V, for which a less evident I_{PL} drop appears at the positive electrode. We can thus conclude that there is a direct relation between I_{PL} drop and applied electric field intensity. Qualitatively, the electric field allows to dissociate charge carrier type (i.e. electron/hole). At the positively biased interface, holes are depleted while electrons accumulate, and *vice-versa* at the opposite electrode. For a purely ambipolar material with μ_p=μ_n, a symmetric I_{PL} profile across the channel would be expected, featuring a symmetric quenching for any bias. On the contrary, assuming μ_p>μ_n, an asymmetric signature on the I_{PL} profile appears as their accumulation and depletion are enhanced. We further evidence these behaviours by introducing 2D simulations realized by a master student (G. Vidon) with Silvaco Atlas in the next sub-section.

6.2.3. FITTING ELECTRON/HOLE MOBILITY

We have simulated and reported the two cases (μ_p>μ_n & μ_p=μ_n) with I_{PL} ratios in Figure 6-5(a), and the electron/hole concentration (for μ_p>μ_n) are mapped in cross-sectional view in Figure 6-4(b)-(c) at t=100ns. They illustrate the effect of the difference between electron and hole mobilities, which eventually impacts the radiative recombination, also shown in Figure 6-4-(d). It is remarkable that this impact on the I_{PL} intensity is sensitive to relatively small asymmetries in mobilities.
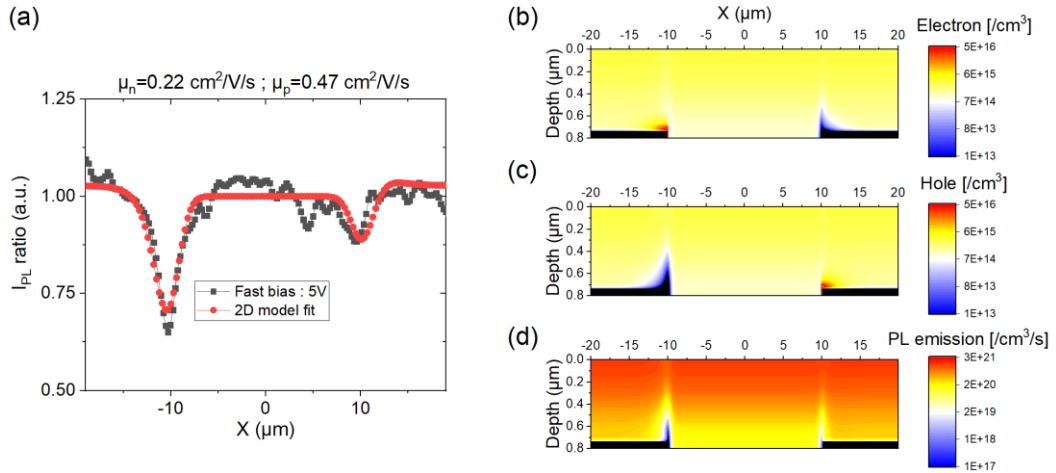
Figure 6-4 Summary of simulation results and fitting of electron/hole mobility (a) Ratio between I_{PL} profiles at t=100ns and t=10ns (dark line), displayed with the fitted curves (red line) for 5V application. (b) Electron concentration at t=100ns for the optimal set of parameters (c) hole concentration at t=100ns, (d) local PL emission at t=100ns. (b)-(d) are modeled with Silvaco Atlas.

In order to quantify the mobilities of electron and hole, a 2D drift-diffusion model is used (Silvaco Atlas). A Matlab routine allows the fitting of experimental data to the numerical outputs of the Silvaco simulation. The model reproduces the experimental

device in which $I_{PL}(x,y,t)$ is probed after a wide field pulsed illumination. The simulation takes into account lateral & in-depth diffusion, radiative and trap-assisted recombination as well as the influence of the applied bias (i.e. external electric field in the channel). Time-resolved radiative recombination maps were derived, and in-depth integrated profiles R_{rad} emitted by the perovskite layer are derived.

$$R_{rad}(x) = \int_{z=0}^{z_0} [R_{eh}\, np](x,z) \exp(-\alpha_{PL}z)\, dz \tag{6-2}$$

In addition to this in-depth integration, a spatial convolution is applied according to eq. (6-3) with convolution radius σ_{cv}=1µm, to account for the spatial resolution of the imaging system. This corresponds to the fact that too sharp I_{PL} spikes or cliffs would not be resolved by the system.

$$I_{PL}(x) = \frac{\int_{x'=0}^{x'=1} dx' \exp\left(-\frac{(x-x')^2}{2\sigma_{cv}^2}\right) \int_{z=0}^{z_0} [R_{eh}\, np](x',z) \exp(-\alpha_{PL}z)\, dz}{\int_{x'=0}^{x'=1} dx' \exp\left(-\frac{(x-x')^2}{2\sigma_{cv}^2}\right)} \tag{6-3}$$

In order not to be affected by optical artifacts (i.e. flatfield and light outcoupling), the fitting is considered for I_{PL} ratio at long and short time scale: $I_{PL}(x,t$=100ns$,V$=5V) / $I_{PL}(x,t$=10ns$,V$=5V) and $I_{PL}(x,t$=100ns$,V$=-5V) / $I_{PL}(x,t$=10ns$,V$=-5V). The only varying parameters for the fit are the electron and hole mobilities μ_n and μ_p, the other parameters were chosen according to previous work[187,216] in order to be close to the perovskite layers produced in our laboratory (R_{eh}^* and τ_n from section 5.4.2). The curves are fitted simultaneously, and the results are displayed as a superposition of experimental and best-fitted data in Figure 6-4(a) for V=5V. The reconstruction quality is as good for the control experiment realized at for V=-5V. We obtain an electron mobility of μ_n=0.22±0.01 cm^2/Vs and μ_p=0.47±0.02 cm^2/Vs, their ratio being μ_p/μ_n = 2.25±0.23. The model reproduces well the interesting features of the experimental curves, namely the deeps position and amplitude. However, our simulation does not take into account local lifetime inhomogeneities which are the main cause of the rapid variations observed on the experimental curve. A map of the evolution of the error as a function of the mobilities is given in Figure 6-5(c-d), attesting from the precision of the fitting procedure.

(a) Balanced transport $\mu_{\mathrm{n}}/\mu_{\mathrm{p}}$

(b) 10% variation of $\mu_{\mathrm{n}}/\mu_{\mathrm{p}}$

(c) Fit error for V=5V

(d) Fit error for V=-5V
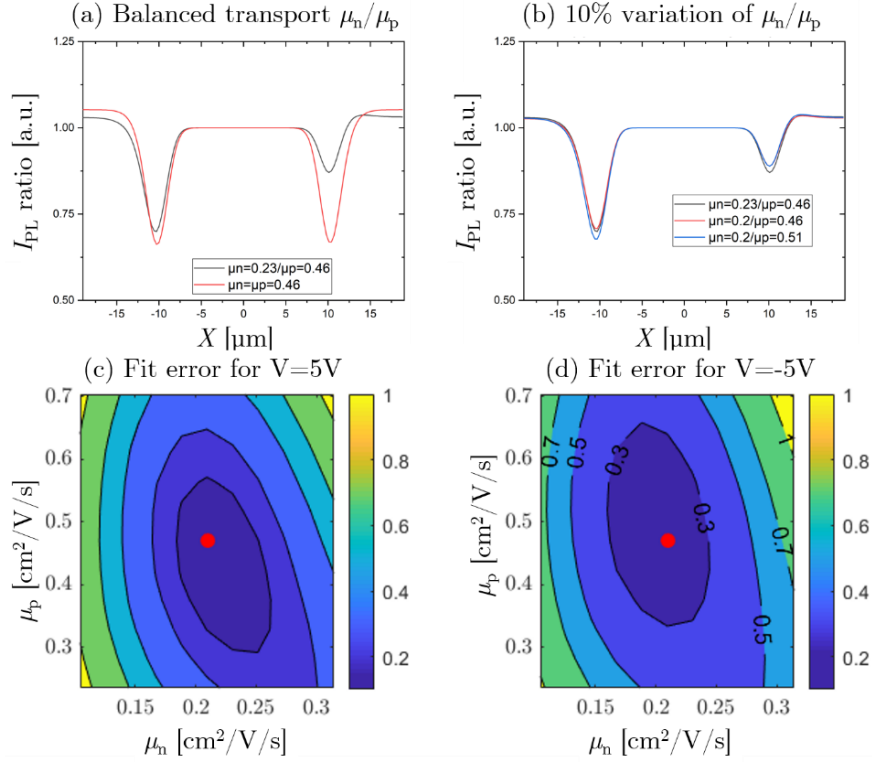
Figure 6-5 Variations of the PL ratio and reconstruction error for different couples (μ_n,μ_p).(a) I_{PL} ratio simulated for μ_n=μ_p=0.46 cm²/V/s and for μ_p =0.46 & μ_n=0.23 cm²/V/s. (b) I_{PL} ratio simulated for small variations of μ_n or μ_p around the fitted point. (c) Variations of the reconstruction error at V=5V .A lower reconstruction error indicates a better fit. A red point designates the optimal point. ((d) for opposite bias)

6.2.4. DISCUSSION & RELEVANCE

As a partial conclusion, we probed electron/hole transport via time-resolved PL imaging of lateral perovskite structure in a coplanar electric field. A pulsed bias was used (<1µs) to avoid any artefact induced by ion migration. This sheds new light on the frequently used assumption of an ambipolar transport in halide peroskites. Indeed, the direct measurements of both μ_{n} and μ_{p} are not common. Most of these measurements were based on time-of-flight principle and applied their bias on a time range sufficient for ions to screen the field[118,204], yielding $\mu_{\mathrm{p}}/\mu_{\mathrm{n}}$ ratios variating between 0.1 and 10 in MAPI[118], and a ratio of 1 on triple cation perovskite[9]. At lower temperature, where ion migration is freezed, ratios of $\mu_{\mathrm{p}}/\mu_{\mathrm{n}}$=1/3 could be measured in transistor structures based on MAPI (both values around 10^{-2} cm²/V/s)[250]. Our measured value of ($\mu_{\mathrm{p}}/\mu_{\mathrm{n}}$=2.25±0.23) is interestingly close to the one derived by DFT simulations in MAPI ($\mu_{\mathrm{p}}/\mu_{\mathrm{n}}$=1.5) [251]. As well, the absolute values for each mobility is remarkably close to values determines in the previous chapters, which attests for the consistency of this work.

6.3. ION MIGRATION AND DEFECT TRANSPORT

6.3.1. SLOW-BIAS HYPERSPECTRAL IMAGING

In order to observe the transport of ionic species which are slower than electrons and holes, we have performed a second experiment where we applied a 5 V bias for several minutes on the same sample architecture (see Figure 6-1(a)). The timing of the experiment is sketched in Figure 6-6. The bias time was chosen because halide ions and vacancies have been reported to drift on similar time scales. In MAPI, several reports give mobility values in the range of 10^{-10} to 10^{-7} cm^2/V/s for I$^-$ ions or V_{I+} vacancies [243,248,252,253] (yielding 20s to 300 minutes for them to cross a 20µm channel). However, I$^-$ is not the only ion concerned as in MAPbBr^3 single crystal, Br$^-$/V_{Br+} migration over 10 µm was observed after 20 minutes exposure to a similar electric field[254]. On the contrary, organic MA$^+$ / FA$^+$ / Pb^{2+} ions are expected to drift more slowly[91,92,243].
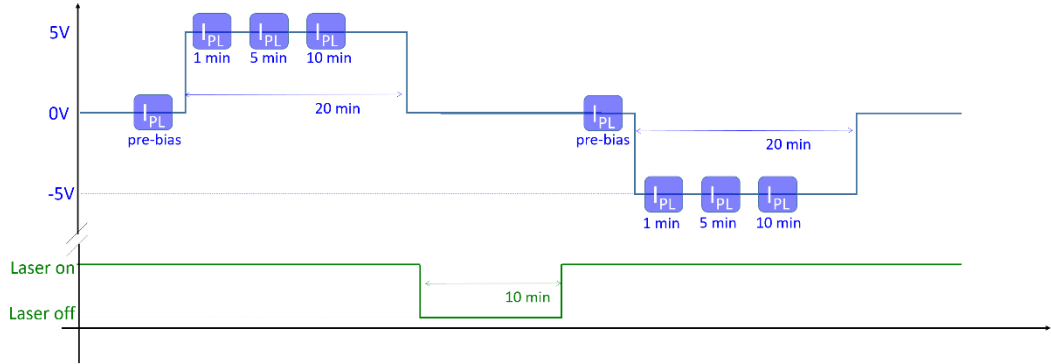
Figure 6-6 Temporal sketch of the slow bias experiment. A blue square indicates each HI acquistion

In this section, we use a hyperspectral imager leading to spectrally-resolved and absolute PL images (i.e. luminance images) of the channel. We then fit the full PL absolute emission spectrum at each spatial location using the generalized Planck law, according to the procedure described by Katahara *et al.*[21]. A typical experimental spectrum and its corresponding fit are displayed in Figure 6-7(b). The fitting procedure allows us to derive the local bandgap E_g and the quasi-Fermi level splitting $\Delta\mu$. While the former is mainly defined by I/Br ratio in mixed halide perovskite[54], the latter corresponds to the electrochemical potential difference of the charge carriers inside the absorber material (i.e. internal voltage). The difference between $\Delta\mu$ and E_g – in equation (6-4) and sketched in Figure 6-7(c) – gives an estimation of the non-radiative recombination current in the solar cell[255] and will be considered to highlight bias-induced defect formation.

$$\Delta(\Delta\mu - E_g) = \Delta\Delta\mu - \Delta E_g \qquad (6\text{-}4)$$

6.3.2. EVIDENCE OF ION MIGRATION

Three acquisitions are made: one just before the electric bias application (+5V) and two after 1 min and 5 min. More information about the timing of the experiment is displayed in Figure 6-6. On each of the three data, maps of the bandgap, of the quasi-Fermi level splitting $\Delta\mu$ and of the sub-bandgap absorption parameter E_u are determined[26]. Variations of the sub-bandgap absorption are not significant, also with exposition to light and bias. On the contrary, E_g and $\Delta\mu$ evolve significantly. To properly identify the effect of the electric bias we analyze differential maps for the bandgap (ΔE_g),

and for the quasi-Fermi level splitting ($\Delta\Delta\mu$). In this normalization process, the first acquisition just before bias exposure is taken as a reference and the derived parameters map (E_g(0V, 0min) or $\Delta\mu$(0V, 0min)) are subtracted from maps extracted from t=1min or t=5min acquisitions..
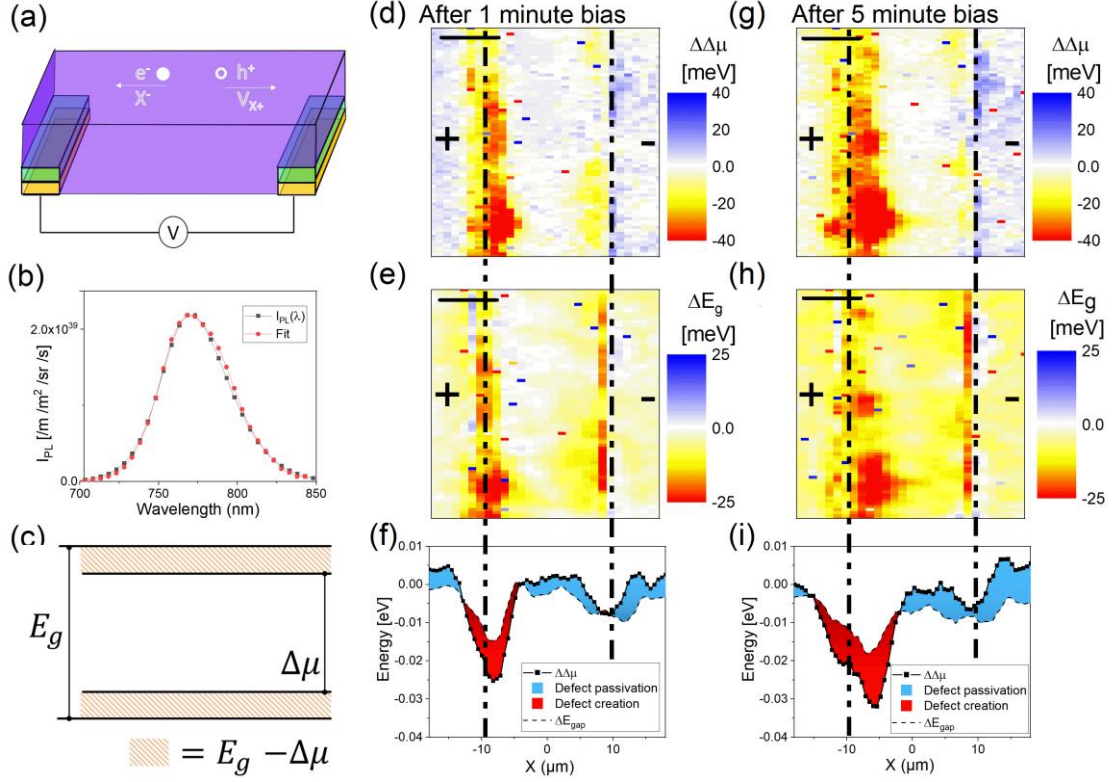
Figure 6-7 Summary of slow-bias experimental results on the HI(a) Sketch of the lateral structure investigated as a 5V bias is applied on the left electrode for 10 minutes. (b) PL spectrum taken at one pixel of the image, displayed with its fit to generalized Planck law. (c) Sketch of the band structure with bandgap E_g and quasi-Fermi level splitting $\Delta\mu$. After 1 minute of bias, we display the variation of quasi-Fermi level splitting $\Delta\Delta\mu$ in (d) (and after 5 min in (g)). The bandgap change ΔE_g image is also displayed in (e) after 1 min and after 5 min in (h). Finally, the bandgap ΔE_g change and quasi-Fermi level change are spatially averaged across the channel in (f) & (i). The defect creation can be assessed in (f) ((i) for t=5min), where negative values of $\Delta(\Delta\mu-E_g)$ appear red. (For details see text). Scale bar is 10 µm on the images.

We first look at the spatial variations of the bandgap. For instance to probe the change in the bandgap after 1min, we look at ΔE_g(5V,1min) = E_g(5V,1min) - E_g(0V,0min) as it is displayed in Figure 6-7(e). The situation after 5 minutes ΔE_g(5V,5min) is seen in Figure 6-7(h). After 1 minute of electric bias exposure under continuous illumination, the bandgap is slightly narrowed at the negative electrode, and strongly narrowed on the positive electrode. After 5 minutes the trend is enhanced: the red-shifted zone close to the positive electrode becomes wider. The bandgap modification is a clear indication that the electric bias induced a chemical change of the materials probably associated with the ionic migration. At the positive electrode, halide ions accumulate, while halide vacancies drift to the negative one. We suggest that the red shift is related to the local enrichment in iodine I^-, which is known to diminish E_g in mixed halide perovskite[54]. As a direct consequence, we suggest that I^- drifts faster than Br^- in the considered mixed halide

perovskite. If I⁻ were less mobile than Br⁻, an alternative scenario leading to an apparent bandgap narrowing remains possible. Indeed, Br⁻ could be accumulated at the positive electrode. The formed perovskite could segregate under illumination, whereby only the I-rich phase would be luminescing[87,256]. However, we tend to exclude this scenario as halide vacancies, which play a crucial role in this phase segregation[257], are repelled from the positive electrode.

6.3.3. CORRELATION TO DEFECT CREATION

We now correlate the bandgap variations to the electrochemical potential variations. In Figure 6-7(e)-(h), $\Delta\Delta\mu$ and ΔE_g profiles are extracted along the channel direction (x-axis). Both profiles show similar behaviors and are reduced in the vicinity of the positive electrode. Specifically, after one minute we noticed a drop of $\Delta\mu$ of 25 meV across 4 µm from the positive electrode (Figure 6-7(d)), and of 35 meV across 6 µm after 5 min of bias exposure (Figure 6-7(g)). Simultaneously, we have underlined a drop of E_g in the same area. As we mention previously a good indicator to quantify the defects creation[255] is the evolution of the difference between the quasi-Fermi level splitting and the bandgap : $\Delta(\Delta\mu\text{-}E_g)$. In the vicinity of the contact, the bandgap decreases ($\Delta E_g < 0$) and still we have negative values of $\Delta(\Delta\mu\text{-}E_g)$, which means that $\Delta\mu$ is not only affected by E_g but also by the creation of defects. This is highlighted in Figure 6-7(f)&(i) by the red zone. Therefore, there is a significant increase of non-radiative recombination at the positive electrode appearing within 5 min. Notably, no significant change appears around the positive electrode between 5 min and 10 min, as shown in Figure 6-9 (p.117). This indicates that the electric field is then screened by the charged species accumulated next to the positive electrode, and further strengthen the scenario in which charged species (halide ions) accumulate.

Outside of the defect creation zone, we observe a zone where the difference $\Delta(\Delta\mu\text{-}E_g)$ is positive and highlighted in blue in Figure 6-7(f)&(i). The lower non-radiative recombination current is not related to the electric field, as the same defect passivation is observed for the perovskite deposited on top of the electrodes, far away from any inter-electrode electric field. As well after 5 minutes, we can observe a global narrowing of the bandgap in Figure 6-7(h) (approx. 5 meV decrease), also coincident with a rise in $\Delta\mu$ (approx. 5meV). These values are consistent to what was observed under continuous light and ambient atmosphere elsewhere.[258]

An important control experiment consisted in applying an opposite bias on the same channel. The results are displayed in Figure 6-10: defects are created at the other electrode of the channel, which is then positively biased, and bandgap shifts are also observed. The reversibility of the ion migration is not complete and bandgap variations trends are not so pronounced.

6.3.4. SLOW-BIAS TIME-RESOLVED IMAGING

Also, the same long-time bias exposure has been realized under the TR-FLIM set-up. I_{PL} ratio profiles (similar as those used in Figure 6-4) are displayed in Figure 6-8. We

underline here that the spectral shifts due to bandgap change during the bias exposure are corrected by considering I_{PL} ratio. As displayed in the equations below, the E-dependence disappears as we have observed on a streak camera that $I_{\mathrm{PL}}(E)$ spectrum was unchanged between t=10ns & t=100ns. (section 2.3) The spectral sensitivity of the TR-FLIM set-up is called $f_{\mathrm{system}}(E)$ here under.

$$\frac{I_{\mathrm{PL}}(t\text{=100ns})}{I_{\mathrm{PL}}(t\text{=10ns})} = \frac{\int_{\mathrm{E}} f_{\mathrm{system}}(E)\, I_{\mathrm{PL}}\big(E\,,\ t\text{=100ns},\ t_{\mathrm{bias}}\text{=1min}\big)\ dE}{\int_{\mathrm{E}} f_{\mathrm{system}}(E)\, I_{\mathrm{PL}}\big(E\,,\ t\text{=10ns},\ t_{\mathrm{bias}}\text{=1min}\big)\ dE} \tag{6-5}$$

$$\frac{I_{\mathrm{PL}}(t\text{=100ns})}{I_{\mathrm{PL}}(t\text{=10ns})} = \frac{[R^{*}_{\mathrm{eh}}np](t\text{=100ns},\ t_{\mathrm{bias}}\text{=1min})}{[R^{*}_{\mathrm{eh}}np](t\text{=10ns},\ t_{\mathrm{bias}}\text{=1min})} \tag{6-6}$$

Now, for each bias direction, a drop appears near the positive electric contact after 1 minute of biasing. This drop is about 5 µm large, which is significantly higher than the 1µm-wide drop observed after fast-bias exposure. For the fast-bias experiment, this drop was due to electron/hole motion and was recovered as soon as the bias was turned off. In this slow-bias experiment, the decay at the positive electrode can be correlated to the defect creation created by halide ion motion. Due to these defects, the PL lifetime is locally lower, which ultimately results in a lower $I_{\mathrm{PL}}(t$=100ns$)/I_{\mathrm{PL}}(t$=10ns$)$ ratio.

As seen previously with the evolution of $\Delta(\Delta\mu\text{-}E_g)$, a few defect are created between t_{bias}=1 and t_{bias}=10min. Consistently, the I_{PL} ratio is almost unchanged between 1 and 10 min. This is explained by the progressive accumulation of charged species at the positive electrode, which tends to screen the electric field. Furthermore, the I_{PL} ratio profile remains almost constant at the positive edge some seconds after disconnecting the electric bias (Bias Off curve), while a drop appears on the other edge. This points out ionic effects, as accumulated electronic charges would migrate back immediately. The presence of the induced opposite electric field (the screening field), is thus also evidenced by the quenching at opposite edge. Eventually, recovery of the I_{PL} ratio profile after 10 min without electric field (in dark) proves the back migration of ions, or at least the passivation of the field-activated traps.

Similar field screening effects were observed previously in a MAPbI$_3$ channel[238], as well as on a hybrid mixed halide perovskite channel, in which it was attributed to the appearance of surface charge and to ionic migration[249]. Our observations are also consistent with previous reports from a progressive PL quenching at the positive electrode of a lateral contact structure[236,248,252,254]. This PL quenching could be suppressed by insulating the channel from the contact with a thin PMMA layer[259]. Henceforth, electrochemical reactions at the perovskite interface might induce the generation of non-radiative pathways at the vicinity of the electrode.
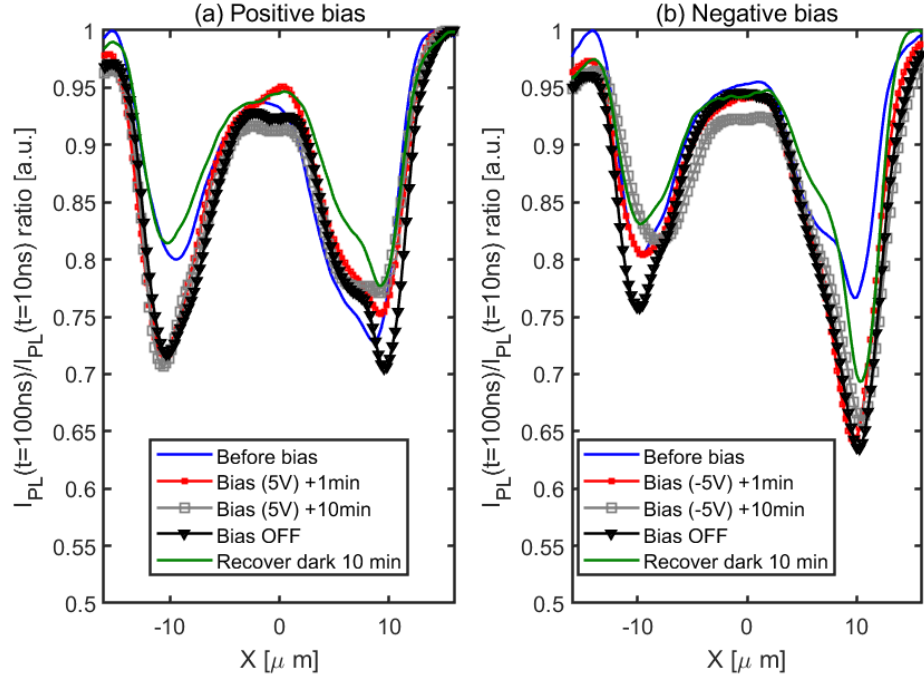
Figure 6-8 Summary of slow-bias experimental results on the TR-FLIM(a) Slow-bias (5V) application on the time-resolved set-up (similar timing as HI experiment) and resulting PL ratios between 10ns and 100ns after the laser pulse. (On the right) Control experiment with reverse bias is displayed

6.4.   CONCLUSION

By means of different multidimensional luminescence imaging techniques, we have studied the drift mechanisms in hybrid mixed halide perovskites. Time-resolved images with pulsed electric bias in the nanosecond time scale allow us to separate the individual contributions of electrons and holes in the transport mechanisms, without being impacted by ion migration. Carrier mobilities are determined to be around 0.3 cm^2/V/s, with a hole mobility for holes twice that of electrons. Thereafter, we apply a longer electric bias (>1 s) and highlight the key role played by ion migration in transport phenomena, as well as their impact on non-radiative recombination. We observe that the enrichment in halide induces local change in the chemical composition and lower the bandgap of the materials. Measurement of the quasi-Fermi level splitting indicates the formation of non-radiative pathways due to the accumulation of halide.
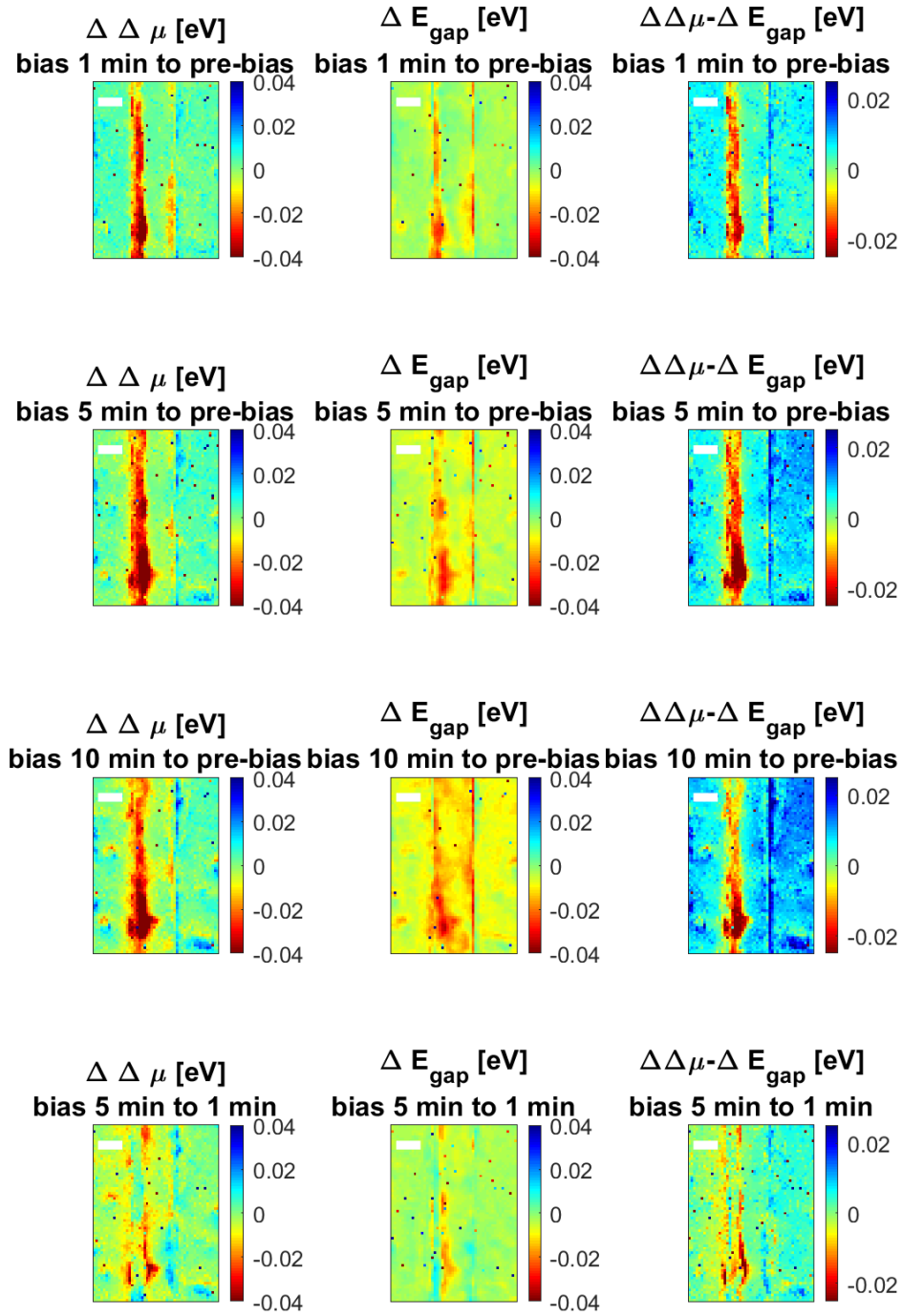
Figure 6-9 Optoelectronic parameters mapped for slow bias experiment (positive)Δμ evolution (first column), Bandgap evolution (second column), quasi-Fermi level splitting evolution corrected from bandgap variations Δ(Δμ-E_g) (third column). For 5V exposure, differential maps between 1 minute and pre-bias exposure (top row), between 5 min and pre-bias (second row), between 10 min and pre-bias (second row), between 5 minutes and 1 minute bias exposure (fourth row). Bias is applied on the left electrode for each image. Scaling bar is 10μm.
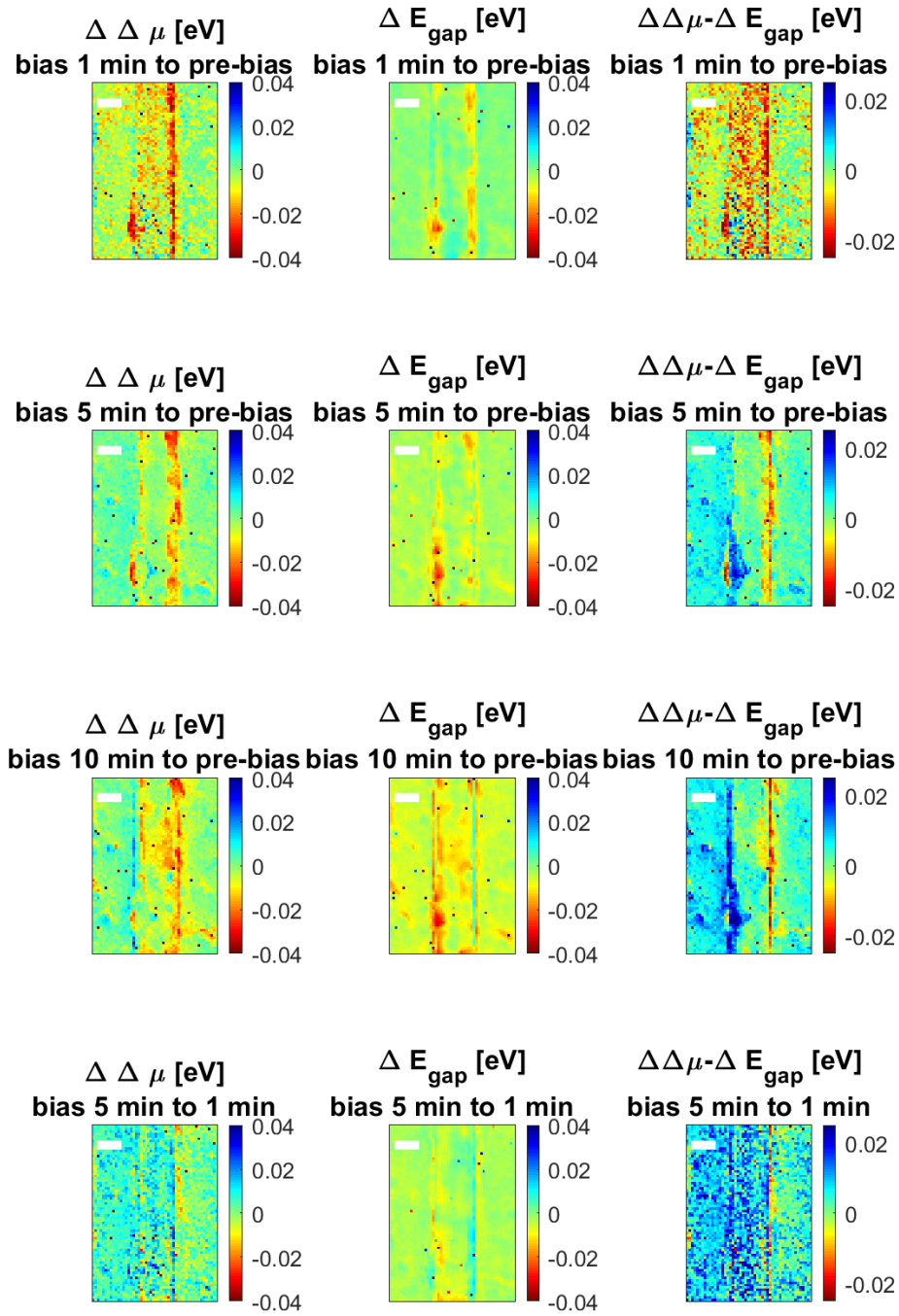
Figure 6-10 Optoelectronic parameters mapped for slow bias experiment (negative) Δμ evolution (first column), Bandgap evolution (second column), quasi-Fermi level splitting evolution corrected from bandgap variations Δ(Δμ-E_g) (third column). For -5V exposure, differential maps between 1 minute and pre-bias exposure (top row), between 5 min and pre-bias (second row), between 10 min and pre-bias (second row), between 5 minutes and 1 minute bias exposure (fourth row). Bias is applied on the left electrode for each image. Scaling bar is 10μm.

General conclusion

In this thesis, we have focused on describing optical methods to quantitatively assess charge carrier transport properties in photovoltaic absorbers and devices. The experimental investigation was based on multidimensional luminescence imaging techniques. They include spatial, spectral and temporal analysis of the light flux emitted by photovoltaic materials under excitation. Its implementation required the development of optical assemblies as well as digital methods of data processing. Two set-ups have been mostly used throughout this doctoral work: (i) the hyperspectral imager (HI), which provides access to spectrally-resolved images (one image per wavelength) and (ii) the time-resolved fluorescence imager (TR-FLIM) which outputs time-resolved images (one image per unit of time). While the HI was already fully assembled when this work began, the TR-FLIM set-up was at preliminary stage and its development was finished during the thesis. Its two main components are a pulsed laser and a fast camera. Its operating principles were thoroughly described, and its proof of concept on a reference photovoltaic cell (GaAs-based) was also presented. It demonstrated that TR-FLIM allows the assessment of charge transport and recombination properties with a single experiment. In particular, we could quantify the lateral charge transport in the device. We have shown how the use of wide-field illumination and collection allows to get rid of artefacts linked to local illumination. Furthermore, this wide-field illumination constitutes a realistic excitation scenario for photovoltaic materials and devices, due to its large area and relatively low power.

We then used these advanced characterization techniques to study charge transport in an emerging class of materials with very promising photovoltaic properties: halide perovskites. Throughout this manuscript, charge carrier diffusion in mixed cation halide perovskites have been brought to light thanks to several transport experiments. The first experiment was based on a large surface excitation, after which the charge carriers diffuse in-depth into the perovskite thin film. Therefore, we can probe the transport properties within the thickness of this layer. Remarkably it is possible to quantify the recombination at both the front and back surfaces as well as the recombination mechanisms within the bulk. The second experiment was based on a point excitation, following which the charge transport is essentially radial, at least after a certain time when we can neglect the in-depth diffusion. The carrier diffusion was distinguished from photon recycling, which constitutes a complementary transport mechanism whereby a luminescence photon is reabsorbed and regenerates a charge. Here again, the diffusion and recombination of charge carriers have been imaged with a high temporal and spectral resolution. This allowed to quantify them by means of optimization algorithms that fit the experimental results to the developed physical models (time-resolved diffusion equation).

Imaging methods are also adapted to the investigation of the impact of chemical and morphological inhomogeneities on local optoelectronic properties. This was illustrated by

the study of the influence of wrinkles appearing at the surface of Cs-rich perovskite. We noticed that morphological features change the light out-coupling properties, thereby hampering straightforward analysis of I_{PL} signal. We could still correlate chemical heterogeneities to bandgap and lifetime ones, which underlined the beneficial role of Cs-rich wrinkles in transport properties. Nonetheless, further development on the coupling between 2D-3D modeling and I_{PL} imaging should be conducted to obtain a proper quantification of transport in inhomogeneous materials.

Eventually, we have applied multidimensional I_{PL} imaging techniques to probe lateral structures featuring a 20µm wide perovskite channel in-between two electrodes. The main goal was to go further than our previous studies and separate the electron and hole transport properties which is difficult in such an intrinsic layer as perovskite. The stability of the material linked to ion migration had also to be considered. By applying a fast electric bias across the channel ($<$1µs), we first isolated the drift of charge carriers from that of the ions composing perovskite. Electron and hole mobilities were quantified separately (μ_p/μ_n=2.25$\pm$0.23). Their almost equal value justified their previous symmetrical (ambipolar) treatment. Then, experiments at longer time scale (electric field applied for 10 minutes) also allowed us to image the transport of halide ions. This multi-dimensional experiment brought us as close as ever to the operating principles of a PV device, which operates with light and bias. The accumulation of ions at the positive electrode leads to a local reduction in the lifetime of the charge carriers.

As a summary concerning transport in halide perovskite, we can state that interface recombination surely is the main loss channel in perovskite solar cells. This assertion gives precious orientations for the next synthetic approaches focusing on interface design. For what concerns charge transport in bulk perovskite, we systematically quantified relatively low values of charge carrier mobilities (between 0.2 and 1 cm^2/V/s), whereby the fundamental reason for this value remains unclear. In any case, this slow diffusion remains compensated by the long lifetime of charge carriers ($\approx$1µs), which guarantees their collection in a PV device. Two main pitfalls on the way to industrialization of perovskite solar cells remain - the stability of the devices and the up-scalability of fabrication techniques. The set of characterization techniques introduced in this manuscript would apply for a study tackling these issues. On the stability side, next measurement campaigns could focus on the evolution of optoelectronic properties as the material is exposed to environmental stresses (moisture, light, oxygen). On the upscaling side, the high versatility from the micro scale to the macro scale could allow to identify localize and circumvent the defects related to large scale production. Moreover, having spectrally and time-resolved images available at each step of the production/ageing triggers the need for efficient post-treatment algorithms, in which machine learning approaches could play a role.

To go deeper than these already refined study of charge transport in halide perovskites, a new set-up dedicated to 4D I_{PL} imaging was designed. It allows to acquire 4D I_{PL} data sets (2D spatial + spectral + temporal in a single experiment) by combining the concept

of single pixel imaging to a streak camera. As compared to a simple combination of HI and TR-FLIM setups, it allows having a better optical sensitivity (we here do not select both the energy and decay time of the signal) as well as a better time and spectral resolution. In this manuscript, we described its operating principles, which are protected by a filed patent, as well as its initial development realized with the help of a master student. A first proof of concept obtained on a perovskite layer was presented. It paved the way towards further advanced characterization of PV materials. Next developments of this set-up notably includes its calibration, thanks to which one could fit the acquired hypercube to the generalized Planck law, in order to map the QFLS with a picosecond resolution. This should unveil fundamental mechanisms of charge separation, transport, collection and recombination in the presence of electric field, or at hetero-interfaces, which is of high interest at the moment.

References

1   IEA (International Energy Agency), *World Energy Lookout*, 2018.

2   W. Shockley and H. J. Queisser, *J. Appl. Phys.*, 1961, 32, 510–519.

3   J.-F. Guillemoles, T. Kirchartz, D. Cahen and U. Rau, *Nat. Photonics*, 2019, 13, 501–505.

4   G. Carr, *Econ.*, 2012.

5   F. Oliva, S. Kretzschmar, D. Colombara, S. Tombolato, C. M. Ruiz, A. Redinger, E. Saucedo, C. Broussillou, T. G. de Monsabert, T. Unold, P. J. Dale, V. Izquierdo-Roca and A. Perez-Rodriguez, *Sol. Energy Mater. Sol. Cells*, 2016, 158, 168–183.

6   T. Trupke and R. A. Bardos, *Appl. Phys. Lett.*, 2006, 89, 044107.

7   NREL, Best Research-Cell Efficiencies, https://www.nrel.gov/pv/assets/images/efficiency-chart.png.

8   H. J. Snaith, *Nat. Mater.*, 2018, 17, 372–376.

9   Y. Rong, Y. Hu, A. Mei, H. Tan, M. I. Saidaminov, S. Il Seok, M. D. McGehee, E. H. Sargent and H. Han, *Science (80-.).*, 2018, 361, eaat8235.

10   J. Huang, Y. Yuan, Y. Shao and Y. Yan, *Nat. Rev. Mater.*, 2017, 2, 17042.

11   E. Becquerel, *Compte-rendus l'académie des Sci.*, 1839, 9, 561.

12   G. Kirchoff, *Ann. Phys.*

13   A. Einstein, in *The old quantum theory*, 1917, pp. 167–183.

14   W. van Roosbroeck and W. Shockley, *Phys. Rev.*, 1954, 94, 1558–1560.

15   E. H. Kennard, *Phys. Rev.*, 1918, 11, 29–38.

16   G. Lasher and F. Stern, *Phys. Rev.*

17   P. Würfel, *J. Phys. C Solid State Phys.*, 1982, 15, 3967–3985.

18   J. H. Lambert, *Photometria, sive de Mensura et gradibus luminis, colorum et umbrae*, 1760.

19   S. M. Sze and K. K. Ng, *Physics of semi-conductor devices*, John Wiley & Sons, 2006.

20   R. K. Ahrenkiel, D. J. Dunlavy, B. Keyes, S. M. Vernon, T. M. Dixon, S. P. Tobin, K. L. Miller and R. E. Hayes, *Appl. Phys. Lett.*, 1989, 55, 1088–1090.

21   J. K. Katahara and H. W. Hillhouse, *J. Appl. Phys.*, 2014, 116, 173504.

22 M. Maiberg, F. Bertram, M. Muller and R. Scheer, *J. Appl. Phys.*, 2017, 121, 085703.

23 L. M. Pazos-Outón, M. Szumilo, R. Lamboll, J. M. Richter, M. Crespo-Quesada, M. Abdi-Jalebi, H. J. Beeson, M. Vrućinić, M. Alsari, H. J. Snaith, B. Ehrler, R. H. Friend and F. Deschler, *Science (80-.).*, 2016, 351, 1430–1433.

24 T. Yamada, Y. Yamada, Y. Nakaike, A. Wakamiya and Y. Kanemitsu, *Phys. Rev. Appl.*, 2017, 7, 1–8.

25 F. Urbach, *Phys. Rev.*, 1953, 92, 1324.

26 N. Paul, V. Le Guen, D. Ory and L. Lombez, in *2017 IEEE 44th Photovoltaic Specialist Conference (PVSC)*, 2017, pp. 1–4.

27 D. König, K. Casalenuovo, Y. Takeda, G. Conibeer, J.-F. Guillemoles, R. Patterson, L. M. Huang and M. A. Green, *Phys. E*, 2010, 42, 2862–2866.

28 M. Li, J. Fu, Q. Xu and T. C. Sum, *Adv. Mater.*, 2018, 1802486, 1–17.

29 P. Drude, *Ann. Phys.*, 1900, 306, 566–613.

30 H. C. Casey and F. Stern, *J. Appl. Phys.*, 1976, 47, 631–643.

31 A. Einstein, *Ann. Phys.*, 1905, 322, 549–560.

32 D. Paget, F. Cadiz, A. C. H. Rowe, F. Moreau, S. Arscott and E. Peytavit, *J. Appl. Phys.*, 2012, 111, 123720.

33 P. Auger, *Compte-rendus l'académie des Sci.*, 1923, 177, 169–171.

34 L. Meitner, *Phys Z.*, 1922, 9, 131–144.

35 W. Shockley and W. T. Read, *Phys. Rev.*, 1952, 87, 835.

36 R. N. Hall, *Phys. Rev.*, 1952, 87, 387.

37 S. D. Stranks, V. M. Burlakov, T. Leijtens, J. M. Ball, A. Goriely and H. J. Snaith, *Phys. Rev. Appl.*, 2014, 2, 034007.

38 Q. Lin, Z. Wang, H. J. Snaith, M. B. Johnston and L. M. Herz, *Adv. Sci.*, 2018, 1700792, 1–8.

39 E. Edri, S. Kirmayer, S. Mukhopadhyay, K. Gartsman, G. Hodes and D. Cahen, *Nat. Commun.*, 2014, 5, 1–8.

40 P. J. Verlinden, M. Aleman, N. Posthuma, J. Fernandez, B. Pawlak, J. Robbelein, M. Debucquoy, K. Van Wichelen and J. Poortmans, *Sol. Energy Mater. Sol. Cells*, 2012, 106, 37–41.

41 U. Rau, *Phys. Rev. B*, 2007, 76, 085303.

42 C. Donolato, *Appl. Phys. Lett.*, 1985, 46, 270.

43 K. Toprasertpong, A. Delamarre, Y. Nakano, J. F. Guillemoles and M.

Sugiyama, *Phys. Rev. Appl.*, 2019, 11, 1.

44   U. Rau, B. Blank, T. C. M. Müller and T. Kirchartz, *Phys. Rev. Appl.*, 2017, 7, 44016.

45   D. B. Mitzi, C. A. Feild, W. T. A. Harrison and A. M. Guloy, *Nature*, 1994, 369, 467–469.

46   C. R. Kagan, D. B. Mitzi and C. D. Dimitrakopoulos, *Science (80-.)*., 1999, 286, 945–947.

47   A. Kojima, K. Teshima, Y. Shirai and T. Miyasaka, *J. Am. Chem. Soc.*, 2009, 131, 6050–6051.

48   N. K. Noel, S. D. Stranks, A. Abate, C. Wehrenfennig, S. Guarnera, A.-A. Haghighirad, A. Sadhanala, G. E. Eperon, S. K. Pathak, M. B. Johnston, A. Petrozza, L. M. Herz and H. J. Snaith, *Energy Environ. Sci.*, 2014, 7, 3061.

49   F. Hao, C. C. Stoumpos, D. H. Cao, R. P. H. Chang and M. G. Kanatzidis, *Nat. Photonics*, 2014, 8, 489–494.

50   N. Pellet, P. Gao, G. Gregori, T. Y. Yang, M. K. Nazeeruddin, J. Maier and M. Grätzel, *Angew. Chemie - Int. Ed.*, 2014, 53, 3151–3157.

51   V. D'innocenzo, A. R. S. Kandada, M. De Bastiani, M. Gandini and A. Petrozza, *J. Am. Chem. Soc.*, 2014, 136, 17730–17733.

52   Z. Yang, C. C. Chueh, P. W. Liang, M. Crump, F. Lin, Z. Zhu and A. K. Y. Jen, *Nano Energy*, 2016, 22, 328–337.

53   N. J. Jeon, J. H. Noh, W. S. Yang, Y. C. Kim, S. Ryu, J. Seo and S. Il Seok, *Nature*, 2015, 517, 476–480.

54   G. E. Eperon, S. D. Stranks, C. Menelaou, M. B. Johnston, L. M. Herz and H. J. Snaith, *Energy Environ. Sci.*, 2014, 7, 982.

55   M. Saliba, T. Matsui, J.-Y. Seo, K. Domanski, J.-P. Correa-Baena, M. K. Nazeeruddin, S. M. Zakeeruddin, W. Tress, A. Abate, A. Hagfeldt and M. Grätzel, *Energy Environ. Sci.*, 2016, 9, 1989–1997.

56   M. Saliba, T. Matsui, K. Domanski, J.-Y. Seo, A. Ummadisingu, S. M. Zakeeruddin, J.-P. Correa-Baena, W. Tress, A. Abate, A. Hagfeldt and M. Grätzel, *Science (80-.)*., 2016, 354, 206–209.

57   T. Duong, Y. L. Wu, H. Shen, J. Peng, X. Fu, D. Jacobs, E. C. Wang, T. C. Kho, K. C. Fong, M. Stocks, E. Franklin, A. Blakers, N. Zin, K. McIntosh, W. Li, Y. B. Cheng, T. P. White, K. Weber and K. Catchpole, *Adv. Energy Mater.*, 2017, 7, 1–11.

58   Z. Li, M. Yang, J.-S. Park, S.-H. Wei, J. J. Berry and K. Zhu, *Chem. Mater.*, 2016, 28, 284–292.

59   M. A. Green, A. Ho-Baillie and H. J. Snaith, *Nat. Photonics*, 2014, 8, 506–514.

60 S. Motti, T. Crothers, R. Yang, Y. Cao, R. Li, M. B. Johnston, J. Wang and L. M. Herz, *Nano Lett.*, 2019, 19, 3953–3960.

61 J. Byun, H. Cho, C. M. Wolff, A. Sadhanala, R. H. Friend, H. Yang and T. Lee, *Adv. Mater.*, 2016, 28, 7515–7520.

62 E. M. Sanehira, A. R. Marshall, J. A. Christians, S. P. Harvey, P. N. Ciesielski, L. M. Wheeler, P. Schulz, L. Y. Lin, M. C. Beard and J. M. Luther, *Sci. Adv.*, 2017, 3, eaao4204.

63 A. Swarnkar, A. R. Marshall, E. M. Sanehira, B. D. Chernomordik, D. T. Moore, J. A. Christians, T. Chakrabarti and J. M. Luther, *Science (80-.).*, 2016, 354, 92–95.

64 Q. A. Akkerman, G. Rainò, M. V. Kovalenko and L. Manna, *Nat. Mater.*, 2018, 1–12.

65 M. Abdi-Jalebi, Z. Andaji-Garmaroudi, S. Cacovich, C. Stavrakas, B. Philippe, J. M. Richter, M. Alsari, E. P. Booker, E. M. Hutter, A. J. Pearson, S. Lilliu, T. J. Savenije, H. Rensmo, G. Divitini, C. Ducati, R. H. Friend and S. D. Stranks, *Nature*, 2018, 555, 497–501.

66 D. J. Kubicki, D. Prochowicz, A. Hofstetter, S. M. Zakeeruddin, M. Grätzel and L. Emsley, *J. Am. Chem. Soc.*, 2017, 139, 14173–14180.

67 J. Beilsten-Edmands, G. E. Eperon, R. D. Johnson, H. J. Snaith and P. G. Radaelli, *Appl. Phys. Lett.*, 2015, 106, 173502.

68 J. E. Moser, *Nat. Mater.*, 2016, 16, 4–6.

69 T. Wang, B. Daiber, J. M. Frost, S. A. Mann, E. C. Garnett, A. Walsh and B. Ehrler, *Energy Environ. Sci.*, 2017, 10, 509–515.

70 F. Zheng, L. Z. Tan, S. Liu and A. M. Rappe, *Nano Lett.*, 2015, 15, 7794–7800.

71 J. M. Richter, K. Chen, A. Sadhanala, J. Butkus, J. P. H. Rivett, R. H. Friend, B. Monserrat, J. M. Hodgkiss and F. Deschler, *Adv. Mater.*, 2018, 1803379, 1803379.

72 D. W. deQuilettes, K. Frohna, D. Emin, T. Kirchartz, V. Bulovic, D. S. Ginger and S. D. Stranks, *Chem. Rev.*, , DOI:10.1021/acs.chemrev.9b00169.

73 G. E. Eperon, M. T. Hörantner and H. J. Snaith, *Nat. Rev. Chem.*, 2017, 1, 0095.

74 F. J. Ramos, S. Jutteau, J. Posada, A. Bercegol, A. Rebai, T. Guillemot, R. Bodeux, N. Schneider, N. Loones, D. Ory, C. Broussillou, G. Goaer, L. Lombez and J. Rousset, *Sci. Rep.*, 2018, 8, 16139.

75 J. Burschka, N. Pellet, S.-J. Moon, R. Humphry-Baker, P. Gao, M. K. Nazeeruddin and M. Grätzel, *Nature*, 2013, 499, 316–319.

76 N. J. Jeon, J. H. Noh, Y. C. Kim, W. S. Yang, S. Ryu and S. Il Seok, *Nat.*

Mater., 2014, 13, 897–903.

77   N. Ahn, D. Y. Son, I. H. Jang, S. M. Kang, M. Choi and N. G. Park, *J. Am. Chem. Soc.*, 2015, 137, 8696–8699.

78   Q. Chen, H. Zhou, Z. Hong, S. Luo, H.-S. Duan, H.-H. Wang, Y. Liu, G. Li and Y. Yang, *J. Am. Chem. Soc.*, 2014, 136, 622–625.

79   W. S. Yang, B.-W. Park, E. H. Jung, N. J. Jeon, Y. C. Kim, D. U. Lee, S. S. Shin, J. Seo, E. K. Kim, J. H. Noh and S. Il Seok, *Science (80-.).*, 2017, 356, 1376–1379.

80   Q. Chen, H. Zhou, Y. Fang, A. Z. Stieg, T.-B. Song, H.-H. Wang, X. Xu, Y. Liu, S. Lu, J. You, P. Sun, J. McKay, M. S. Goorsky and Y. Yang, *Nat. Commun.*, 2015, 6, 7269.

81   M. R. Leyden, Y.Jiang and Y. Qi, *J. Mater. Chem. A*, 2016, 4, 13125–13132.

82   C. Pareja-Rivera, A. L. Solís-Cambero, M. Sánchez-Torres, E. Lima and D. Solis-Ibarra, *ACS Energy Lett.*, 2018, 2366–2367.

83   C. C. Boyd, R. Cheacharoen, T. Leijtens and M. D. McGehee, *Chem. Rev.*, 2019, 119, 3418–3451.

84   G. Divitini, S. Cacovich, F. Matteocci, L. Cinà, A. Di Carlo and C. Ducati, *Nat. Energy*, 2016, 1, 15012.

85   R. Brenes, D. Guo, A. Osherov, N. K. Noel, C. Eames, E. M. Hutter, S. K. Pathak, F. Niroui, R. H. Friend, M. S. Islam, H. J. Snaith, V. Bulović, T. J. Savenije and S. D. Stranks, *Joule*, 2017, 1, 155–167.

86   R. E. Beal, D. J. Slotcavage, T. Leijtens, A. R. Bowring, R. A. Belisle, W. H. Nguyen, G. F. Burkhard, E. T. Hoke and M. D. McGehee, *J. Phys. Chem. Lett.*, 2016, 7, 746–751.

87   D. J. Slotcavage, H. I. Karunadasa and M. D. McGehee, *ACS Energy Lett.*, 2016, 1, 1199–1205.

88   C. G. Bischak, A. B. Wong, E. Lin, D. T. Limmer, P. Yang and N. S. Ginsberg, *J. Phys. Chem. Lett.*, 2018, 9, 3998–4005.

89   O. Almora, A. Guerrero and G. Garcia-Belmonte, *Appl. Phys. Lett.*, 2016, 108, 043903.

90   J. M. Frost and A. Walsh, *Acc. Chem. Res.*, 2016, 49, 528–535.

91   A. Senocrate and J. Maier, *J. Am. Chem. Soc.*, 2019, 141, 8382–8396.

92   A. Walsh and S. D. Stranks, *ACS Energy Lett.*, 2018, 3, 1983–1990.

93   G. Y. Kim, A. Senocrate, T. Y. Yang, G. Gregori, M. Grätzel and J. Maier, *Nat. Mater.*, 2018, 17, 445–449.

94   C. L. Davies, M. R. Filip, J. B. Patel, T. W. Crothers, C. Verdi, A. D. Wright,

R. L. Milot, F. Giustino, M. B. Johnston and L. M. Herz, *Nat. Commun.*, 2018, 9, 1–9.

95   A. Miyata, A. Mitioglu, P. Plochocka, O. Portugall, J. T.-W. Wang, S. D. Stranks, H. J. Snaith and R. J. Nicholas, *Nat. Phys.*, 2015, 11, 582–588.

96   K. Galkowski, A. Mitioglu, A. Miyata, P. Plochocka, O. Portugall, G. E. Eperon, J. T.-W. Wang, T. Stergiopoulos, S. D. Stranks, H. J. Snaith and R. J. Nicholas, *Energy Environ. Sci.*, 2016, 9, 962–970.

97   A. Mahboubi Soufiani, Z. Yang, T. Young, A. Miyata, A. Surrente, A. Pascoe, K. Galkowski, M. Abdi-Jalebi, R. Brenes, J. Urban, N. Zhang, V. Bulović, O. Portugall, Y.-B. Cheng, R. J. Nicholas, A. Ho-Baillie, M. A. Green, P. Plochocka and S. D. Stranks, *Energy Environ. Sci.*, 2017, 10, 1358–1366.

98   G. Xing, N. Mathews, S. Sun, S. S. Lim, Y. M. Lam, M. Gratzel, S. Mhaisalkar and T. C. Sum, *Science (80-.).*, 2013, 342, 344–347.

99   D. Shi, V. Adinolfi, R. Comin, M. Yuan, E. Alarousu, A. Buin, Y. Chen, S. Hoogland, A. Rothenberger, K. Katsiev, Y. Losovyj, X. Zhang, P. A. Dowben, O. F. Mohammed, E. H. Sargent and O. M. Bakr, *Science (80-.).*, 2015, 347, 519–522.

100   Y. Yamada, T. Yamada, L. Q. Phuong, N. Maruyama, H. Nishimura, A. Wakamiya, Y. Murata and Y. Kanemitsu, *J. Am. Chem. Soc.*, 2015, 137, 10456–10459.

101   E. M. Hutter, G. E. Eperon, S. D. Stranks and T. J. Savenije, *J. Phys. Chem. Lett.*, 2015, 6, 3082–3090.

102   J. M. Richter, M. Abdi-Jalebi, A. Sadhanala, M. Tabachnyk, J. P. H. Rivett, L. M. Pazos-Outón, K. C. Gödel, M. Price, F. Deschler and R. H. Friend, *Nat. Commun.*, 2016, 7, 13941.

103   C. Wehrenfennig, G. E. Eperon, M. B. Johnston, H. J. Snaith and L. M. Herz, *Adv. Mater.*, 2014, 26, 1584–1589.

104   M. B. Johnston and L. M. Herz, *Acc. Chem. Res.*, 2016, 49, 146–154.

105   W. Rehman, D. P. McMeekin, J. B. Patel, R. L. Milot, M. B. Johnston, H. J. Snaith and L. M. Herz, *Energy Environ. Sci.*, 2017, 10, 361–369.

106   X. Fu, K. J. Weber and T. P. White, *J. Appl. Phys.*, 2018, 124, 073102.

107   H. Do Kim and H. Ohkita, *Jpn. J. Appl. Phys.*, 2018, 57, 08RE03.

108   I. Levine, O. G. Vera, M. Kulbak, D.-R. Ceratti, C. Rehermann, J. A. Márquez, S. Levcenko, T. Unold, G. Hodes, I. Balberg, D. Cahen and T. Dittrich, *ACS Energy Lett.*, 2019, 1150–1157.

109   W. Tress, *Adv. Energy Mater.*, 2017, 7, 1602358.

110   D. A. Egger, A. Bera, D. Cahen, G. Hodes, T. Kirchartz, L. Kronik, R.

Lovrincic, A. M. Rappe, D. R. Reichman and O. Yaffe, *Adv. Mater.*, 2018, 1800691, 1–11.

111   W. J. Yin, T. Shi and Y. Yan, *Appl. Phys. Lett.*, 2014, 104, 063903.

112   N. Liu and C. Y. Yam, *Phys. Chem. Chem. Phys.*, 2018, 20, 6800–6804.

113   T. Kirchartz, T. Markvart, U. Rau and D. A. Egger, *J. Phys. Chem. Lett.*, 2018, 9, 939–946.

114   Y. Chen, H. T. Yi, X. Wu, R. Haroldson, Y. N. Gartstein, Y. I. Rodionov, K. S. Tikhonov, A. Zakhidov, X.-Y. Zhu and V. Podzorov, *Nat. Commun.*, 2016, 7, 12253.

115   R. Fan, Y. Huang, L. Wang, L. Li, G. Zheng and H. Zhou, *Adv. Energy Mater.*, 2016, 6, 1–32.

116   L. M. Herz, *ACS Energy Lett.*, 2017, 2, 1539–1548.

117   J. Peng, Y. Chen, K. Zheng and Z. Liang, *Chem. Soc. Rev.*, 2017, 46, 5714–5729.

118   B. Maynard, Q. Long, E. A. Schiff, M. Yang, K. Zhu, R. Kottokkaran, H. Abbas and V. L. Dalal, *Appl. Phys. Lett.*, 2016, 108, 173505.

119   Z. Guo, N. Zhou, O. F. Williams, J. Hu, W. You and A. M. Moran, *J. Phys. Chem. C*, 2018, 122, 10650–10656.

120   Z. Guo, J. S. Manser, Y. Wan, P. V. Kamat and L. Huang, *Nat. Commun.*, 2015, 6, 1–8.

121   J. M. Snaider, Z. Guo, T. Wang, M. Yang, L. Yuan, K. Zhu and L. Huang, *ACS Energy Lett.*, 2018, 1402–1408.

122   T. W. Crothers, R. L. Milot, J. B. Patel, E. S. Parrott, J. Schlipf, P. Muller-Buschbaum, M. B. Johnston and L. M. Herz, *Nano Lett.*, 2017, 17, 5782–5789.

123   S. D. Stranks, G. E. Eperon, G. Grancini, C. Menelaou, M. J. P. Alcocer, T. Leijtens, L. M. Herz, A. Petrozza and H. J. Snaith, *Science (80-.)*., 2013, 432, 341–344.

124   W. Tian, R. Cui, J. Leng, J. Liu, Y. Li, C. Zhao, J. Zhang, W. Deng, T. Lian and S. Jin, *Angew. Chemie - Int. Ed.*, 2016, 128, 13261–13265.

125   D. W. de Quilettes, W. Zhang, V. M. Burlakov, D. J. Graham, T. Leijtens, A. Osherov, V. Bulovic, H. J. Snaith, D. S. Ginger and S. D. Stranks, *Nat. Commun.*, 2016, 7, 11683.

126   F. Sahli, J. Werner, B. A. Kamino, M. Bräuninger, R. Monnard, B. Paviet-salomon, L. Barraud, L. Ding, J. J. D. Leon, D. Sacchetto, G. Cattaneo, M. Boccard, M. Despeisse, S. Nicolay, Q. Jeangros, B. Niesen and C. Ballif, *Nat. Mater.*, 2018, 17, 820–826.

127   H. J. Snaith, *Nat. Mater.*, 2018, 17, 372–376.

128   M. M. Lee, J. Teuscher, T. Miyasaka, T. N. Murakami and H. J. Snaith, *Science (80-.).*, 2012, 338, 643–647.

129   X. Lin, A. N. Jumabekov, N. N. Lal, A. R. Pascoe, D. E. Gómez, N. W. Duffy, A. S. R. Chesman, K. Sears, M. Fournier, Y. Zhang, Q. Bao, Y. B. Cheng, L. Spiccia and U. Bach, *Nat. Commun.*, , DOI:10.1038/s41467-017-00588-3.

130   T. Leijtens, G. E. Eperon, S. K. Pathak, A. Abate, M. M. Lee and H. J. Snaith, *Nat. Commun.*

131   G. Liu, B. Yang, B. Liu, C. Zhang, S. Xiao, Y. Yuan, H. Xie, D. Niu, J. Yang, Y. Gao and C. Zhou, *Appl. Phys. Lett.*, 2017, 111, 153501.

132   J. Cao, B. Wu, R. Chen, Y. Wu, Y. Hui, B. W. Mao and N. Zheng, *Adv. Mater.*, 2018, 30, 1–9.

133   P. Caprioglio, M. Stolterfoht, C. M. Wolff, T. Unold, B. Rech, S. Albrecht and D. Neher, *Adv. Energy Mater.*, 2019, 1901631.

134   G. El-Hajje, C. Momblona, L. Gil-Escrig, J. Ávila, T. Guillemot, J.-F. Guillemoles, M. Sessolo, H. J. Bolink and L. Lombez, *Energy Environ. Sci.*, 2016, 9, 2286–2294.

135   F. Staub, H. Hempel, J. C. Hebig, J. Mock, U. W. Paetzold, U. Rau, T. Unold and T. Kirchartz, *Phys. Rev. Appl.*, 2016, 6, 1–13.

136   J. Peng, Y. Wu, W. Ye, D. A. Jacobs, H. Shen, X. Fu, Y. Wan, T. Duong, N. Wu, C. Barugkin, H. T. Nguyen, D. Zhong, J. Li, T. Lu, Y. Liu, M. N. Lockrey, K. J. Weber, K. R. Catchpole and T. P. White, *Energy Environ. Sci.*, 2017, 10, 1792–1800.

137   F. Yang, H. E. Lim, F. Wang, M. Ozaki, A. Shimazaki, J. Liu, N. B. Mohamed, K. Shinokita, Y. Miyauchi, A. Wakamiya, Y. Murata and K. Matsuda, *Adv. Mater. Interfaces*, 2018, 5, 1–10.

138   C. S. Jiang, M. Yang, Y. Zhou, B. To, S. U. Nanayakkara, J. M. Luther, W. Zhou, J. J. Berry, J. Van De Lagemaat, N. P. Padture, K. Zhu and M. M. Al-Jassim, *Nat. Commun.*, 2015, 6, 1–10.

139   P. Schulz, *ACS Energy Lett.*, 2018, 3, 1287–1293.

140   S. Van Reenen, M. Kemerink and H. J. Snaith, *J. Phys. Chem. Lett.*, 2015, 6, 3808–3814.

141   S. A. L. Weber, I. M. Hermes, S. H. Turren-Cruz, C. Gort, V. W. Bergmann, L. Gilson, A. Hagfeldt, M. Graetzel, W. Tress and R. Berger, *Energy Environ. Sci.*, 2018, 11, 2404.

142   P. Lopez-Varo, J. A. Jiménez-Tejada, M. García-Rosell, S. Ravishankar, G. Garcia-Belmonte, J. Bisquert and O. Almora, *Adv. Energy Mater.*, 2018, 1702772, 1–36.

143   H. Tsai, R. Asadpour, J. C. Blancon, C. C. Stoumpos, O. Durand, J. W. Strzalka, B. Chen, R. Verduzco, P. M. Ajayan, S. Tretiak, J. Even, M. A. Alam, M. G. Kanatzidis, W. Nie and A. D. Mohite, *Science (80-.).*, 2018, 360, 67–70.

144   R. Brenes, C. Eames, V. Bulović, M. S. Islam and S. D. Stranks, *Adv. Mater.*, 2018, 30, 1–8.

145   R. J. Stoddard, F. T. Eickemeyer, J. K. Katahara and H. W. Hillhouse, *J. Phys. Chem. Lett.*, 2017, 8, 3289–3298.

146   A. Delamarre, UPMC Sorbonne Universités, 2013.

147   F. Gibelli, L. Lombez and J. Guillemoles, *J. Phys. Condens. Matter.*

148   A. Delamarre, M. Paire, J.-F. Guillemoles and L. Lombez, *Prog. Photovoltaics*, 2015, 23, 1305–1312.

149   A. Delamarre, L. Lombez and J. Guillemoles, *J. Photonics Energy2*, 2012, 2, 027004.

150   M. Legrand, Ecole Centrale de Lyon, 2019.

151   M. P. Edgar, G. M. Gibson and M. J. Padgett, *Nat. Photonics*, 2019, 13, 13–20.

152   M. F. Duarte, M. A. Davenport, D. Takbar, J. N. Laska, T. Sun, K. F. Kelly and R. G. Baraniuk, *IEEE Signal Process. Mag.*, 2008, 25, 83–91.

153   Y. Zhu, M. K. Juhl, T. Trupke and Z. Hameiri, *IEEE J. Photovoltaics*, 2017, 7, 1087–1091.

154   Z. Zhang, X. Wang, G. Zheng and J. Zhong, *Opt. Express*, 2017, 25, 19619–19639.

155   Princeton Instruments, *SpectraPro HRS Datasheet*, .

156   Hamamatsu, *C10910_InstructionManual(English)_118E*, .

157   V. Le Guen, N. Paul, D. Ory and L. Lombez, 1–4.

158   MATLAB, Solve 1-D parabolic and elliptic PDEs, https://fr.mathworks.com/help/matlab/ref/pdepe.html?, (accessed 18 October 2019).

159   MATLAB, Unconstrained nonlinear optimization algorithms, https://fr.mathworks.com/help/optim/ug/unconstrained-nonlinear-optimization-algorithms.html, (accessed 18 October 2019).

160   I. Ioffe, Gallium Arsenide Electronic and electrical Properties, http://www.ioffe.ru/SVA/NSM/Semicond/GaAs/electric.html#Recombination.

161   C. Honsberg and S. Bowden, Solving for Depletion Region, http://www.pveducation.org/pvcdrom/solving-for-depletion-region.

162   M. Maiberg and R. Scheer, *J. Appl. Phys.*, 2014, 116, 123711.

163   D. Hinken, K. Bothe, K. Ramspeck, S. Herlufsen and R. Brendel, *J. Appl. Phys.*, 2009, 105, 104516.

164   R. K. Ahrenkiel, *Solid State Electron.*, 1992, 35, 239–250.

165   B. M. Keyes, D. J. Dunlavy, R. K. Ahrenkiel, S. E. Asher, L. D. Partain, D. D. Liu and M. S. Kuryla, *J. Vac. Sci. Technol. A Vacuum, Surfaces, Film.*, 1990, 8, 2004–2008.

166   R. Brüggemann, *J. Phys. Conf. Ser.*, 2010, 253, 012081.

167   K. Chen, N. Sheehan, F. He, X. Meng, S. C. Mason, S. R. Bank and Y. Wang, *ACS Photonics*, 2017, 4, 1440–1446.

168   F. Cadiz, D. Paget, A. C. H. Rowe, T. Amand, P. Barate and S. Arscott, *Phys. Rev. B*, 2015, 91, 165203.

169   T. Dullweber, O. Lundberg, J. Malmström, M. Bodegard, L. Stolt, U. Rau, H. W. Schock and J. H. Werner, *Thin Solid Films*, 2001, 387, 11–13.

170   T. Gessmann and E. F. Schubert, *J. Appl. Phys.*, 2004, 95, 2203–2216.

171   D. Hinken, K. Ramspeck, K. Bothe, B. Fischer and R. Brendel, *Appl. Phys. Lett.*, 2007, 91, 89–92.

172   M. Paire, L. Lombez, J. F. Guillemoles and D. Lincot, *Thin Solid Films*, 2011, 519, 7493–7496.

173   R. J. Nelson and R. G. Sobers, *J. Appl. Phys.*, 1979, 49, 6103.

174   F. Cadiz, D. Paget, A. C. H. Rowe, V. L. Berkovits, V. P. Ulin, S. Arscott and E. Peytavit, *J. Appl. Phys.*, 2013, 114, 103711.

175   P. Gundel, F. D. Heinz, M. C. Schubert, J. A. Giesecke and W. Warta, *J. Appl. Phys.*, 2010, 108, 033705.

176   D. Kuciauskas, T. H. Myers, T. M. Barnes, S. A. Jensen and A. M. Allende Motz, *Appl. Phys. Lett.*, 2017, 110, 083905.

177   F. D. Heinz, J. A. Giesecke, L. E. Mundt, M. Kasemann and W. Warta, *J. Appl. Phys.*, 2015, 118, 5706.

178   A. Bercegol, G. El-Hajje, D. Ory and L. Lombez, *J. Appl. Phys.*, 2017, 122, 203102.

179   A. Edler, V. D. Mihailetchi, L. J. Koduvelikulathu, R. Kopecek and R. Harney, 2015, 620–627.

180   A. Marchioro, J. Teuscher, D. Friedrich, M. Kunst, R. van de Krol, T. Moehl, M. Grätzel and J.-E. Moser, *Nat. Photonics*, 2014, 8, 250–255.

181   B. Krogmeier, F. Staub, D. Grabowski, U. Rau and T. Kirchartz, *Sustain. Energy Fuels*, 2018, 2, 1027–1034.

182   Y. Yang, M. Yang, D. T. Moore, Y. Yan, E. M. Miller, K. Zhu and M. C. Beard, *Nat. Energy*, 2017, 2, 1–7.

183   T. Leijtens, S. D. Stranks, G. E. Eperon, R. Lindblad, E. M. J. Johansson, J. M. Ball, M. M. Lee, H. J. Snaith and I. J. Mcpherson, *ACS Nano*, 2014, 7147–7155.

184   M. Deepa, M. Salado, L. Calio, S. Kazim, S. M. Shivaprasad and S. Ahmad, *Phys. Chem. Chem. Phys.*, 2017, 19, 4069–4077.

185   S. Colella, E. Mosconi, P. Fedeli, A. Listorti, F. Gazza, F. Orlandi, P. Ferro, T. Besagni, A. Rizzo, G. Calestani, G. Gigli, F. De Angelis and R. Mosca, *Chem. Mater.*, 2013, 25, 4613–4618.

186   J. T.-W. Wang, Z. Wang, S. Pathak, W. Zhang, D. W. deQuilettes, F. Wisnivesky-Rocca-Rivarola, J. Huang, P. K. Nayak, J. B. Patel, H. A. Mohd Yusof, Y. Vaynzof, R. Zhu, I. Ramirez, J. Zhang, C. Ducati, C. Grovenor, M. B. Johnston, D. S. Ginger, R. J. Nicholas and H. J. Snaith, *Energy Environ. Sci.*, 2016, 9, 2892–2901.

187   A. Bercegol, F. J. Ramos, A. Rebai, T. Guillemot, D. Ory, J. Rousset and L. Lombez, *J. Phys. Chem. C*, 2018, 122, 24570–24577.

188   D. W. de Quilettes, S. M. Vorpahl, S. D. Stranks, H. Nagaoka, G. E. Eperon, M. E. Ziffer, H. J. Snaith and D. S. Ginger, *Science (80-.).*, 2015, 348, 683–686.

189   M. Maiberg, T. Hölscher, S. Zahedi-Azad and R. Scheer, *J. Appl. Phys.*, 2015, 118, 105701.

190   T. Duong, H. K. Mulmudi, H. Shen, Y. L. Wu, C. Barugkin, Y. O. Mayon, H. T. Nguyen, D. Macdonald, J. Peng, M. Lockrey, W. Li, Y. B. Cheng, T. P. White, K. Weber and K. Catchpole, *Nano Energy*, 2016, 30, 330–340.

191   J. W. Lee, D. H. Kim, H. S. Kim, S. W. Seo, S. M. Cho and N. G. Park, *Adv. Energy Mater.*, 2015, 5, 1501310.

192   Y. Sun, J. Peng, Y. Chen, Y. Yao and Z. Liang, *Sci. Rep.*, 2017, 7, 1–7.

193   W. K. Metzger, R. K. Ahrenkiel, J. Dashdorj and D. J. Friedman, *Phys. Rev. B - Condens. Matter Mater. Phys.*, 2005, 71, 1–9.

194   L. M. Pazos-Outon, M. Szumilo, R. Lamboll, J. M. Richter, M. Crespo-quesada, M. Abdi-jalebi, H. J. Beeson, M. Vrucinic, M. Alsari, H. J. Snaith, B. Ehrler, R. H. Friend and F. Deschler, *Science (80-.).*, 2016, 351, 1430–1434.

195   A. Redinger, S. Levcenko, C. J. Hages, D. Greiner, C. A. Kaufmann and T. Unold, *Appl. Phys. Lett.*, 2017, 110, 122104.

196   S. Garud, N. Gampa, T. G. Allen, R. Kotipalli, D. Flandre, M. Batuk, J. Hadermann, M. Meuris, J. Poortmans, A. Smets and B. Vermang, *Phys. Status Solidi a-Applications Mater. Sci.*, 2018, 1700826, 1–6.

197   A. Bercegol, B. Chacko, R. Klenk, I. Lauermann, M. C. Lux-Steiner and M. Liero, *J. Appl. Phys.*, 2016, 119, 155304.

133

198   A. G. Aberle, S. Glunz and W. Warta, *J. Appl. Phys.*, 1992, 71, 4422.

199   M. Kepenekian, R. Robles, C. Katan, D. Sapori, L. Pedesseau and J. Even, *ACS Nano*, 2015, 9, 11557–11567.

200   A. Marronnier, H. Lee, B. Geffroy, J. Even, Y. Bonnassieux and G. Roma, *J. Phys. Chem. Lett.*, 2017, 8, 2659–2665.

201   E. M. Hutter, M. C. Gélvez-Rueda, A. Osherov, V. Bulović, F. C. Grozema, S. D. Stranks and T. J. Savenije, *Nat. Mater.*, 2017, 16, 115–120.

202   T. Kirchartz and U. Rau, *J. Phys. Chem. Lett.*, 2017, 8, 1265–1271.

203   H.-S. Duan, H. Zhou, Q. Chen, P. Sun, S. Luo, T.-B. Song, B. Bob and Y. Yang, *Phys. Chem. Chem. Phys.*, 2015, 17, 112–116.

204   Y. Hu, E. M. Hutter, P. Rieder, I. Grill, J. Hanisch, M. F. Aygüler, A. G. Hufnagel, M. Handloser, T. Bein, A. Hartschuh, K. Tvingstedt, V. Dyakonov, A. Baumann, T. J. Savenije, M. L. Petrus and P. Docampo, *Adv. Energy Mater.*, 2018, 1703057, 1–11.

205   T. P. Weiss, B. Bissig, T. Feurer, R. Carron, S. Buecheler and A. N. Tiwari, *Sci. Rep.*, 2019, 9, 1–13.

206   V. S. Chirvony, K. S. Sekerbayev, D. Pérez-del-Rey, J. P. Martínez-Pastor, F. Palazon, P. P. Boix, T. I. Taurbayev, M. Sessolo and H. J. Bolink, *J. Phys. Chem. Lett.*, 2019, 5167–5172.

207   A. A. B. Baloch, F. H. Alharbi, G. Grancini, M. I. Hossain, M. K. Nazeeruddin and N. Tabet, *J. Phys. Chem. C*, 2018, 122, 26805–26815.

208   D. W. DeQuilettes, S. Jariwala, S. Burke, M. E. Ziffer, J. T. W. Wang, H. J. Snaith and D. S. Ginger, *ACS Nano*, 2017, 11, 11488–11496.

209   A. Olsson, D. J. Erskine, Z. Y. Xu, A. Schremer and C. L. Tang, *Appl. Phys. Lett.*, 1982, 41, 659–661.

210   A. Richter, M. Süptitz, D. Heinrich, C. Lienau, T. Elsaesser, M. Ramsteiner, R. Nötzel, K. H. Ploog, D. Heinrich, C. Lienau and T. Elsaesser, 1998, 2176, 10–13.

211   L. M. Smith, D. R. Wake, J. P. Wolfe, D. Levi, M. V Klein, J. Klem, T. Henderson and H. Morkoc, *Phys. Rev. B*, 1988, 38, 5788–5791.

212   M. Kulig, J. Zipfel, P. Nagler, S. Blanter, C. Schüller, T. Korn, N. Paradiso, M. M. Glazov and A. Chernikov, *Phys. Rev. Lett.*, 2018, 120, 207401.

213   M. A. Steiner, J. F. Geisz, I. García, D. J. Friedman, A. Duda and S. R. Kurtz, *J. Appl. Phys.*, 2013, 113, 0–11.

214   F. Staub, T. Kirchartz, K. Bittkau and U. Rau, *J. Phys. Chem. Lett.*, 2017, 8, 5084–5090.

215   Y. Fang, H. Wei, Q. Dong and J. Huang, *Nat. Commun.*, 2017, 8, 1–9.

216   A. Bercegol, D. Ory, D. Suchet, S. Cacovich, O. Fournier, J. Rousset and L. Lombez, *Nat. Commun.*, 2019, 10:1586.

217   H. Diab, C. Arnold, F. Lédée, G. Trippé-Allard, G. Delport, C. Vilar, F. Bretenaker, J. Barjon, J.-S. Lauret, E. Deleporte and D. Garrot, *J. Phys. Chem. Lett.*, 2017, 8, 2977–2983.

218   M. Ansari-Rad and J. Bisquert, *Phys. Rev. Appl.*, 2018, 10, 034062.

219   T. Yamada, T. Aharen and Y. Kanemitsu, *Phys. Rev. Lett.*, 2018, 120, 57404.

220   E. Yablonovitch, *J. Opt. Soc. Am.*, 1982, 72, 899–907.

221   I. Dursun, Y. Zheng, T. Guo, M. De Bastiani, B. Turedi, L. Sinatra, M. A. Haque, B. Sun, A. A. Zhumekenov, M. I. Saidaminov, F. P. García De Arquer, E. H. Sargent, T. Wu, Y. N. Gartstein, O. M. Bakr, O. F. Mohammed and A. V. Malko, *ACS Energy Lett.*, 2018, 3, 1492–1498.

222   I. L. Braly, W. Dane, L. M. Pazos-outón, S. Burke, M. E. Ziffer, D. S. Ginger and H. W. Hillhouse, *Nat. Photonics*.

223   S. D. Stranks, R. L. Z. Hoye, D. Di, R. H. Friend* and F. Deschler*, *Adv. Mater.*, 2018, 1803336.

224   M. Yang, Y. Zeng, Z. Li, D. H. Kim, C. Jiang, J. Van De Lagemaat and K. Zhu, *Phys. Chem. Chem. Phys.*, 2017, 19, 5043–5050.

225   T. Kirchartz, F. Staub and U. Rau, *ACS Energy Lett.*, 2016, 1, 731–739.

226   M. G. Abebe, A. Abass, G. Gomard, L. Zschiedrich, U. Lemmer, B. S. Richards, C. Rockstuhl and U. W. Paetzold, *Phys. Rev. B*, 2018, 98, 1–12.

227   D. Ory, A. Bercegol, D. Suchet, M. Legrand, J.-B. Puel, A. Michaud, A. Ben Slimane, S. Collin, S. Cacovich, O. Fournier, A. Rebai, J. Rousset, J.-F. Guillemoles and L. Lombez, in *46th IEEE Photovoltaics Specialists Conference*, 2019.

228   K. Lee, K. W. J. Barnham, J. S. Roberts, D. Alonso-Alvarez, N. P. Hylton, M. FAhrer and N. J. Ekins-Daukes, *IEEE J. Photovoltaics*, 2017, 7, 817–821.

229   A. Bercegol, F. J. Ramos, A. Rebai, T. Guillemot, J.-B. Puel, J.-F. Guillemoles, D. Ory, J. Rousset and L. Lombez, *J. Phys. Chem. C*, 2018, 122, 23345–23351.

230   K. Sveinbjörnsson, K. Aitola, J. Zhang, M. B. Johansson, X. Zhang, J. P. Correa-Baena, A. Hagfeldt, G. Boschloo and E. M. J. Johansson, *J. Mater. Chem. A*, 2016, 4, 16536–16545.

231   K. A. Bush, N. Rolston, A. Gold-Parker, S. Manzoor, J. Hausele, Z. Yu, J. A. Raiford, R. Cheacharoen, Z. C. Holman, M. F. Toney, R. H. Dauskardt and M. D. McGehee, *ACS Energy Lett.*, 2018, 3, 1225–1232.

232   S. Braunger, L. E. Mundt, C. M. Wolff, M. Mews, C. Rehermann, M. Jost, A. T. ESTEVES, D. Eisenhauer, C. Becker, J. A. G. Torres, E. Unger, L. Korte, D.

Neher, M. C. Schubert, B. Rech and S. Albrecht, *J. Phys. Chem. C*, 2018, 122, 17123–17135.

233   A. Delamarre, L. Lombez and J. F. Guillemoles, *Appl. Phys. Lett.*, 2012, 100, 131108.

234   E. M. Tennyson, J. M. Howard and M. S. Leite, *ACS Energy Lett.*, 2017, 2, 1825–1834.

235   G. Grancini, A. R. Srimath Kandada, J. M. Frost, A. J. Barker, M. De Bastiani, M. Gandini, S. Marras, G. Lanzani, A. Walsh and A. Petrozza, *Nat. Photonics*, 2015, 9, 695.

236   Y. C. Zhao, W. K. Zhou, X. Zhou, K. H. Liu, D. P. Yu and Q. Zhao, *Light Sci. Appl.*, 2017, 6, e16243-8.

237   Z. Xiao, Y. Yuan, Y. Shao, Q. Wang, Q. Dong, C. Bi, P. Sharma, A. Gruverman and J. Huang, *Nat. Mater.*, 2015, 14, 193–197.

238   D. Li, H. Wu, H. Cheng, G. Wang, Y. Huang and X. Duan, *ACS Nano*, 2016, 10, 6933–6941.

239   C. Li, S. Tscheuschner, F. Paulus, P. E. Hopkinson, J. Kießling, A. Köhler, Y. Vaynzof and S. Huettner, *Adv. Mater.*, 2016, 28, 2446–2454.

240   N. E. Courtier, J. M. Cave, J. M. Foster, A. B. Walker and G. Richardson, *Energy Environ. Sci.*, 2019, 12, 396–409.

241   G. Richardson, S. E. J. O. Kane, R. G. Niemann, T. A. Peltola, J. M. Foster, J. Cameron and A. B. Walker, *Energy Environ. Sci.*, 2016, 9, 1476–1485.

242   D. Moia, I. Gelmetti, P. Calado, W. Fisher, M. Stringer, O. Game, Y. Hu, P. Docampo, D. Lidzey, E. Palomares, J. Nelson and P. R. F. Barnes, *Energy Environ. Sci.*, 2019, 12, 1296–1308.

243   W. Tress, *J. Phys. Chem. Lett.*, 2017, 8, 3106–3114.

244   Y. Lin, B. Chen, Y. Fang, J. Zhao, C. Bao, Z. Yu, Y. Deng, P. N. Rudd, Y. Yan, Y. Yuan and J. Huang, *Nat. Commun.*, 2018, 9:4981.

245   F. De Angelis, *Nat. Mater.*, 2018, 17, 383–384.

246   N. E. Courtier, G. Richardson and J. M. Foster, *Appl. Math. Model.*, 2018, 63, 329–348.

247   S. Bai, P. Da, C. Li, Z. Wang, Z. Yuan, F. Fu, M. Kawecki, X. Liu, N. Sakai, J. T. W. Wang, S. Huettner, S. Buecheler, M. Fahlman, F. Gao and H. J. Snaith, *Nature*, 2019, 571, 245–250.

248   C. Li, A. Guerrero, S. Huettner and J. Bisquert, *Nat. Commun.*, 2018, 9, 5113.

249   S. A. L. Weber, I. M. Hermes, S. H. Turren-Cruz, C. Gort, V. W. Bergmann, L. Gilson, A. Hagfeldt, M. Graetzel, W. Tress and R. Berger, *Energy Environ. Sci.*,

2018, 11, 2404–2413.

250   X. Y. Chin, D. Cortecchia, J. Yin, A. Bruno and C. Soci, *Nat. Commun.*, 2015, 6, 1–9.

251   C. Motta, F. El-Mellouhi and S. Sanvito, *Sci. Rep.*, 2015, 5, 1–8.

252   C. Li, A. Guerrero, Y. Zhong, A. Gräser, C. A. M. Luna, J. Köhler, J. Bisquert, R. Hildner and S. Huettner, *Small*, 2017, 13, 1–10.

253   Y. Yuan, J. Chae, Y. Shao, Q. Wang, Z. Xiao, A. Centrone and J. Huang, *Adv. Energy Mater.*, 2015, 5, 1–7.

254   Y. Luo, P. Khoram, S. Brittman, Z. Zhu, B. Lai, S. P. Ong, E. C. Garnett and D. P. Fenning, *Adv. Mater.*, 2017, 29, 1–7.

255   R. King, D. Bhusari, A. Boca, D. Larrabee, X. Q. Liu, W. Hong, C. M. Fetzer, D. C. Law and N. H. Karam, *Prog. Photovoltaics Res. Appl.*, 2011, 19, 797–812.

256   S. J. Yoon, S. Draguta, J. S. Manser, O. Sharia, W. F. Schneider, M. Kuno and P. V Kamat, *ACS Energy Lett.*, 2016, 1, 290–296.

257   S. J. Yoon, M. Kuno and P. V Kamat, *ACS Energy Lett.*, 2017, 2, 1507–1514.

258   C. Stavrakas, A. A. Zhemekenov, R. Brenes, M. Abdi-Jelabi, V. Bulovic, O. M. Bakr, E. S. Barnard and S. D. Stranks, *Energy Environ. Sci.*, 2018, 11, 2846–2852.

259   S. T. Birkhold, J. T. Precht, H. Liu, R. Giridharagopal, G. E. Eperon, L. Schmidt-Mende, X. Li and D. S. Ginger, *ACS Energy Lett.*, 2018, 3, 1279–1286.

Résumé en langue française

Chapitre 0 : Introduction

Les dispositifs photovoltaïques (PV) convertissent directement la lumière en électricité, offrant une solution indispensable pour atteindre les objectifs climatiques et progresser vers une économie sobre en carbone. En effet, la consommation d'électricité de l'humanité en 2018 pourrait être compensée par la production de 100 000 km^2 de panneaux photovoltaïques (0,07% de la surface de la Terre). L'Agence Internationale de l'Énergie (IEA) prévoit que l'énergie photovoltaïque dépassera l'énergie éolienne en 2025, l'hydroélectricité en 2030 et le charbon en 2040 (en termes de capacité installée). Ceci est dû non seulement à son coût de production en diminution constante, mais également à l'augmentation continue du rendement de conversion d'énergie (PCE) au cours des dernières décennies. L'influence des deux facteurs est explicite dans la Figure R1 (a), qui affiche le prix moyen du module (en USD / Watt de pointe) en fonction des expéditions cumulées. Pour approcher la limite théorique du rendement de conversion d'énergie, qui est d'environ 31% dans les dispositifs classiques et d'environ 47% dans les dispositifs tandem combinant deux matériaux absorbants, il est crucial de travailler à la fois sur les performances électroniques et optiques, affectant à la fois puissance de sortie.

Dans cette thèse, nous nous concentrons sur les matériaux et les dispositifs photovoltaïques produits à l'Institut du Photovoltaïque d'Ile-de-France (IPVF). Cet institut de recherche vise notamment à développer des cellules solaires tandem. Elles consistent en la superposition d'une cellule solaire en silicium, déjà mature sur le plan industriel, qui collecte efficacement les photons dans le proche infrarouge (NIR) et d'une autre cellule solaire avec un absorbeur à bande interdite plus large. Plusieurs matériaux et architectures de dispositifs sont actuellement à l'étude, mais ils devraient convertir plus efficacement les photons énergétiques (bleu, UV) et transmettre les photons rouges / NIR à la cellule inférieure (Si). Ceci est esquissé à la Figure R1(b), dans laquelle le spectre de puissance de chaque cellule est représenté, ainsi que le spectre de puissance disponible dans le rayonnement solaire incident à la surface de la Terre.
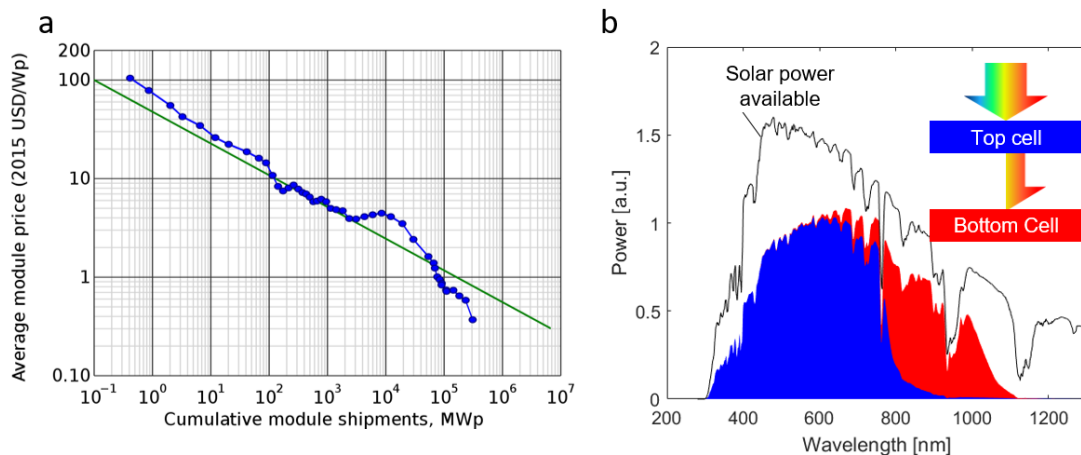

Figure R1 (a) La production de modules (ligne bleue) est fittée par la ligne verte qui montre que le prix du module diminue de 20% pour chaque doublement des expéditions cumulées (également appelée la loi de Swanson). (b)

En optoélectronique, et en particulier dans le domaine de la photovoltaïque, des méthodes d'analyse par photoluminescence (I_{PL}) sont utilisées pour optimiser les dispositifs. Sans contact et non destructifs, ils peuvent être utilisés à différentes étapes du cycle de vie d'une cellule solaire, de la croissance (in situ) à l'utilisation (in-operando). Par exemple, leur utilisation pour des contrôles de qualité en ligne pendant la production ou pour la détection de défauts sur des champs photovoltaïques est déjà rapportée. Les méthodes d'analyse I_{PL} sont basées sur le fait que l'intensité de la luminescence est directement liée au produit des concentrations de porteurs de charge (électron / trou). Ils constituent donc un puissant outil de caractérisation des mécanismes de transport de charges (voir chapitre 1). Dans cette thèse, nous nous concentrons sur la description de méthodes basées sur l'imagerie multidimensionnelle par luminescence. Cette technique comprend l'analyse spatiale, spectrale et temporelle du flux lumineux émis par des matériaux photovoltaïques sous excitation. Sa mise en œuvre nécessite le développement d'assemblages optiques ainsi que de méthodes numériques de traitement de données.

Deux configurations ont été principalement utilisées tout au long de cette thèse: (i) l'imageur hyperspectral (HI, section 2.1), qui donne accès à des images résolues spectralement (une image par longueur d'onde) et (ii) la TR-FLIM (section 2.2) qui produit des images résolues en temps (une image par unité de temps). Alors que le HI était déjà complètement assemblé au début de ces travaux, le montage de TR-FLIM était à peine assemblé et son développement s'est achevé au cours de la thèse. Ses deux composants principaux sont un laser pulsé et une caméra rapide. Ses principes de fonctionnement sont décrits en détail et sa preuve de concept sur un matériau photovoltaïque de référence (GaAs) est également présentée (chapitre 3). Il démontre que la TR-FLIM permet l'évaluation des propriétés de transport et de recombinaison avec une seule expérience. Nous montrerons comment l'utilisation de l'éclairage et de la collecte à grand champ (WF) permet de supprimer les artefacts liés à la microscopie optique classique (par exemple, la microscopie confocale). Ces artefacts sont induits par le transport de charges en dehors de la zone d'éclairage. En outre, cet éclairage WF constitue un scénario d'excitation réaliste pour les matériaux et les dispositifs PV, en raison de sa grande surface et de sa puissance relativement faible. Pour aller plus loin que ces études déjà poussées du transport de charges dans les pérovskites aux halogénures, une nouvelle configuration dédiée à l'imagerie I_{PL} 4D a été conçue et est en cours de développement (section 2.3). Il permet d'acquérir des ensembles de données I_{PL} 4D (2D spatiales + spectrale + temporelle) en combinant le concept d'imagerie à pixel unique à une caméra à balayage de fente. Dans ce manuscrit, nous décrirons ses principes de fonctionnement, protégés par un brevet déposé, ainsi que son développement initial réalisé avec l'aide d'une stagiaire de master. Une première preuve de concept obtenue sur une couche de pérovskite sera présentée.

Ces techniques de caractérisation avancées permettent notamment d'étudier le transport de charges dans une classe émergente de matériaux aux propriétés photovoltaïques très prometteuses: les pérovskites aux halogénures. Les cellules solaires dotées d'absorbeurs de pérovskite ont en effet connu une augmentation considérable en termes de PCE au cours de la dernière décennie, alors qu'elles étaient fabriquées avec des matières premières abondantes et bon marché et utilisaient un faible budget thermique lors de leur production. Néanmoins, les facteurs limitants empêchant leur commercialisation sont l' « upscale » des techniques de fabrication et la stabilité à long terme des dispositifs. En effet, la physique fondamentale et les différentes propriétés de transport des pérovskites aux halogénures n'ont toujours pas été pleinement comprises et décrites (section 1.3). Tout au long de ce manuscrit, plusieurs expériences de transport permettent de mettre en lumière la diffusion de porteurs de charge dans des pérovskites à halogénures de cations mixtes. Cette diffusion sera également distinguée du recyclage des photons, qui constitue un mécanisme de transport complémentaire par lequel un photon de luminescence est réabsorbé et régénère une charge. La première expérience est basée sur une excitation de surface, après laquelle les porteurs de charge diffusent en profondeur dans le film mince de pérovskite (chapitre 4). La deuxième expérience est basée sur une excitation ponctuelle, à la suite de laquelle le transport de charge est essentiellement radial (chapitre 5). Dans les deux cas, la diffusion et la recombinaison des porteurs de charge sont imagées avec une résolution temporelle et spectrale élevée. Cela devrait permettre de quantifier leur impact au moyen d'algorithmes d'optimisation en fittant les résultats expérimentaux aux modèles physiques (équation de continuité).

Les méthodes d'imagerie sont également adaptées à l'étude de l'impact des inhomogénéités chimiques et morphologiques sur les propriétés optoélectroniques locales. Ceci sera illustré par l'étude de l'influence des rides apparaissant à la surface de la pérovskite riche en Cs (section 5.5).

Enfin, nous utiliserons des techniques d'imagerie multidimensionnelles pour sonder les structures latérales comportant un canal de pérovskite de 20 µm de large entre deux électrodes (chapitre 6). En appliquant une polarisation électrique rapide sur le canal (<1 µs), nous isolons la dérive des porteurs de charge de celle des ions composant la pérovskite. Des expériences à plus grande échelle de temps (champ électrique appliqué pendant 10 minutes) nous permettront également de visualiser le mouvement des ions halogénures. Cette expérience multidimensionnelle devrait nous amener au plus près des principes de fonctionnement d'un dispositif PV, qui fonctionne avec lumière et champ électrique.

Chapitre 1 : Contexte scientifique

L'analyse des signaux de luminescence émis par les matériaux photovoltaïques est au cœur de la thèse présentée. Si on considère un volume V (d'indice optique n_{opt}) avec une concentration homogène de porteurs de charge excités n (potentiel $E_{f,n}$) & p (potentiel $E_{f,p}$) à la température T, on peut exprimer l'émission spontanée R_{sp} sous forme de densité de photons par énergie par angle solide Ω, où l'isotropicité de R_{sp} explique le facteur

1/4π. L'écart entre les quasi-niveaux de Fermi ($\Delta\mu$=$E_{f,n}$-$E_{f,p}$) apparait dans la formule. Il représente le potentiel chimique emmagasiné dans le matériau sous éclairement. Sa valeur sous un éclairement de 1 soleil borne la tension de court-circuit V_{oc} de la cellule photovoltaïque éventuellement construite avec ce matériau.

$$R_{sp}(E,\Omega) = \frac{n_{opt}^3}{4\pi\bar{h}^3\pi^2c^3}\frac{a(E)E^2}{\exp\left(\frac{E-\Delta\mu}{k_BT}\right)-1} \tag{R-1}$$

Avoir une expression appropriée pour l'absorptivité $a(E)$ du volume considéré est maintenant nécessaire pour extraire les propriétés optoélectroniques des mesures I_{PL}. Dans cette thèse, nous nous appuyons sur Katahara *et al.* qui ont permis un traitement des spectres prenant en compte l'absorption sous-bande interdite. Dans la section 1.1.3, les formules décrivant $a(E)$ en fonction du gap E_g, et de la décroissance des états sous le gap sont données. Ces considérations nous laissent avec 6 paramètres libres pour décrire un spectre $I_{PL}(E)$ et nous donnons ici un bref aperçu de leur influence. Pour ce faire, nous calculons le spectre I_{PL} émis par une couche semi-conductrice à l'aide des équations (1-5), (1-8) et (1-10). Plus précisément, nous effectuons une variation de paramètre autour des valeurs attendues pour la pérovskite, qui est le matériau le plus étudié dans cette thèse. Même si ces paramètres peuvent parfois être corrélés, nous modifions un paramètre à la fois dans un souci de simplicité. Le résultat est présenté dans la figure R2 et commenté en anglais dans la section 1.1.4.
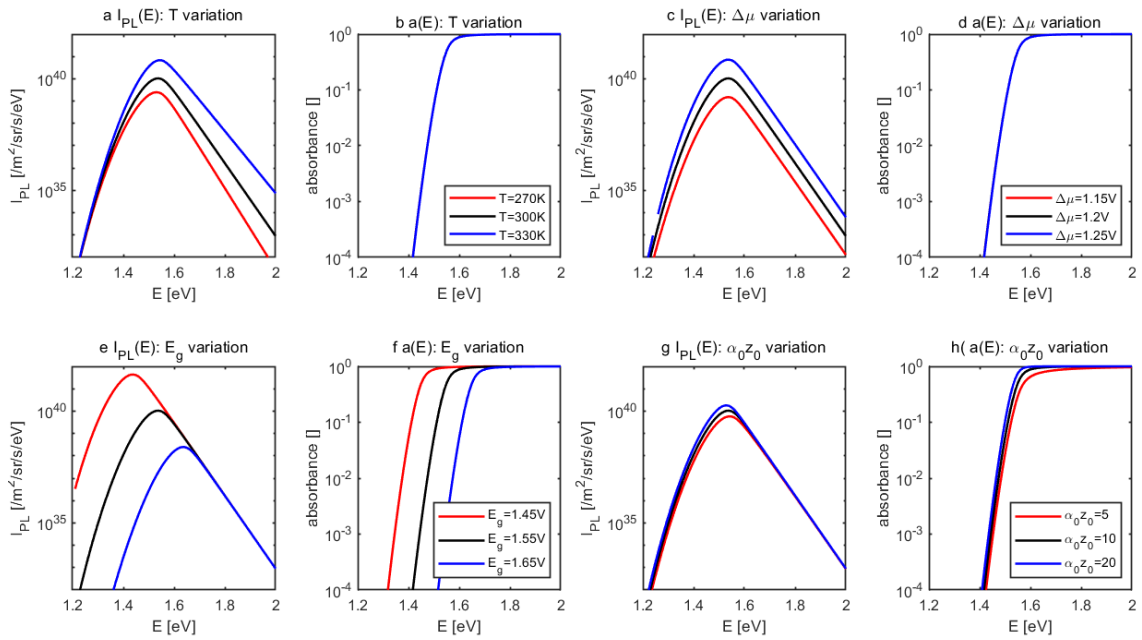
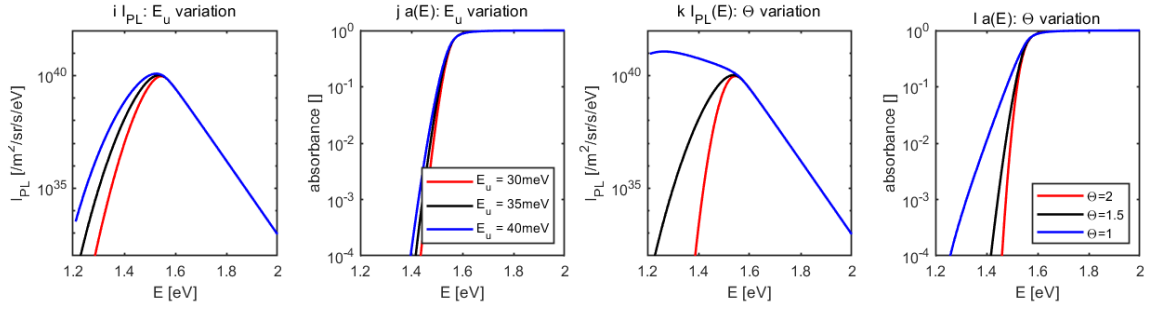*Figure R2 Emission de photoluminescence et coefficient d'absorption calculés à partir de la loi de Planck généralisée eq. (1 5). (a) (b) représente la variation de T, (c) (d) variation de Δμ, (e) (f) variation de Eu, (g) (h) variation i, (i) (j) variation de Eg, (k) (l) variation α₀z₀, tandis que les autres facteurs restent constants aux valeurs de (T = 300K, Δμ = 1,2V; E_u = 35meV; Θ = 1,5; E_g = 1,55eV; α₀d = 10)*

Dans la section 1.2, on dérive les équations décrivant le transport de charge dans un matériau photovoltaïque. Le modèle s'applique pour des populations d'électron et de trou à des pas de temps supérieurs à la picoseconde. On le démontre à l'aide d'un bilan local, prenant en compte la diffusion (coefficient de diffusion D_n), la dérive (mobilité $\mu_{n,p}$ et champ électrique E), génération $G_{n,p}$ et recombinaison $R_{n,p}$.

$$\frac{\partial n}{\partial t}(x) = G_n(x) \text{ - } R_n(x) + D_n \frac{\partial^2 n}{\partial x^2} + \mu_n \frac{\partial(n\,\mathrm{E})}{\partial x}$$

$$\frac{\partial p}{\partial t}(x) = G_p(x) \text{ - } R_p(x) + D_p \frac{\partial^2 p}{\partial x^2} \text{ - } \mu_p \frac{\partial(p\,\mathrm{E})}{\partial x} \tag{R-2}$$

Un intérêt plus particulier est accordé au terme de recombinaison. Ce dernier se décompose en une part non-radiative liée à des défauts, qu'on cherche à minimiser lors de la synthèse, et une part radiative que l'on observe avec la photoluminescence et qui est inhérente au matériau photovoltaïque. Les conditions aux limites du système différentiel décrit en (R-2) permettent d'inclure les recombinaisons aux interfaces, qui seront particulièrement étudiées au chapitre 4.

Dans la section 1.3, on propose une revue de littérature des avancées récentes dans la caractérisation optoélectronique des pérovskites halogénées, qui sera détaillée dans l'exposition de la problématique de chaque chapitre de résultats (3 à 6) ici.

Chapitre 2 : Dispositifs expérimentaux

Dans cette section, on donne les principes de fonctionnement des systèmes d'imagerie de luminescence utilisés dans cette thèse. L'imageur hyperspectral (HI) est décrit en premier (section 2.1). Ses acquisitions peuvent être vues à la fois comme une collection d'images spectrales (une image par "λ") ou comme une collection de spectres I_{PL} (une par pixel). Ces spectres sont exprimés en unités absolues (photons / eV / s / m² / sr) de luminance et peuvent donc être équipés de la loi de Planck généralisée. Vient ensuite le setup d'imagerie de fluorescence à résolution temporelle (TR-FLIM), qui donne des images I_{PL} résolues en temps (section 2.2). Les composants principaux de ce setup sont la caméra em-ICCD (PIMAX4, Princeton Instruments) et le laser pulsé (Talisker, Cohenrent), comme représenté sur le schéma ci-dessous en Figure R3.
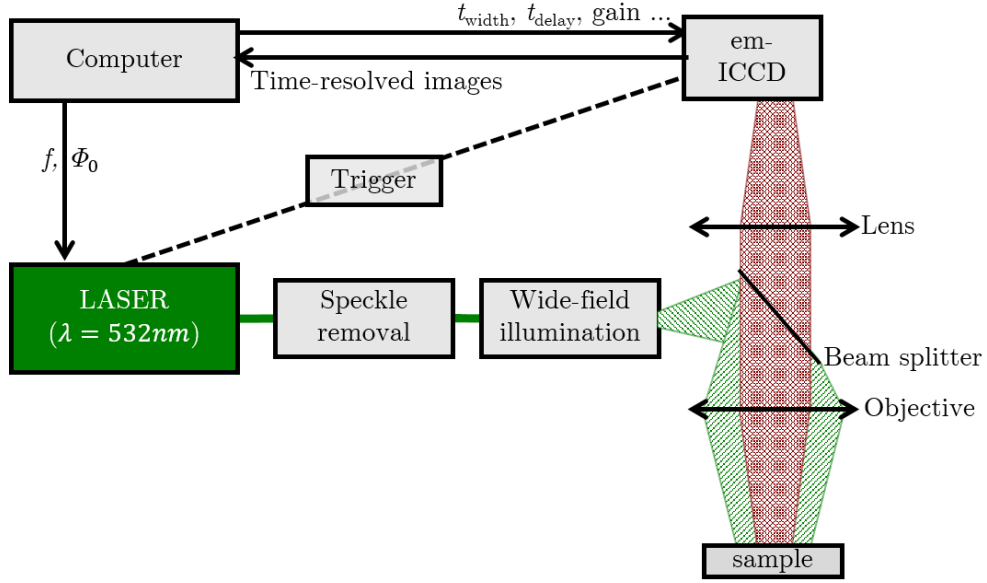
Figure R3 Schéma du set-up TR-FLIM (Computer : ordinateur / Time-resolved images : images résolues en temps / Speckle removal : filtre anti-speckle / Wide-field illumination : illumination grand champ / Lens : objectif / Beam Splitter : lame séparatrice / Objective : objectif / Sample : échantillon)

Finalement, une nouvelle configuration adaptée pour obtenir des images 4D I_{PL} (2D spatiale, spectrale, temporelle) est présentée (section 2.3). Cette configuration a été conçue par le candidat au doctorat et développée par un stagiaire de master sous sa supervision. Un brevet protégeant ses principes de fonctionnement a été déposé (numéro de dépôt 19315037.2). Il repose sur des principes liés à l'imagerie à pixel unique (SPI) ainsi que sur l'utilisation d'une caméra à balayage de fente.

Chapitre 3 : Transport de charge latéral dans une cellule PV

Dans ce premier chapitre expérimental, on introduit la TR-FLIM comme méthode de caractérisation optique des dispositifs optoélectroniques. Sous illumination à champ large, nous étudierons la diffusion latérale et la recombinaison des porteurs de charge minoritaires dans une cellule solaire à base d'arséniure de gallium (GaAs). Cette cellule sert de dispositif de validation de principe. En effectuant l'analyse de son signal I_{PL}, on entend démontrer la pertinence de la caractérisation optoélectronique par TR-FLIM. Dans un premier temps, les détails expérimentaux spécifiques à ce chapitre sont présentés (section 3.1). Ensuite, on mène une exploration approfondie des acquisitions en traçant les données le long de leurs dimensions spatiale et temporelle (section 3.2). Grâce à cette analyse de données, on arrive à concevoir un modèle adapté aux phénomènes physiques en jeu, à savoir le transport et la recombinaison dans le volume ou à proximité du contact (section 3.3). Le modèle est dérivé de l'équation de continuité et est ensuite résolu analytiquement. Une procédure de fit adapté aux données acquises par la TR-FLIM est développée et appliquée pour reconstruire les déclins I_{PL} expérimentaux (section 3.4). Les propriétés optoélectroniques clés du dispositif considéré seront ensuite extraites de ces ajustements. Enfin, on commente l'avantage particulier de l'éclairage à champ large (section 3.5).

Chapitre 4 : Transport de charge dans l'épaisseur d'une pérovskite

Dans ce chapitre, on se concentre sur les propriétés de diffusion dans les matériaux à base de pérovskite, car ils jouent un rôle crucial dans le fonctionnement des cellules solaires, au cours desquels les porteurs de charge se diffusent vers les couches de transport. Ces propriétés de diffusion ont deux aspects complémentaires: la sensibilité à un gradient de concentration de porteurs (coefficient de diffusion D) et le temps moyen disponible pour le processus de diffusion (durée de vie τ). Une large gamme de valeurs de D ont été rapportées dans la littérature. On propose ici d'évaluer D et τ en mesurant les déclins I_{PL} dans les couches de pérovskite.

On décrit d'abord brièvement le jeu d'échantillons considéré, qui inclut plusieurs compositions chimiques et conditions d'interface (section 4.1.1) et conduit à diverses performances PV (section 4.1.2). Après avoir présenté un aperçu du jeu de données (aspects spatiaux et temporels) dans la section 4.2, nous développons un modèle de transport de porteurs de charge capable de reconstruire les déclins I_{PL} dans la section 4.3. On ajuste les coefficients du modèle différentiel de transport pour qu'il reproduise les déclins I_{PL} acquis, ce qui permet de caractériser complètement le transport en profondeur et la recombinaison. Un exemple de reconstruction de déclins expérimentaux se trouve en Figure R4 (a-b) pour deux interfaces arrières différentes et 3 niveaux d'illumination croissants (Φ_0). La figure R4(c) représente l'évolution de l'erreur de reconstruction à proximité de la solution retenue, qui s'accroit rapidement pour des petits écarts de paramètres et témoigne de la précision du fit. Comme ces coefficients de diffusion et recombinaison ont été ajustés sur un jeu de conditions expérimentales assez large, ils s'appliquent en particulier pour décrire le comportement du matériau sous un éclairement constant de 1 soleil.
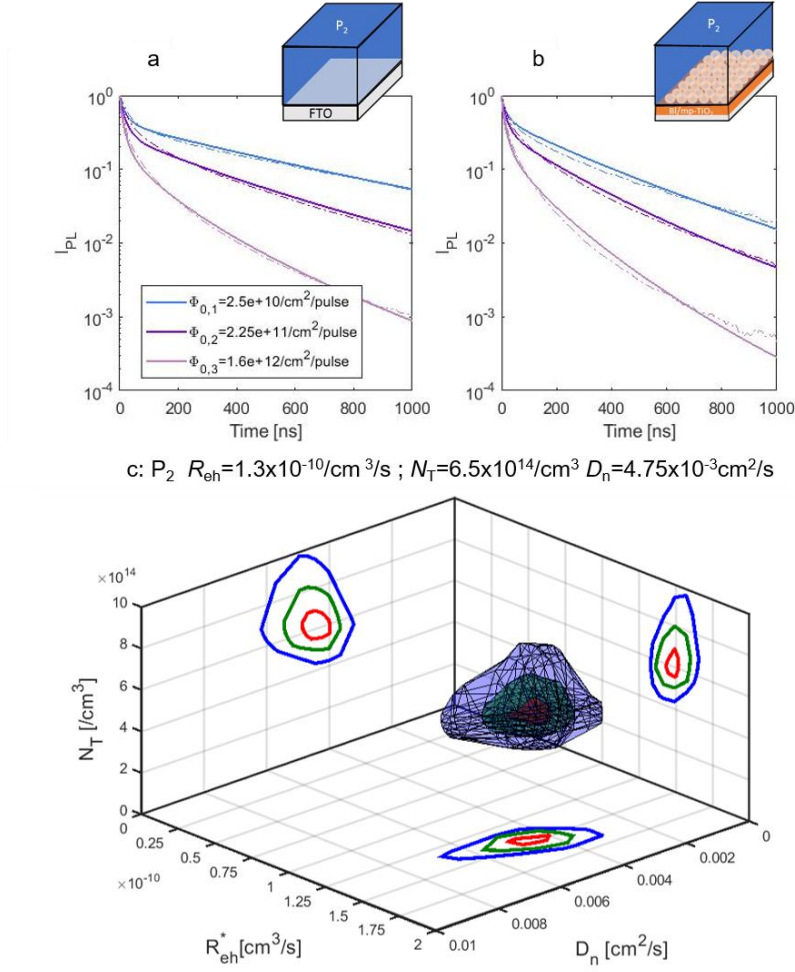
*Figure R4 Déclins de I_{PL} expérimentaux (lignes en pointillés) et ajustés numériquement (lignes simples) pour une perovskite à cations mixtes b). Différents ordres de grandeur du niveau d'illumination ont été testés. (c) Les iso-surfaces montrant un ensemble de paramètres (R_{eh} * D_n N_T) conduisant à une erreur de reconstruction ne dépassant pas 10% (rouge), 20% (vert), 50% (bleu) de l'erreur de reconstruction optimale.*

Cette expérience est réalisée dans différents absorbeurs de pérovskite. On en compare les résultats pour dégager des propriétés communes (section 4.4). Enfin, on discute de la validité de différents modèles et de la signification physique des paramètres d'ajustement dans la section 4.5.

Chapitre 5 : Transport de charge latéral dans une pérovskite

Le développement de cellules solaires à haute efficacité repose sur la gestion des propriétés électroniques et optiques qui doivent être mesurées avec précision. Au fur et à mesure que les rendements de conversion augmentent, un apport électronique et photonique concomitant affecte les performances globales des dispositifs photovoltaïques. On montre ici une méthode optique basée sur l'utilisation de techniques d'imagerie multidimensionnelles complémentaires (voir Figure R5-(b)). Elle nous permet de collecter et d'analyser le signal de luminescence avec une résolution spatiale, spectrale et temporelle élevée. On l'applique pour sonder plusieurs propriétés de transport de matériaux semi-conducteurs, permettant ainsi de découpler et de quantifier les

contributions électroniques et photoniques. Un exemple d'application est présenté sur une couche mince de pérovskite halogénée pour laquelle une large gamme de propriétés de transport est donnée dans la littérature, en fonction du procédé de fabrication du film mais également de la technique de mesure (voir section 1.3).

Nous nous concentrons ici plus précisément sur les utilisations antérieures de l'éclairage local sur une pérovskite. L'examen des images I_{PL} a permis d'évaluer la longueur de diffusion latérale des porteurs de charge et de souligner l'anisotropie du transport dans des films CH$_3$NH$_3$PbI$_3$ polycristallins non passivés. Des profils de diffusion résolus dans le temps ont également été observés et l'élargissement des profils I_{PL} permet de mieux comprendre la mobilité des porteurs. Néanmoins, les approches multidimensionnelles étaient toujours manquantes. En ce qui concerne le recyclage de photons, plusieurs études ont souligné ce processus optique dans l'absorbeur de pérovskite, soit en mettant l'accent sur le processus de recombinaison radiative lente, soit en soulignant la régénération des porteurs de charge à longue distance. Cependant, un modèle capable de décorréler les contributions électroniques et photoniques au transport fait toujours défaut.

Dans ce chapitre, on utilise la plate-forme d'imagerie I_{PL} développée sur des couches minces en pérovskite, grâce à laquelle on réalise une expérience optique quantitative basée sur un éclairage ponctuelle pulsé. Les détails expérimentaux spécifiques à ce chapitre sont présentés dans la section 5.1, avant que la section 5.2 ne donne un aperçu rapide de l'ensemble de données. Par son analyse, nous mettons en évidence la contribution d'effets optiques tels que le recyclage de photons ainsi que la propagation de photons lorsque la lumière émise est transportée latéralement sans être résorbée (section 5.3, également Figure R5(a)). Ce dernier effet doit être pris en compte pour éviter des propriétés de transport surestimées.

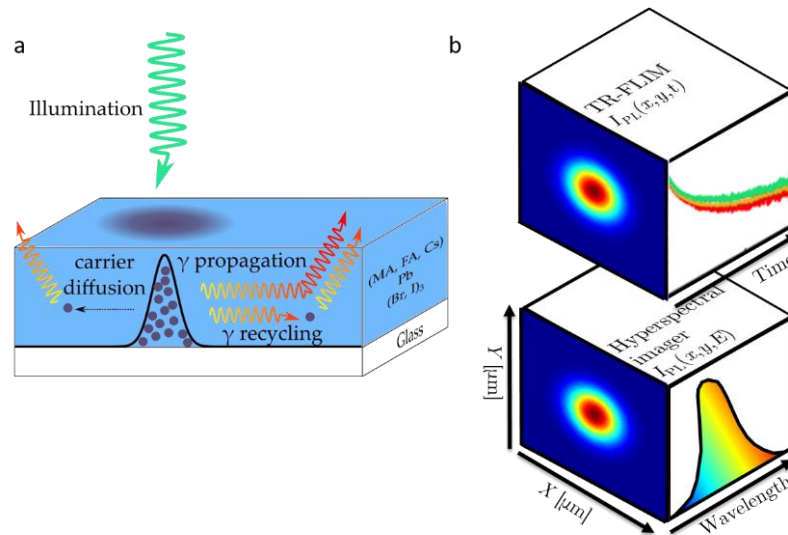*Figure R5 Schéma des observations expérimentales et des mécanismes physiques en jeu (a) Structure de l'échantillon et schéma montrant le mécanisme triple (diffusion des porteurs, propagation des photons et recyclage des photons) étudié ici (b) Schéma illustrant l'acquisition en 3 dimensions avec la fluorescence résolue en temps imagerie (TR-FLIM) ou hyperspectrale (HI), pour un éclairage ponctuel esquissé sur la face gauche.*

Dans la section 5.4, nous quantifions ces propriétés de transport en résolvant de manière rigoureuse l'équation de continuité dépendante du temps, donnant une méthode valable pour plusieurs matériaux semi-conducteurs (validation sur échantillons III-V InGaP produits à l'IPVF). La section 5.5 présente d'autres applications de la plateforme d'imagerie multidimensionnelle sur un échantillon présentant des hétérogénéités. (veinules à la surface de pérovskite riches en Cs).

Chapitre 6 : Transport de charge ambipolaire et migration ionique dans une pérovskite

La physique fondamentale et les différentes propriétés de transport des pérovskites aux halogénures n'ont pas encore été entièrement comprises et décrites En particulier, une compréhension profonde de l'interaction entre les phénomènes de transport électronique et ionique est cruciale pour l'optimisation de la collecte d'énergie après absorption de la lumière. C'est également une question fondamentale, car le mouvement ionique est généralement associé à la création de défauts, à des difficultés de contrôle du dopage et à la faible durée de vie des porteurs. On ne s'attend pas à ce qu'un conducteur semi-ionique soit aussi un excellent convertisseur photovoltaïque.

D'une part, le transport de charges électroniques dans les pérovskites aux halogénures a été étudié de manière approfondie à l'aide de méthodes optiques avancées, qui ont permis d'observer et de démêler les deux phénomènes principaux: la diffusion de charges et le recyclage de photons (également décrit au chapitre précédent). En raison de la faible énergie de liaison des excitons, les électrons et les trous se comportent comme des porteurs libres à la température ambiante. Dans la plupart des études, on suppose un transport de charge ambipolaire, la concentration de dopage étant connue pour être faible. Jusqu'à présent, seuls quelques éléments de preuve d'un transport équilibré électron / trou (à savoir, la mobilité électronique μ_n = la mobilité des trous μ_p) ont été fournis jusqu'à présent.

D'autre part, la migration des ions a été étudiée tôt dans les pérovskites aux halogénures. En 2014, Xiao et al. appliqué un champ électrique sur une structure latérale $CH_3NH_3PbI_3$ (MAPI) signalant un effet photovoltaïque commutable, expliqué ultérieurement par la migration des ions. La migration des ions est également considérée comme le principal responsable du comportement hystérétique des cellules PV. Malgré un grand nombre d'observations expérimentales, la physique derrière une telle migration ionique reste incertaine. En effet, leur énergie d'activation est toujours débattue, de même que l'influence des joints de grains et l'impact de la température et de la lumière. Les ions halogénures (I- / Br-) sont principalement concernés, étant donné que les MA^+ organiques / FA^+ et les Pb^{2+} inorganiques devraient dériver sur des échelles de temps beaucoup plus longues.

Dans l'ensemble, les interactions complexes entre les ions, les électrons et les trous ont récemment été soulignées, car il a été démontré que l'excès de porteurs de charge accélère la migration des ions et que la création de défauts induite par l'iodure a été

147

dérivée en théorie. Des modèles numériques de diffusion de la dérive tenant compte à la fois du mouvement des espèces ioniques et des porteurs de charge électroniques ont été proposés. Le groupe de recherche de H. Snaith a récemment présenté l'incorporation du BMIBF4, un sel ionique additif, comme moyen efficace de prévenir la migration des ions, ouvrant ainsi la voie à la stabilité du PSC.

Dans ce chapitre, nous présentons un ensemble d'expériences sous polarisation électrique basées sur une imagerie multidimensionnelle par luminescence afin de sonder le transport électronique individuel ainsi que le transport ionique. Grâce à l'imagerie multidimensionnelle, nous avons déjà pu étudier le transport latéral des porteurs de charge dans des pérovskites mixtes à base d'halogénures (chapitres 4, 5). Ici, la mesure des variations locales du signal de luminescence sous polarisation électrique permet un accès direct aux propriétés de collecte et de transport des porteurs de charge pour chaque type de porteur de charge. Dans une première série d'expériences, nous inhibons la migration des ions en appliquant une polarisation électrique pulsée et observons uniquement le transport électronique (section 6.2). Les images résolues dans le temps à l'échelle nanoseconde nous permettent de séparer les contributions individuelles d'électrons et de trous dans les mécanismes de transport. Les mobilités des porteurs sont déterminées à environ 0.3 cm^2 / V / s, avec une mobilité pour les trous deux fois supérieure à celle des électrons. Ensuite, nous appliquons un biais électrique plus long ($>$ 1 s) et mettons en évidence le rôle clé joué par la migration des ions dans les phénomènes de transport (section 6.3), ainsi que leur impact sur la recombinaison non radiative. Nous observons que l'enrichissement en halogénure induit un changement local de la composition chimique et diminue la bande interdite des matériaux. La mesure de la division du niveau de quasi-Fermi indique la formation de voies non radiatives dues à l'accumulation d'halogénures. Les conclusions de ce chapitre sont résumées dans la Figure R6.
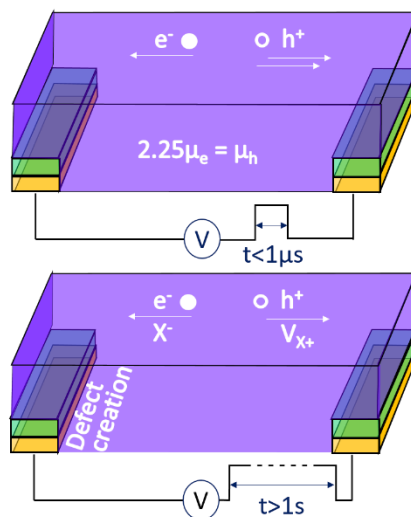

Figure R6 Résumé des 2 expériences à l'étude dans le chapitre 6. La couche mince de pérovskite (violet) est contacté latéralement par des couches d'ITO (vert) et or (jaune). Un biais électrique rapide (<1μs) ou plus long est appliqué. Le champ résiduel est de 2500V/cm, car on considère un canal de 20μm avec un potentiel électrique de 5V.

Conclusion

Cette thèse se concentre sur la description de méthodes optiques permettant d'évaluer quantitativement les propriétés de transport de porteurs de charge dans des absorbeurs et des dispositifs photovoltaïques. Les expériences consistent en l'application de techniques d'imagerie multidimensionnelle de luminescence. Elles incluent l'analyse spatiale, spectrale et temporelle du flux lumineux émis par des matériaux photovoltaïques sous excitation. Leur mise en œuvre a nécessité le développement d'assemblages optiques ainsi que de méthodes numériques de traitement de données. Deux configurations ont été principalement utilisées tout au long de cette thèse: (i) l'imageur hyperspectral (HI), qui permet d'accéder aux images à résolution spectrale (une image par longueur d'onde) et (ii) l'imageur à fluorescence à résolution temporelle (TR-FLIM) qui produit des images à résolution temporelle (une image par unité de temps). Alors que le HI était déjà complètement assemblé au début de ce travail, la configuration du TR-FLIM en était à un stade préliminaire et son développement s'était terminé au cours de la thèse. Ses deux composants principaux sont un laser pulsé et une caméra rapide. Ses principes de fonctionnement ont été décrits en détail et sa preuve de concept sur une cellule photovoltaïque de référence (à base de GaAs) a également été présentée. Il a démontré que TR-FLIM permet l'évaluation du transport de charge et des propriétés de recombinaison avec une seule expérience. En particulier, nous pourrions quantifier le transport de charge latérale dans l'appareil. Nous avons montré comment l'utilisation de l'éclairage et de la collecte à grand champ permettait de supprimer les artefacts liés à l'éclairage local. En outre, cet éclairage à large champ constitue un scénario d'excitation réaliste pour les matériaux et les dispositifs photovoltaïques, en raison de sa grande surface et de sa puissance relativement faible.

Nous avons ensuite utilisé ces techniques de caractérisation avancées pour étudier le transport de charges dans une classe émergente de matériaux aux propriétés photovoltaïques très prometteuses: les pérovskites aux halogénures. Tout au long de ce manuscrit, plusieurs expériences de transport ont permis de mettre en évidence la diffusion de porteurs de charge dans des pérovskites à halogénures mixtes. La première expérience était basée sur une excitation de surface importante, à la suite de laquelle les porteurs de charge diffusent en profondeur dans la couche mince de pérovskite. Par conséquent, nous pouvons sonder les propriétés de transport dans l'épaisseur de cette couche. De manière remarquable, il est possible de quantifier la recombinaison sur les surfaces avant et arrière ainsi que les mécanismes de recombinaison dans la masse. La deuxième expérience était basée sur une excitation ponctuelle, à la suite de laquelle le transport de charge est essentiellement radial, au moins après un certain temps où nous pouvons négliger la diffusion en profondeur. La diffusion des porteurs s'est distinguée du recyclage des photons, qui constitue un mécanisme de transport complémentaire par lequel un photon de luminescence est réabsorbé et régénère une charge. Là encore, la diffusion et la recombinaison des porteurs de charge ont été imagées avec une résolution temporelle et spectrale élevée. Cela a permis de les quantifier au moyen d'algorithmes

d'optimisation qui adaptent les résultats expérimentaux aux modèles physiques développés (équation de diffusion résolue dans le temps).

Les méthodes d'imagerie sont également adaptées à l'étude de l'impact des inhomogénéités chimique et morphologique sur les propriétés optoélectroniques locales. Ceci a été illustré par l'étude de l'influence des veinules apparaissant à la surface de la pérovskite riche en Cs. Nous avons remarqué que les caractéristiques morphologiques modifient les propriétés de découplage de la lumière, ce qui entrave l'analyse directe du signal I_{PL}. Nous avons également pu établir une corrélation entre les hétérogénéités chimiques, les variations de bandes interdites et celles de durées de vie. Ces corrélations soulignent le rôle bénéfique des rides riches en Cs dans les propriétés de transport. Néanmoins, il conviendrait de poursuivre le développement du couplage entre la modélisation 2D-3D et l'imagerie I_{PL} afin d'obtenir une quantification appropriée du transport dans des matériaux non homogènes.

Finalement, nous avons appliqué des techniques d'imagerie I_{PL} multidimensionnelles pour sonder des structures latérales dotées d'un canal pérovskite de 20 µm de large entre deux électrodes. L'objectif principal était d'aller plus loin que nos études précédentes et de séparer les propriétés de transport d'électrons et de trous, ce qui est difficile dans une couche intrinsèque telle que la pérovskite. La stabilité du matériau liée à la migration des ions devait également être prise en compte. En appliquant une polarisation électrique rapide sur le canal (<1 µs), nous avons d'abord isolé la dérive des porteurs de charge de celle des ions composant la pérovskite. Les mobilités des électrons et des trous ont été quantifiées séparément ($\mu_p/\mu_n = 2.25 \pm 0.23$). Leur valeur presque égale justifie leur traitement symétrique précédent (ambipolaire). Ensuite, des expériences à plus longue échelle (champ électrique appliqué pendant 10 minutes) nous ont également permis d'imager le transport des ions halogénures. Cette expérience multidimensionnelle nous a rapprochés plus que jamais des principes de fonctionnement d'un appareil PV, qui fonctionne avec lumière et biais. L'accumulation d'ions au niveau de l'électrode positive entraîne une réduction locale de la durée de vie des porteurs de charge.

En résumé, concernant le transport dans les pérovskites halogénées, nous pouvons affirmer que les recombinaisons aux interfaces constituent certainement le principal canal de perte dans les cellules solaires à pérovskite. Cette affirmation donne de précieuses orientations pour les prochaines approches synthétiques qui devraient se concentrer sur le design d'interfaces passivées. En ce qui concerne le transport de charges dans le volume de la pérovskite, nous avons systématiquement quantifié des valeurs relativement faibles de la mobilité des porteurs de charges (entre 0.2 et 1 cm² / V / s). Dans tous les cas, cette diffusion lente reste compensée par la longue durée de vie des porteurs de charge (1µs), ce qui garantit leur collecte dans un appareil PV. L'industrialisation des cellules solaires en pérovskite devra être précédée de réels progrès sur deux points majeurs : la stabilité des dispositifs et l' « upscale » des techniques de fabrication. L'ensemble des techniques de caractérisation introduites dans ce manuscrit s'appliquerait à une étude

traitant de ces questions. Du côté de la stabilité, les prochaines campagnes de mesure pourraient porter sur l'évolution des propriétés optoélectroniques du fait que le matériau est soumis à des contraintes environnementales (humidité, lumière, oxygène). Du côté de l'« upscale », la grande polyvalence de l'échelle micro à la macro pourrait permettre de localiser et d'identifier les défauts liés à la production à grande échelle. De plus, le fait de disposer d'images à résolution spectrale et temporelle disponibles à chaque étape de la production / du vieillissement met en évidence le besoin d'algorithmes de post-traitement efficaces, dans lesquels les approches d'apprentissage automatique pourraient jouer un rôle.

Pour approfondir encore ces études du transport de charges dans les pérovskites halogénées, une nouvelle configuration dédiée à l'imagerie I_{PL} 4D a été conçue. Il permet d'acquérir des ensembles de données I_{PL} 4D (2D spatiales + spectrales + temporelles en une seule expérience) en combinant le concept d'imagerie à pixel unique à une caméra à balayage. Comparé à une simple combinaison de configurations HI et TR-FLIM, il permet d'avoir une meilleure sensibilité optique (nous ne sélectionnons pas à la fois l'énergie et le temps de décroissance du signal), ainsi qu'une meilleure résolution temporelle et spectrale. Dans ce manuscrit, nous avons décrit ses principes de fonctionnement, protégés par un brevet déposé, ainsi que son développement initial réalisé avec l'aide d'un étudiant à la maîtrise. Une première preuve de concept obtenue sur une couche de pérovskite a été présentée. Cela a ouvert la voie à une caractérisation plus avancée des matériaux PV. Les prochains développements de cette configuration incluent notamment la calibration, grâce auquel on pourrait fitter l'hypercube acquis à la loi de Planck généralisée, afin de cartographier les QFLS avec une résolution de l'ordre de la picoseconde. Cela devrait révéler les mécanismes fondamentaux de séparation, de transport, de collecte et de recombinaison de charge en présence de champ électrique ou d'hétéro-interfaces qui présentent un grand intérêt pour le moment.

Communication & Recognition

Peer-reviewed publications:

1. A. Bercegol, G. El-Hajje, D. Ory, and L. Lombez, « Determination of transport properties in optoelectronic devices by time-resolved fluorescence imaging » *J. Appl. Phys.*, 2017, 122 (20), p. 203102

2. A. Bercegol, J.F. Ramos, A. Rebai, T. Guillemot, D. Ory, J. Rousset, L.Lombez, « Slow diffusion and long lifetime in metal halide perovskite for photovoltaics », *J. Phys. Chem. C*, 2018, 122 (43), pp 24570–24577

3. A. Bercegol, J.F. Ramos, D. Ory, A. Rebai, J-F. Guillemoles , J. Rousset, L. Lombez, « Spatial inhomogeneity analysis of Cs-rich wrinkles in triple cation perovskite », *J. Phys. Chem. C*, 2018 122 (41), pp 23345–23351

4. J. F. Ramos, S. Jutteau, J. Posada, A. Bercegol, A. Rebai, T. Guillemot, R. Bodeux, N. Schneider, N. Loones, D. Ory, C. Broussillou, G. Goaer, L. Lombez, J. Rousset « Highly efficient MoOx-free semitransparent perovskite solar cell for 4T tandem application improving the efficiency of commercially-available Al-BSF silicon » *Scientific Reports* 2018 8:16139

5. A. Bercegol, D. Ory, D. Suchet, S. Cacovich, O. Fournier, J. Rousset, L. Lombez, « Quantitative optical assessment of electronic and photonic properties in halide perovskite », *Nature Communications* 2019, 10:1586

6. A. Bercegol, S. Cacovich, S. Mejaouri, A. Yaïche, G. Vidon, J-B. Puel, C. Longeaud, J-F. Guillemoles, S. Jutteau, J. Rousset, D. Ory, L. Lombez, « Imaging electron, hole and ion transport in halide perovskite », *submitted* 2019

7. Ben Slimane, A. Michaud, O. Mauguin, X. Lafosse, A. Bercegol, L. Lombez, J-C. Harmand, S. Collin, « 1.73 eV AlGaAs/InGaP heterojunction solar cell grown by MBE with 18.7% efficiency », *Progress in Photovoltaics, under revision* 2019

8. S. Cacovich, D. Messou, A. Bercegol, S Bechu, A. Yaïche, H. Shafique, J. Rousset, P. Schulz, M. Bouttemy, L. Lombez, « Light-induced passivation in triple cation halide perovskites: interplay between surface chemistry and transport properties », *in preparation* 2019

Patent

1. A. Bercegol, D. Ory, and L. Lombez, « Time-resolved hyperspectral single pixel imaging (THYSPI) of low-emissive objects » *deposit number* 19315037.2 2019

Conference proceedings:

1. A. Bercegol, D. Ory, J. F. Ramos, A. Rebai, J. Rousset, L. Lombez, « Determination of transport properties in optoelectronic devices by time-resolved fluorescence imaging », *SPIE Photonics West Proceedings* 2018

2. A. Bercegol, G. El-Hajje, D. Ory, L. Lombez, « Time-resolved fluorescence imaging as a self-consistent characterization method for photovoltaic materials », *7th WCPEC Proceedings* 2018

3. A. Bercegol, J.F. Ramos, A. Rebai, D. Ory, J. Rousset, L. Lombez « Investigation of in-depth transport and absorption properties of various perovskite materials using luminescence imaging », *7th WCPEC Proceedings* 2018

4. A. Bercegol, D. Ory, L. Lombez, « Time-resolved imaging of lateral charge carrier transport in photovoltaic absorbers » *SPIE Photonics West Proceedings* 2019

5. A. Bercegol, D. Ory, D. Suchet, S. Cacovich, O. Fournier, J. Rousset, L. Lombez, « Quantitative optical assessment of electronic and photonic properties », *46th IEEE PVSC Proceedings* 2019

6. D. Ory, A. Bercegol, D. Suchet, M. Legrand, J-B. Puel, A. Michaud, A. Ben Slimane, S. Collin, S. Cacovich, O. Fournier, A. Rebai, J. Rousset, J-F. Guillemoles, L. Lombez, « Multi-dimensional luminescence imaging: accessing to transport properties », *46th IEEE PVSC Proceedings* 2019

7. A. Michaud, A. Ben Slimane, A. Bercegol, R. Lachaume, J-C. Harmand, J.F. Martin, S. Collin, « Elaboration of III-V top cell for tandem with Silicon », *46th IEEE PVSC Proceedings* 2019

Awards

45th IEEE PVSC: Graduate student assistant

46th IEEE PVSC: Finalist for best student award (presentation: « Quantitative optical assessment of electronic and photonic properties »)

36th EU-PVSEC: Student award (presentation: « Multi-dimensional imaging of electron/hole transport in triple cation perovskites »)

RÉSUMÉ

En optoélectronique, et dans le domaine du photovoltaïque en particulier, les méthodes d'analyse de luminescence servent à optimiser les dispositifs. Étant sans contact et non destructives, elles peuvent être utilisées à différentes étapes de la fabrication d'une cellule solaire. Elles s'appuient sur le fait que l'intensité de luminescence est directement liée au produit des concentrations de porteur de charges. Dans cette thèse, on s'intéresse plus particulièrement à l'imagerie multidimensionnelle de luminescence, qui inclut l'analyse spatiale, spectrale et temporelle de la luminescence des matériaux photovoltaïques. Sa mise en œuvre requiert le développement de montages optiques ainsi que de méthodes numériques de traitement des données. On s'appuie sur un imageur hyperspectral (spatial-spectral) et sur la TR-FLIM (spatial-temporel). La corrélation des résultats acquis permet l'étude d'une famille émergente de matériaux aux propriétés photovoltaïques prometteuses : les pérovskites halogénées. Leurs propriétés de transport électronique (diffusion/recombinaison), photonique et ionique sont caractérisées.

MOTS CLÉS

Transport de charge / Caractérisation optique / Photoluminescence / Pérovskite / Photovoltaïque

ABSTRACT

In optoelectronics, and in the field of photovoltaics in particular, luminescence analysis methods are used to optimize devices. Being contactless and non-destructive, they can be used at different stages in the manufacture of a solar cell. They are based on the fact that the luminescence intensity is directly related to the product of charge carrier concentrations. In this thesis, we focus on describing methods based on multidimensional luminescence imaging. This technique includes the spatial, spectral and temporal analysis of light flux emitted by photovoltaic materials. Its implementation requires the development of optical assemblies as well as digital methods of data processing. We rely on hyperspectral imaging (spatial-spectral) and TR-FLIM (spatial-temporal) techniques. Correlative analyzes of the acquired luminescence cubes enables the study of an emerging class of materials with very promising photovoltaic properties: halide perovskites. Their electronic (diffusion/recombination), photonic and ionic transport properties are characterized thanks to multi-dimensional luminescence imaging.

KEYWORDS

Charge transport / Optical chatacterization / Photoluminescence / Pérovskite / Photovoltaics